UNIVERSITAT DE BARCELONA

Study of cell response over nanopatterned ligands on diblock copolymer surfaces

Verónica Hortigüela Lázaro

Study of cell response over nanopatterned ligands on diblock copolymer surfaces

by

Verónica Hortigüela Lázaro

A thesis
submitted in partial fulfillment of the requirements for the degree of
Doctor of Philosophy in Biomedicine
Barcelona, 2017

Doctoral Program in Biomedicine
Institute for Bioengineering of Catalonia
Biomimetic systems for cell engineering group
Departament d'Enginyeries: Secció d'Electrònica

Verónica Hortigüela Lázaro	Elena Martínez Fraiz	Josep Samitier Martí
Ph.D. Student	Supervisor	Tutor

Table of Contents

Abstract

Cells in tissues are exposed to extracellular signals that integrate and appropriately translate into specific responses. Receptors at the cell membrane recognize a variety of soluble ligands, extracellular matrix proteins and molecules presented by the neighboring cells. Ligand-receptor recognition event triggers intracellular signal transduction pathways modulating the resulting cell function. Some receptors do not function individually as signaling units but require interactions and associations with other receptors in multimolecular complexes. This process is known as receptor clustering and is an evolutionarily preserved mechanism responsible for the integration of highly complex signals. Increasing evidences suggest that this exceptional integration is subjected to spatially controlled ligand distribution at the nanoscale. Recent developments in highly sophisticated nanofabrication approaches have allowed to experimentally address this detailed spatial regulation on cell signaling. However, it is still unclear how the nanoscale distribution of ligands can impact on the dynamics of receptor activation and signaling processes.

Herein we present a nanostructured platform to create patterns of ligands in regular nanosized (< 30 nm) clusters. We based our platform in self-assembled diblock copolymers composed of poly(styrene) (PS) and poly(methyl methacrylate) (PMMA) that tend to segregate into nanodomains. The hexagonal arrangement of the PMMA domains acts as template to be replicated by the ligand distribution. Thanks to the versatile functionalization strategy developed, any amine-bearing molecule can be covalently immobilized. The spatial distribution of ligand was analyzed by Atomic force microscopy (AFM) and stochastic reconstruction microscopy (STORM), unveiling the high level of fidelity between the nanopatterned ligands and the underlying polymeric template.

To validate these substrates as platforms for systematic study of receptor clustering processes, an adhesive peptide which promotes focal adhesion formation, was immobilized on the nanopatterned surfaces. While the overall ligand surface density was maintained constant, the spatial distribution of ligands showed a remarkable impact on focal adhesion formation. Cells on nanopatterns showed an increased number of focal contacts, which were, in turn, more matured

than those found in cells cultured on randomly presenting ligands. These findings suggest that ligand presentation in a clustered format might promote multivalent ligand-receptor interactions which can help to shed light on receptor oligomerization processes.

In addition, the nanopatterned substrates developed were used to investigate the dynamics of the process of Eph receptor assembly into oligomeric clusters upon stimulation with ephrin ligands. It is known that Eph receptor oligomer composition is crucial in the fine-tuning of receptor signaling, as it will trigger intracellular signals feedback which will modulate cell response. Oligomerization processes, which imply resolving the temporal evolution of nanometric size objects in diffusive environments such as cell membranes are beyond the reach of live-imaging tools. We in here resolve the oligomerization kinetics of the Eph receptor in live cells with the required spatial and temporal resolution by using an enhanced version of the Number and Brightness (eN&B) technique, which can discriminate with molecular sensitivity the oligomeric species. The results demonstrated that stimulation through surface-bound ligands with a random distribution was not sufficient to activate the receptor signaling. Conversely, when nanopatterned on our substrates, ligands effectively induced receptor oligomerization. In addition, surface-induced ligand clustering by our nanopatterning approach accelerated the dynamics of receptor oligomerization process when compared to antibody-induced ligand clustering. Such an efficiency was induced even when ligand surface coverage was 9-fold lower in the nanopatterned presentation. Therefore, our ligand presenting platform is thought to induce multivalent ligand-receptor interactions, and might be a useful strategy to precisely tune and potentiate receptor responses. It has promising applications in biotechnology and biomedicine, such as cell culture systems to provide insight into relevant receptor clustering processes and design of new bioactive materials and drug-delivery systems.

Abbreviations

ADAM	**A D**esintegrin **A**nd **M**etalloprotease
AFM	**A**tomic **F**orce **M**icroscopy
AGE	**A**lkyl **G**lycidyl **E**ther
ALP	**A**lkaline **P**hosphatase
APC	**A**ntigen **P**resenting **C**ells
APTES	(3-**a**mino**p**ropyl)**t**ri**e**thoxy**s**ilane
ATR-FTIR	**A**ttenuated **T**otal **R**eflection-**F**ourier **T**ransform **I**nfrared **S**pectroscopy
BCP	**B**lock **C**o**p**olymer
BCPML	**B**lock **C**opolymer **M**icelle **L**ithography
BSA	**B**ovine **S**erum **A**lbumin
CCD	**C**oupled **C**harge **D**evice
CGRGDS	Cysteine-glycine-arginine-glycine-aspartic acid-serine
CL	**C**olloidal **L**ithography
DAPI	4 ',6-**d**i**a**mino-2-**p**heni**l**indol
DMEM	**D**ulbecco's **M**odified **E**agle **M**edium
DMSO	**D**i**m**ethyl **S**ulf**o**xide
DNA	**D**eoxyribo**n**ucleic **A**cid
DPN	**D**ip-**p**en **N**anolithography
DTGS	**D**euterated **T**ri**g**lycine **S**ulfate
EBL	**E**lectron **B**eam **L**ithography
ECM	**E**xtra**c**ellular **M**atrix
EDC	N-(3-dimethylaminopropyl)-N'-ethyl carbodiimide
EGFR	**E**pidermal **G**rowth **F**actor **R**eceptor
ELISA	**E**nzyme-**l**inked **I**mmuno**s**orbent **A**ssay
EMCCD	**E**lectron **M**ultiplying **C**harge **C**oupled **D**evice
eN&B	**e**nhanced **N**umber and **B**rightness
EPH	Erythropoietin-producing Human Hepatocellular Receptors
FA	**F**ocal **A**dhesion
FAK	**F**ocal **A**dhesion **K**inase
FBS	**F**etal **B**ovine **S**erum
FFT	**F**ast **F**ourier **T**ransform
FIB	**F**ocus **I**on **B**eam
FITC	**F**luorescein **i**so**t**hio**c**yanate
FPALM	**F**luorescence **P**hoto**a**ctivation **L**ocalization **M**icroscopy
fPS	**P**oly**s**tyrene **f**raction
FT-IR	**F**ourier **T**ransformed-**I**nfra**r**ed Spectroscopy

FWHM	**F**ull **W**idth at **H**alf **M**aximum
GFOGER	Glycine-fenilalanine-hydroxyproline-glycine-glutamic acid-arginine
GFP	**G**reen **F**luorescence **P**rotein
GTP	**G**uanosine-5'-**t**ri**p**hosphate
H NMR	**H N**uclear **M**agnetic **R**esonance
HA	**H**yaluronic **A**cid
HEK	**H**uman **E**mbryonic **K**idney
HEX	**Hex**agonal
HIV	**H**uman **I**mmunodeficiency **V**irus
IBM	**I**nternational **B**usiness **M**achines
IDA	**I**mino**d**i**a**cetic group
IgG	**I**mmuno**g**lobulin **G**
LAM	**Lam**ellar
MAA	**M**eth**a**crylic **a**cid
MMA	**M**ethyl **m**eth**a**crylate
MSC	**M**esenchymal **S**tem **C**ell
N&B	**N**umber and **B**rightness
nano-FTIR	**F**ourier **T**ransform **I**nfra**r**ed **Nano**spectroscopy
NHS	**N**-**h**ydroxy**s**uccinimide
NIL	**N**ano-**i**mprint **L**ithography
NMR	**N**uclear **M**agnetic **R**esonance
NSOM	**N**ear-field **S**canning **O**ptical **M**icroscopy
ODT	**O**rder-**d**isorder **T**ransition
PALM	**P**hoto**a**ctivated **L**ocalization **M**icroscopy
PBS	**P**hosphate **B**uffered **S**aline
PDI	**P**oly**d**ispersity **I**ndex
PDMS	**P**oly(**d**i**m**ethyl **s**iloxane)
PEG	**P**oly**e**thylene **G**lycol
PEO	**P**oly(**e**thylene **O**xide)
PFA	**P**ara**f**orm**a**ldehyde
PFOS	Trichloro(1H,1H,2H,2H-**p**er**f**luoro**o**ctyl) **s**ilane
PFOT	**P**er**f**luoro**o**ctane**t**hiol
PH	**P**otential of **H**ydrogen
PHEMA	**P**oly(2-**H**ydroxy**e**thyl **M**eth**a**crylate)
PLA	**P**oly(**l**actic **a**cid)
PLL	**P**oly-**L**-**l**ysine
PMAA	**P**oly (**M**eth**a**crylic **A**cid)
PMMA	**P**oly (**M**ethyl **M**eth**a**crylate)
PMPI	N-(**p**-**m**aleimido**p**henyl)**i**socyanate
PS	**P**oly**s**tyrene

PSA	**A**lkyne-functionalized **P**oly**s**tyrene
PVDMA	**P**oly(2-**v**inil-4,4-**d**i**m**ethyl**a**zlactone)
RESOLFT	**R**eversible **S**aturable **O**ptically **L**inear **F**luorescence **T**ransitions
RGD	Arginine-glycine-aspartic Acid Peptide
RMS	**R**oot **M**ean **S**quare
RPM	**R**evolutions **P**er **M**inute
RTK	**R**eceptor **T**yrosine **K**inases
SAM	**S**elf-**a**ssembled **M**onolayer
SEM	**S**canning **E**lectron **M**icroscopy
SMAC	**S**upra**m**olecular **A**ctivation **C**lusters
SPL	**S**canning **P**robe **L**ithography
SPR	**S**urface **P**lasmon **R**esonance
SSIM	**S**aturated **S**tructured-**i**llumination **M**icroscopy
STED	**St**imulated **E**mission **D**epletion
STM	**S**canning **T**unneling **M**icroscopy
STORM	**St**ochastic **O**ptical **R**econstruction **M**icroscopy
TBS	**T**ris-**B**uffered **S**aline
TCR	**T C**ell **R**eceptor
TEM	**T**ransmission **E**lectron **M**icroscopy
THF	**T**etra**h**ydro**f**uran
TIRF	**T**otal **I**nternal **R**eflection **F**luorescence
TK	**T**yrosine **K**inase
TLD	**T**hrough the **L**ens **D**etector
TMR	**T**etra**m**ethyl**r**hodamine
UHV	**U**ltra**h**igh **V**acuum
UV	**U**ltra **v**iolet
VISP	**Vi**sual **S**ervoing **P**latform
WCA	**W**ater **C**ontact **A**ngles
XPS	**X**-ray **P**hotoelectron **S**pectroscopy
3D	**T**hree-**d**imensional

1. Introduction

In living organisms, cell function is a hierarchical orchestrated phenomenon governed by a multitude of simultaneous cellular processes arising at different spatial and time scales. Cells can interact, recognize and specifically respond to a vast range of physico-chemical cues.[1–3] The remarkable ability to coordinate these inputs ensures the proper functioning of cells. When this network integration malfunctions, complications on the signaling mechanisms emerge, which may lead to functional disorders of cells or even a pathological condition for the organism.[4,5] Understanding of the dynamic combination of molecular interactions will be vitally important for advanced therapeutic and healthcare applications.

Cell membrane serves as the intercommunication system where cell receptors differentially integrate the information provided by soluble factors, extracellular matrix proteins, external mechanical stimuli and neighboring cells (Figure 1).

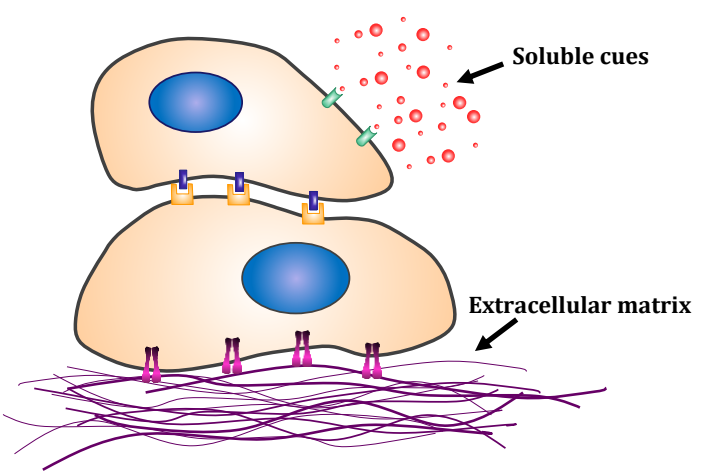

Figure 1. Cell microenvironment. Cell behavior is regulated by intricate molecular interactions between cells and the extracellular microenvironment. Signaling molecules can arise from soluble cues, neighboring cells and extracellular matrix (ECM) (extracellular molecules secreted by cells that provide them with structural and biochemical support).

This multifactorial microenvironment encompasses complex molecular interactions at the micro and nanometer scales. Numerous relevant cellular processes such as cell shape, adhesion, motility, differentiation and gene expression are spatially modulated, meaning that signal intensity variations at the

micro and nanoscale drive varying cellular outcomes.[6–8] Thus, the spatial arrangement of cell receptors on the cell membrane is a crucial factor controlling the downstream signaling pathways and related functions. This has been evidenced in diverse well-preserved processes such as stem cell differentiation, adaptive immune response, axon guidance or cell adhesion.[9–11] Deciphering the intriguing signaling pathways involved in cell function has been addressed mainly from the biomolecular facet. However, the understanding of the spatial aspects guiding cellular responses remains incomplete.[12] In the context of immune recognition, a pertinent clustering and reorganization of proteins on the plasma membrane of lymphocytes and antigen presenting cells triggers the formation of the immunological synapse.[13,14] The spatial arrangement of integrin receptors play an essential role in the dynamics of the so-called focal adhesion contacts, which rule cell adhesion.[15,16] Focal adhesions contacts are hierarchical complexes of cytosolic recruited molecules rooted on a cell membrane portion where integrins, the receptors responsible for cell adhesion, link the cell membrane with the extracellular matrix (ECM) when displaying a proper spatial arrangement. Therefore, it is highly pertinent to explore those molecular processes with the required spatiotemporal resolution to provide a better understanding of the underlying mechanisms through which cells interpret the spatial organization of signaling molecules. The complexity of those fundamental questions regarding information processing requires of a multifactorial analysis.

The goal of bioengineered materials is to mimic the native cell micro and nanoenvironments by the spatially controlled presentation of biologically relevant molecular signals.[12] These materials provide unique tools to discriminate the effects of individual biomolecular cues by modifying, for instance, their concentration, local density or spatial distribution. In that sense, the specific contribution of each variable to a given cellular process can be unambiguously identified. Combining the information extracted from those interfaces it would be possible to understand and predict the cell behavior.

The successful transition of biomaterials from experimental investigations to clinical applications lies in the faithful recapitulation of the physical and biochemical features of the microniche.[17,18] To this end, advances in biomolecule patterning have enable the design of biomaterials with controlled size features that span from the micrometer to the nanometer scale. Bioactive molecules immobilized on two-dimensional substrates have allowed the investigation of

fundamental questions regarding cellular interactions with their environment, contributing to build strong foundations for developing three dimensional scaffolds that more closely mimic the *in vivo* conditions.[19–21]

1.1. Top-down and bottom-up techniques for biomolecular micro and nanopatterning

Nanotechnology has facilitated unprecedented growth of knowledge of the specific properties related to fascinating nanostructures and procedures to construct engineered nanomaterials. Fabrication techniques to produce nanometric features are commonly classified into top-down and bottom-up approaches. The top-down patterning techniques stem from the traditional methods of the semiconductor industry where continuous efforts are exerted towards miniaturization of electronic devices.[22,23] Dimensional limits are reduced to increase the capabilities of semiconductor fabrication technology and currently feature sizes are approaching atomic dimensions.[24] Manufacturing improvements have prompted innovations in information technology (electronics and photonics) and renewable energy alternatives, but they also have revolutionized medical and bioengineering applications. DNA microarray platforms contributed to a rapid and high-throughput identification of single nucleotide polymorphisms associated with genetic variants and diseases.[25] The reduction of DNA patterned features to nanoarrays have enable the parallel sequencing of human genome with high accuracy and affordable cost.[26] A very impressive example of a miniaturized biosensor was recently given by Lee *et al*. who fabricated an antibody nanoarray *via* Dip-pen nanolithography (DPN) in order to detect HIV Type1 in blood plasma. The nanometric platform not only detected the antigen but even exceeded the detection limit of the conventional ELISA immunoassay by more than 1000-fold.[27] Biomaterials with nanotopographical features[28] guide the cell growth and determine differentiation responses of stem cells by alterations in cell adhesion.[11,28,29]

A common hallmark for top-down techniques is the gradual reduction in size of a bulk material to form objects at the micro- or nanoscale by physical or chemical treatment. Well-defined patterns are imposed on the substrates by means of a mask or a master. The most common top-down techniques include: lithographic methods such as photolithography, electron beam lithography and focus ion beam lithography; molding and embossing methods such as nanoimprint

lithography, and printing methods such as microcontact printing from soft lithography fabricated stamps (Figure 2).[30,31]

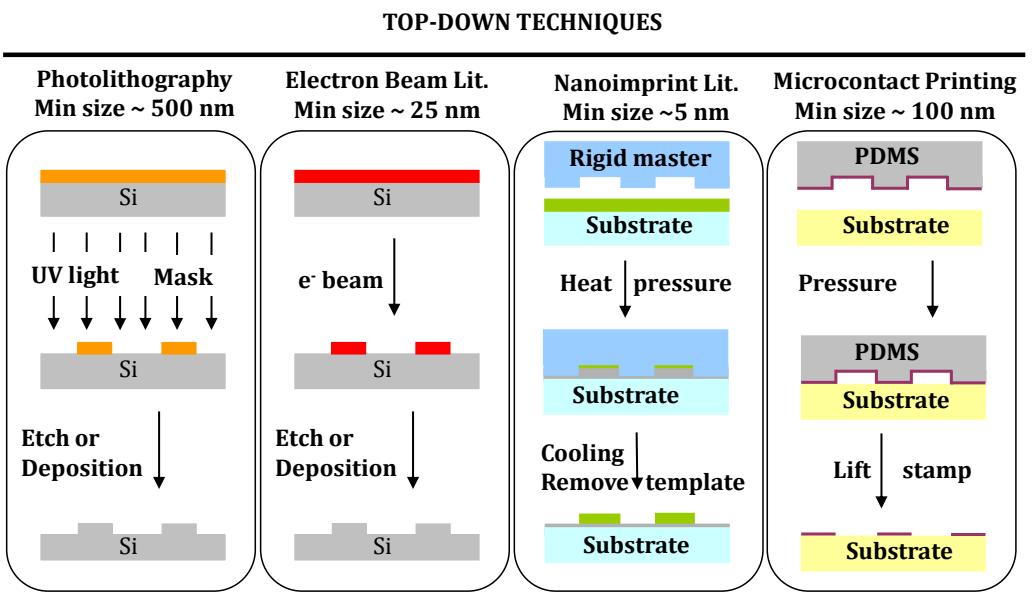

Figure 2. Overview of the some top-down fabrication methods presented in the text

Photolithographic techniques rely on the exposure of a photosensitive material to electromagnetic irradiation, which alters its chemical properties to make it more or less soluble in a developing solution. A patterned photomask can be placed between the energy source and the photoresist, mediating the transfer of the pattern signature. Topographical structures resulting after the development of the photoresist are commonly used as masks for further etching steps or deposition of additional material. Ultraviolet (UV) light has been extensively used for micropatterning fabrication in electronic applications, integrated circuits manufacturing, microfluidic devices and biomaterials[30,32]. However, the lateral resolution of the pattern is dictated by the light diffraction limit and nanoscale-sized features are out of the reach for conventional photolithography.

To overcome light diffraction issues and produce smaller features, an electron beam can be used. Electron beam lithography (EBL) is the practice of scanning a focused beam of electrons over a surface coated with an electron sensitive material to define micro- and nanostructures.[33] The resolution obtained is greatly influenced by the beam spot size, which is focused by magnetic lenses. Features in the order of tens of nanometers can be produced. Adsorbed collagen bundles were confined on 30-90 nm chemically modified patterns prepared by this

technique, nanostructures which are significantly smaller than the length of the collagen molecule (300 nm).[34] Even narrower lines with 5-7 nm in width have been patterned over poly(methyl methacrylate) (PMMA) resist.[35] As drawbacks, this technique requires high-cost equipment and it is a time-consuming multi-step process. Each individual feature is sequentially written into a reduced area of the surface rather than produced in parallel. Moreover, to perform systematic cellular studies, a large number of reproducible substrates should be used. To improve the fabrication rate, the nanostructured substrates can be repeatedly used as hard masters, replicated by soft lithography or nanoimprint lithography (which are explained below). Surface gradients of digital nanodot arrays (100 nm in diameter) were initially patterned by EBL and faithfully reproduced by nanocontact printing, accomplishing a noticeable cost-reduction. Gradients of nanodots modified with adhesive ligands were used to investigate C2C12 mouse myoblast cells spreading and migrating rates.[36]

The electron beam is replaced by an ion beam focused on the surface through electrostatic lenses in a type of top-down microfabrication approach named focused ion beam (FIB) lithography. As a maskless technique, patterns can be directly transferred to the substrate by the selective etching or deposition of materials.[30] Focused ion beam lithography has a high spatial resolution, down to a few tens of nanometers. Oligonucleotide nanopatterns with sub-micrometer features have been created (stripes down to 100 nm in width).[37] Still, this lithographic technique suffers from relevant limitations because it is time-consuming and expensive.

Nanoimprint lithography (NIL) is a molding-based technique that replicates the three dimensional relief template of a hard mold, often generated by a more expensive technique (such as EBL) on a polymeric thin film or sheet by applying pressure and increasing the temperature. A thin film or sheet of a thermoplastic polymer with a relative low glass transition temperature is placed in contact with the master forming a sandwich. Under temperatures above the glass transition temperatures of the polymeric materials and high pressures, the polymer flows adopting the complementary topography of the hard mold. This technique has been applied to transparent biocompatible thermoplastic polymers such as PMMA or poly(lactic acid) (PLA).[38] Biocompatible materials displaying disordered nanotopographic features have potential applications in osseointegration of prosthetic implants.[39] Nanostructured PMMA substrates with

disordered 120 nm pits induced the production of bone mineral on human mesenchymal stem cells.[40]

Of particular interest in the biomedical field is a molding technique called soft lithography. This technique utilizes a hard microstructured master (mold) that is replicated by elastomeric materials. Poly(dimethyl siloxane) (PDMS) is the most common elastomer, but soft lithography offers access to a broader range of biocompatible materials.[41] The use of flexible elastomers enables pattern transfer to substrates with non-planar geometries.[42] Basic shapes are mainly designed for cell culture assays, including microgrooves, micropits or micropillars in an ordered or random disposition. Substrate microtopography on PDMS substrates has been reported to regulate cell function and direct cell fate of different stem cell types, including neuronal stem cells, mesenchymal stem cells or neural progenitor embryonic stem cells.[11] Although soft lithography still resorts to photolithography, EBL or FIB for master manufacturing, the polymer replicas can be prepared outside a clean room, reducing the fabrication costs.

Taking advantage of microstructured PDMS replicas produced by soft lithography, microcontact printing technique basically transfers adsorbed molecules from the surface of PDMS (now called stamp) onto a substrate by conformal contact between the stamp and the surface.[43] Before printing, the PDMS stamp is immersed in a desired molecule solution, for example with a determined protein concentration. The stamp is then placed onto the substrates and a controlled pressure is applied, so that the molecule pattern is transferred to the surface. Microcontact printing was originally developed in 1993 for patterning of self-assembled alkanethiol monolayers on gold, but their applications for biological studies have thrived in multiple directions including protein patterning, DNA patterning and cell confinement.[44,45] Stamps made of alternative materials offered advantages such as the ones reported for a new polyolefin plastomer, which facilitated the fabrication of fibrinogen patterns with sub-micrometer resolution.[46] Serial repetition of microcontact printing process can be applied on a single substrate varying feature sizes or ink solutions to create multicomponent microscale patterns.[47,48] To increase resolution, microcontact printing is combined with molds produced by electron beam lithography.[36,49]

The selection of one of the mentioned top-down approaches for protein nanopatterns is subjected to a compromised decision between resolution, time and cost. High-throughput techniques are limited by the feature size resolution

and pattern fidelity when patterning sub-100 nm features. Nanopatterns with the nanometer-size resolution are time consuming and require expensive and highly specialized equipment.[31] In particular, biomedical applications usually require a lot of replicas of samples containing large areas (larger than 1 cm^2) of highly-dense patterns. Therefore, manufacturing of nanopatterned biomaterials with dimensions in the range of 10-100 nm is hardly achieved by conventional top-down techniques or otherwise, cost ineffective.

The bottom-up approaches inferred a revolution in the way materials are made. It turns upside-down the usual direction of the fabrication process and gets rid of expensive equipment. Starting from the fundamental components, atoms and molecules are assembled to form macromolecular complexes. Molecular interactions drive molecules to arrange themselves in a determined and predictable way. This auto-organization is termed self-assembly and has been of immense interest due to its potential to yield desired features at the nanoscale. Self-assembly provide periodically ordered nanostructures (Figure 3).[50] To control the rearrangement of the building blocks, a thorough understanding of the intra- and intermolecular forces is mandatory. Short-range forces of attraction and repulsion such as, electrostatic forces or Van der Waals forces, will drive the molecules to self-assemble and build up specific structures.[51] In nature, many cellular structures follow these rules: phospholipids are arranged in an amphiphilic bilayer comprising the plasma membrane or cytosolic proteins interact to create supramolecular structures.[52,53] Manufacturing nanomaterials through self-assembling methods stems from the appropriate design and synthesis of the building blocks to encode the sufficient information for a precise macromolecular assembly.[54] In general, the length scale of building units are below the size of the target construct. A myriad of nanoscopic geometries have been created from organosilanes, DNA molecules, block copolymers o colloidal crystals among other materials.[55–57] Currently, the primary challenges associated with self-assembled systems involve complex geometries and long-range ordering.

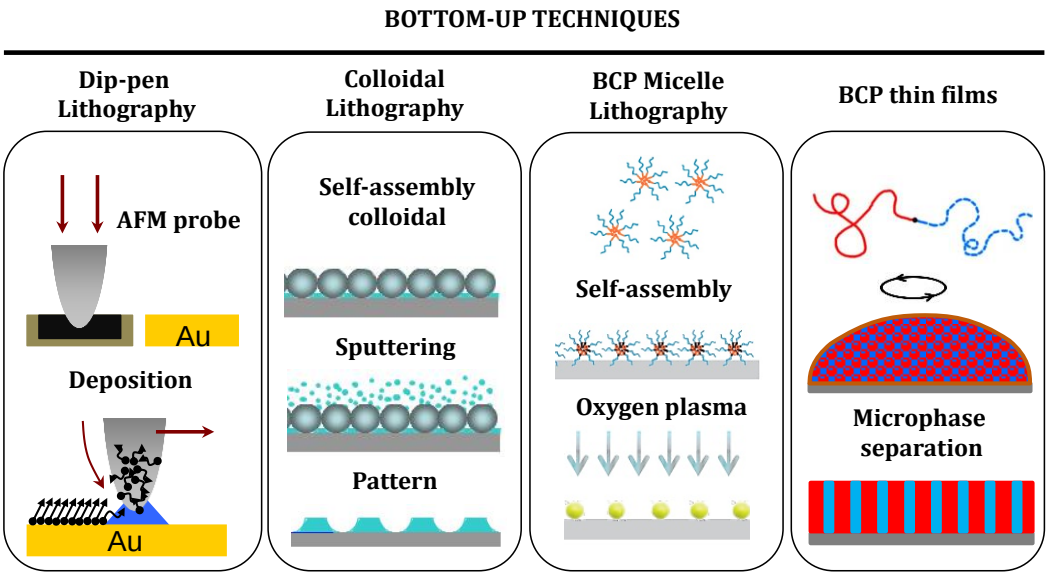

Figure 3. Overview of some of the bottom-up fabrication methods presented in the text

Considered a direct writing technique, scanning probe lithography (SPL) encompasses a group of techniques that have as common feature that a micro- or nano sized probe is scanned over a surface producing the pattern (Figure 3). SPL techniques include scanning tunneling microscopy (STM), atomic force microscopy (AFM) and near-field scanning optical microscopy (NSOM). Dip-pen nanolithography (DPN) provide access to self-assembled biomolecule patterns using an Atomic Force Microscopy (AFM) probe as a drawing tool. From the AFM tip, molecules can be chemically deposited on a substrate under strict control over humidity. DPN is regarded as a versatile approach to create stable DNA and protein nanopatterns on diverse substrates for biosensor applications and cellular assays.[58,59] Recent innovations in the field offer multiplexing possibilities with the simultaneous deposition of phospholipid membranes with different functionalities on glass or graphene substrates for biosensor applications.[60] The biomimetic membrane patterns (200 nm width and 500 nm spaced) selectively modified with antibodies were able to induce T-cell activation,[61] which demonstrated the suitability of DPN for protein nanopatterning. However, the reduction of the feature size beyond sub-100 nm is extremely difficult, while the technique suffers from slow write speeds for large patterns.

As an interesting alternative to conventional lithographic masks, colloidal crystals can self-assemble into highly packed arrays generating interparticle spaces with nanometer dimensions. Colloidal lithography (CL) can be used for

nanopatterning of macroscopic areas by coupling the array formation with some additional processing either by deposition or etching of a polymeric material.[57] Topographic nanopatterns of cylindrical columns (100 nm in diameter) were obtained when closely-packed sulphate modified polystyrene beads were etched by EBL. An increase in cell filopodia projection was reported for anchorage dependent cells cultured on such nanocolumns, suggesting the role of filopodia as information recruiters of the surrounding microenvironment.[62] Organosilane nanostructures with varying coverage and periodicity (periodicity ranges limited to 100 nm) were patterned by vapor deposition using different mesosphere diameters as colloidal masks.[63] Compared with other lithographic techniques, colloidal lithography is a practical approach to generate nanopatterns over large areas without expensive instrumentation.

Block copolymer (BCP) self-assembly is a rapid, inexpensive and versatile technique to access nanofeatures ranging from 5 to 200 nm.[64] Block copolymers are molecules comprised of two or more immiscible polymer fractions joined end to end by a covalent bond. Block copolymers undergo microphase separation due to the immiscibility between covalent-linked blocks (Figure 4). The resultant microdomains can be easily tuned in size according to their relative composition, the chain molecular weight, the chain architecture and the fabrication conditions.[65,66] The potential uses of block copolymers in nanotechnology are diverse including nanostructured membranes, high-density information storage devices, solar cells, or nanopatterning.[67] Focused on the applicability of block copolymers on protein nanopatterning, two main configurations have been explored: block copolymer micelles and block copolymer thin films.

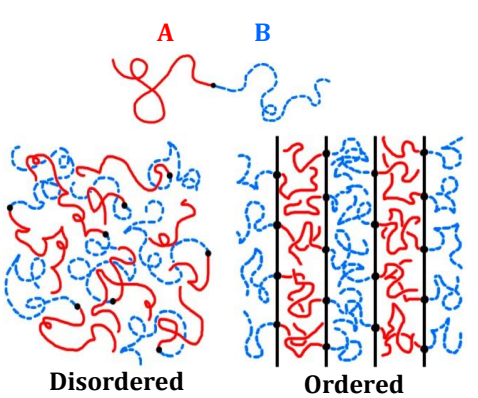

Figure 4. Block copolymer comprised of two immiscible blocks (A and B) that self-assemble into ordered parallel structures.

Block copolymer micelle lithography (BCPML) exploits the self-organization of diblock copolymers micelles to generate nanoparticle arrays (Figure 3).[55] A transition metal salt is carried as a cargo inside the polar core of diblock copolymer micelles in solution. By oxygen plasma treatment, polymer chains are removed from the surface leaving a regular pattern of nanoparticles. The nanoparticle size and spacing can be controlled by the concentration of the metal precursor and the molecular weight of the polymer, respectively. Applying these principles, Spatz and co-workers performed an impressive work where hexagonal lattices of gold nanoparticles were fabricated with a characteristic lattice period ranging from 30 nm to 140 nm.[68,69] Single thiol-peptides were bound to the Au-nanoparticle arrays, replicating the defined spatial distribution of gold nanoparticles. Relevant findings have shed light into cellular processes including focal adhesion formation and mechanosensing thanks to a tight control of order parameters such as interligand spacing, local ligand density, and global ligand density among others.[70,71]

On the other side, block copolymers self-assembled in thin films result in domains with reduced sizes and high periodicity (10 nm).[72] Densely packed nanostructures with different geometries can be generated by block copolymer self-assembly, which is considered a high-throughput method with low-associated costs. Easily tunable self-assembled nanostructures could be a viable approach to control the precise spatial distribution of protein patterns at the nanometer scale. For this reason, nanostructured templates produced by block copolymer self-assembly will be extensively review in the next section.

1.2. Block copolymers

Block copolymers are molecules comprised of two or more immiscible polymer fractions joined end to end by a covalent bond that tend to self-assemble into a wide variety of well-ordered structures.[73] Currently, block copolymers are synthetized by living anionic polymerization. This process requires a continuous presence of a living chain that remains free of termination or transfer reactions. Monomers are sequentially added and polymerized. A high degree of molecular complexity can be achieved by the combination of two, three or even more types of monomers ordered into diblock, triblock, alternating block or random block copolymers.[74] Another factor providing complexity to the system is the final chain

architecture, which under controlled conditions may result in linear or star-like chain configurations (Figure 5).

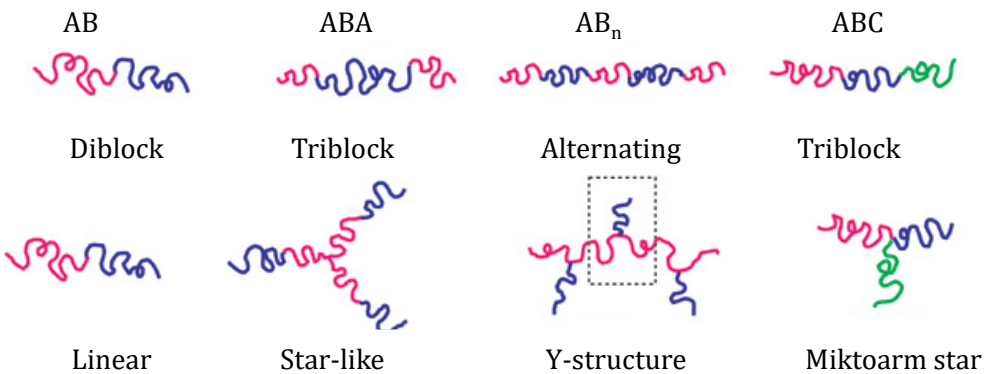

Figure 5. Some examples of well-studied block copolymer architectures including linear di-, tri- and alternating copolymers, star-like structures, and more complex symmetries such as Y structures, and miktoarm star terpolymer. Adapted with permission from Macmillan Publishers Ltd: Nature materials [74], Copyright (2005).

The ability of block copolymers to spontaneously yield nanometer-sized features has been historically examined in bulk morphologies.[75] Block copolymer self-assemble into periodic structures ranging from body-centered cubic spheres, hexagonally packed cylinders, lamellae or more complex morphologies, mainly depending on four independent parameters: the Flory-Huggins segment-segment interaction parameter (χ), the degree of polymerization (N) the block volume fraction (f) and the molecular architecture (Figure 6).[76] The Flory Huggins interaction parameter describes the incompatibility of the two chemically distinct block copolymer components, showing the degree of immiscibility between them. The degree of polymerization is the number of monomeric units in the polymer chain. Minimization of free energy in block copolymers is the driving force that leads microphase separation. In microphase separation, enthalpy drives the blocks to self-assemble and spatially segregate, while the opposite energy, entropy, force them to remain disordered distributed in a homogeneous mixture. Both enthalpic and entropic energetic contributions are considered in the product $\chi \cdot N$, which is the segregation strength.[77] The most commonly used diagram to represent microphase segregation is computed by applying the self-consistent mean-field theory to the system.[78,79] By this mathematical formalism, the phase behavior of the system is summarized via a two dimensional phase diagram showing the equilibrium microphases as a function of $\chi \cdot N$ and f_A, the volume fraction of one of the components (Figure 6).

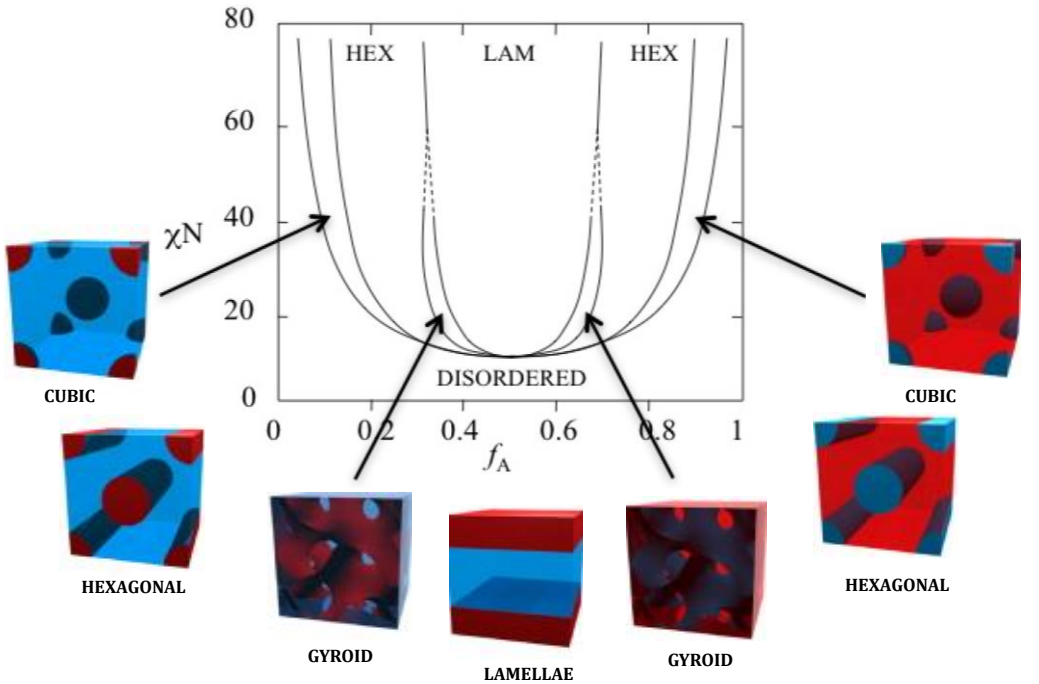

Figure 6. Theoretical phase diagram and predicted morphologies by the self-consistent mean-field theory for diblock copolymers. The phases are indicated as follows: body centered cubic, hexagonal cylinders (HEX), gyroid and lamellar (LAM). f_A is the volume fraction of polymer block A, χ the Flory-Huggins interaction parameter and N the total degree of polymerization. Adapted with permission from [80]. Copyright 1996 American Chemical Society. Adapted with permission form [81] Copyright 2007 Elsevier Ltd.

This theory is considered as a successful tool to predict the microdomain symmetry, size and periodicity from the parameters $\chi \cdot N$ and f whenever away from the order-disorder transition (ODT).[82,83] In the bulk state, different thermostable morphologies are adopted depending on the $\chi \cdot N$ parameter and the volumetric contribution of each component (f_A-f_B). For a symmetric (f_A=f_B=0.5) diblock copolymer with equal segment sizes, the critical order-disorder transition is predicted by mean field theory to occur at $(\chi \cdot N)_{ODT}$=10.5. When the product $\chi \cdot N$ is lower than this critical value ($\chi \cdot N \leq 10$), the entropy is high enough to maintain a mixture of block copolymer fractions over the enthalpic penalty of mixing polymers. As a result, a disordered structure stands out (Figure 7).

At a certain $\chi \cdot N$ value, polymers comprising blocks become immiscible causing an order-disorder transition (ODT), where the chemically distinct blocks tend to segregate into ordered domains separated at a maximum distance. This separation is limited by the covalent bond between the polymer fractions, which restricts their macroscopic separation. The covalent link between blocks is what

differs block copolymers from homopolymer mixtures: in the former, phase separation results in nanometric heterogeneities in composition at length scales comparable with block dimensions while in the later, the binary mixtures lead macrophase separation (Figure 8).

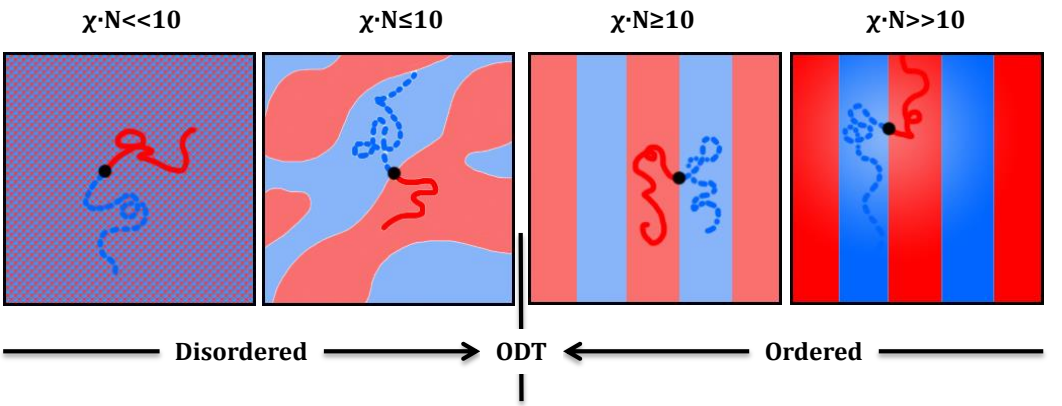

Figure 7. Evolution of the structure of a symmetric diblock copolymer ($f_A = f_B = 0.5$) as a function of $\chi \cdot N$. ODT stands for ordered-disordered transition, which is predicted to happen when $\chi \cdot N \leq 10$ according to self-consistent mean-field theory.

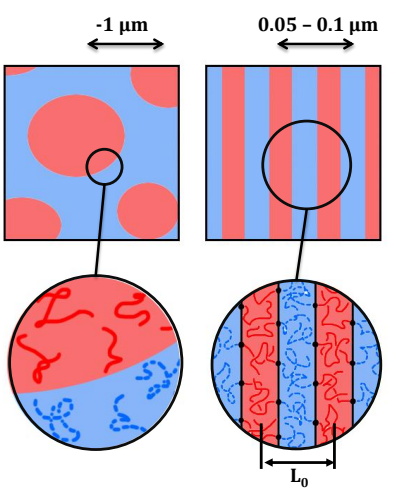

Figure 8. Phase behaviors of polymer-polymer systems. (A) Macrophase separation of thermodynamically incompatible homopolymer mixture and (B) microphase separation of covalently bound blocks in a diblock copolymer structure. L_0: lattice spacing or bulk periodicity, understood as the distance between the centers of two adjacent domains.

The geometry of the resulting periodic structures depends on the relative volume fraction for each polymer (Figure 6). Symmetric block copolymer with comparable volume fractions of A and B polymers form alternating lamellae. By slightly varying the polymer fraction ratio from the symmetry, more complex structures can be formed, such as perforated lamellar phase or bicontinuous

gyroid geometries. Asymmetric block copolymers are those with different A and B volume fractions. Typically, when the A block occupies around one third of the total polymer volume ($f_A \approx 0.3$; $f_B \approx 0.7$), microphase segregation give rise to cylindrical domains of A block immersed in a B matrix. At higher molecular asymmetries, A block is reduced in volume and, as a minor component, it forms spheres in a close-packed body centered cubic arrangement.[82] This thesis is focused on asymmetric cylinder forming diblock copolymers.

Historically, the large range ordering of block copolymers was firstly considered a mere laboratory curiosity of academic interest, which could potentially have some creative applications if control over materials, domain sizes and interdomain spacing was experimentally addressed.[84] Over the years, diverse diblock-copolymer systems were indeed experimentally characterized and an increasing number of applications have been described in many fields such as nanolithography,[67,85] high-density storage media,[86,87] nanoporous membranes,[88,89] drug delivery systems[90] or nanotemplating.[73,91] The company IBM has patented since 2006 several assisted self-assembly procedures for computer chip manufacturing based on diblock copolymer systems, and these self-assembling processes have been successfully incorporated in the manufacturing lines.[92] Block copolymer vesicles or polymersomes formed by an internal hydrophilic core have been used for drug delivery purposes. This polymeric entities are more robust and stable than conventional liposomes and can be easily decorated to target the delivery of encapsulated drugs to specific tissues.[93] Miniaturized actuators based on block copolymers can convert an external stimuli into mechanical energy.[94] For example, triblock copolymers with hydrophobic ends comprised of poly(methyl methacrylate)-*block*-poly(methacrylic acid)-*block*-poly(methyl methacrylate) (PMMA-*b*-PMAA-*b*-PMMA) undergo volume changes driven by pH oscillations between 3.1 and 7.0 pH, while the material preserves good mechanical properties required for appropriate process manufacturing.[95]

The use of block copolymers as templates have attracted much attention not only because of their small feature sizes, but also in view of their capability to reduce the number of processing steps in comparison with other nanopatterning techniques. Block copolymers have been used for direct patterning of metal nanoparticles or as hybrid materials, also termed nanocomposites, formed by the co-assembly of block copolymers with biomolecules or nanoparticles.[96,97]

Because of their potential applications, considerable research efforts have been put into understanding the energetic contributions modulating diblock copolymers self-assembly when confined into thin films.[98–100] The four "classical" factors (Flory-Huggins interaction parameter, degree of polymerization, block fraction and molecular architecture) dictate microphase separation, but microdomain orientation in a thin film is governed by the interfacial interactions at the substrate and free interfaces.

Substrates can be classified as preferential surfaces for one of the blocks of a diblock copolymer molecule or as non-preferential for any of them. One block (A block) preferentially wets a surface when the interfacial interaction energy between the surface and that block ($\Delta\gamma_{\text{surface-A block}}$) is smaller than the interfacial interaction energy between the surface and the second block ($\Delta\gamma_{\text{surface-B block}}$). Then, the A block coats the surface, leading to a parallel disposition of microdomains (Figure 9). Perpendicular microdomain orientations occur when the interfacial interaction energies of both blocks with the surface are balanced. These surfaces, referred as "neutral surfaces" for that specific block copolymer composition, are equally wetted by both blocks (Figure 9).

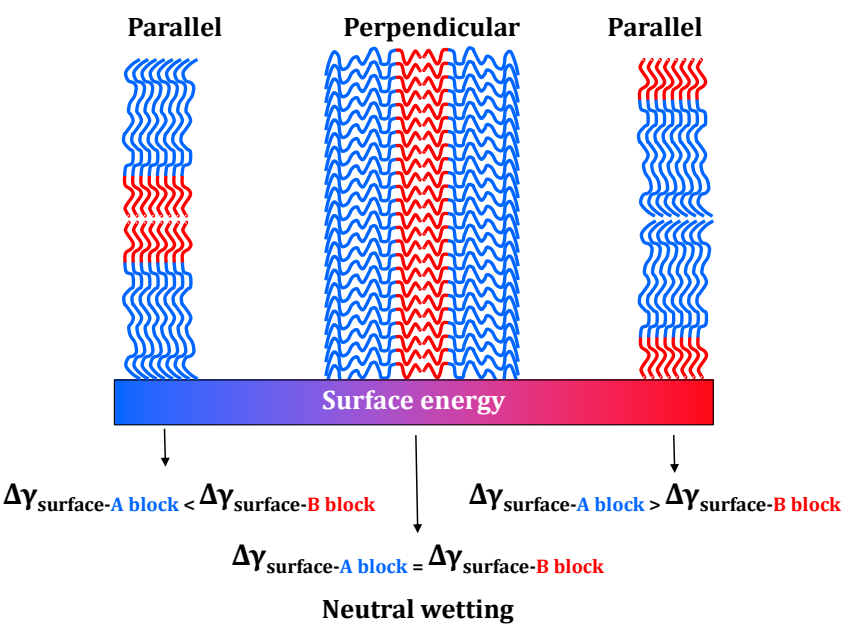

Figure 9. Surface wetting scenarios for parallel or perpendicular microdomain orientation of block copolymers depending on the substrate surface energy. Left: A block wets the surface resulting in parallel orientation of microdomains. Middle: interfacial energies are balanced between A and B blocks and both blocks wet the surface, resulting in perpendicular microdomain orientation. Right: B block wets the surface resulting in parallel orientation.

Not only the interfacial energy ($\Delta\gamma$) of the substrate, but also the commensurability of the film thickness with the polymer domain spacing (L_0) determine which microdomain orientation is energetically favored. The confinement of block copolymers into a film thickness (t) comparable to the bulk periodicity (L_0) entails the stretching or compression of the polymer chains. This physical constrain is energetically unfavorable, and the entropic energetic penalty is mitigated by the orientation of blocks in the most favorable conformation, i.e., the one with the minimum Gibbs free energy.[76] Under "hard" confinement, where block copolymers films are delimited by two rigid surfaces, energy relief is only possible through perpendicular orientation of microdomains.[101] Often, thin films are supported on a solid substrate while the upper surface is a free interface in contact with air or a solvent atmosphere. This is known as "soft" confinement and it will be discussed over this dissertation. The polymer chains can compensate the incommensurability originated under soft confinement by the perpendicular or the parallel orientation of microdomains.

On preferential wetting surfaces, where a block tends to establish contact with the surface leading parallel-oriented microdomains, the most energetically favored film thickness is an integer multiple (n) of the polymer domain spacing ($t=n\cdot L_0$).[102] The film thickness quantization still governs the film morphology when the spin-coated thickness is different from those discrete values. For incommensurable film thicknesses (smaller or larger than an integer multiple of the polymer domain spacing) ($t < n\cdot L_0$ or $t > n\cdot L_0$), the film will adopt a mixed morphology termed as "island" and "hole" topography where two thicknesses are simultaneously present at different proportions: the film thickness corresponding to the immediately lower ($t_1 = [n-1]\cdot L_0$) and higher ($t_2 = [n+1]\cdot L_0$) integer multiple of the polymer domain spacing (Figure 10).

On non-preferential wetting surfaces, film thickness quantization is suppressed because both blocks are in contact with the surface. The potential polymer chain stretching/compression is neglected thanks to the perpendicular microdomain orientation. This energetic compensation is independent from the spin-coated film thickness as shown in Figure 10.

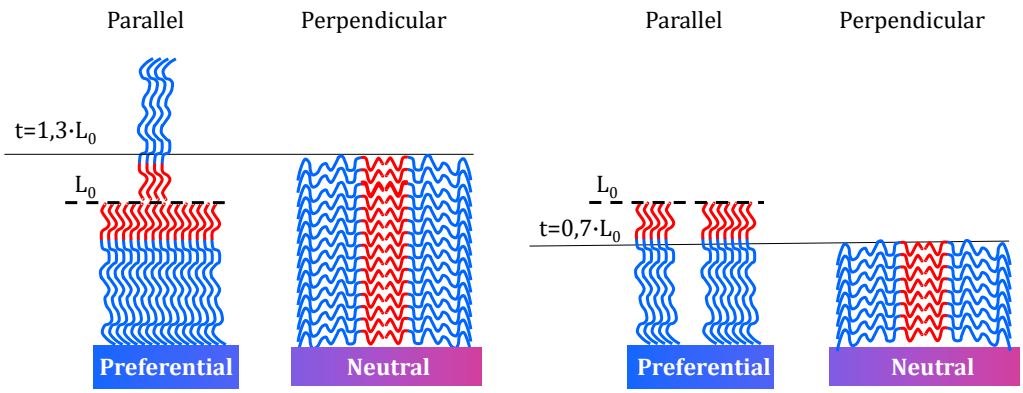

Figure 10. Microdomain orientation of diblock copolymers under "soft" confinement. Schematic representation of film thickness (t) quantization to integer multiples of polymer domain spacing (L_0) on preferential wetting surfaces leading island (left) and hole (right) structures. On neutral (non-preferential) surfaces where microdomains are oriented perpendicular to the surface, film thickness is not quantized.

For many nanotechnological applications, the perpendicular orientation of asymmetric cylinder-forming diblock copolymers is desired.[75,103] A variety of strategies have been developed to control the microdomain orientation including grapoepitaxy,[104,105] chemical patterning,[106,107] nanoimprint lithography,[108] electric and magnetic fields,[109,110] solvent[111,112] and thermal annealing[113] or neutral surfaces[114–117]. Perhaps, the simplest among them all is the control of substrate interfacial interactions by tuning the surface energetics of the substrate.

Tailoring the chemical properties of a substrate to obtain a neutral surface has been widely used to direct the disposition of cylinders normal to non-preferential surfaces. The first method was described in 1996 for lamellae-forming PS-*b*-PMMA diblock copolymers. A random copolymer molecule composed of an equal mixture of PS and PMMA monomers was spun-coated on the substrate in such way that similar interfacial energy with both blocks was exhibited.[118] This methodology was improved by the incorporation of a chemical group at one end of the random polymer.[119,120] This chemical moiety interacted with the surface allowing the stable engraftment of random polymer brushes. However, substrate specific-chemistries are required to ensure a covalent bond with the surface and to guarantee a high density of the grafted chains that completely fills up the space available. Cross-linked random copolymers offered a generalized surface modification approach independent of the nature of the substrate.[121] A cross-linked random film thicker than ~5.5 nm provided a neutral surface where cylindrical microdomains were perpendicularly oriented.[122] Self-assembled monolayers (SAMs) have been used as an alternative to render interfacial energies

neutral. Myriads of silanes with different functionalities are commercially available, which facilitates their use.[98] A strict control of alkylchlorosilanes grafting densities is imperative to balance the interfacial interactions of blocks with silicon oxide surfaces.[123,124] The surface wettability of SAMs can be also tuned by diverse chemical treatments such as irradiation with synchrotron soft- X-rays,[125] CO_2 plasma treatment,[126] and UV irradiation.[127]

Regardless the surface modification strategy, the formation of perpendicular cylinders is only comprehended in terms of the equilibration of the whole system, not simply in terms of interfacial energy.[114] The film thickness, block copolymer composition, annealing conditions and the surface modification method are parameters concurrently influencing the perpendicular orientation. On substrates modified with random copolymers (PS-*r*-PMMA) of varying block fractions, the neutral surface compositions are experimentally identified. For a PMMA cylinder forming diblock copolymer (PS-*b*-PMMA) with a PS fraction of 0.72, cylinders are perpendicularly structured over a hydroxyl-terminated random copolymer coating with PS fraction ranging from 0.59 to 0.72. However, this perpendicular window is shifted to higher PS fractions when the random copolymer is side-grafted or cross-linked on the surface. This exemplifies the complex implications of small changes in the equilibrated balance of energies.[128]

The equilibrium morphology of the block copolymer thin films is also thickness dependent, so that the perpendicular disposition of microdomains over a neutral surface occurs for a certain range of film thicknesses. Out of this thickness window, perpendicular orientation is no longer exhibited.[115] According to these observations, lamellae-forming diblock copolymers showed larger thickness windows than cylinder-forming diblock copolymers, which indicates an easier orientation of lamellae normal to the surface in comparison with cylindrical structures. The film thickness window for cylindrical structures is circumscribed to the vicinity of the lattice spacing value (L_0).[129,130]

Theoretical predictions often failed to recapitulate the combined effects of the numerous variables finally affecting the free energy of the film. For these reasons, many studies[113–115,131,132] claimed that perpendicular windows are unique for every combination of block copolymer composition, chemical substrate modification (such as random copolymer composition and grafting method), film thickness and annealing conditions. The selection of the appropriate parameters

leading the overall equilibration process necessary for the perpendicular orientation of microdomains is a noteworthy challenge and should be experimentally verified for every particular diblock copolymer system.[76]

1.3. The reference material: Polystyrene-*block*-poly(methyl-methacrylate) (PS-*b*-PMMA)

There is a great variety of commercially available block copolymers offering a wide window of chemical properties. Among them, polystyrene-*block*-poly(methyl methacrylate) (PS-*b*-PMMA) is a good candidate to generate self-assembled nanopatterned templates. In particular, asymmetric PS-*b*-PMMA diblock copolymer accesses the formation of PMMA cylindrical arrays immersed in a PS matrix.

PS and PMMA are transparent and biocompatible thermoplastic materials extensively used for biomedical applications and cellular studies.[133,134] PS and PMMA are immiscible polymers characterized by relatively high glass transition temperatures (T_g= 100°C for PS; T_g= 115°C for PMMA).[115] These attributes, together with a Flory-Huggins interaction parameter whose temperature dependence is weaker than for other polymers,[135] potentiate the structural integrity and obtaining nanopatterns with high resolution.[136] Nanostructured thin films featuring PMMA cylinder with diameters close to 10 nm were oriented normal to the underlying surface by a rigorous control of the annealing conditions (Figure 11).[137]

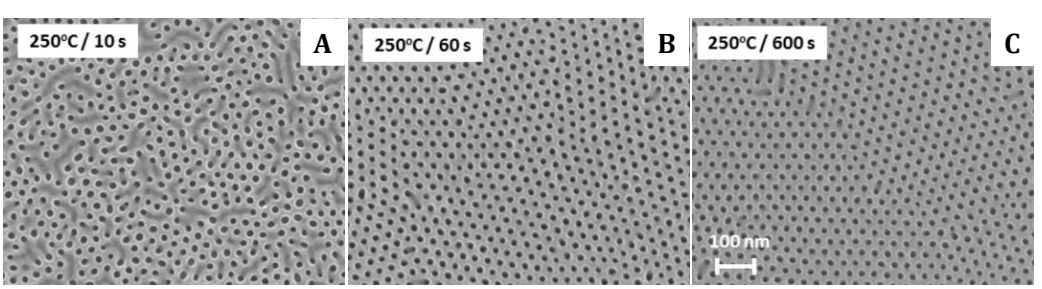

Figure 11. Cylindrical PMMA domains with 10 nm in diameter. Morphological evolution of perpendicular domains as a function of time. Scanning electron microscopy (SEM) images of UV etched PS-b-PMMA thin films. Holes correspond to the regions of the PMMA cylinder domains (Molecular weight: 39000 g/mol). Adapted with permission from [72] Copyright 2013 IOP Publishing Ltd.

The cylindrical domain dimensions and spacing can be tuned according to the Flory-Huggins interaction parameter (χ), the polymerization degree (N) and

the block volume fractions (*f*).[138] Self-assembled PS-*b*-PMMA thin films have been often generated under "soft" confinement on silicon oxide wafers. Under such conditions, PS-*b*-PMMA diblock copolymers are confined between two interfaces with different interfacial energies. PMMA is a polar polyacid chain that spontaneously segregates to the silicon oxide interface, while the PS block exhibits an affinity for the free interface. The lower interfacial energy of PMMA drives the formation of a primary underlying coating of PMMA at the film bottom interface.[124] This wetting layer is an undesired element for further lithographic applications.[86]

The perpendicular orientation of cylindrical domains is of high interest for the fabrication of nanoporous membranes and nanostructured templates. Several surface modification techniques providing a neutral bottom interface for both PS and PMMA blocks have been described in the previous section. The most commonly used strategy utilizes end-grafted hydroxyl-terminated random copolymer brushes with a monomer composition similar to the diblock copolymer molecule. On the other side, the PS-*b*-PMMA is in contact with the free interface, which is preferentially wetted by PS. It has been reported that the interfacial interaction energies of PS and PMMA are essentially identical at high temperatures (170°C-230°C).[139] Therefore, to get this balanced interaction at the free interface, PS-*b*-PMMA thin films are thermally annealed. The combination of a random brush and an annealing step facilitates the required control of the interfacial energies.

Nanoporous membranes can be easily originated from perpendicularly oriented PS-*b*-PMMA thin films for the fabrication of nanolithographic masks, semiconductor capacitors and metallic nanostructures.[73] The great advantage of this polymeric system is that PMMA block can be selectively photodegraded under ultraviolet (UV) light and easily removed by rinsing the surface with glacial acetic acid. As a result, the PMMA domains are replaced by nanometric pores and the cross-linked PS forms a stable holed matrix (Figure 11).[88] The nanopattern can be replicated in various materials by additional etching or deposition processes.[140] PMMA microdomains can be also selectively loaded with alumina by a sequential infiltration synthesis.[141] The self-assembled alumina pattern provides a robust template with strong etch resistance that enable the fabrication of nanotextured structures whose particular optical properties have potential applications in solar cell technology (Figure 12).[142]

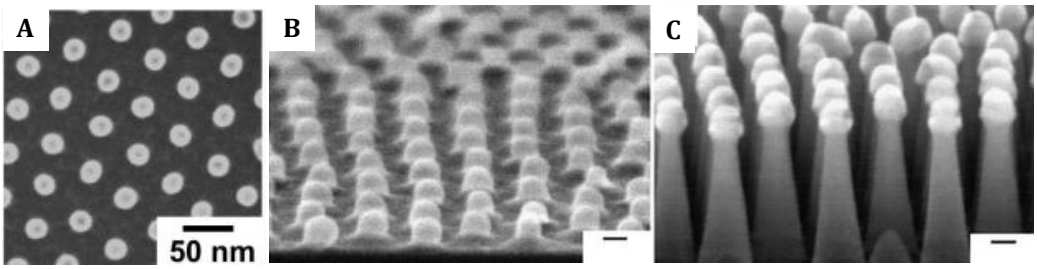

Figure 12. Alumina-infiltrated PS-b-PMMA thin films. (A) Top-down and (B) 70° angled cross-sectional SEM image of alumina-loaded PS-b-PMMA block copolymer thin film (Molecular weight 99000 g/mol). (C) 70° angled cross-sectional SEM image of nanotextures fabricated by 60 s of plasma etch (Scale bars of B and C images: 20 nm). Adapted with permission from Macmillan Publishers Ltd: Nature Communications [142], Copyright 2015.

Diblock copolymer thin films have also been explored as templates for selective protein functionalization. Self–assembled PS-*b*-PMMA thin films exhibit two different chemical components arranged into nanopatterns. The differences in hydrophilicity/hydrophobicity between both blocks have been postulated as the driving force for preferential protein physisorption onto only one of them[143,144], as reported for other block copolymer thin films.[145,146] Bovine immunoglobulin G (IgG) was incubated for 20 s on parallel oriented PS-*b*-PMMA domains and extensively rinsed. Such functionalization conditions lead the selective segregation of several proteins, such as horseradish peroxidase, protein G and IgG, on PS domains (Figure 13). In comparison with PS homopolymer, protein adsorption was 4-fold higher on PS-b-PMMA thin films, and specifically located at the boundaries between PS and PMMA.[147]

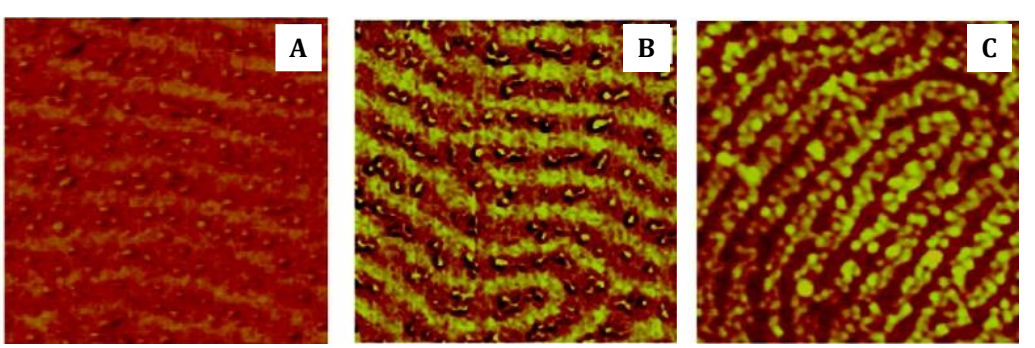

Figure 13. Protein adsorption behavior on PS-b-PMMA diblock copolymer. AFM images (400 x 400 nm) of (A) horseradish peroxidase (B) protein G and (C) immunoglobulin G physically adsorbed on parallel-oriented asymmetric PS-b-PMMA (Molecular weight: 71400 g/mol). Adapted with permission from [147] Copyright (2008) American Chemical Society.

The protein adsorption mechanisms on surfaces presenting this chemical contrast were examined and the protein pattern fidelity was subjected to a particular rinsing procedure.[144] However, robust procedures are desired for

protein patterning at such level of resolution. Moreover, physically adsorbed proteins on hydrophobic environments are highly susceptible to protein denaturalization phenomena and the preservation of the resulting protein patterns over time might be compromised.

PMMA offers an attractive route for covalent protein binding. The PMMA backbone has a methyl pending group which can act as a reactive group for protein functionalization. Under alkaline conditions, the methyl group is hydrolyzed into a carboxylic group.[148] This carboxylic moiety can react to form an amide bond with any amine-terminated molecule, which includes any aminoacid sequence.[149] Therefore, PMMA provides an anchoring point for covalent protein functionalization of PMMA domains.

1.4. Biomolecular nanopatterns over diblock copolymer templates

Biomolecules can be covalently fused to block copolymers by two different strategies: the pre-functionalization of the block copolymer backbone or the post-modification of the block copolymer once the thin film is generated.

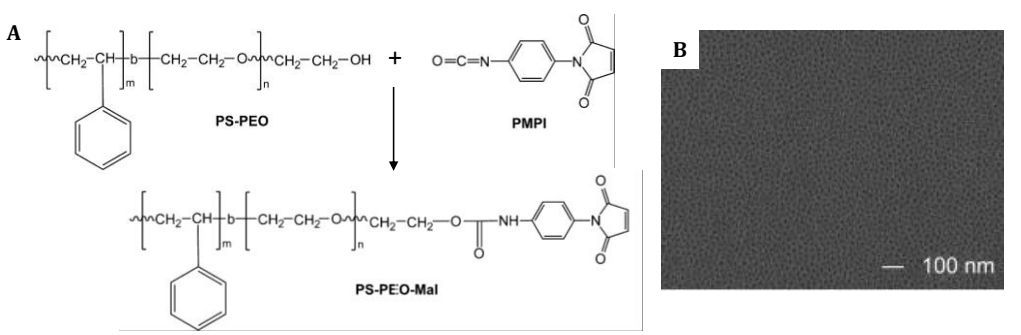

Figure 14. (A) Schematics of the reaction between polystyrene-block-poly(ethylene oxide) (PS-b-PEO) copolymer with N-(p-maleimidophenyl)isocyanate (PMPI) to originate end terminated maleimide PS-b-PEO (PS-b-PEO-mal). (B) SEM image of self-assembled PS-b-PEO-mal thin film with perpendicularly oriented PEO cylinders. Adapted from [150] Copyright (2009), with permission from Elsevier Ltd.

A variety of functional groups have been covalently incorporated into the molecular structure of diblock copolymers. An original approach was developed by Cooper-White and co-workers based on asymmetric polystyrene-*block*-poly(ethylene oxide) (PS-*b*-PEO) diblock copolymer. The intrinsic resistance to protein adhesion shown by PS-*b*-PEO thin films[151] was selectively modified by the incorporation of a functional group. The hydroxyl-terminated group of the PEO domain of PS-*b*-PEO reacted with N-(p-maleimidophenyl)isocyanate (PMPI)

adding a maleimide group to the molecule (PS-PEO-mal). The microphase separation behavior of PS-*b*-PEO was unaffected by the incorporation of the maleimide end group and PS-*b*-PEO-mal polymers self-assembled into perpendicularly ordered PEO-mal cylinders featuring a small diameter (8-14 nm) (Figure 14).[150] Maleimide group is an electrophilic compound with high selectivity towards thiols. It is widely used for bioconjugation of peptides or proteins containing cysteine residues.[152] To extend the versatility of this functionalization to poly-histidine tagged molecules, a zinc chelating linker was bound to the maleimide group and His-tagged green fluorescence protein (GFP) was selectively attached and visualized by fluorescence microscopy. Synthetic cysteine-terminated adhesive peptides (CGRGDS) were individually immobilized on PS-*b*-PEO-mal thin films with varying densities of PEO-mal nanodomains. NIH-3T3 fibroblast spreading was enhanced on thin films with increasing adhesive peptide density. These bioconjugated surfaces were additionally used to investigate the differentiation process of human bone-marrow-derived mesenchymal stem cells upon specific presentation of short adhesive-peptide combinations.[153]

Alternatively, individual protein arrays were generated on hexagonally packed alkyne-modified PS cylinders. Polystyrene-*block*-poly(2-hydroxyethyl methacrylate) (PS-*b*-PHEMA) was mixed with alkyne-functionalized polystyrene-*block*-poly(2hydroxyethyl methacrylate)(PSA-*b*-PHEMA). PS cylindrical domains were oriented normal to the gold surface by solvent annealing in such a way that the alkyne group was exposed following the self-assembled templated. In the presence of alkyne groups, azide moieties efficiently interact leading triazole formation through a so-called “click” reaction.[58] This reaction, which can be performed both with and without a catalyst,[154,155] was proven to be successful for surface modification of polymeric substrates.[156,157] Azide-tagged proteins were immobilized on the cylindrical domains of alkyne-functionalized PS of self-assembled PSA-*b*-PHEMA thin films *via* click chemistry (Figure 15). Azide-modified proteins including fibronectin, myosin and lysozyme were covalently attached to the nanostructured surface while their biological activity was preserved.[158] The reduced size of PS domains was proposed as a restricting parameter that limited the protein immobilization to the molecular level, i.e., to a single molecule per PS domain.

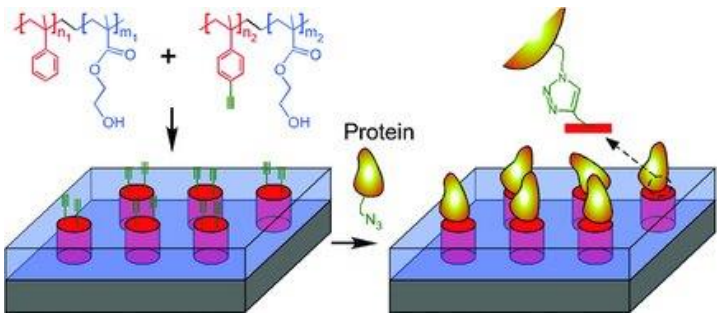

Figure 15. Schematic representation of the alkyne-functionalized PS-b-PHEMA block copolymer thin film (alkyne-modified PS cylinders coloured in red and PHEMA matrix colour in blue). Specific immobilization of single azide-tagged proteins via click chemistry on alkyne-modified PS domains.

To control the oriented protein conformation on high-density nanoarrays, proteins should be modified with a unique chemical functionality located at a certain position on the protein structure, which leads to a site-specific covalent linkage with the surface. Recombinant proteins are commonly expressed fused to a poly-histidine-tag that facilitates the posterior purification processes. PS-*b*-PHEMA diblock copolymer molecules were mixed with iminodiacetic-terminated PS (IDA-PS-IDA), which became integrated within the PS nanodomains. The chelate group IDA can strongly bind copper (Cu^{2+}) while the metal ion selectively coordinates imidazole groups of poly-histidine tagged proteins (Figure 16).[159] The surface density of His-tagged green fluorescence protein (His-GFP) immobilized on PS-*b*-PHEMA nanoarrays was characterized by surface plasmon resonance (SPR). Calculations from SPR revealed that ~2-4 His-GFP molecules were attached to each PS nanodomain. This value, found to be lower than the presumed adsorbed amount of protein (60 His-GFP molecules/PS domain), is thought to be limited by the relative low content of IDA immobilized on the surface (0.6% mol). The high sensitivity of self-assembling processes to small chemical variations frustrate the blending of PS-*b*-PHEMA with higher concentrations of IDA-PS-IDA chelate group which will distort the self-assembled cylinder array nanostructures.[160]

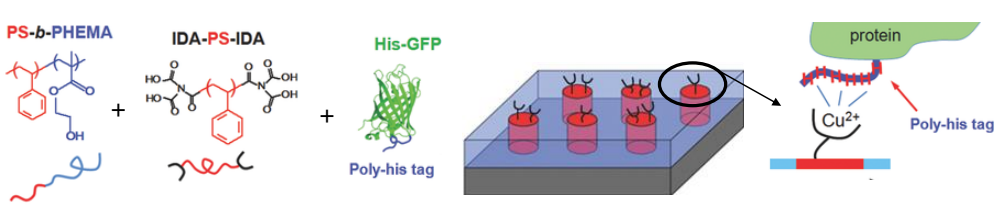

Figure 16. Schematic illustration of PS-b-PHEMA block copolymer, chelate group iminodiacetic-terminated PS (IDA-PS-IDA) and His-tagged green fluorescence protein (His-GFP). Site-specific immobilization of His-GFP on IDA-modified PS cylindrical nanodomains via Cu^{2+} coordination. Adapted with permission from [159]. Copyright (2016) John Wiley and Sons.

Custom-synthetized block copolymers offer exciting possibilities to design and incorporate diverse functional groups into block copolymer nanopatterns. Recently, a modular synthesis of polystyrene-*block*-poly(ethylene-oxide-*co*-alkyl glycidyl ether) (PS-*b*-P(EO-*co*-AGE)[161] was applied to functionalize PEO backbone with cell adhesive peptides. Cysteine-terminated adhesive peptides (CRGDS) were bound to the AGE group of the diblock copolymer via thiolene "click" chemistry.[162] However, this structural modification greatly impacted on the strength of phase segregation between both blocks, and the resultant nanostructures were irregular, featuring sizes from 15 to 70 nm (Figure 17 B). Preserving the nanostructured geometry while incorporating a molecule of interest might require an additional modification that promotes phase segregation.[163] A dual functionalized PS-*b*-P(EO-*co*-AGE) was synthetized containing the mentioned adhesive peptide and a perfluorooctanethiol (PFOT) that increased the immiscibility between blocks.[164] Block copolymers modified with a ratio of 1:1 peptide/perfluoro groups were shown to self-assemble again into cylindrical domains, but in this case the nanopatterned structures display a noticeable topography which intrinsically has the potential to affect cell adhesion.[165,166]

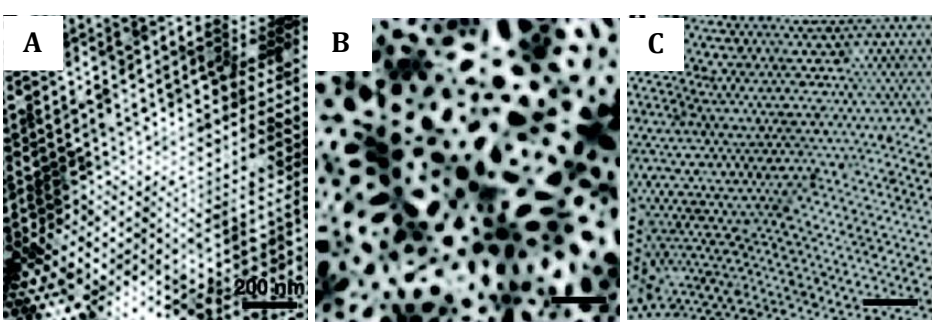

PS-*b*-P(EO-*co*-AGE) CRGDS-functionalized BCP 1:1 CRGDS/PFOT-BCP

Figure 17. Topographic atomic force microscopy images of self-assembled thin films of (A) PS-b-P(EO-co-AGE) block copolymer, (B) cysteine-terminated adhesive peptide (CRGDS) modified PS-b-P(EO-co-AGE), and (C) 1:1 CRGDS/perfluoroctanethiol (PFOT) modified PS-b-P(EO-co-AGE). Adapted with permission from [164]. Copyright (2014) American Chemical Society.

Although the opportunities to tailor well-studied block copolymer systems exponentially increases by customizing their synthesis, the consequences on the self-assembled nanostructure are not negligible.[128] It often remains difficult to predict the effect in phase behavior and microdomain orientation of small structural modifications of block copolymers. Thefore, post-functionalization strategies have been proposed to be advantageous for the selective immobilization of biomolecules on block copolymer templates. The functionalization process is directly performed on substrate-supported block copolymer thin films.

Thin films of perpendicularly oriented lamellae comprised of a "reactive"-block (poly(2-vinil-4,4-dimethylazlactone) (PVDMA)) and a "non-reactive" block (PS) enabled the presentation of chemical and biological relevant molecules at the nanoscale. The surface exposed azlactone group can be activated by ring-opening reactions to form stable amide bonds with amine-terminated molecules (Figure 18). These reactions occur rapidly without relevant byproduct generation and the anchoring points are stable under thermal annealing conditions used for microdomain orientation. The interfacial properties of block copolymer thin films were tailored by selectively coupling a primary amine-functionalize fluorophore. The uniform fluorescence intensity recorded on the functionalized block copolymer thin film arises from the specific reaction with the azlactone group, as demonstrated by the absence of fluorescence for surfaces with amine-free fluorophores.[167] Scanning electron microscopy (SEM) images proved that domain orientation was retained after functionalization (Figure 18). These post-fabrication approaches enable the precise control of biomolecule nanopatterning replicating the length scales of the underlying block copolymer template (sub-50 nm) without compromising the nanoscale morphology. Thanks to the rapid linkage formed by any amine-terminated molecule and the block copolymer surface, this system offers an enormous versatility to immobilize complex chemical or biological entities otherwise difficult to position with such nanometric resolution.

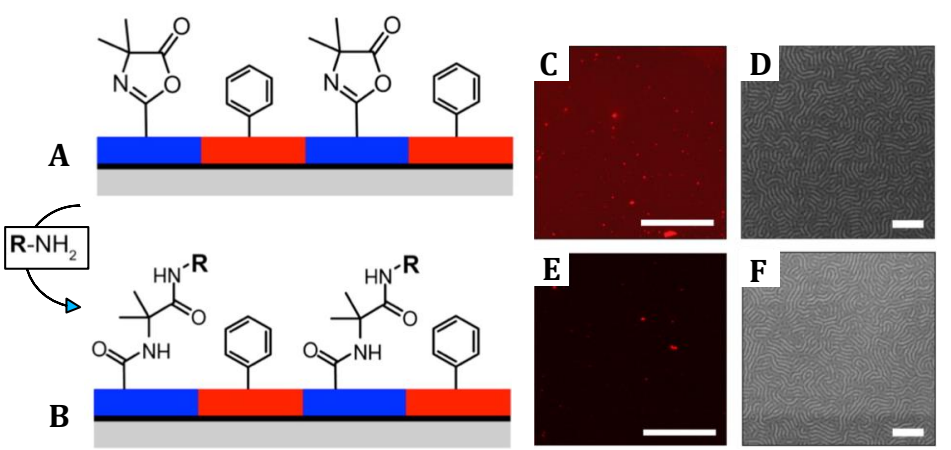

Figure 18. Schematic representation of (A) surface-exposed stripes of azlactone-group (PVDMA block coloured in blue) alternated with non-reactive PS stripes (PS coloured in red). (B) Amine-terminated molecules are surface-bounded on PVDMA via selective ring-opening reaction with the exposed azlactone moieties. (C-F) Fluorescence images and SEM images of PS-b-PVDMA films functionalized with a primary amine-modified fluorophore (tetramethylrhodamine cadaverine;TMR-cad) or (E, F) a non-reactive (amine-free) analogue (tetramethylrhodamine;TMR). Scale bars in (C) and (E) are 125 µm. Scale bars for SEM images: 200 nm. Adapted with permission from [167]. Copyright (2014) American Chemical Society.

Nanofabrication techniques have thus far enabled the accurate protein nanopatterning over large areas by minimal processing and low costs. Nonetheless, protein nanopattern characterization is still challenging.

Currently, atomic force microscopy (AFM) is the most-widely applied technique to investigate the spatial distribution of surface-bound proteins. Topographic AFM images provides evidences of the spatial distribution and periodicity of molecular patterns based on the contrast that arises from height variations. Minimal sample treatment is required for observation with this technique and imaging in liquid environment is feasible. However, molecules with similar sizes will not be discriminated.[168] Another constraint of AFM when imaging small features over long-range areas is its reduced field of view and low throughput. Typically, imaging areas of 1 μm^2 to 25 μm^2 by AFM requires acquisition times of 10-20 min per image, so it provides accurate information only over local areas. Likewise, scanning electron microscopy (SEM) and transmission electron microscopy (TEM) are high resolution techniques used to investigate nanostructured materials.[24] However, both techniques work in vacuum and require a previous process of contrasting to scan biomolecules.[169] Moreover, many polymeric samples including block copolymers are composed of non-conductive materials that tend to acquire charge while the electron beam raster the sample surface, which results in images with poor resolution.[170]

Fluorescence microscopy is widely used to study immobilized protein patterns.[47,171,172] Multiple protein species can be directly detected on a single sample *via* site-specific fluorescent labelling.[173] Fluorescence microscopes equipped with a CCD camera require short acquisition times for imaging large sample areas (field of view: 50 μm^2 to 300 μm^2).[168] Although the characterization of micron-sized patterns by optical microscopy is straightforward,[171,174] the light diffraction limit inherently constrains its lateral resolution to about half the wavelength used for imaging.[175] Therefore, the global intensity of fluorescent nanopatterned molecules has been often analyzed accounting for success of the immobilization technique, but lacking the required resolution to confirm their spatial distribution at the nanoscale (Figure 19 A).[150,159] Recent advances in super-resolution fluorescence microscopy have enabled the visualization of features at the nanometer-length scale with lateral resolution down to approximately 20 nm. Super-resolution fluorescence microscopy methods include techniques based on non-linear optical effects to sharpen the point-spread function of the microscope,

such as stimulated emission depletion (STED)[176]. Other methods use reversible saturable optically linear fluorescence transitions (RESOLFT)[177] and saturated structured-illumination microscopy (SSIM)[178]. There are also methods using sharp probe tip to scan the surface such as near-field scanning optical microscopy (NSOM)[179]. Finally, another set of techniques employ the localization of individual fluorescent molecules (Figure 19 B), these including stochastic optical reconstruction microscopy (STORM)[180], photoactivated localization microscopy (PALM)[181], and fluorescence photoactivation localization microscopy (FPALM)[182].

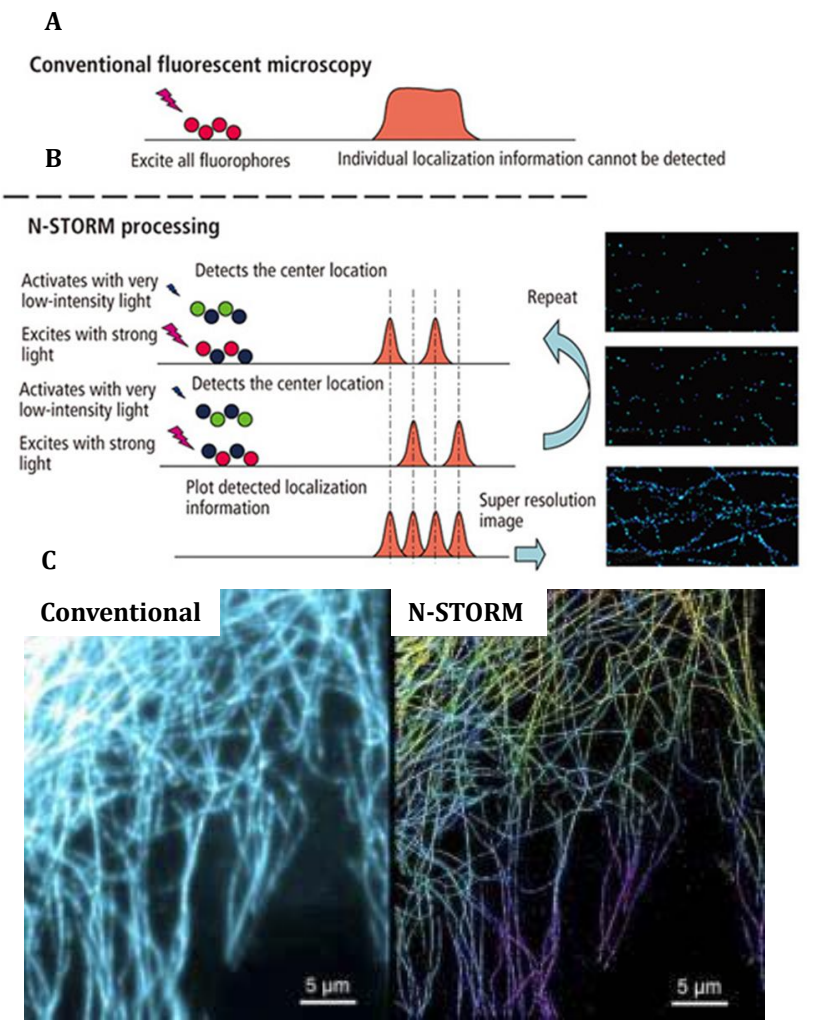

Figure 19. Conventional fluorescent microscopy methodology compared with super-resolution stochastic optical reconstruction microscopy (STORM) processing. (A) Conventional fluorescence microscopy simultaneously excite the emission of fluorescence of the whole group of fluorophores present in the sample. (B) N-STORM uses stochastic activation of relatively small numbers of fluorophores using very low-intensity light. This random stochastic "activation" of fluorophores allows temporal separation of individual molecules and reconstruct the image from the high-accuracy localization information of every fluorophore in the sample. (C) Comparison of conventional light microscopy (left) and N-STORM imaging (right) of microtubules. (www.nikoninstruments.com)

These high-resolution fluorescence techniques are attractive new methods for chemical and structural characterization of protein nanopatterns[183] on block copolymer surfaces.

1.5. Deciphering cellular processes at the nanoscale

Cells recognize and respond to a myriad of molecular signals and it is increasing evidenced that signaling processes are sensitive to the nanoscale spatial organization of such cues.[21,184,185] Traditionally, signaling pathways have been investigated at the biomolecular level discovering complex cascades that involve multiple signaling elements responsible of the propagation, amplification or inhibition of the signal. Nonetheless, understanding the role of the spatial modulation of intracellular signaling remains incomplete. Latest improvements in nanofabrication techniques (discussed in Section 1.1) provide means to define and control the spatial organization of signaling molecules, thus, opening a door for modeling spatially resolved cell signaling.

In response to an extracellular signal, also named ligand, a cell surface receptor is activated triggering a signaling pathway through interactions with intermediate signaling molecules. In most cases, these intermediaries transmit the signal from the cell membrane to a variety of intracellular targets, which converge to regulate gene expression and, ultimately, cell fate.

Tissue homeostasis is the result of the coordinated communication of cells with their surrounding environment, including extracellular matrix proteins, soluble factors and cell-cell interactions.[8] The extracellular matrix (ECM) is a highly hydrated network comprised of multifunctional adhesion ligands, such as fibronectin, vitronectin or laminin, surface-bound growth factors and proteoglycans. The stiffness, structure, chemical composition and spatial organization the extracellular matrix guide tissue dynamics.[3,186] The complex and variable three-dimensional (3D) architecture of the extracellular matrix is considered an obstacle to accurately engineer biomimetic materials that recapitulate the native spatial arrangement of cell-binding epitopes. However, the dimensions of protein dictates the relevance of the nanoscale distribution of extracellular signals in cell response. At this length scale, bioengineered features can potentially match the individual receptor dimensions, which provides the means to elucidate receptor responses upon molecular recognition.

Integrins are a large family of transmembrane receptors that mediate cell adhesion by the specific recognition of adhesion molecules, such as fibronectin, laminin or the well described adhesive peptide formed by arginine, glycine and aspartic acid (RGD). Integrins are heterodimeric protein receptors containing a α- and a β-subunit, with an extracellular domain that binds ECM proteins, and an cytoplasmic domain which recruits cytosolic mediators such as non-receptor tyrosine kinases Src and focal adhesion kinase (FAK).[187] Integrins are involved in many different signaling pathways including calcium channels, kinases, phosphatases and the Rho family of GTP binding proteins, among others. Upon ligand binding, integrins transmit the information across the membrane and regulate relevant cellular functions such as cell survival, membrane extension, mechanosensing, cytoskeletal tension, cell motility, cell differentiation and tissue invasion.[188]

Initially, integrins bind the adhesive peptide and its activation is followed by a receptor clustering process to form larger integrin complexes.[189] Integrin clustering is a crucial step that promotes the recruitment of cytosolic adaptor proteins such as paxillin and talin to form a macromolecular structure, which is approximately 250 nm in size, called nascent adhesion (Figure 20). These clusters trigger a positive feedback loop that mediates further cell spreading. The cellular cytoskeleton is connected to the nascent adhesion and pull on the ligands, acting as a sensing mechanism of the ECM stiffness.[190,191] The applied mechanical tension is counterbalanced by the ECM mechanical properties and the neighboring cells. This increase in mechanical tension at the integrin-ECM connection mediates the maturation of adhesions into focal complexes of about 500 nm in size.[192] Additional structural and mediator proteins are localized in the supramolecular structure including focal adhesion kinase (FAK) and α-actinin.[193] Eventually, focal adhesions ranging from 1 to 5 μm are arranged comprising other signaling proteins such as vinculin and zyxin. The focal adhesion lifetime directly depends on the mechanical resistance of the whole structure to the applied tension generated by the intracellular acto-myosin contraction. At the same time, contractility prompts focal adhesion disassembly by recruiting endocytosis protein mediators.[194] This focal adhesion turnover is essential for example at the rear of migrating cell, allowing it to move forward.[195]

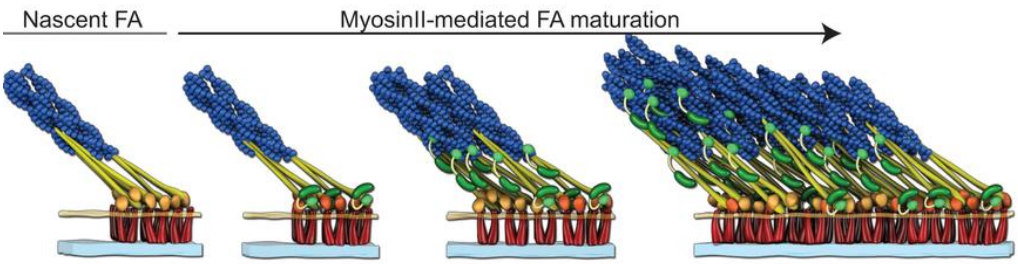

Figure 20. Scheme of nanoscale architecture of nascent focal adhesion (FA), depicting the experimentally determined protein adaptor positions during the myosin II- mediated FA maturation. Adapted with permission from [189]. Copyright 2010, Nature Publishing group.

Cell adhesion studies on bioengineered materials with adhesive peptides arranged in a controlled spatial distribution have proved that cells are sensitive to their different spatial organization at the nanoscale. It is worth mentioning that the outstanding identification of the recognition epitopes (such as the amino acid sequence RGD) within ECM adhesion proteins assisted the fabrication of nanopatterned ligand-presenting substrates.[196] These synthetic adhesive peptide analogs have been precisely bound to diverse nanostructures to unveil the mechanism through which cells interpret the nanoscale details of the extracellular environment.[197,198]

A pioneering method based on block copolymer micelle nanolithography was developed by Spatz and co-workers to precisely control ligand positioning on substrates.[69,71] through this technology (described in Section 1.1), gold nanodot patterns (~ 10 nm in diameter) were designed with an interdot spacing distance ranging from 15 to 250 nm. Once functionalized with ligands, the nanodot size ensured a single integrin receptor binding event per dot (Figure 21).

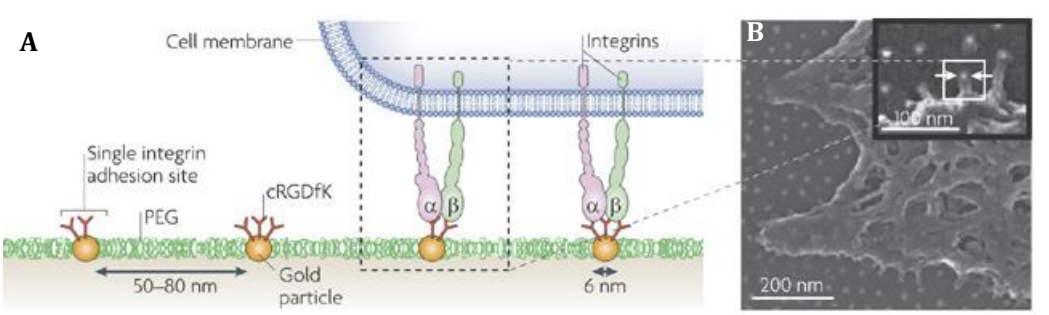

Figure 21. Nanopatterns of adhesive peptides. (A) Scheme of a cRGDfK-functionalized gold particle nanoarray interacting with integrin receptors at a cell membrane. (B) Scanning electron micrograph of a cell that is adhering to a gold particle (inset). Adapted with permission from [199] Copyright 2009 Nature Publishing group.

Functionalized nanodot arrays with a lattice spacing beyond 58 nm promotes focal adhesion formation and polymerization of contractile actin cytoskeletal stress fibers, as demonstrated by immunostaining of actin, focal adhesion kinase and β3 integrins subunit. In contrast, cells cultured on RGD-tethering nanoparticles with an interdot spacing larger than 73 nm were poorly spread and displayed an erratic migratory behaviour.[71] These results pointed out a threshold distance between adjacent integrins (approximately 50-70 nm) above which integrin clustering and adhesion signalling cannot be triggered.

A systematic analysis of variations in nanoparticle spacing was performed by a straightforward adaptation of the block copolymer micelle nanolithography to generate gradients.[200] Controlling the retraction velocity and the polymer length a variety of spacing ranges were obtained yielding distances between 50-250 nm.[201] It was shown that the velocity of migrating cells was inversely proportional to adhesive patch spacing. Cells showed a preferential elongation in the direction of the gradient and become polarized in response to a minimum spacing slope of 15 nm per mm. This exemplifies the high sensitivity of cells to subtle variations in interparticle spacing. It seems reasonable that cells discriminate between spatially arranged cues in this nanometer-length range since some components of the natural cellular environment, such as collagen fibers exhibit periodic nanoscale epitopes. For example, GFOGER peptide motifs appear in the collagen fibrils with a banding periodicity of ~65 nm.[202]

Mesenchymal stem cell (MSC) morphology and differentiation was investigated on polyethylene glycol (PEG) hydrogels where a gold nanoparticle pattern was transferred.[203] Cell spreading of MSC was consistently reported to be dependent on the nanospacing, but in a continuous fashion, without a drastic effect of the threshold nanospacing reported for non-stem cells (above ~70 nm spacing). Both osteogenic and adipogenic induction was more efficient on larger RGD nanospacing although under co-induction of both lineages, osteoblast differentiation was predominant over adipogenesis when global and local concentration of adhesive motifs decreased (Figure 22).[204]

Local RGD surface density has also been proposed as a regulator of chondrogenic commitment of adult mesenchymal stem cells. Polymeric substrates were decorated with RGD-tethering dendrimers at different surface densities.

Mesenchymal cell condensation and early chondrogenic commitment was favored on substrates where an intermediate adhesiveness of cells was sustained.[205]

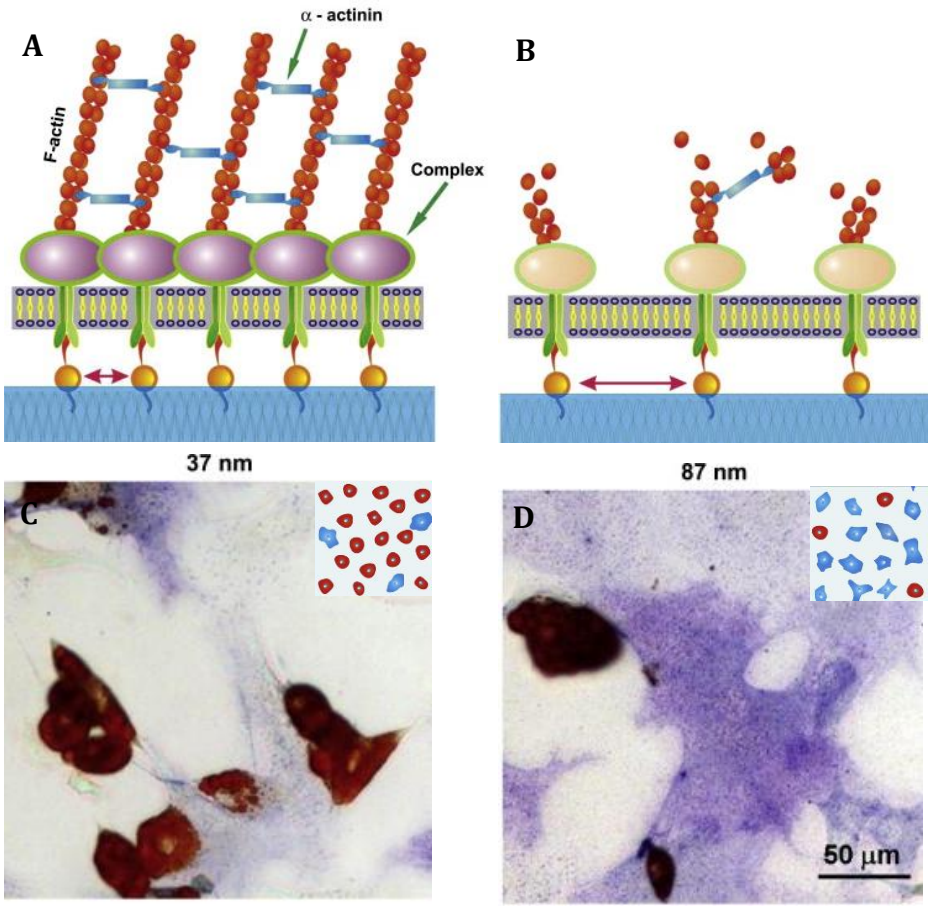

Figure 22. Schematic illustration of the effect of RGD nanospacing on mesenchymal stem cell differentiation. (A) Focal adhesion complex formed on substrates presenting RGD nanospacings smaller than the critical value about 70 nm and (B) the incomplete architecture of focal adhesions despite the RGD-integrin complex formation when RGD lateral spacing increases over 70 nm. Bright field micrographs of co-induced mesenchymal stem cells cultured on adhesive nanopatterns with (C) 38 nm and (D) 87 nm spacing. Cells positive for alkaline phosphatase (ALP) were stained in blue, as a marker of osteoblast differentiation and cells forming lipid droplets were stained in red by Oil Red O, as a marker for adipocytes. Adapted with permission from [204] Copyright 2013 Elsevier Ltd.

These techniques are ideal for patterning cell adhesive ligands at the same scale as integrin receptor sizes and have provided substantial information about the relevant role of integrin interspacing. However, these methodologies do not allow the independent modification of the RGD interspacing and the global ligand concentration. To this end, additional processing steps might be necessary. Deeg and co-workers combined block copolymer micelle lithography with photolithography or electron beam lithography to create micropatches displaying

gold nanoparticle arrays surrounded by non-patterned areas.[206] The resultant "micro-nanopatterned surfaces" revealed that local ligand concentration was more important for cell attachment and spreading than global ligand concentration and cells required a higher detachment force to be applied when cultured on the micro-nanopatches.

Complementarily to single receptor spacing, another tunable variable that might provide insight in signal transduction processes is presenting ligands in a clustered fashion. As integrin receptors cluster on the cell membrane to form nascent adhesions, the underlying ligands might be aggregated as well. Not only integrin receptors form clusters to trigger the signaling process. Many other membrane receptors such as epidermal growth factor receptor (EGFR)[7], T-cell receptor (TCR)[184] or Eph receptor[207] require an oligomerization step for the coordination of the multiple signals into an orchestrated cellular response. In fact, some cellular responses are not elicited by individual ligands[208] and different strategies have been developed to present ligands in clusters, either in a soluble format or in a surface-bound configuration. These processes, in which it happens the simultaneous binding of multiple ligands on one entity to multiple receptors on another one are called multivalent interactions. Ligand-receptor multivalent interactions is a key fundamental principle in many biological processes such as viral entry, immune responses and cellular phase separations[209,210].

Many basic principles governing the importance of ligand presentation in multivalent configuration come from the study of the largest subfamily of receptor tyrosine kinases (RTK), the Eph receptors (Ephs) and their specific ligands, the ephrins. Ephs and ephrins play a relevant role in cell-cell communication during developmental processes and organ morphogenesis through the modulation of cellular functions including cell attraction, repulsion, motility, differentiation and survival.[211] They are down-regulated in adult tissues but often re-emerge in cancers.[212] Eph receptors localized in the plasma membrane of one cell interacts with their ephrin ligands anchored to the neighboring cell. There are nine human isoforms of EphA receptors that recognize five transmembrane ephrinA ligands, while five EphB receptors bind to three different types of ephrinB ligands.[208] Upon ligand-receptor interaction, signaling cascades are initiated in a bidirectional fashion; forward signaling mediated by the Eph receptor and reverse signaling mediated by the ephrin ligand. Eph receptors do not respond to monomeric soluble ephrin ligands.[207] This bidirectional downstream signaling is only

effectively activated after the aggregation of Ephs and ephrins into tetramers, which induce the cross-phosphorylation of Eph receptors (Figure 23).[213] Therefore, clustering is essential for receptor activation and signaling in such a way that downstream signaling can be further modulated within the cluster by interactions with ephrin ligands in *cis* or by heteromeric associations with other receptor types. The size and lifetime of the resulting Eph receptor clusters determines their cell adhesive or repulsive function. [214]

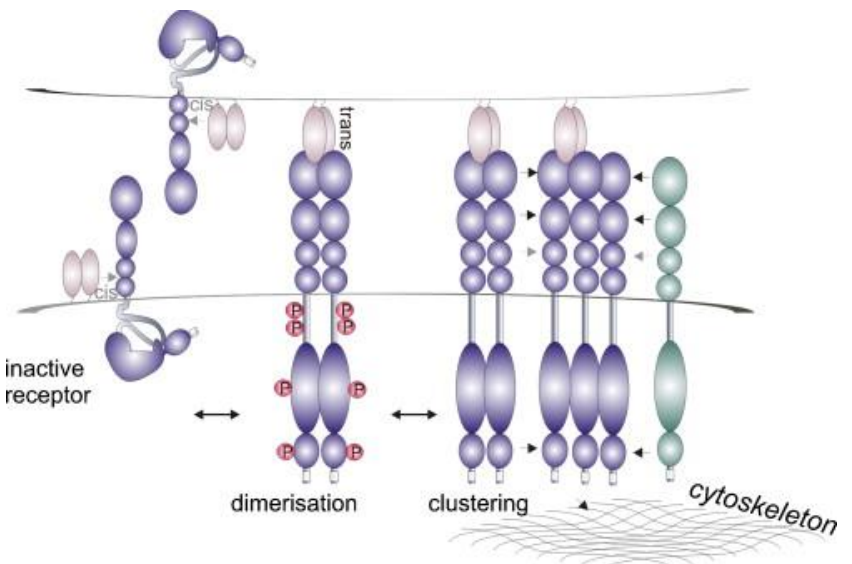

Figure 23. Model for Eph receptor clustering and activation. The inactive Eph receptor is held in a closed, auto-inhibited conformation, released upon phosphorylation and activation. Ephrin binding to one receptor initiates dimerisation into an Eph/ephrin hetero-tetramer. Further clustering is facilitated by receptor–receptor interactions between multiple domains of adjacent Ephs, including co-clustering of A and B type Ephs (indicated by different colours; grey arrows indicate proposed interactions with conflicting data). Interactions with cytoplasmic proteins and the cytoskeleton may contribute to clustering, as well as transmitting biological responses. Adapted with permission from [214] Copyright 2012 Elsevier Ltd.

To effectively foster the receptor activation and downstream functions, ephrin ligands have been traditionally aggregated by antibody-conjugation strategies.[207] However, recent advances in nanostructured materials have enable the design of multivalent ligand conjugates that potently induce receptor clustering. With a precise control of the number of ligands (valency) per entity, Conway and co-workers create synthetic hyaluronic acid chains about 100 nm in size conjugated with the ectodomain of ephrinB2 ligand. The stoichiometries covered with this strategy range from 2 to 25 ephrinB2 molecules per hyaluronic acid chain.[215] When administered in solution, the conjugated biopolymers propelled the formation of more and larger EphB4 receptor clusters in neural stem

cells and promote neural differentiation both *in vitro* and *in vivo* (Figure 24 A). To end up with equivalent levels of neuronal differentiation, the ligand concentration of ephrinB2-hyaluronic acid conjugates with a 1:22 valency required was 37-fold lower than in the case of antibody mediated-clusters. It is noticeable the high potency of nanomaterial based multivalent entities compared with the standard antibody-conjugated forms.

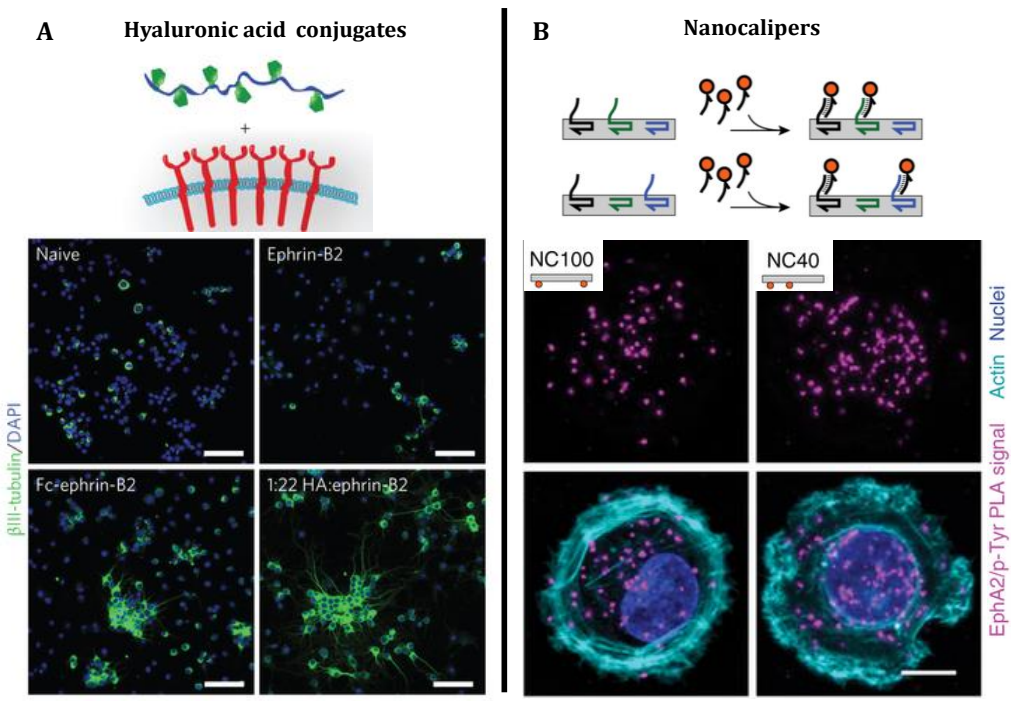

Figure 24. Multivalent conjugates delivered in solution. (A) Schematic representation of hyaluronic acid (HA) chain conjugated with 6 ephrinB2 ligands; Representative images of cultured neural stem cells differentiated for 6 days in media alone (naive) or in the presence of unclustered ephrin-B2, antibody clustered Fc-ephrin-B2 or multivalent 1:22 HA:ephrin-B2, then immunostained for the neuronal marker βIII-tubulin (green) and total nuclei (blue). Scale bars, 100mm. Adapted with permission from [215], Copyright (2014), Nature Publishing Group. (B) Schematic representation of DNA nanocalipers with varying the DNA oligonucleotide sequences (as depicted by different colours) used to control the spacing (NC40: 40 nm, NC100:100 nm) between binding sites for protein ligands (orange circles) bearing a complementary binding sequence (black strands); Phosphorylated EphA2 receptor (purple dots) in a human breast cancer cell line treated with NC100. Cells were stained for the actin cytoskeleton using Alexa 488–phalloidin (turquoise), and the nuclei using DAPI (blue).Adapted with permission from [216], Copyright (2014), Nature Publishing Group.

Rationally designed DNA strands can self-assemble to form origami nanostructures.[217] DNA sequences have been engineered to bind single-strand DNA-decorated ligands with a precise nanoscale separation. This DNA origami-based nanostructures, termed nanocalipers, were fused to ephrin dimers spaced ~40 nm (NC40) or 100 nm (NC100) (Figure 24 B). When used as soluble cues, Eph

receptor phosphorylation was rapidly observed upon stimulation with NC40 ligand conjugates in comparison with the phosphorylation level induced by individual ligands or NC100. Interestingly, these results suggest that ligands spaced approximately 100 nm produce no proximity effects and the signaling machinery interpret them as individual ligands and not as multivalent conjugates. Once again, this work brought to light the relevance of ligand nanospacing in the downstream signaling events.

Ligand spacing can be accurately controlled by different techniques in multivalent conjugates. However, as delivered in solution they can freely diffuse in the three dimensions. Thus, the spatial distribution of ligands encountering the cell membrane remains uncertain. Surface-bound ligand presenting strategies address these challenging prerequisites by providing the precise control on ligand spacing even at the moment of ligand-receptor interaction. The primary advantage of these functionalized substrates is that a single environmental cue can be isolated to unambiguously identify the contribution of a particular signal under a defined spatial configuration in a given cellular response. Although in most cases the immobilized ligands are ECM proteins, surface-bound presenting platforms are versatile and the functionalization strategy can be easily extended to attach soluble growth factors[218] or membrane-bound proteins[219] involved in paracrine and juxtacrine signaling (Figure 25).

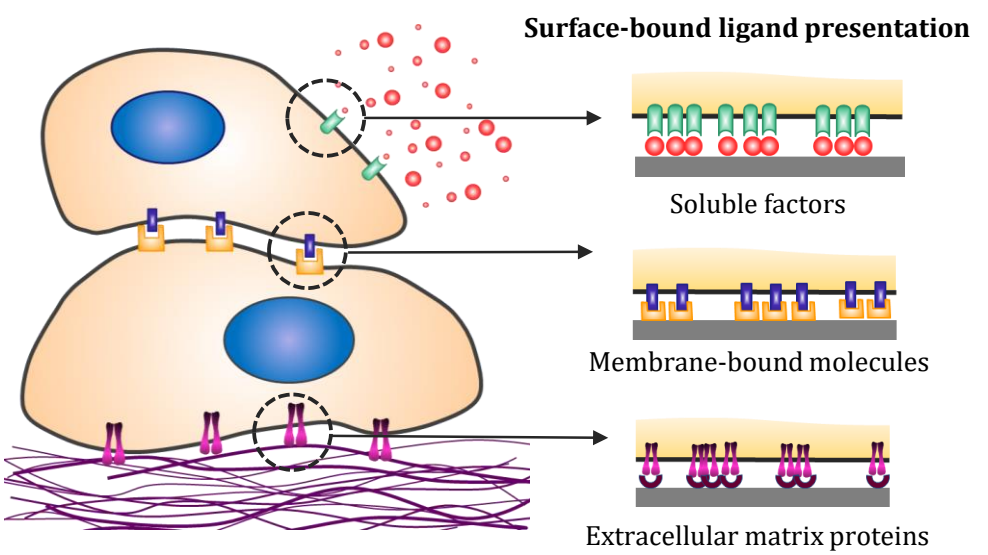

Figure 25. Schematic illustration of ligand-receptor interactions at the cell membrane. Surface-bound ligand presentation provide means to interrogate cells in the ligand-receptor interactions under spatially controlled distribution of any existing cue in the extracellular microenvironment, from soluble factors, membrane bound molecules or extracellular matrix proteins.

In 2000, Griffith and co-workers designed an original strategy to investigate the clustered presentation of ligands on surfaces. Polyethylene oxide (PEO) star-like dendrimers were decorated with 1, 5 or 9 RGD ligands in such a way that the adhesive ligand was presented either homogenously (1 RGD/star) or in a clustered format (multiple RGD/star).[198] Cell culture surfaces were coated with the appropriate combination of these RGD-modified PEO stars with blank PEO stars to generate high *versus* low density ligands either in as individuals or in clustered configurations (Figure 26). For each clustered arrangement, cell adhesion strength was enhanced while increasing global ligand densities. Additionally, at a given global density, cell adhesion strength increased with increasing number of RGD ligands/star. RGD-functionalized polymers were also used to investigate other fundamental cell functions such as, migration, proliferation and differentiation.[16,220] As one of the first works in the field, the spatial ligand distribution on the surface was only theoretically predicted by mathematical models.[221]

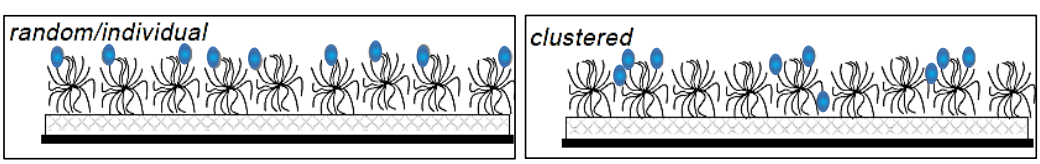

Figure 26. Schematic illustration of star polymer as a tether to present ligand (blue oval) in different spatial distributions, from homogeneous to highly clustered (left to right). Local ligand density can be independently varied from the global ligand density.[198]

Diverse membrane bound proteins involved in cell-cell communication are displayed in aggregated surface-bound configuration.[7,14] For example, during the initiation of the immune recognition, lymphocytes contact with antigen presenting cells (APC) to form the immunological synapse. At the lymphocyte plasma membrane T cell receptors (TCR) as well as integrins are reorganized into microclusters.[184,222] Recently, a similar arranged organization has been identified for TCR ligands on the surface of antigen presenting cells.[223–225] After effective ligand induction, TCR clusters are centripetally dragged to form the supramolecular activation clusters (SMACs) *via* actin dependent translocation.[219] The acting retrograde flow guides the inward transport of TCR clusters.[226] In the light of these findings, Dillard and co-workers engineered a patterned substrate to mimic the clustered presentation of TCR ligands by a "surrogate" antigen presenting strategy (Figure 27 A).[14] The antibody (α-CD3) was immobilized in arrays of dots featuring sizes ranging from 0.3 μm to1.3 μm (Figure 27 B). On these micropatterned surfaces, T cell receptors formed larger and more numerous

clusters than on homogenously coated surfaces, which manifests the ability of T cells to sense the local differences in ligand density. On the other hand, the global density was the parameter governing the cell spreading response in a dose-dependent way. TCR clusters connected to immobilized ligands showed a reduced radial transportation and no centralization of the TCR was observed (Figure 27 D and E). The non-ligated T cell receptors can diffuse through the plasma membrane and form clusters, however these non-ligated TCR clusters were not centripetally transported, which indicated a weak or non-existent coupling to actin. A frictional coupling has been proposed to connect ligated-TCR with the actin cytoskeleton.[227]

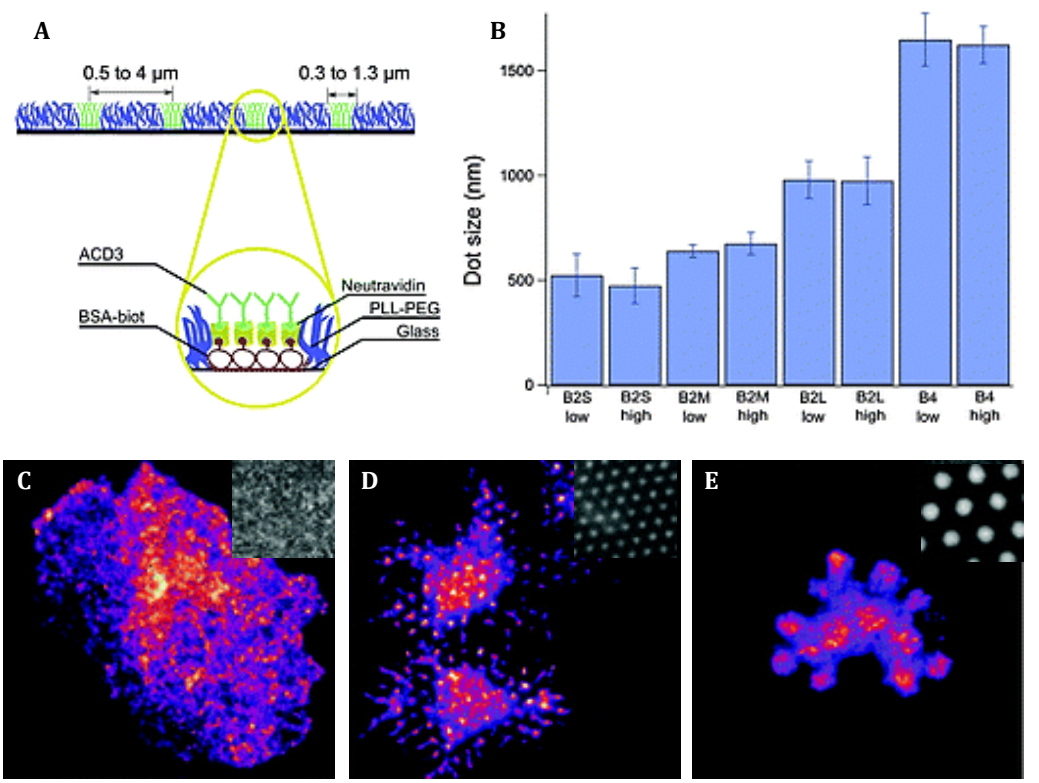

Figure 27. TCR clustering on ligand-tailored patterns. (A) Schematic representation of the patterned substrate. (B) Quantification of the size of the antibody nanodots from fluorescence images of the underling neutravidin. B2S, B2M, B2L and B4 refer respectively to dots with 2 or 4 µm spacing and small, medium or large size; high or low refers to PEG surface density. Distribution of T cell receptors (TCRs) on cells seeded on ligand presenting surfaces: (C) positive control surfaces with homogenous ligand distribution; (D) "B2M high" dots (inset: dot array of approx. 600 nm in size); (E) on "B4 high dots" (inset: dot array of approx. 1.5 µm in size). On the patterned substrates TCR clusters are clearly visible and are usually well localized on the site of the underlying antibody dots. Adapted with permission from [14] Copyright 2016 Royal Society of Chemistry.

The role of ligand mobility, receptor cluster diffusion and actin-dependent transportation of membrane receptors has been extensively investigated on surface-bound ligand presenting substrates.[222,228–230] This is the particular case of

the ligand-receptor pair formed by ephrin and Eph receptor.[231] In an elegant and sophisticated work performed by Salaita and co-workers, supported lipid bilayers were used for the surrogate presentation of ephrin ligands. To manipulate the assembly of receptor clusters at the microscale, micron-sized patterns of nanometric barriers fabricated by electron beam lithography were imposed within the supported-lipid membranes. This technique was proposed as a spatial mutation approach, where membrane-tethered ephrin ligand diffusion was restricted to micron-sized areas. Different sizes of square-micropatterned barriers were fabricated on membranes with equivalent ligand densities (800 molecules/μm^2) in such a way that only the spatial distribution was varied. The restricted lateral diffusion of ephrinA1 ligand inferred differences in EphA2 cluster transport, cytoskeleton organization and recruitment of a desintegrin and metalloprotease 10 (ADAM10).[232] The micropatterned grid mechanically impede the radial transportation of EphA2 clusters which are retained at the edges of the barriers (Figure 28). To obstruct their transport, the mechanical barriers should exert a force on them of equal magnitude and in the opposite direction to the force applied by cells via acto-myosin contraction. The co-presentation of RGD ligands in ephrinA1 decorated membranes demonstrated that the centripetal transport of EphA2 is independent of integrin mediated adhesion and signalling. Another functional consequence of this physical interference is the reduced recruitment of ADAM10 by the receptor-ligand complexes (Figure 28). ADAM10 is a transmembrane metalloprotease leading the proteolytic cleavage of the extracellular ephrinA1-EphA2 interaction, which initiates the cell-cell detachment and the endocytosis of the EphA2 clusters.[233] The systematic study on 26 mammary epithelial cell lines revealed a significant association between the EphA2 radial transport phenotype and the invasion potential of cells.

The substitution of the micropatterned barriers by arrays of gold nanoparticles[229] have revealed that upon stimulation with diffusive ephrinA1 ligands, EphA2 microcluster transport is not hindered by the presence of nanodot-like barriers. In these cases, no restriction of inward transport was observed even when the receptor microcluster sizes exceed the nanodot interspacing. [234]

These findings exemplify how controlled surface-ligand presentation can shed new light on spatially-modulated receptor activation and oligomerization processes, which might modulate pathological processes such as cancer progression. However, whereas receptor microclusters (high-order oligomers)

have been thoroughly analysed, much less attention has been paid to initial stages of oligomerization (low-order oligomers).

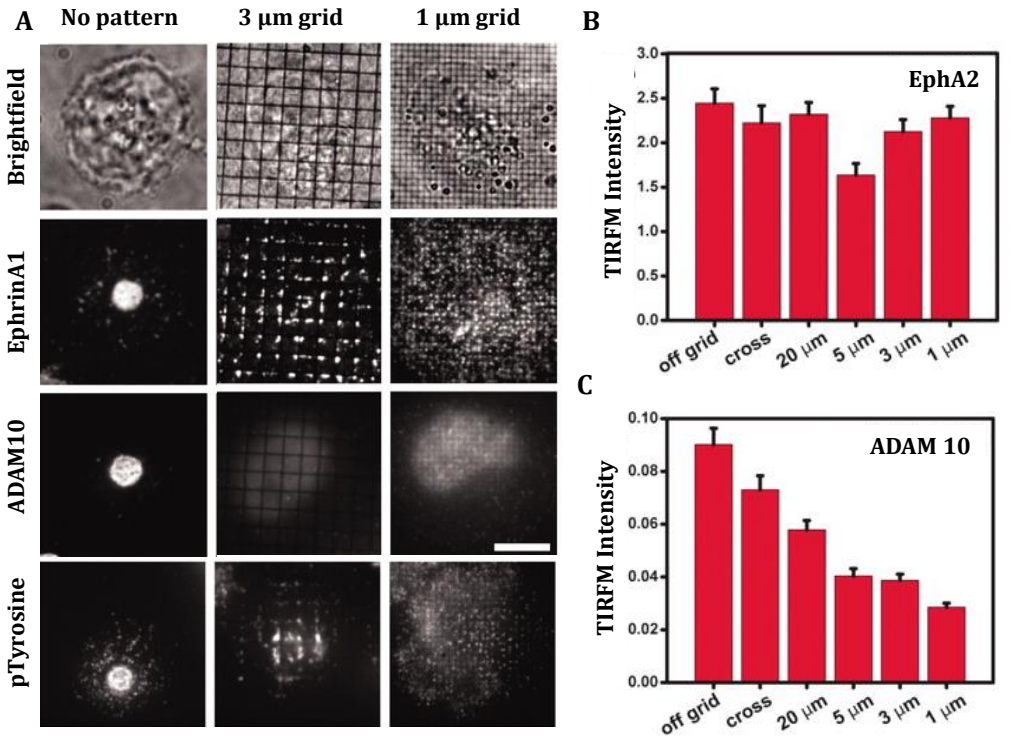

Figure 28. The functional consequences of EphA2 spatial mutation. (A) Lateral diffusion of the EphrinA1 as well as the lateral transport of the EphA2 receptor is hindered by micropatterned grids prefabricated onto the glass support. Breast cancer cells were seeded on the ephrin-A1 functionalized supported membrane, fixed and stained for receptor phosphorylation and recruitment of the downstream effector molecules ADAM10. (B)ADAM10 colocalized with the EphA2-ephrin-A1 assembly on unrestricted supported membranes. However, when EphA2 transport was restricted by physical barriers, the measured colocalization decreased (n = 477 cells). This indicates that mechanical restriction of EphA2 modulates ADAM10 recruitment. Adapted with permission from [232] Copyright 2010, The American Association for the Advancement of Science.

A prominent precedent that cleverly illustrates the relevance of low order species during receptor activation and signalling was performed by the use of chemical dimerizers. COS7 cells were genetically modified to transiently express mutant EphB2 isoforms with various dimerizer-binding domains (Figure 29). Receptors with a single dimerizer-binding domain lead the formation of dimers. Receptor molecules fused to two dimerizer-binding domains resulted in the generation of EphB2 oligomers where trimers are the predominant species, followed by dimers and other low-order oligomers (up to pentamers). Increasing the dimerizer-binding domains up to three insertions per receptor molecule, abruptly changed the cluster composition toward high-order oligomers. Although

the EphB2 cluster populations artificially activated upon dimerizer stimulation are heterogeneous, differences in the abundance of low and high order species dictated the strength of the signalling response. If receptor dimers are predominant, the collapse response is significantly weaker than for trimers and tetramers (Figure 29). The results suggested that EphB2-mediated cytoskeleton remodeling is proportional to the abundance of EphB2 high-order species (multimers) over dimers.

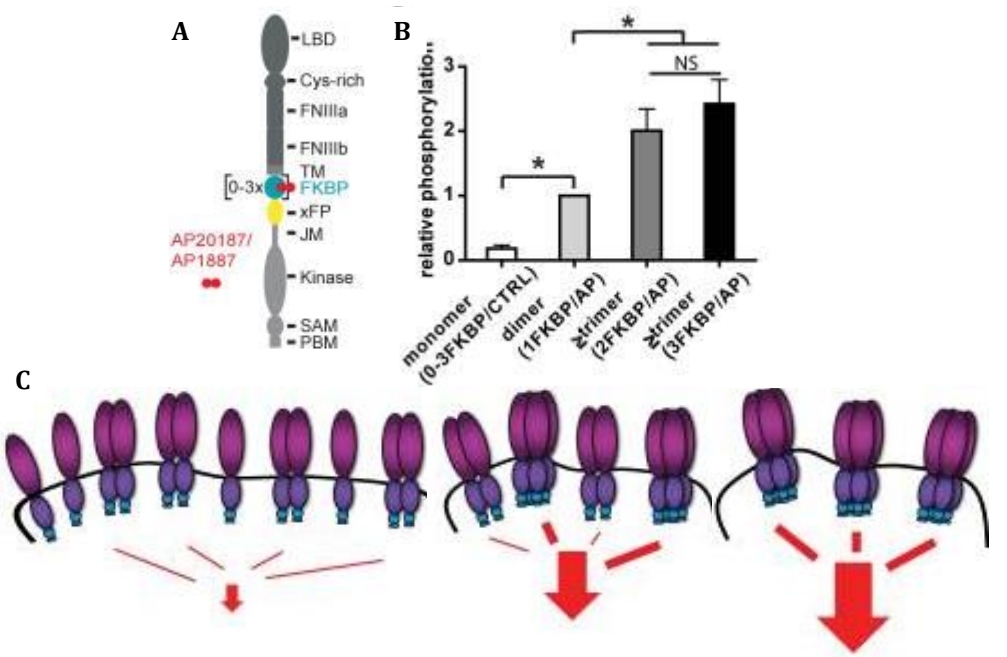

Figure 29. Artificial generation of EphB2 cluster populations. (A) Domain structure of EphB2/A4 with 1 to 3FKBP domains and a single fluorescent. Homodimerizers AP20187 or AP1887noncovalently cross-link FKBP domains of neighboring Eph receptors. (B) Quantification of the cumulative relative phosphorylation versus total EphB2 for each receptor oligomer population. (C) Model depicting regulation of EphB2 clustering: a mixture of monomers and dimers is essentially inactive because dimers have weak signaling output. A mixture of dimers and multimers leads to a physiological response; however, the response gets stronger when all dimers are converted to multimer.

Alternatively to artificial receptor clustering or spatial mutation approaches, patterns of surface-bound ligands with nanometric resolution might effectively elicit receptor oligomerization when presented in a multivalent format. This surrogate presentation of ligands with a defined spatial distribution can serve as an advantageous tool to study the initial stages of receptor oligomerization. However, understanding the assembly of receptor complexes is limited by the availability of methods capable to reach single molecule sensitivity in the membrane of living cells. Currently, receptor clusters are visualized and tracked

mostly when multiple number of receptors have been aggregated into the complex. Conventional microscopy techniques such as time-lapse microscopy or confocal fluorescence microscopy are commonly used to analyse downstream signalling effects on cell adhesion, cell migration, or cell fate. Methods such as single molecule fluorescence and single particle tracking have limited capacity to discriminate between oligomer populations. Near-field scanning optical microscopy (NSOM) has a spatial resolution below 100 nm but cannot be performed on live cells.[235]

If the final goal is the evaluation of the receptor oligomerization dynamics, the selected technique should provide quantitative information to evaluate the stoichiometry of the different protein complexes as well as molecular level sensitivity over large areas. Moreover, receptor dynamics should be understood as a process involving broad temporal scales, ranging from the msec-sec to tens of minutes: the smallest time-scale corresponding to molecule-molecule interactions and the largest one to the time that cells take to orchestrate the response. A recently described correlation method, named Number and Brightness (N&B), directly evaluates the molecular size of diffusing oligomers in living cells. Sequential confocal images are acquired to measure the fluorescence intensity fluctuations for each single pixel over the consecutive acquired data. This molecular brightness is directly related to the oligomerization state of the fluorescence molecule.[236]

In the present work, we describe a controlled protein nanopatterning strategy for the in depth study of receptor clustering processes, overcoming some of the limitations and difficulties associated with current methodologies. We demonstrate the utility of this strategy by generating two nanopatterned substrates and using them to examine the cell adhesion and receptor dynamics, upon multivalent substrate-bound ligand clusters presentation.

2. Objectives

Numerous experimental evidences outline a remarkable impact of ligand presentation on the cell receptor activation and downstream signaling. Towards a thorough understanding of these spatially modulated processes, herein we propose to develop nanopatterned-ligand presenting platforms on diblock copolymer surfaces to investigate ligand-mediated receptor signaling. To achieve this ambitious goal, the following specific objectives are defined:

- Design, fabrication and characterization of nanopatterned substrates based on self-assembled diblock copolymer technology. Precise control of the regular size and spacing between features with sub-100 nm dimensions.

- Development, optimization and characterization of a functionalization strategy to covalently link biomolecules on diblock copolymer thin films following the template beneath. Generation of a versatile method that enables the immobilization of any protein or small peptides.

- Study of cell response over surface-bound nanopatterned ligands, depicting the relevance of spatial distribution of ligands at the nanometer scale and the multivalent effects of ligand clusters on receptor signaling.

3. Experimental procedures

3.1. Factors driving block copolymer thin film formation

Figure 30 shows the required steps to create a poly(styrene)-*b*-poly(methyl methacrylate) thin film with perpendicular PMMA cylinders immersed in a PS matrix. Initially, a surface modification is necessary to obtain an energetically neutral surface for both polymer components enabling the perpendicular orientation of PS-*b*-PMMA domains.[103,237] Block copolymers are spun coated onto the non-preferential surface forming a thin film and undergo a thermal annealing step at a high temperature to increase molecule mobility and promote the ultimate self-assembling into ordered nanostructures.[104]

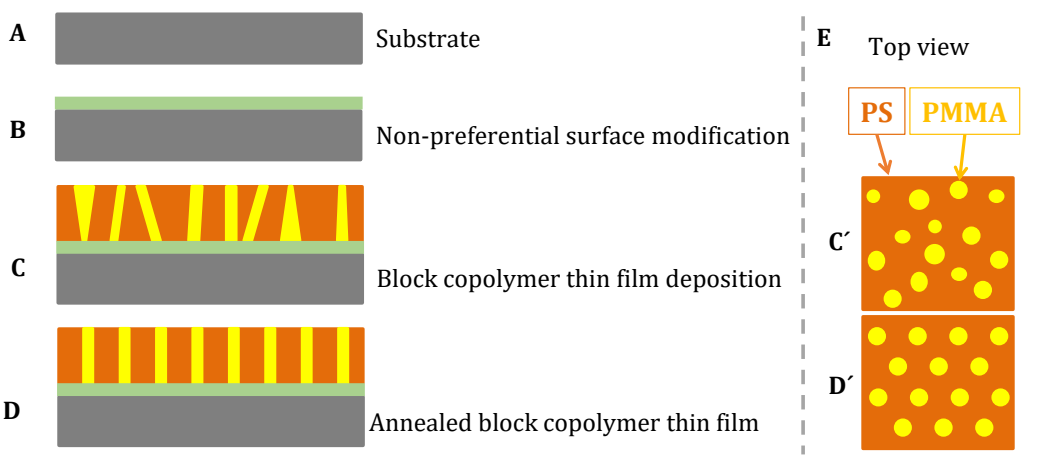

Figure 30. Scheme of the steps for block copolymer thin film fabrication: (A) Substrate activation, (B) non preferential surface modification, (C) PS-b-PMMA block copolymer thin film deposition by spin coating and segregation of PMMA fraction into cylindrical domains (yellow) immersed in a polystyrene matrix (orange), (D) thermal annealing of block copolymer thin film generating perpendicular and ordered nanostructures, (E) top view of (C´) PS-b-PMMA block copolymer thin films before (C) and (D´) thermal annealing (D).

3.2. Chemical surface modification to ensure non-preferential affinities

Phase segregation of diblock copolymers is determined by the interactions between the two polymers comprising the molecule and the energetic balance between the blocks and the contact interfaces: the substrate and the free surface in the case of semi-confined systems (thin films).

Surface modification of the substrates can be performed to tailor surface properties in a controllable fashion and achieve a proper energetic balance. None of the block copolymer components should show any preferential interfacial segregation to the substrate. In order to obtain a neutral wetting surface, silicon substrates were modified with silane self-assembled monolayers and copolymer brushes.

3.2.1. Surface modification by silane self-assembled monolayers

Square silicon substrates (native oxide wafer, D+T Microelectrónica, Spain) of 4 cm^2 area were cleaned with piranha solution (H_2SO_4/H_2O_2 (7:3; v:v)) (sulphuric acid 95-98% (Panreac Química S. A. U., Spain) and hydrogen peroxide (BASF , Spain)) for 20 min. (*Caution: Piranha solution is highly corrosive and reacts violently with organic matter*). Milli-Q water was used to remove the cleaning solution and samples were dried under a nitrogen flow. Silanization is a strategy widely reported in literature for the modification of the physical and chemical properties of a surface. Organosilanes form self-assembled monolayers (SAMs) and can be used to tune surface wettability generating an intermediate adhesion layer for subsequent depositions. Two different organosilane molecules were tested, selected because of their excellent binding properties to hydroxyl terminated surfaces such as native oxide layer of silicon or glass after piranha treatment: (3-aminopropyl)triethoxysilane (APTES) (Sigma-Aldrich Química, Spain) and trichloro(1H,1H,2H,2H-perfluorooctyl) silane (PFOS) (Sigma-Aldrich Química, Spain). These molecules can react with the hydroxyl groups forming a covalent siloxane bond (Figure 31).[238]

Vapor-phase deposition of silanes is known to uniformly form a reproducible monolayer modifying the physical and chemical properties of the surface.[239] The cleaned silicon substrates were placed together with an opened vessel with a 200 µL drop of silane solution in a dedicate desiccator for each organosilane molecule. The silane atmosphere was generated and maintained for 1 h. The silanized substrates were baked at 80°C for 1 h and cleaned in an ultrasonic bath with a solution of 50% (v/v) isopropanol/ethanol (Panreac, Spain) for 15 min to remove any potential agglomerate. After air drying, samples were imaged with an atomic force microscope for the characterization of monolayer and evaluation of its uniformity. Tapping-mode atomic force microscopy (AFM) measurements were performed using a Dimension AFM instrument (Veeco Instruments, USA) equipped with a rectangular silicon AFM tip (Nanosensors, PPP-

NCHR, spring constant 42 N/m, resonance frequency 330 KHz radius of curvature about 10 nm, aluminium backside coating, and 125 μm in length). Representative images of 4 μm^2 were acquired from separated areas over at least three independent substrates presenting different silane-modified surfaces. Topographic AFM images were processed using WSxM Software (Nanotec Electrónica, Spain), applying simple flatten algorithm.[240] Replicas of these substrates will be used in further experiments detailed in Section 3.3.

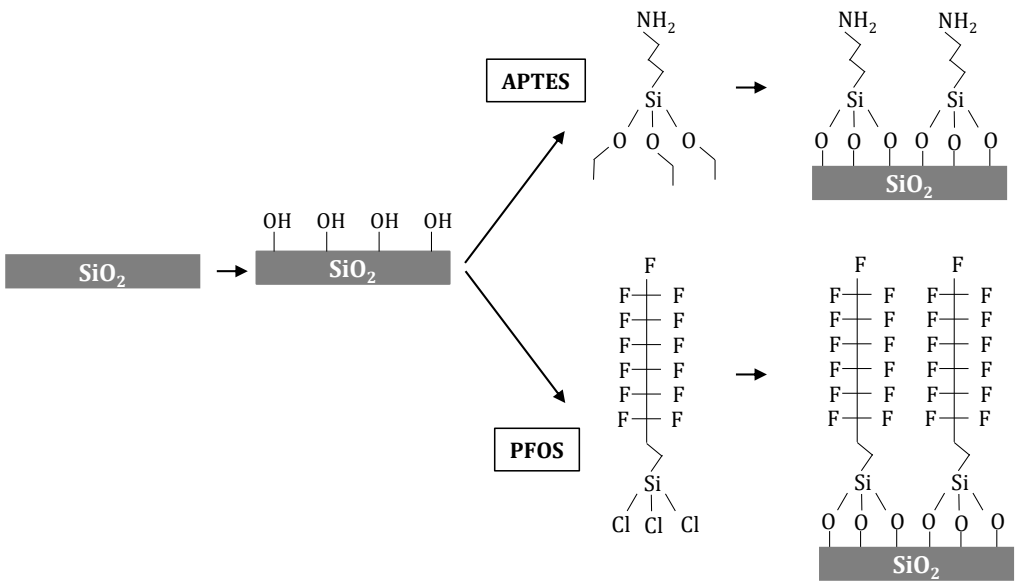

Figure 31. Schematic representation of surface modification using organosilanes on –OH terminated silicon or glass substrates. Silicon oxide wafers or glass coverslips were initially activated with piranha solution to generate an enriched surface presenting hydroxyl groups. A siloxane bond can be formed between the terminal -0H moieties and the (3-aminopropyl)triethoxysilane (APTES) or trichloro(1H,1H,2H,2H-perfluorooctyl) silane (PFOS). Ultimately, a self-assembled monolayer (SAM) of silanes is generated modifying the surface properties of the substrate

3.2.2. Surface modification by random copolymer brushes

Poly(styrene-co-methyl methacrylate) α-hydroxyl-ω-tempo moiety terminated random polymers (PS-r-PMMA-OH) (Polymer Source Inc., Canada) were selected as neutral wetting brushes (Figure 32) based on their polystyrene (PS) content and were used without further purification.

Two random copolymer brushes with different styrene fractions (f_{PS}) were used according to the block copolymer physico-chemical characteristics defined in Table 1.

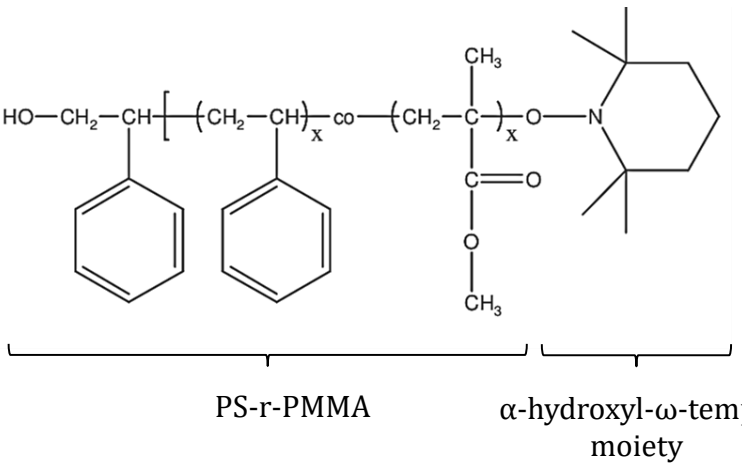

Figure 32. Chemical structure of poly(styrene-co-methyl methacrylate) α-hydroxyl-ω-tempo moiety terminated random polymer (PS-r-PMMA-OH) and separated with curly brackets are indicated the PS-r-PMMA fraction and the α-hydroxyl-ω-tempo moiety.

Table 1. Physico-chemical parameters defining random copolymer brushes.

Copolymer brush	Polystyrene fraction (f_{PS})	Molecular weight (M_n)	Polydispersity Index (PDI)	Glass transition temperature (T_g) (°C)
Brush-71	**0.71**	**15500**	**1.15**	**-**
Brush-74	**0.74**	**14000**	**2.09**	**94**

Glass coverslips (18 mm in diameter, Neuvitro, USA) of 2x2 cm square silicon pieces (D+T Microelectrónica, Spain) were used as substrates. Firstly, they were mechanically cleaned with a cleanroom wiper pre-wet with 96% ethanol solution and subsequently immersed in piranha solution (*Caution: Piranha solution is highly corrosive and reacts violently with organic matter*). Once cleaned, substrates were place into Milli-Q water bath and preserved there for a minimum period of time, preferably less than 15 min. A pressurized nitrogen flow was used to blown dry the substrates and excessive moisture was removed by a hot air gun. Substrates were then activated prior the deposition of random copolymer brushes by exposure to an oxygen plasma (Expanded Plasma Cleaner PDC-002, Harrick Scientific Corporation, USA) for 2 min at 30 W.

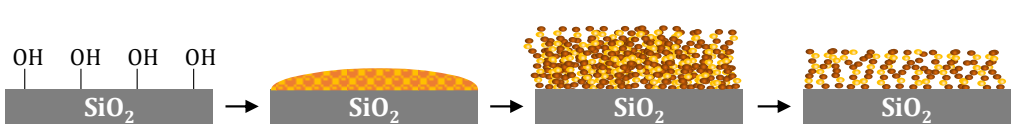

Figure 33. Schematic representation of non-preferential surface modification using copolymer brushes.

Through this process the maximum number possible of hydroxyl groups (silanol) were generated on the surface, increasing the reactive anchoring points

for copolymer brush binding. Copolymer brush solutions were prepared at 2.5 mg/mL concentration in toluene anhydrous (Sigma-Aldrich Química, Spain) and were spun-coated on the oxygen plasma-activated surfaces using a Laurell Model WS-400A-6TFM/LITE spinner. A two-step recipe was set with a first step for a rapid acceleration (500 rpm, 5 s, acceleration 300 rpm^2) and a second step for spinning (3000 rpm, 40 s, 300 rpm^2). The generated thin films were annealed under vacuum at 220ºC for 7 days (Vaciotem-T J.P. Selecta, Spain). Temperature is a critical parameter to control during the engraftment process. In a vacuum oven, conduction and radiation are the two phenomena leading heat transfer under low pressure conditions. Small variations in sample-shelf contact can impair the heat transfer between surfaces and, as a consequence, the sample temperature can differ from the temperature recorded with the thermometer of the oven. For this reason, a Spot Check® surface thermometer (PTC Instruments, USA) was directly place in contact with a representative sample surface during each thermal annealing cycle. During this time, hydroxyl-terminated molecules are chemically attached to the substrate forming a brush layer. These controlled thermal conditions are required to ensure the desired grafting density, in our case, a compact array of polymer brushes at a maximum packing density.[241] Glass transition temperature of the copolymers components (T_g of PS: 103°C; T_g of PMMA: 115°C)[165,242] was exceed to allow polymer chains to diffuse and interact with the surface.[103] Annealing treatment was performed under vacuum to reduce the possible oxygen presence that would cause oxidation of the copolymer brush. Once the surface is covered with the copolymer brush layer, samples can be stored for 2 weeks at room temperature. Previously to their further use, the remaining non-grafted polymer chains of the layer were removed by immersion in 5 mL of fresh toluene for 30 s under agitation. Finally, substrates were blown dried under a pressurized nitrogen flow. Tapping-mode AFM measurements were performed to determine copolymer brush thickness and coverage. These samples were used as substrates for experiments described in Section 3.3.

3.3. Block copolymer thin film formation on surface modified substrates and characterization of self-assembled nanodomains

Three cylinder-forming PS-*b*-PMMA copolymers were purchased (Polymer Source Inc., Canada) and used without further purification. The molecular weight

and polymer fraction will both determine the cylinder diameter of the PMMA domains and interdomain spacing. A random copolymer PS-*r*-PMMA (RandomCP) presenting comparable styrene fraction was also purchased (Polymer Source Inc., Canada) to be used as control for "non-patterned" surfaces. Polymer composition details are described in Table 2.

Table 2. Physico-chemical parameters defining cylinder-forming PS-b-PMMA copolymers and random PS-r-PMMA copoylmer.

Type	Abbrev.	Molecular weight (M_n)	PS M_n	PMMA M_n	Polystyrene fraction (f_{PS})	PDI
Cylinder -forming	**BCP small**	**67000**	**46000**	**21000**	**0.69**	**1.09**
	BCP medium	**158000**	**123000**	**35000**	**0.78**	**1.09**
	BCP large	**353500**	**201500**	**152000**	**0.57**	**1.09**
Random	**RandomCP**	**14000**	**-**	**-**	**0.76**	**1.24**

All polymer solutions were prepared for each experiment (storage is not recommended) by dissolution of the polymer powder in 5 mL of anhydrous toluene at the desired concentration. Solutions were stirred for 2 h at room temperature and then filtered (Millex® syringe filter unit form Sigma-Aldrich Química, Spain). Diblock copolymers were deposited by spin coating on top of the surface modified substrates with either self-assembled monolayers of silanes or copolymer brushes.

Microdomain orientation of PMMA cylinders is sensitive to thin film thickness. Under neutral conditions, perpendicularly oriented morphology is adopted in a narrow film thickness window located near the lattice spacing value (L_0: natural domain period). L_0 is different for each diblock copolymer, depending on the molecular weight (degree of polymerization (N)) and the copolymer fraction interaction (Flory-Huggins segment-segment interaction parameter (χ)) (described previously in Section 1.2). Film thickness can be tuned varying spinning speed or polymer concentration.

To determine the spinning parameters, two spinning speeds were tested: 3000 rpm and 6000 rpm. Silicon samples were cleaned with piranha solution (H_2SO_4/H_2O_2 (7:3; v:v)) for 20 min. Once cleaned, substrates were rinsed with Milli-Q water and blown dried with nitrogen. BCP large was dissolved in anhydrous toluene at the different concentrations (1 mg/mL, 1.5 mg/mL and 2.5 mg/mL) and samples were spun coated at 3000 or 6000 rpm for 40 s.

To measure film thicknesses, we followed the scratch test, where a sharp instrument (razor blade or splinter tip tweezers) was used to perform a scratch in the polymer film.[132] Topographic images were obtained where the film thickness was determined from the difference in height found in the edge of the scratch between the mean surface plane and the scratch below.[243] Scratches were performed crossing the sample length. At least three samples and three regions per sample along the scratch were imaged in air by tapping mode AFM to obtain statistical meaningful values. Imaging was done in the central portion of the samples, avoiding the peripheral substrate areas. Scratch tests on bare silicon or glass substrates using the same scratching methodology shown no damage. Gwyddion software (Czech Metrology Institute, Czech Republic) was used to analyse topographic AFM images levelling the data to make facets point upward. A single-pixel line width profile was plotted and the closest points to the vertical wall of the scratch were taken as measuring points. Thickness values are shown as the mean value ± the standard deviation.

Complementarily to variations in spinning speed, variations in polymer concentrations are used to get film thicknesses matching the corresponding natural domain period. A range of polymer concentrations were scanned to define the relation between solution concentration and film thickness. BCP large was dissolved in anhydrous toluene at 1 mg/mL, 1.5 mg/mL, 2.5 mg/mL, 5 mg/mL and 10 mg/mL. Piranha-cleaned silicon samples were spun coated at 3000 rpm for 40 s. Film thickness of was measured by the scratching method as previously described.

Once film thickness was optimized, surface roughness analysis and morphology of the self-assembled diblock copolymer thin films was evaluated. Surface modified silicon substrates described in Section 3.2 were used as substrates providing neutral interfacial energies. Thin films were prepared by spin-casting the following copolymer concentrations:

- 7.5 mg/mL concentrated BCP medium solution.
- 5 mg/mL concentrated BCP small solution.
- 5 mg/mL concentrated RandomCP solution.

An annealing step is necessary to promote self-organization of PMMA domains into an array of hexagonally arranged cylinders (Figure 34A). For that purpose, thin films were heated in a vacuum oven (Vaciotem-T, J.P. Selecta, Spain)

at 220°C under vacuum for 3 h. For a convenient annealing, temperature should be properly controlled with a Spot Check® surface thermometer. Tapping mode AFM measurements of the thin films in air were performed before and after annealing to capture subtle variations in topography due to phase segregation. Root mean square (RMS) roughness is a widely used parameter for describing the height variations in the surface by computing the root mean square average of the roughness profile ordinates. RMS roughness calculations were performed from 4 μm^2 images acquired from randomly selected areas over at least three samples from independent experiments. Simple flatten algorithm was performed with WxSM software before roughness evaluation.

Self-assembled periodic structures are characterized by the PMMA cylinder diameter (Φ) and the interdomain spacing (L_0). The interdomain spacing is the distance between the nearest cylinder neighbors, which is a constant value for hexagonally-packed cylinder arrays (Figure 34B).

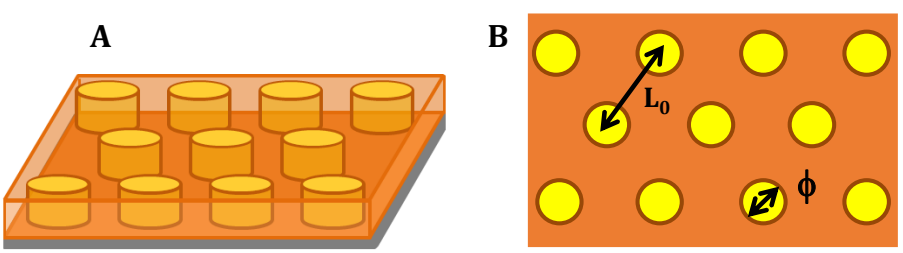

Figure 34. Scheme of a block copolymer thin film. (A) 3D-representation of an asymmetric cylinder forming block copolymer thin film (PS and PMMA fraction represented in orange and yellow respectively) and (B) top-view representation of the self-assembled thin film with the main characteristic parameters: cylinder diameter [Φ] and interdomain spacing [L_0].

The perpendicular orientation of PMMA cylinders after annealing of diblock copolymer thin films was evaluated by AFM and scanning electron microscopy (SEM). Selective PMMA photooxidative degradation can be conducted to enhance the contrast between PS and PMMA phases. Photodegradable properties of PS and PMMA are significantly different. PMMA is known to be degraded upon ultraviolet (UV) light exposure by the random scission of carbon-carbon bonds from the polymer chain backbone and becomes soluble in acidic solutions (such as glacial acetic acid).[140,244] On the other hand, under UV light irradiation of PS-containing materials, a combination of chemical reactions are triggered mainly dominated by the cross linking process.[245] Then, PS component is stiffened and becomes insoluble in acidic solutions.

By taking advantage of this property, PMMA domains of BCP medium and BCP small thin films before and after annealing were selectively etched. Samples were UV-irradiated for 90 min with a high intensity mercury vapour lamp (UV/Ozone cleaner ProCleaner™, BioForce Nanoscience Inc., USA). PMMA degradation products were removed by immersion of the samples in 5 mL glacial acetic acid (17.4 M) (Sigma-Aldrich Química, Spain) for 15 min under agitation. A final rinsing with fresh glacial acetic acid was carried out before samples were blown dried with a pressurized nitrogen flow. Etched thin films were then imaged by a NOVA NanoSEM 230 scanning electron microscope (SEM) (FEI, The Netherlands). An acceleration voltage of 10 keV in high-vacuum mode was set and secondary electron images were acquired with a Through the Lens Detector (TLD). The nanoporous structures were additionally characterized by topographical images acquired by AFM in tapping mode as previously described in this section. The resultant perforated three-dimensional structure after thermal annealing revealed the alignment of PMMA cylinders normal to the substrate.

The Fast Fourier Transform (FFT) algorithm can be applied to image processing for many application: such as filtering, noise removal or pattern recognition.[246] Applying this mathematical expression, a spatial domain, i.e., a specific image, can be computed as a frequency domain, where the image is captured in terms of variation in colour and brightness over the image plane.[247] When the original image shows a periodic pattern, the magnitudes of its Fourier spectrum reflects the regular structure on certain directions.[248] Block copolymer thin films self-assemble into regular arrays of hexagonally packed PMMA cylinders immersed in a PS matrix.

The efficiency of thermal annealing in PMMA cylinder ordering was evaluated on photochemically etched PS-*b*-PMMA thin films. Topographic images were acquired and we compared the resultant nanodomain segregation before and after thermal annealing. The Fourier analysis was performed on 4 μm^2 images to illustrate the characteristic period of the cylinder array.[249]

In addition, the presence of defect in the in the crystal-like structure, ws evaluated by plotting the Voronoi diagrams corresponding to AFM images of BCP medium and BCP small thin films. Voronoi plots were obtained by applying the Delaunay/Voronoi plugin of ImageJ free software ImageJ free software (http://rsb.info.nih.gov/ij, National Institutes of Health, USA) to the AFM images.

From the Voronoi diagrams obtained, the density of defects with respect to a perfect crystalline hexagonally packed structure was calculated.

BCP medium and RandomCP thin films were analyzed in terms of surface wettability. Static water contact angles (WCAs) were measured by the sessile-drop method with an OCA contact angle system (Dataphysics, Germany). A droplet of a liquid with a known surface energy, is placed onto a surface. The surface energy of the surface can be calculated from the shape, specifically the contact angle between the droplet and the surface. We used water (Milli-Q ultrapure water, Merck Millipore, Spain) droplets of 1 µL volume that were dispensed with a syringe. Images of the droplets contacting surfaces were immediately recorded after droplet stabilization (approx. 5 s).[250] The droplet profile was acquired and fitted with SCA20 software (Dataphysics, Germany) applying elliptic fitting method. Three samples of BCP medium and RandomCP thin films after thermal annealing were characterized and at least three droplet-shape analysis were performed for each substrate. The resulting values were compared with the ones obtained from pristine PS sheets (Goodfellow, UK) and PMMA surfaces. Flat PMMA films were generated by spin casting a 950PMMA 11% solution in anisole (950PMMA A Resist from MicroChem Corp., USA) onto PMMA sheets of 500 µm in thickness (Goodfellow, UK). Static water contact angles of at least three droplets were measured on a minimum of three samples for PS and PMMA surfaces, respectively.

3.4. Generation of carboxylate groups by PMMA selective hydrolysis

PMMA consists of a non-polar backbone with pendant methyl ester groups that can be regarded as reactive points for surface modification and molecule binding. Hydrolysis of these methyl ester groups under basic conditions leads the formation of carboxylic groups on the PMMA nanodomain (Figure 35).

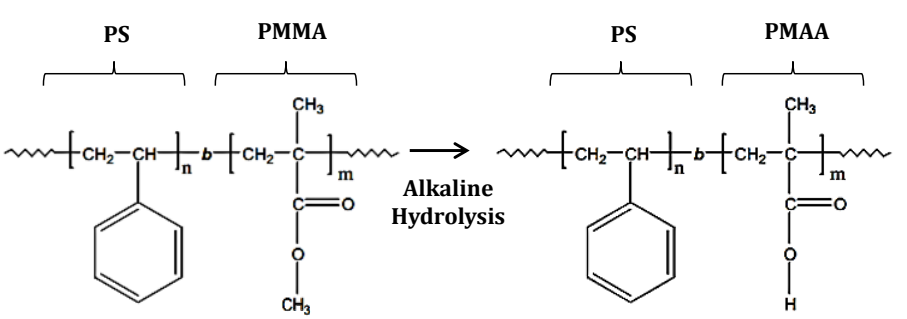

Figure 35. Alkaline hydrolysis. Chemical structure of PS-b-PMMA and PS-b-PMAA product.

In this work we tested two strategies for hydrolyzing PMMA molecules under alkaline conditions: hydrolysis of molecules in the bulk state and superficial hydrolysis of polymeric thin films.

3.4.1. Hydrolysis in the bulk state

Hydrolysis of block copolymers in the bulk state is referred to the cleavage of methyl ester groups in a batch hydrolysis process. Once the block copolymer is hydrolyzed, non-preferential substrates are spun-coated with the desired concentration of the polymeric solution. Then, the thin film is generated and PMMA fraction can be functionalized.

Hydrolysis procedure of the BCP medium was performed following the protocol described by the group of Prof. Müller.[251] 50 mg of BCP medium were dissolved in 0.5 mL of 1,4-Dioxane Reagent Plus (Sigma-Aldrich Química, Spain). The solution was prepared under argon ensuring an inert atmosphere in a sealed high-pressure tube. PMMA methyl ester groups were hydrolyzed by potassium hydroxide (KOH) at a molar ratio of 3:1 (18.62 mg in 0.5 mL of BCP medium dissolution) (KOH pellets, Sigma-Aldrich Química, Spain). For dissolution of the KOH salt, 18-crown-6 ether was selected as a phase transfer catalyst and used at a molar ratio of 1:5 (5.58 mg in 0.5 mL of BCP medium dissolution). Hydrolysis reaction was performed at 110°C under stirring during different time periods (1 h, 8 h, 16 h, 24 h and 120 h). The hydrolyzed polymer was then precipitated with 330 µL of hydrochloric acid at 1 M concentration under magnetic agitation until the reaction product was visible. The solution was filtered with a Bünchen funnel to separate the precipitated polymer from the solvent and then rinsed with approximately 10 mL of Milli-Q water. With the help of a spoon, the filtered powder was collected into a vial and was placed in a desiccator for 24 h to remove the excess of humidity. The final product was characterized by nuclear magnetic resonance (NMR) and Fourier Transformed-Infrared spectroscopy (FT-IR) to determine the success of the hydrolysis procedure.

BCP medium was analyzed at different hydrolysis times: 1 h, 8 h, 16 h, 24 h and 120 h of alkaline hydrolysis. The degree of hydrolysis was calculated compared with the values obtained from non-hydrolyzed BCP medium. ^{1}H-NMR spectra from deuterated dichloromethane solution of the different samples were acquired using a Bruker DMX-500 high resolution NMR spectrometer (400 MHz) (Bruker, USA). Sample concentration was higher than 20 mg/mL in deuterated

chloroform (Chloroform-d 99.8 atom % D, Sigma-Aldrich Química, Spain) in all the experiments performed and the resultant spectrum were analyzed and compared. All spectra were presented with Mnova NMR software (Mestrelab Research, Spain). The degree of hydrolysis was calculated from ^{1}H-NMR spectra by comparing the varying ratios between the peak area of the phenyl protons at 6.8-7.4 ppm and the peak area of methacrylate at 3.6 ppm after the different hydrolysis times.

In parallel to NMR analysis, Fourier Transform-Infrared spectroscopy measurements were performed. A Thermo Scientific™ Nicolet™ iS10 FT-IR (Thermo Electron Scientific Instruments LLC, USA) equipped with a deuterated triglycine sulfate (DTGS) detector was used to monitor the degree of hydrolysis achieved for the BCP medium after 1 h, 8 h, 16 h, 24 h or 120 h of reaction. BCP medium samples were dissolved approximately at a concentration of 50 mg/mL in chloroform (Sigma-Aldrich Química, Spain). An aliquot of 20 µL was placed on a KBr plate and measurements were performed only when solvent was completely evaporated. Omnic™ Series software (Thermo Fisher Scientific Inc., USA) was used for data collection and visualization. A background spectrum was collected before each sample analysis. Absorption FT-IR spectra were recorded with 32 scans and a resolution of 4 cm^{-1}. Native BCP medium was also evaluated as control. Data processing was performed using Origin® software (OriginLab, USA). The shift of the C=0 valence vibration from 1731 cm-1 (ester) to 1706 cm-1 (acid)[252] was monitored to visualize the degree of hydrolysis.

3.4.2. Superficial hydrolysis of polymeric thin films

Thin films of BCP medium, BCP small and RandomCP after thermal annealing were used as substrates for hydrolysis of the outermost layer of the phase segregated PMMA domains in the case of BCP medium and BCP small thin films, or the randomly distributed PMMA molecules for the RandomCP thin films.

Samples were immersed in 10 mL of sodium hydroxide (Sodium hydroxide pellets from Panreac Química S. A. U., Spain) 2M aqueous solution at 40°C under cautiously stirring. Different hydrolysis times were tested ranging from 30 min to 5 h to find the optimal conditions preserving thin film integrity.[149] After hydrolysis, surface carboxylic groups were neutralized with 5 mL of 0.1 M hydrochloric acid solution (Hydrochloric acid 37 % from Panreac Química S. A. U., Spain) and rinsed first with MilliQ water and then with absolute ethanol (Panreac Química S. A. U.,

Spain). Finally, thin films were dried under a nitrogen flow and stored at room temperature until further use for a maximum period of time of a week.

Hydrolysis process of the above mentioned thin films was evaluated through surface sensitive techniques such as X-ray Photoelectron Spectroscopy (XPS) and Fourier transform Infrared nanospectroscopy (nano-FTIR). Film integrity and morphology was also evaluated after the hydrolysis procedure by AFM.

XPS measurements were performed on BCP medium BCP small and RandomCP thin films after 1 h and 5 h of hydrolysis compared with non-hydrolyzed substrates. For these experiments, thin films were generated and annealed on double side polished silicon wafers (D+T Microelectrónica, Spain). The analized area was a circle of 0.8 mm diameter. A Perkin-Elmer PHI 5500 Multitechnique System (Physical Electronics, USA) was used with a monochromatic X-ray source (Aluminium Kα line of 1486.6 eV energy and 350 W), placed perpendicular to the analyser axis and calibrated using the $3d^{5/2}$ line of Ag with a full width at half maximum (FWHM) of 0.8 eV. For each sample, carbon 1s (C 1s), oxygen 1s (O 1s) and silicon 1s (Si 1s) core levels high-resolution XPS scan spectra were recorded. The resolution for the general spectra was determined as 187.5 eV of Pass Energy and 0.8 eV/step, and 23.5 eV of Pass Energy and 0.1 eV/step were the selected values for high-resolution C 1s, O 1s and Si 1s spectra. The ultrahigh vacuum (UHV) chamber pressure was set between $5x10^{-9}$ and $2x10^{-8}$ torr for all measurements. When necessary, a low energy electron flood gun (0-3 eV) was used to discharge the samples. Data processing was performed using MultiPak® V6.0A software (Physical Electronics Inc., USA) and comparative graphs were created with Origin® software.

Topographic AFM images were acquired on BCP medium thin films before and after 0.5 h, 1 h and 5 h of hydrolysis. The persistence of structural integrity on thin films after hydrolysis is of substantial importance for further experimental steps such us biomolecule functionalization and cell culture. At least three representative areas of 4 cm^2 were imaged for each sample and simple flatten algorithm (WxSM software) was applied before height profiles along a straight line picked at random were acquired.

Nanoscale Fourier transform infrared (nano-FTIR) spectroscopy, which is an AFM based technique that enable infrared imaging and spectroscopy with nanoscale spatial resolution, was also attempted (Appendices, 9.2 Nanoscale Fourier transform infrared (nano-FTIR) spectroscopy). These measurements were performed in collaboration with Dr. Andreas Huber from Neaspec GmbH. Nano-FTIR thin film absorption and reflectivity of hydrolyzed and non-hydrolyzed (30 min) BCP medium samples deposited onto glass coverslips were obtained by employing a commercial nano-FTIR set-up (Neaspec GmbH, Germany). Spectra were recorded within the 1600 to 1800 cm^{-1} wavenumber range, by illuminating an Au-coated AFM with a tunable laser continuum.[253] Peaks appearing at 1731 cm^{-1} and 1706 cm^{-1}, this is, on resonance with the ester and the acid vibrational frequencies respectively were monitored. The ester signals disappears with the hydrolysis of the methyl ester group of the PMMA leading the appearance of the acid signal.[252]

3.5. Selective protein functionalization of block copolymer thin films

Protein nanopatterns can be easily fabricated using a PS-*b*-PMMA thin film as template by selectively functionalizing the hydrolyzed PMMA block. For these experiments, annealed and superficially hydrolyzed BCP medium, BCP small and RandomCP thin films were used as substrates, fabricated indistinctly on 4 cm^2 pieces of silicon wafer or on 18 mm in diameter coverslips.

Prior to biomolecule binding, carboxylic acid moieties generated at the hydrolyzed surface of the PMMA cylinders were activated by EDC/NHS chemistry (Figure 36). Substrates were submerged in a solution of *N*-(3-dimethylaminopropyl)-*N*'-ethyl carbodiimide (EDC) (Sigma-Aldrich Química S. A., Spain) (73.4 mg, 0.38 mmol) and *N*-hydroxysuccinimide (NHS) (Sigma-Aldrich Química S. A., Spain) (8.9 mg, 0.08 mmol) in water Milli-Q (5 mL) at room temperature for 15 and 30 min (Activation conditions, Table 3). The fresh mixture of EDC–NHS cannot be stored and any remaining aliquot should be discarded. After reaction, thin films were rinsed with Milli-Q water and absolute ethanol and dried under a stream of nitrogen. Nanopatterns of different molecules such us peptides (adhesive peptide cyclic(RGDfK)-PEG_3-NH_2 and ephrinB1-Fc) and fluorophores (Alexa Fluor 647 hydrazide) were produced following the nanostructured template. To evaluate the spatial distribution of molecules at the nanometer scale,

high-resolution imaging techniques are required.[254] AFM and Stochastic Optical Reconstruction Microscopy (STORM) (Appendices, 9.1 Stochastic optical reconstruction microscopy) were used to analyze the resulting functionalized surfaces, calculating, for example, the number of molecule clusters per area, spacing between clusters or surface coverage.

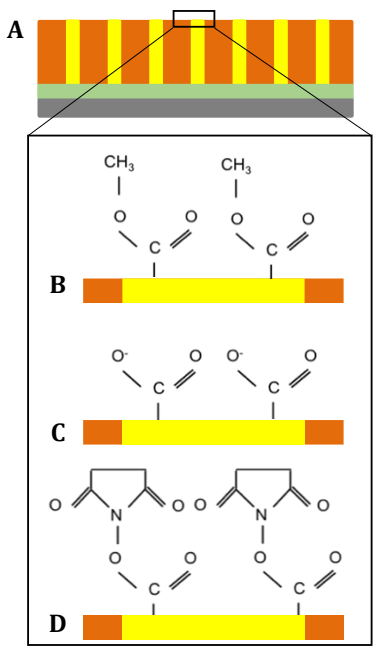

Figure 36. Schematic representation of carboxylic acid activation on the PMMA cylinders. A) schematics of a cross-sectioned PS-b-PMMA thin film annealed with perpendicular PMMA domains (yellow) in a PS matrix (orange); B) Inset shows the chemical structure of the methyl methacrylate monomers pending from the polymeric chain; C) after hydrolysis the methyl group is removed to form methacrylic acid (PMAA); D) activation of the acid functionalities with N-(3-dimethylaminopropyl)-N'-ethyl carbodiimide (EDC) and N-hydroxysuccinimide (NHS) to enable the covalent binding of amine-terminated molecules.

3.5.1. Surface functionalization with cyclic (RGDfK)-PEG_3-NH_2 adhesive peptide

Cyclic peptide with the integrin-specific aminoacid sequence[255] of arginine-glycine-aspartic acid (c(RGDfK)-PEG_3-NH_2) was kindly synthetized and provided by Prof. Albericio's group (IRB, Barcelona, Spain)(Figure 37). This cyclic structure was coupled with a flexible hydrophilic polymer chain of poly(ethylene glycol)(PEG) end-functionalized with an amine group. The PEG moiety is included as a spacer arm required by surface-bound bioactive molecules to overcome the geometric constrains affecting its functionality.[256–258] The incorporated primary amine can react with the carboxylic groups exposed by the hydrolyzed surfaces after activation with EDC/NHS.[259]

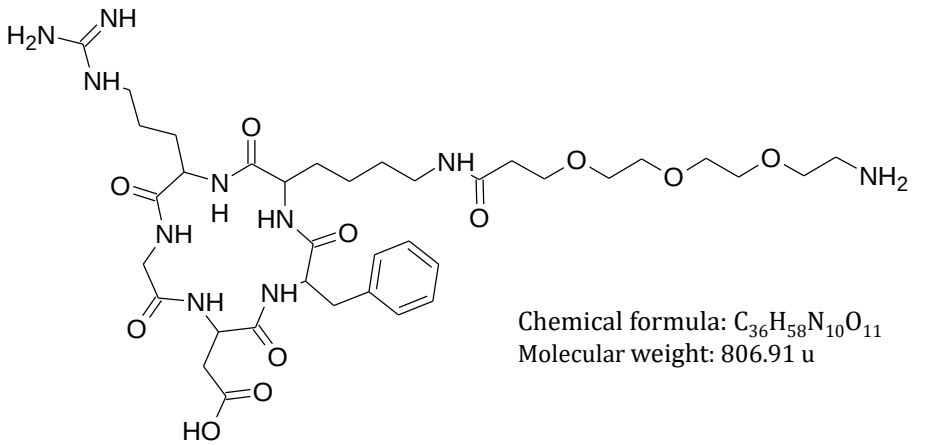

Figure 37. Chemical structure, chemical formula and molecular weight of cyclic(L-arginylglycyl-L-α-aspartyl-D-phenylalanyl-L-lysyl)triethylene glycol amine (purity ≥ 97% by HPLC analysis) synthetized and kindly provided by Prof. Albericio (IRB, Barcelona, Spain).

BCP medium, BCP small RandomCP thin films were hydrolyzed and activated following the procedure named as "C" in Table 3 and then incubated in contact with 300 µL of c(RGDfK)-PEG_3-NH_2 solution at 10 µM concentration in 0.05% Tween® 20 (Sigma-Aldrich Química, Spain) phosphate buffered saline (PBS) for 16 h at room temperature preserving sterile conditions. PBS powder (Sigma-Aldrich Química, Spain) was dissolved in 1 L of Milli-Q water solution following provider instructions to get a PBS solution at pH 7.4 and 0.01M (1X) concentration. Samples were then rinsed 3 times with 0.05% Tween® 20 PBS and finally stored at 4°C in PBS for the minimum period of time. This functionalization strategy drives the formation of covalent bonds between the molecule of interest and the desired block or random copolymer thin film, leading the formation of a nanopatterned or non-patterned ligand-presenting substrate respectively for each case.

These samples were characterized by tapping mode AFM in liquid to visualize the resulting spatial molecule distribution over the surface depending on the underlying PMMA template and the differences observed from the height profiles randomly performed on the imaged area. Images were acquired in PBS using indistinctly a Dimension AFM instrument (Veeco Instruments, USA) or a Bruker MultiMode 8 AFM (Bruker, USA). Microscopes were equipped with triangular silicon nitride AFM probe (Bruker AFM Probes, DNP-S10, spring constant 0.12 N/m, resonance frequency 23 KHz, radius of curvature about 10 nm, reflective gold as back side coating and 205 µm and 40 µm in length and width respectively). WSxM software was used for image processing and simple flatten algorithm was applied previously to height profile acquisition.The covalent

immobilization of adhesive peptides on polymeric thin films is directly related with the success of the designed hydrolysis and functionalization strategies. As a control to depict the individual effect of the hydrolysis process, functionalization procedure was performed without preceding hydrolysis following the same conditions previously described. In this manner, merely physisorption could lead any noticeable molecule-surface interaction.

Non-selective protein adsorption was tested on annealed BCP medium, BCP small and RandomCP thin films, without any preceding hydrolysis step. Non-hydrolyzed thin films were incubated with 300 µL of 10 µM c(RGDfK)-PEG_3-NH_2 solution in PBS. Incubation was extended for 16 h at room temperature. After this time, samples were rinsed three times with PBS and stored at 4°C for a maximum period of 24 h prior to their use. The resulting protein arrangement attributable to physical adsorption was evaluated by tapping mode AFM imaging in liquid, as previously described in this section for covalently bound protein patterns. At least three samples of chemically bound (covalent coupling) or physisorbed (non-covalent interaction) protein patterns on thin films generated from independent experiments were analyzed and a minimum of three representative images were examined.

Replicas of these samples (adjusting the functionalization parameters to meet the optimum ones described as "C" in the following Section 3.5.2, Table 3) fabricated on glass coverslips were used for further cellular experiments investigating cell adhesion response to c(RGDfK)-PEG_3-NH_2 ligand spatial distribution at the nanometer scale. Functionalized samples are freshly prepared and stored at 4°C for a maximum of 24 h before cell culture.

3.5.2. Functionalization optimization for covalent molecule-binding onto hydrolyzed polymeric thin films using Alexa Fluor® 647 hydrazide

Once covalent binding of molecules on hydrolyzed PS-PMMA containing thin films was probed to give an advantage compared with physisorbed peptides, optimal functionalization conditions were investigated. For this purpose, the fluorophore Alexa Fluor® 647 hydrazide (Alexa Fluor® 647 hydrazide, tris(triethylammonium salt) from Thermo Fisher Scientific Inc., USA)(Absorption wavelength: 649 nm; Emission wavelength: 666 nm), suitable not only for scanning probe microscopy (AFM) but also for direct observation with Stochastic

Optical Reconstruction Microscopy (STORM)[260], was selected. Alexa Fluor® 647 hydrazide is reported to present chemical reactivity to carboxylic acid moieties such as the carboxylic acid groups originated on hydrolyzed polymeric thin films. Functionalization of BCP medium thin films was explored under certain combination of conditions described in Table 3. Alkaline hydrolysis was performed with 10 mL of aqueous 2M of sodium hydroxide solution at 40°C for different time periods and stirring conditions. Activation of carboxylic groups with EDC/NHS (0.38 mmol/0.08 mmol in 5 mL of Milli-Q water) was extended for 15 to 30 mins under shaking. Activated surfaces were incubated with 300 µL of Alexa Fluor® 647 hydrazide fluorescent dye at a concentration of 0.5 mg/mL in different buffer solutions for increasing periods of time.

Table 3. Functionalization parameters tested with Alexa Fluor 647 hydrazide.

Condition	Functionalization parameters		
	Hydrolysis	**Activation**	**Incubation**
A	30 min	15 min	1 h in PBS
B	30 min under shaking	15 min under shaking	1.5h under shaking in PBS
C	1h under shaking	30 min under shaking	16 h in 0.05% Tween® 20 PBS under shaking
D	5h under shaking	30 min under shaking	16 h in 0.05% Tween® 20 PBS under shaking

After incubation time, samples were rinsed with 300 µL of 0.05% Tween® 20 PBS solution and then PBS solution three times for 5 min. In case of storage, samples were preserved at 4°C for a week as maximum. The obtained samples applying "A" functionalization condition were characterized by AFM and STORM at different magnifications. Tapping mode AFM imaging was performed as previously described for c(RGDfK)-PEG_3-NH_2 adhesive peptide (Section 3.5.1). These substrates were additionally imaged with a commercial super-resolution stochastic optical reconstruction microscope (STORM) system from Nikon instruments (Nikon Instruments Europe B.V., The Netherlands). Samples were excited with laser light at 647 nm through an oil immersion 100x objective. The emission fluorescence was obtained using an electron multiplying charge coupled device (EMCCD) camera at an exposure time of 100 ms per frame. The polymeric thin films employed for STORM analysis were fabricated on 18 mm in diameter coverslip and mounted on an in-house-made-bottom glass petri dish. Imaging was performed in a 5% glucose solution in PBS in the presence of a primary thiol (25 µL of 0.1 µg/mL mercaptoethylamine in 1M hydrochloric acid solution purchased

from Sigma-Aldrich Química, Spain) and an enzymatic oxygen–scavenging system (2.5 µL of glucose oxydase (Sigma-Aldrich Química, Spain)) which enhances photostability and photoswitching properties of the dye.[261] For data analysis we used Visual Servoing Platform (VISP) software [262] and the ThunderSTORM plugin of ImageJ free software (http://rsb.info.nih.gov/ij, National Institutes of Health, USA).

Comparable information was extracted from both imaging techniques (AFM and STORM) in terms of ligand-cluster diameters. For its simplicity and accessibility-related reasons, AFM was selected to characterize the rest of Alexa Fluor® hydrazide functionalization conditions ("B", "C" and "D" conditions) tested for optimization. At least three topographic AFM images of 4 μm^2 area were acquired for each functionalization condition assayed. Image analysis was performed with WSxM software using a simple flatten algorithm for nanopattern visualization and the flooding algorithm for cluster discrimination. Optimum functionalization methodology was determined based on a combination of three calculated parameters: mean cluster size, number of functionalised domains per μm^2 and the spacing distance between clusters. The resulting optimum functionalization methodology ("C condition") was later on applied to BCP medium, BCP small and RandomCP for c(RGDfK)-PEG_3-NH_2 and ephrinB1-Fc molecules and to subsequent cellular assays.

3.5.3. Covalent surface functionalization of polymeric thin films with EphrinB1-Fc ligand

Recombinant mouse ephrinB1-Fc Chimera (Jackson ImmunoResearch Europe Ltd., UK) (referred as ephrinB1-Fc hereafter) is provided as a dimer at a concentration of 0.1 mg/mL in PBS. BCP medium and RandomCP thin films fabricated on 18 mm in diameter coverslips were functionalized following the optimal established conditions ("C" condition, Table 3). Samples were incubated with a solution of ephrinB1-Fc at 0.2 µM concentration in 0.05% Tween® 20 PBS for 16 h under sterile conditions. After incubation substrates were firstly washed with 0.05% Tween® 20 PBS and then with PBS three times for 5 min. If stored, ephrinB1-Fc functionalized samples were preserved at 4°C for a period of time no longer than a week. Tapping mode AFM in liquid was used to study the nanometric arrangement of ephrinB1/Fc as previously described in Section 3.5.1 for other molecule-presenting surfaces. The characteristic ephrinB1/Fc nanopatterning

observed on BCP medium thin films was selected to investigate EphB2 receptor clustering dynamics and replicas of these substrates were used in Section 3.7.4.

For fluorescence microscopy imaging, ephrinB1-Fc nanopatterned BCP medium and RandomCP thin films were incubated with 200 µL per substrate of the secondary antibody goat anti-human IgG Alexa Fluor® 647 (Thermo Fisher Scientific Inc., USA) at a 1:200 dilution in 0.05% Tween® 20 PBS for 45 min. The Fc fragment of the recombinant ephrinB1-Fc chimeric molecule is recognized by this secondary antibody. After incubation, substrates were washed with 0.05% Tween® 20 PBS for 5 min three times. Washing procedure was repeated with PBS before sample storage at 4°C. Alexa Fluor® 647 fluorophore is ideal for imaging low-abundance targets and useful for high-resolution STORM analysis. Following the protocol described in Section 3.5.2 for STORM analysis, BCP medium and RandomCP thin films were evaluated after immunostaining. Additionally, tapping mode AFM measurements in liquid were also performed to determine the functionalization ratio of ephrinB1-Fc, the cluster density, and the spacing between ephrinB1-Fc clusters.

3.6. Cell adhesion and spreading under nanopatterned adhesion peptides

Upon cell culture on substrate-bounded ligands, integrin transmembrane receptor assembly into small aggregates or large clusters will depend on several factors such as ligand density, ligand arrangement, ligand affinity, and substrate topography and rigidity. Cell spreading and focal adhesion formation are integrin mediated processes sensitive to the ligand spatial distribution at the nanometer scale.[206,263] To validate the developed nanopatterned substrates as tools/platforms for systematic receptor clustering studies, thin films functionalized with adhesive peptides were used to check cell adhesion and spreading.

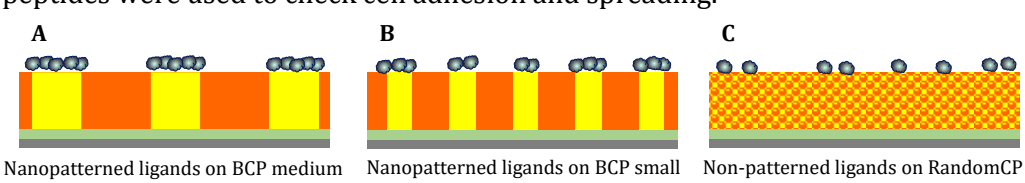

Figure 38. Schematic representation of ligand distribution according to the underlying nanostructured templates. A) Nanopatterned ligands on BCP medium thin film (PMMA cylinder diameter= 28 nm, intedomain spacing= 64 nm), B) Nanopatterned ligands on BCP small thin film

(PMMA cylinder diameter= 21 nm, intedomain spacing= 37 nm) and C) Non-patterned ligands on RandomCP thin film.

Two nanostructured substrates presenting different PMMA cylinder diameters and interdomain spacings (BCP medium and BCP small thin films) and one non-structured substrate (RandomCP thin film) were selected as substrates and functionalized with c(RGDfK)-PEG_3-NH_2 adhesive peptide. Global ligand density is dictated by the PMMA fraction susceptible to bound protein molecules. For these selected thin films, the PMMA fraction is equivalent (Table 2), so the functionalized substrates should present a similar global ligand density. Local ligand density is governed in PS-b-PMMMA thin films by the arrangement of PMMA molecules on the surface. BCP medium and BCP small thin films present different nanostructured PMMA domains acting as template to be replicated by the anchored ligands. Therefore, the nanopatterned distribution of ligands causes differences in the local ligand density that can be investigated. In RandomCP thin films, PMMA molecules are randomly distributed over the surface driving a non-patterned ligand distribution.

Two functionalization strategies were checked to present the ligand to cells: physically adsorbed peptides or covalently bound to the surface, following the protocols described in section 3.5.1.

To avoid non-specific protein adsorption of non-functionalized areas (PS areas of polymeric thin films), surfaces were passivated by incubation in Bovine Serum Albumin (BSA, Sigma-Aldrich Química, Spain) at 0.5% in PBS for 30 min. NIH/3T3 mouse embryonic fibroblasts cell line (ATCC® CRL-1658™, ATCC, USA) from passage 7 to 11 were expanded in cell culture flasks for 2 days at 37°C and 10% CO_2 in growth medium (Dulbecco's Modified Eagle Medium (D-MEM, Invitrogen S.A., Barcelona, Spain)) supplemented with 5% Fetal Bovine Serum (FBS), 1% L-glutamine (Invitrogen S.A., Barcelona, Spain), 1% sodium pyruvate (Invitrogen S.A., Barcelona, Spain) and 1% penicillin-streptomycin (Invitrogen S.A., Barcelona, Spain). Functionalized substrates with ligand nanopatterns and ligand random distribution were preincubated for 10 min with 500 µL of PBS at 37°C before cell culture. NIH/3T3 fibroblast were counted with a Neubauer chamber and seeded at a cell density of 4000 cells/cm^2 in serum-starving medium. Cells were cultured for 4 h and non-adhered cells were then carefully washed out with PBS. Adhered cells were fixed with 300 µL of 4% paraformaldehyde (PFA, Merck, USA) in PBS for 20 min at room temperature, rinsed three times with PBS,

incubated with 300 µL of 50 mM ammonium chloride (Sigma-Aldrich Química, Spain) in PBS for 20 min and washed again three times with PBS. For immunolabeling of subcellular structures, cells were permeabilized with 0.1% Triton X-100 (Thermo Fisher Scientific, USA) in 1X (10 mM) Tris-Buffered Saline (TBS) (Sigma-Aldrich Química, Spain) for 15 min at room temperature. To prevent the non-specific binding of antibodies to the target epitopes (specific binding sites of proteins that will be immunolabeled), all proteins comprising the cell should be blocked with proteins that do not have binding affinity to these epitopes of interest. Blocking was performed for 2 h at room temperature, or overnight at 4°C with 3% donkey serum (Jackson ImmunoResearch Europe Ltd., UK) 0.3% Triton X-100 in 1X TBS (denoted hereafter as blocking solution). To investigate cell adhesion and spreading different cellular structures will be stained. Hoetsch 33258 is a blue fluorescent dye that intercalates between double strainded DNA molecules labelling the cell nucleus.[264] The fluorescent nuclei of adhered cells can be then easily counted to calculate the percentage of cell adhesion. Phalloidin is a toxin that stabilizes the actin filaments of cell cytoskeleton. When modified with a fluorescent moiety, can be used to visualize the actin cytoskeleton of spread cells.[265] Paxillin is a focal adhesion associated adaptor protein that anchors transmembrane integrin receptors and to actin cytoskeleton.[193,266,267] Paxillin can be specifically immunostained with fluorescent antibodies to localized and measure focal adhesions.

Cells were incubated overnight at 4°C with: a) Phalloidin-Tetramethylrhodamine B isothiocyanate (TRITC-Phalloidin) (Fluka, Switzerland) diluted 1:500 and B) primary antibody rabbit anti-paxillin [Y113] (Abcam, Cambridge, UK) diluted 1:200 in 3% donkey serum and 0.3% Triton X-100 in 1X TBS. Washing with 0.1% Triton X-100 in 1X TBS was repeated 3 times followed by an incubation with the blocking solution for 2 h at room temperature. Cells were incubated for 2 h at room temperature with the secondary antibody goat anti-rabbit IgG Alexa Fluor 488 (Invitrogen S.A., Spain) diluted 1:500 in 3% donkey serum 0.3% Triton X-100 in 1X TBS. Afterwards, cells were washed three times with 0.1% Triton X-100 in 1X TBS for 15 mins. Finally, cells were incubated with Hoechst 33258 (Invitrogen S.A., Barcelona, Spain) diluted 1:1000 in 3% donkey serum and 0.3% Triton X-100 in 1X TBS for 15 min at room temperature. Samples were washed with 1X TBS for 15 min three times and coverslips were mounted with Fluoromount-G® (Southern Biotechnology Associates, Inc., USA) before storage at 4°C. Cell images were acquired with an Eclipse E1000 upright

microscope (Nikon, Netherlands) equipped with a Charge-Coupled-Device (CCD) camera, an ultraviolet filter, a FITC filter and G-2A long-pass filter. Fluorescent microscope images were acquired with MetaMorph software (Molecular Devices, Sunnyvale, CA, USA) and were analyzed using ImageJ free software (http://rsb.info.nih.gov/ij, National Institutes of Health, USA). Samples were imaged with a 10X objective for adhesion analysis. At least, 10 different random locations over each sample were analyzed. Fluorescent nuclei were counted to determine the density of adhered cells and the percentage of cell adhesion was calculated. Differences in the percentage of adhered cells on covalently and non-covalently functionalized substrates were statistically analyzed using a One-way ANOVA test (Origin software).

A 40X objective was used for focal contact (paxillin immunostaining) and cell morphology analysis of cells cultured on covalently functionalized thin films. Cell images were taken at 25 random positions over the sample surface (minimum number of 30 cells per sample). As morphology describing parameters, projected area (area of the selected cell), circularity (a circularity value of 1 indicates a perfect circular cell following the equation: $circularity=4\pi(area/perimeter^2)$), roundness (roundness = $4(area/\pi \cdot major\ axis^2)$, major axis referred to an ellipse fitting of the cell area) and solidity (solidity= area/convex area, where convex area is the area of the smallest convex polygon comprising the cell area) were evaluated and plotted with the corresponding standard deviation. The number of focal contacts per cell and described size were also analyzed from fluorescence microscopy images.

3.7. Study of the clustering dynamics of EphB2 receptor

Eph/ephrin interaction induces a bidirectional signaling involved in a wide range of developmental processes such as axon guidance and stem cell differentiation[268,269]. Several strategies have been developed to depict the complex signaling mechanisms of Eph receptors (“forward” signaling) and ephrins (“reverse” signaling)[270,271]. It is known that Eph receptors require ligand aggregation for their clustering and activation, so we focus on understanding EphB2 clustering and activation process under predefined multivalent ephrin ligand configurations. Herein we compare the receptor oligomerization dynamics under different surface-bound ligand presentations. As ligand presenting surfaces, we tested: BCP medium nanopatterned templates functionalized with

ephrinB1/Fc, immobilized ephrinB1/Fc dimers on poly-L-lysine-coated glass coverslips, and immobilized antibody-conjugated ephrinB1/Fc aggregates on poly-L-lysine-coated glass coverslips. Also antibody-conjugated ephrinB1/Fc oligomers were used as soluble ligands. HEK293T cells expressing mRuby-labeled EphB2 receptors were cultured on these variety of ligand presenting strategies. EphB2 receptor clustering dynamics was analyzed using an improved version of the Number and Brightness technique, which is described in section 3.7.5..

3.7.1. Preparation of nanopatterned ephrinB1/Fc functionalized substrates

BCP medium thin films fabricated on 18 mm glass coverslips were covalently functionalized with ephrinB1/Fc as previously described in Section 3.5.3.

To study receptor clustering phenomenon at the cell membrane, cell adhesion should be ensured by the surface used for cell culture. For this reason, poly-L-lysine (PLL) (Sigma-Aldrich Química, Spain), an adhesion polypeptide that promotes cell attachment,[272] was prepared at 0.05% (w/v) concentration in PBS. Nanopatterned samples were incubated with 300 μL of 0.05% (w/v) PLL solution for 90 min, rinsed three times with PBS, rinsed three times with Milli-Q water and blown dried. Substrates were carefully bottom-cleaned and mounted on in-house made bottom-glass petri dishes. Control samples were produce by coating the BCP medium thin films only with 300 μL of 0.05% PLL as previously described.

3.7.2. Preparation of immobilized ephrinB1/Fc presenting surfaces

Microcontact printing is a useful technique to create patterns of molecules on surfaces, widely used for biological applications since it was developed by Whitesides in the 90's.[273] Patterns of biomolecules are faithfully reproduced using microstructured elastomeric stamps fabricated by soft lithography.[44,274] Herein we will use microcontact printing as a tool to generate homogeneous protein coatings on PLL-functionalized glass substrates.

Glass bottom dishes of 35 mm in diameter (MatTek Corporation, USA) were coated with PLL solution at 0.05% (w/v) in PBS for 90 min. After washing three times with PBS and Milli-Q water, dishes were air-dried. Flat PDMS stamps were fabricated by mixing a 10:1 mass ratio of silicon elastomer base and curing agent. PDMS was degassed under vacuum and poured on flat Petri dishes generating

PDMS films of approximately 5 mm in thickness. Curing was performed overnight at 60°C. Stamps were cut in 12 mm round discs matching the dimensions of the glass area of one dish. Prior their use, stamps were cleaned with ethanol in an ultrasonic bath for 5 min. EphrinB1/Fc was used as ink in two different configurations: ephrinB1/Fc dimers (as supplied by the provider) or antibody-conjugated ephrinB1/Fc oligomers. Antibody-conjugated ephrinB1/Fc oligomers were generated in solution by antibody-crosslinking using a goat anti-human IgG antibody (Jackson ImmunoResearch Europe Ltd., Suffolk, UK). Goat anti-human IgG was conjugated with 2 μM concentration of ephrinB1/Fc or Fc solution at a 2:5 molar ratio for 30 min under constant shaking. Stamps were inked for 45 min with 100 μL of the prepared solutions: ephrinB1/Fc dimers or antibody-conjugated ephrinB1/Fc oligomers. After incubation, stamps were rinsed three times with PBS and Milli-Q water and air dried. Conformal contact between stamps and previously poly-L-lysine coated surfaces was established for 10 min. EphrinB1/Fc dimers or antibody-conjugated ephrinB1/Fc oligomers were respectively transferred to the surface and flat stamps were carefully removed from the substrate. Once printed, surfaces were rinsed three times with PBS and Milli-Q water for 5 min. Samples were stored overnight at 4°C.

The ligand distribution over the surfaces printed with ephrinB1/Fc dimers and antibody-conjugated ephrinB1/Fc oligomers was analyzed by AFM and STORM, following the protocols described in sections 3.5.1 and 3.5.2, respectively.

3.7.3. Soluble presentation of ephrinB1-Fc oligomers

Cell stimulation with antibody-conjugated ephrinB1/Fc oligomers were also tested in a soluble manner, providing a three dimensional source of ligands compared to the two dimensional configuration of surface-bound ligands previously described. Goat anti-human IgG antibody was conjugated at a 2:5 molar ratio with 0.4 μM concentration of ephrinB1/Fc solution in DMEM for 30 min under constant shaking. Recombinant human IgG1 Fc (Jackson ImmunoResearch Europe Ltd., UK) (hereafter referred as Fc) was used as control. This solution was warmed at 37°C and mixed with the equivalent volume of cell suspension to reach a final 0.2 μM concentration of antibody-conjugated ephrinB1/Fc oligomers.

3.7.4. Cell culture upon ephrinB1/Fc stimulation

HEK293T cells expressing mRuby-labeled EphB2 receptor were produced by infection with lentiviruses. Transfection of HEK293T cells was carried out with

pLenti.CMV:EphB2_mRuby using Lipofectamine 2000 along with the ViraPower Lentiviral Packaging Mix (Thermo Fisher) according to the manufacturer's protocol. After a second passage, cells were infected a second time following the same protocol. Once two more passages were accomplished, cells were trypsinized and mRuby positive cells were selected by cell sorting. The stock of cells was maintained using complete DMEM at 10% FBS supplementation. Cell splitting was carried out using 0.025% trypsin-EDTA (tripsin/EDTA Gibco®, Thermo Fisher Scientific, USA) every 2-3 days. Cells were always kept at low passage for the imaging experiments.

Freshly harvested cells were gently resuspended in DMEM without phenol red. Cells were seeded at a cell density of 100.000 cell/cm^2 either on the nanopatterned ligands, the functionalized substrate plates containing the dimers, the oligomers or with the soluble ephrinB1/Fc oligomers. Cell suspension was smoothly spun down at 1000 rpm in a plate centrifuge for 1 min. The zero-time point of cell culture was considered the ending point of the centrifugation process. The samples were then quickly taken to the STORM microscope for observation. Images were acquired with a commercial STORM microscope system from Nikon instruments (NSTORM) used in TIRF mode. It was equipped with an EMCCD camera and a 1.4 NA 100X objective and a 1.5X lens tube for additional magnification. Every 2.5 min, cells were illuminated with 561 nm light at low laser intensity (3 W/cm^2 power density) for 200 frames with 500 ms exposure time. We acquired multiple time point datasets of the same specimen over approximately 60 minutes and applied N&B analysis to map the EphB2 receptor aggregation over time. Camera calibration for N&B with dark was performed using SimFCS (www.lfd.uci.edu).

3.7.5. Enhanced Number&Brightness analysis

Total internal reflection fluorescence (TIRF) images were analyzed following the enhanced Number and Brightness (eN&B) analysis procedure described elsewhere (Appendices, 9.3 Number and Brightness (N&B) analysis technique).[275] Briefly, the N&B is a powerful tool that distinguishes pixels with different aggregation states by determining the mean intensity and variance of their relative fluorescence intensity fluctuations.[236] The enhanced N&B technique allows following the evolution of such aggregation state over the time. For the calibration of the brightness attributed at the monomeric receptor state, cells were seeded on PLL for 24 h and the value of brightness computed was $B_{monomer}$ =

1.17±0.08. The values of receptor aggregates (n-mers) were calculated as percentages from the brightness histogram using the formula $B_{nmer}=1+(n*(B_{monomer}-1))$ with variance measured from monomer calibration. The acquired data was detrended using boxcar filtering on each pixel. This detrending mode has been demonstrated to maintain fluctuations while improving the performance of N&B.[40,276] Cells undergoing apoptosis and out of the TIRF evanescent wave focal plane were excluded from the analysis. Analysis was done with custom Matlab scripts.

4. Results

4.1. Thin film generation

Microdomain orientation of diblock copolymer thin films is governed by the equilibration of the energetic contributions of all the components of this semi-confined system. For asymmetric cylinder-forming block copolymers with a given composition, the orientation of the minority block will be perpendicular or parallel to the substrate depending on which conformation presents a lower free energy.[114] The free energy (F) of a thin film of block copolymers can be resumed as:

$$F = F_{elastic} + F_{S-MMA} + F_{substrate} + F_{free\ interface} \qquad \textbf{Eq. 1}$$

where $F_{elastic}$ is the energy associated to the entropic phenomena dictating stretching/compression of the polymeric chains, F_{S-MMA} is the interaction energy between the blocks composing the copolymer (styrene and methyl methacrylate in our case), $F_{substrate}$ is the surface energy of the substrate in contact with the block copolymer thin film and $F_{free\ interface}$ is the surface energy of the free interface.

A controlled interplay between the degree of confinement and the energy of both the substrate and the free interfaces rely on the successful selection of thin film thicknesses, chemical modification of the surface energies and the appropriate thermal annealing conditions. It is worth mentioning that although in the bulk state theoretical simulations can predict the block copolymer phase segregation, there are no analytical equations able to recapitulate with sufficient accuracy the optimal conditions driving perpendicular microdomain orientation. In this work we will face these challenges using different strategies to engineer the surface energy of thin film interfaces and to control the thickness of diblock copolymer films.

4.2. Engineering the wetting properties of the polymer-substrate interface

Microdomain orientation in thin films is undouble subject to interactions at the top (free interface) and the bottom interfaces (silicon or glass substrates).

Preferential interactions of PS or PMMA fractions with the thin film interfaces, i.e., the substrate surface or the free interface, dictates the segregation of that polymer block towards the specific wetting of that interface. PS block preferentially wets the air surface interface due to its lower surface energy compared with PMMA. On the substrate interface, native silicon oxide layers and glass, with a preferential affinity on polar moieties, promote the formation of a PMMA wetting layer on the surface. Therefore, in our system both effects eventually dictates the orientation of the PMMA cylindrical microdomains parallel to the substrate. To obtain perpendicular structures, this tendency should be reverted applying some physico-chemical treatment to properly engineer both interfacial energies.

Traditionally, the interfacial interaction at the free surface has been controlled by introducing defined partial pressures of solvent vapors, in a process called solvent annealing,[277] or by thermal annealing[137]. In the case of PS-b-PMMA block copolymers, neutral conditions are ensured at high temperatures (annealing temperature, ranging from 170°C to 230°C) when the estimated surface energies for PS ($\gamma_{PS} \sim 29.9$ mN/m) and PMMA ($\gamma_{PMMA} \sim 30.02$ mN/m) are comparable.[131,278]

Focus of more attention, the polymer substrate has motivated the development of several engineering strategies to modify the interfacial wetting conditions. For this purpose, self-assembled monolayers[88,125], random copolymer brushes[237,278], surface energy-tunable organosilicate substrates[100] and more recently graphene patterns have been used[279]. Herein we tested self-assembled monolayers of chlorosilane molecules and random copolymer brushes as strategies to ensure a neutral coating of the substrate showing similar interfacial energies to the individual blocks of the polymeric thin films, finally resulting in the perpendicular orientation of PMMA microdomains.

4.2.1. Substrate surface modification by silane self-assembled monolayers

Self-assembled monolayers (SAMs) of organosilanes have been successfully used to balance the interfacial interactions of copolymer blocks on silicon oxide substrates. Silane SAMs are an attractive alternative to form neutral surface coatings as a wide variety is commercially available and provide highly reproducible results. Chlorosilanes with a variety of functional groups have been combined into gradients of surface energies in a smart and easily tunable strategy

to match the specific surface energy of the diblock copolymer system.[113] To achieve this goal, single molecule silane SAMs require the uniform functionalization of silicon substrates with a controlled density, lower than the density of a monolayer. As a result, a submonolayer degree of coverage is obtained with molecule chains apparently disordered on the surface.[88] Other complex strategies to finely control surface energy of silane SAMs are chemical post-modifications by UV irradiation or treatment with CO_2 plasma.[127]

Herein we selected two silane molecules, (3-aminopropyl)triethoxysilane (APTES) and trichloro(1H,1H,2H,2H-perfluorooctyl) silane (PFOS) to chemically modify the wetting properties of silicon substrates. Figure 39 shows topographical AFM images of APTES-silicon and PFOS-silicon surfaces obtained in air using tapping mode after gentile sonication with ethanol/isopropanol solution. Nanometer-size aggregates are formed in both cases. The mottled appearance of the APTES covered surface (Figure 39 A) is suggestive of an island growth more than a homogeneous growth of the self-assembled monolayer.

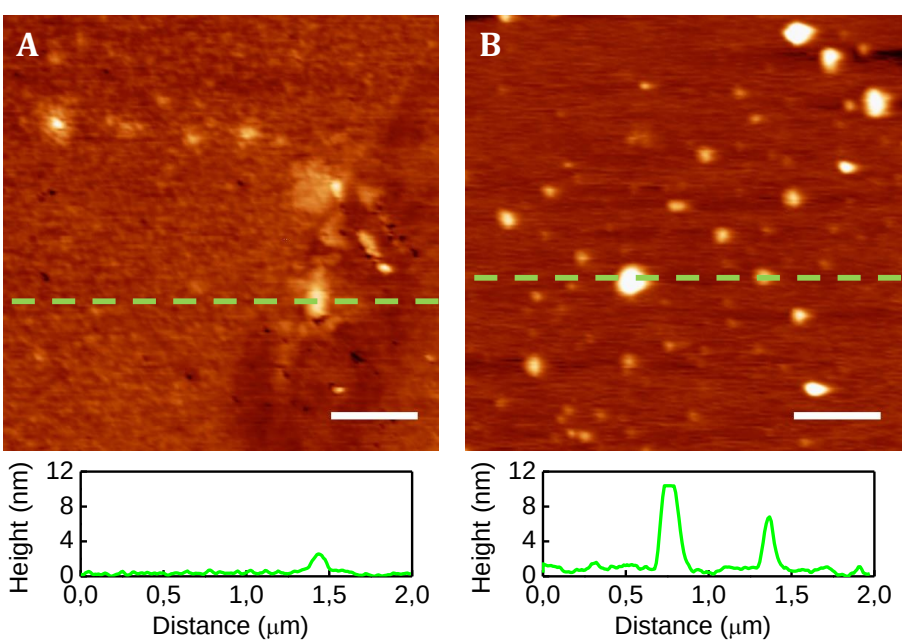

Figure 39. AFM topography images of (A) APTES and (B) trichloro(1H,1H,2H,2H-perfluorooctyl)silane coating on silicon substrates after gentile sonication. The graphs below the pictures plot the height profiles of the dashed lines (Scale bar 400 nm) (Z- scale: (A)5 nm; (B) 12nm).

Larger agglomerates are found all over the surface chemically modified by SAMs of PTOS (Figure 39 B). The dashed lines indicate the agglomerate heights, which in the case of PFOS-silane coating reach up to 12 nm, as shown at the plotted

profile. The mechanism for "island" growth depends on relevant factors such as the water content at the surface, the reaction temperature and the chemical nature of the silane molecules. Small variations in temperature and humidity can provoke structurally different silane coatings characterized by different surface energies.[123] Difficulties in controlling the monolayer density, in particular for trichlorosilane monomers, have been also reported. Trichlorosilane molecules can be covalently bound not only to the silicon surface, but to other monomers. In this way, trichlorosilanes can react and form a two dimensional cross-linked network that result in heterogeneous agglomerates on the surface, such as the ones observed in Figure 39.

The relevance of these structural defects on SAMs rely on the final intentionality of the surface coating. Some applications such as biosensing are not very sensitive to the presence of agglomerates at the surface. However, in our case a completely flat and homogenously coated surface without significant topographic defects must be formed to avoid surface roughness affecting the orientation of the microdomains and any possible interdiffusion coming from the coating layer. The extreme difficulty in finding the processing conditions leading the required homogenous coating in a reproducible way, drove us to direct our efforts towards more fruitful strategies for surface neutralization such as random copolymer brushes.

4.2.2. Surface modification by random copolymer brushes

Random copolymers are composed of two or more different monomer units linked together in a statistically random order. Random copolymers of tailored chemical compositions can be used as coatings to finely tune the interfacial energy of a substrate. In a seminal work, Mansky *et al.* demonstrated that random copolymers of PS and PMMA could form brushes on silicon substrates to modify and control polymer wetting of the surface.[237] Most commonly, brush layers of random copolymers are end-grafted to the substrate by an hydroxyl-terminated group but brush layers can be also formed by copolymers side-grafted to the substrate.[117] Crosslinked layers have been probed as substrate independent coatings to chemically modify the preferential wetting characteristics of alternative materials by the incorporation of either thermal- or photo-crosslinkable moieties to the random copolymer chain.[121,280]

The end-hydroxyl functionalized random copolymers of P(S-*r*-MMA) can react with the silanol groups of the native silicon oxide layer through condensation reaction to form a covalently linked brush. When heated at a temperature well above the glass transition temperature of both monomers (T_g for PS=100°C and T_g for PMMA=104°C) the mobility of polymer chains increases and the OH-terminal groups diffuse to the surface resulting in a highly dense copolymer brush. Non-grafted copolymer chains should be removed by rinsing or sonication to prevent inter-diffusion with the overlaying material.

In our experiments, random copolymer brushes (Brush-71) thin films were spun coated on the silicon or glass coverslips and annealed at 220°C. The removal of unbound copolymer brushes by rinsing with anhydrous toluene was proved to be less aggressive than the previously reported washing treatment using an ultrasonic bath.[131,242] Samples that were sonicated in anhydrous toluene for 5 min showed defects in the brush layer characterized by scarce non-coated areas that were visible when imaging large surface areas by AFM (Figure 40).

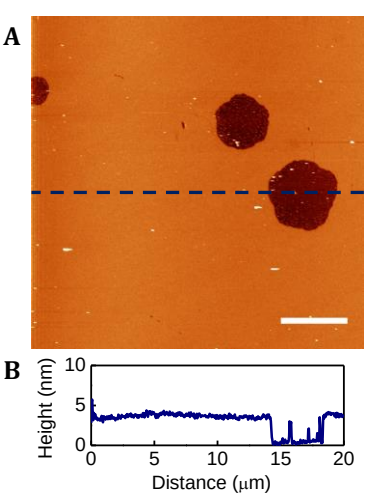

Figure 40. Random brush-71 after washing with toluene in an ultrasonic bath. (A) AFM topography images of the random copolymer brush-71 deposited on top of a silicon substrate. (Scale bar: 4 μm; Z-scale: 10nm). The blue dashed line in A indicates the location of a height cross section across the film surface and the defect found (B) AFM cross section collected along the blue dashed line in A. Transitions from film surface to the bottom surface of a defect appeared as step changes in height in the profile. The resultant thickness of the random copolymer brush was of 4 nm.

The non-coated areas preserved the preferential wetting for PMMA block and biased the wetting behavior of block copolymer thin films spun coated on top of them (Figure 41 A), so island/hole structures of the block copolymer layer were observed. The formation of such structures is prompted by the chain compression

that block copolymer molecules undergo due to incommensurability between the film thickness (t) and the polymer domain spacing (L_0).[100] On neutral interfaces, this compression energy is mitigated by the arrangement of microdomains perpendicularly to the substrate. In preferential wetting conditions, the most energetically favorable configuration is the parallel orientation of microdomains, resulting in thicker regions.[241] A differential microdomain segregation of BCP small thin films is observed on copolymer brushes-functionalized surfaces due to the described inhomogeneities in the brush grafting and, therefore, in surface energies (Figure 41). Featureless, non-ordered regions appeared visible in the AFM images (Figure 41 C and D). These regions showed the PMMA cylinders randomly disseminated without the proper perpendicular alignment, in agreement with the dewetting behavior reported for deficiently or partially neutralized surfaces.[116,279,281] Instead, AFM images of BCP small thin films on densely-grafted copolymer brushes (Figure 41 E and F), show the proper hexagonal arrangement of PMMA cylinders on the surface, according to a neutral wetting behavior of the PS and PMMA copolymers.

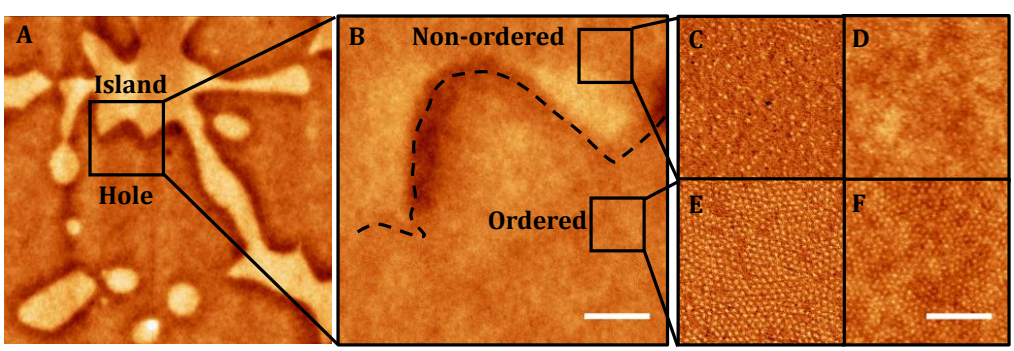

Figure 41. Defective random copolymer brush-71 layer obtained after washing with toluene in an ultrasonic bath leads to BCP small dewetting. AFM image of (A) BCP small over a Brush-71-coated surface (BCP small spun coated at 5mg/ml and annealed at 220°C 3days) (20x20 µm image; Z-scale: 10 nm) and (B) the corresponding zoom over an area with both island and hole structures. (Scale bar 1um; Z-scale: 10 nm) The squares are located on non-ordered and ordered areas, corresponding with island and hole structures respectively. (C) Phase and (D) topography images from the disordered area and (E) phase and (F) topography from the ordered area (Scale bar: 400 nm; Z-scale: 5 nm for topography images and 10 mV for phase images).

The proper engraftment of copolymer brushes ensuring the neutralization of the interfacial energies of silicon substrates was achieved when non-attached copolymer brushes were gently rinsed with anhydrous toluene. The copolymer brush layer obtained, was homogeneously flat over large areas (Figure 42 A shows a 20 x 20 µm area), exhibiting high stability to withstand the subsequent manufacturing processes. The grafted brush thickness measured by the scratching

method (Figure 42 B) was ~4.9 nm. This result, similar to that reported by others,[115,242] is regarded as an effective thickness to inhibit any possible penetration of the overlying block copolymer layer. It has to be noted that annealing for longer time periods did not yield thicker brush layers because the densely engrafted chains constitute an energetic barrier that impede the attachment of additional molecules to the substrate.[121,237]

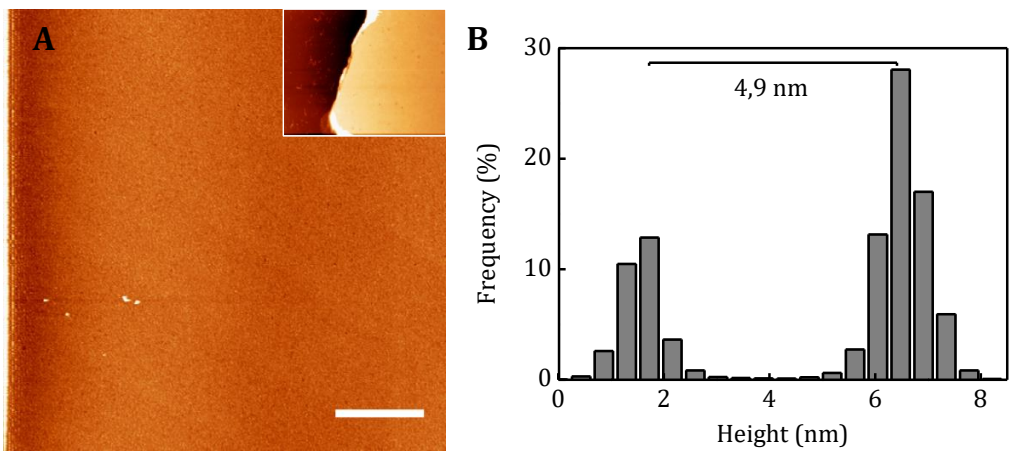

Figure 42. Large areas of random copolymer engrafted on a silicon substrate. (A) Random copolymer brush-71 layer after washing with toluene fresh (Scale bar: 4 µm; Z-scale 5nm). The inset shows an AFM image of the polymer brush once the polymer layer has been scratched. (B) The relative difference in height between the silicon surface and the upper interface of the thin film is measured using a histogram of heights, from which the film thickness is extracted.

When seeking for a perpendicular orientation of microdomains, a controlled chemical composition of end-functionalized copolymer brushes is one of the main parameters that allows the precise balance of the interfacial energy of the substrate. The relative chemical composition range of random copolymer brushes that promotes the perpendicular orientation of block copolymer microdomains in thin films is usually named as perpendicular window. This perpendicular window is unique for every combination of random copolymer brush and block copolymer thin film. Simulations[67,282] and previous studies on PS-*r*-PMMA[131] have demonstrated that PMMA cylinder forming block copolymers showed perpendicular structures on random copolymer brushes with a similar or slightly higher fraction of PS.[114] The chain end of the minority polymer block, i.e., the PMMA in PMMA cylinder forming PS-*b*-PMMA block copolymers has a lower entropic penalty when segregated to a hard surface.[283] For the proper energetic equilibration, the tendency of the majority polymer block, i.e., the PS in PMMA cylinder forming PS-*b*-PMMA block copolymers, to wet the substrate should be

prompted with a random copolymer composition relatively higher for the majority monomer.

We have selected two different random copolymers as neutral coatings for two PS-b-PMMA block copolymers (BCP small and BCP medium) and one PS-r-PMMA random copolymer (Note: the PS-r-PMMA random copolymer, denoted as RandomCP, does not have a OH-termination and should be clearly distinguish from the molecules used as brushes. RandomCP will be used as a non-structured control with an equivalent chemical composition to BCP small and BCP medium polymers) as shown in Table 4.

Table 4. Polystyrene fraction (f_{PS}) of random copolymer brushes used as neutral coatings for the different PS-b-PMMA or PS-r-PMMA copolymer thin films.

Brush		Thin films	
Abbreviation	**Polystyrene fraction (f_{PS})**	**Abbreviation**	**Polystyrene fraction (f_{PS})**
Brush-71	**0.71**	**BCP small**	**0.69**
Brush-74	**0.74**	**BCP medium**	**0.78**
		RandomCP	**0.76**

Random copolymer brushes, Brush-71 and Brush-74, were spun coated at 2.5 mg/mL and annealed at 220°C or silicon or glass substrates. Topographic AFM images acquired before and after the removal of non-grafted polymeric chains by anhydrous toluene rinsing shown flat and homogeneous coated surfaces (Figure 43). Surface roughness (RMS roughness) was measured for both neutral brushes as shown in Table 5. RMS roughness values were in good agreement with that determined for other hydroxyl-terminated brushes.[117]

Table 5. Roughness of thin film and coating of random copolymers brush-71 and brush-74 once thermal annealing was performed and after washing with fresh toluene.

RMS (nm)	**Brush-71**	**Brush-74**
Annealed thin film	**0,33 ± 0,02**	**0,26 ± 0,01**
Resultant copolymer brush	**0,34 ± 0,02**	**0,22 ± 0,01**

The main disadvantage of using random copolymer brushes to tune surface energetics is that, as said previously, the specific volume fraction of their components should match the one of the diblock copolymer thin film to be fabricated on top. Even though the commercial availability of random copolymer brushes has increased in the latest decade, still custom-made polymers with

varying ratios of monomers are synthetized for specific applications. Such approaches require the understanding of polymer synthesis and the specific facilities and equipment to control the kinetic parameters to achieve the desired product. This limits in practice the range of block copolymers that can be driven to hexagonal arrangement using this surface functionalization technique.

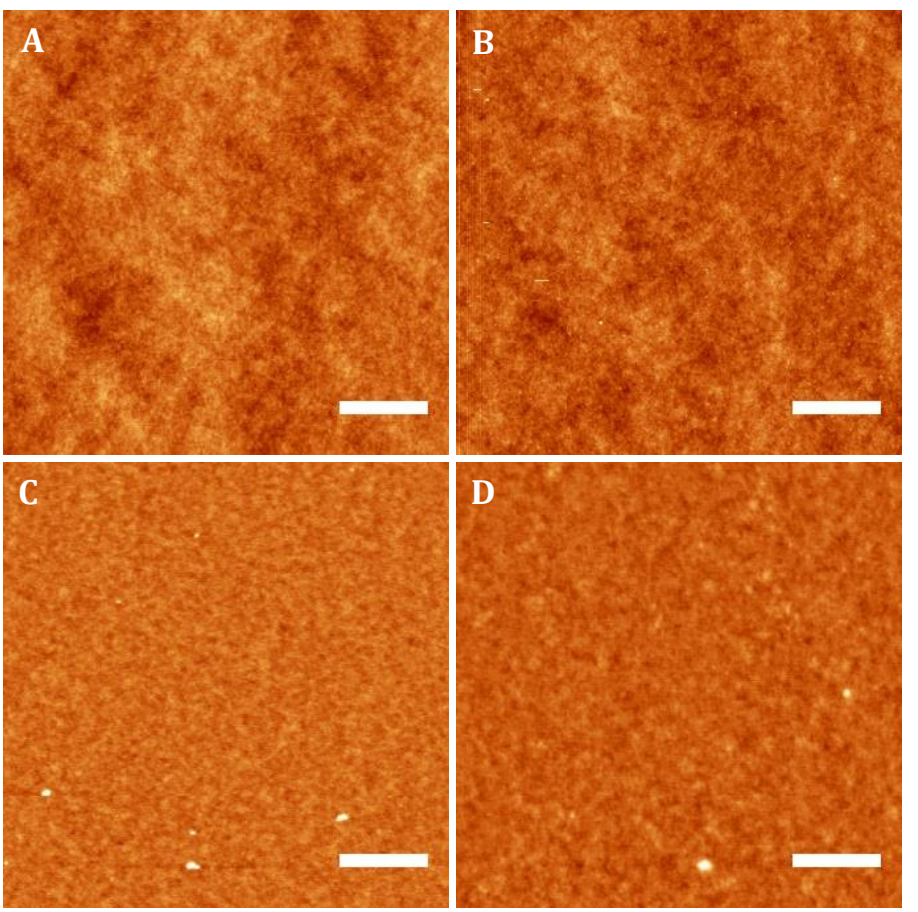

Figure 43. AFM topographical images of thin films of (A) Brush-71 and (B) Brush-74 formed by spin coating at 2.5 mg/mL. Topography of the resulting polymer brush layers after washing with fresh toluene: (C) Brush-71 and (D) Brush-74 (Scale bar: 400 nm; Z-scale: 5 nm).

4.3. Thin film confinement

In comparison with bulk morphologies, diblock copolymers morphologies in thin films are subjected to a degree of confinement that plays an important role in the global energy of the system. As previously commented, the degree of confinement will impact in the $F_{elastic}$ contribution (Section 4.1). Stretching or compression of diblock copolymer chains comes from the incommensurability

between the polymer interdomain spacing (L_0) and the film thickness (t), and is energetically unfavorable.[284] The only intrinsic way of the system to dissipate this energy is the microdomain arrangement in the configuration that favors the enthalpic interactions at the substrate or the free interface, this means, lowering the free energy. There are different morphologies commonly obtained depending on the wetting conditions. On preferential wetting (neutral) surfaces, island/hole formation results from the arrangement of diblock copolymer molecules in quantized L_0-sized thicknesses, this means, compatible with the polymer interdomain spacing.[101] On non-preferential wetting surfaces, microdomains are reoriented perpendicular to the substrate at a broad range of film thicknesses.[116,279,281]

Once neutral wetting conditions were ensured (Section 4.2), the control of film thickness can be accomplished by adjusting either the film deposition parameters (mainly the spinning speed) or the polymer concentration.[100] We checked the relevance of the spinning speed on film thickness using three different solutions of the BCP large polymer with concentrations of 1 mg/mL, 1,5 mg/mL and 2,5 mg/mL at two spinning speeds: 3000 and 6000 rpm. Scratch test was used to resolve film thickness variations determining the thickness value from the analysis of the AFM images of the scratch edge. For the polymer concentration used, statistically significant increases in film thicknesses were obtained when higher polymer concentrations were spun coated. However, the differences in the thickness of the thin films were not relevant when rising the spinning speed from 3000 to 6000 rpm (Figure 44).

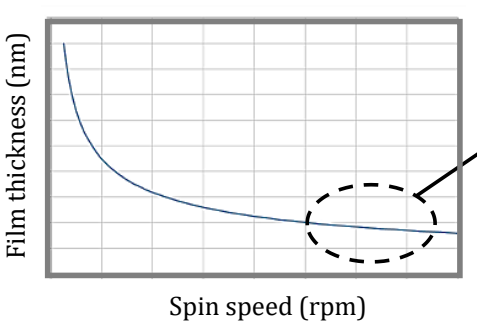

Concentration (mg/mL)	Film thickness (nm)	
	3000 rpm	6000 rpm
1	10,8±0,6	8,3±1,9
1,5	13,4±0,2	13,2±0,6
2,5	21,6±0,1	19,8±0,5

Figure 44. Scheme of the standard spin curve showing the film thickness dependence on the spin speed. Thin film thicknesses of BCP large polymer vary as a function of the concentration and the spin speed. Measurements using the scratch tests were performed by AFM (mean and standard deviation). The small differences in film thickness found between 3000 rpm and 6000 rpm led us to hypothesize that these spin speeds correspond with the right part of the spin curve,

i.e., ***the asymptotic region where increasing speeds will not produce noticeable changes in film thickness.***

Therefore, we can assume that for all the concentrations tested, the asymptotic region of the spinning curves were already achieved at 3000 rpm. This is a mild spinning speed which is convenient for safety reasons. Thus, for all the experiments described thereafter, the spinning speed was settled at 3000 rpm.

As film thickness is a crucial parameter in our system, we investigated in detail the film thickness dependence on polymer concentration. For this purpose, polymers (BCP large and BCP medium) were spun coated at different concentrations ranging from 1 to 10 mg/mL. Film thicknesses were evaluated by AFM which measures the total thickness of the thin film, including the ~5nm of the random copolymer brush layer. The resulting values for each diblock copolymer showed a linear relationship with the polymer concentrations (Figure 45).

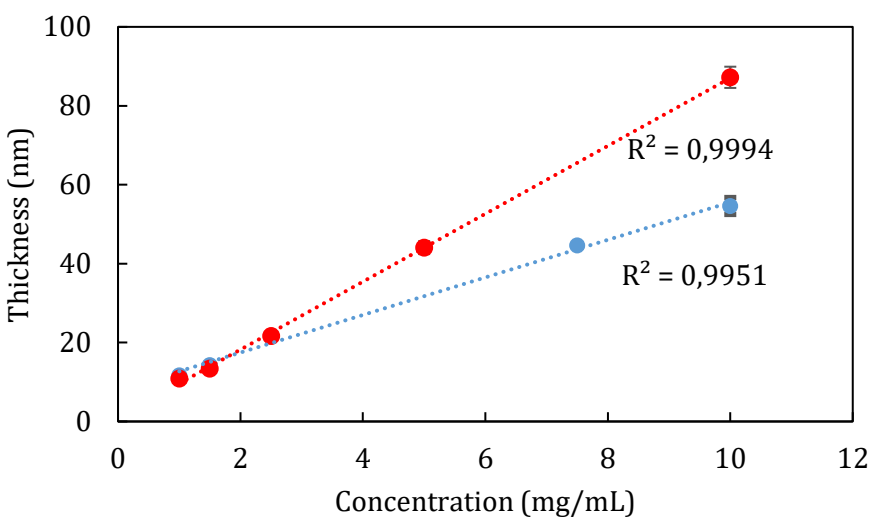

Figure 45. Film thickness dependence on block copolymer concentration. BCP large (red dots) and BCP medium (blue dots) spun-coated at 3000 rpm for 40 s. Calculated linear regression for: BCP medium: y=4.7·x+7.9 (R^2=0.9951) and BCP large: y=8.6·x+1.0 (R^2=0.9994)

It was demonstrated that at the specified spinning conditions (3000 rpm for 40 s), thicknesses of different diblock copolymer thin films can be easily tuned only with a proper selection of polymer concentration. Hence, the polymer concentration will be the factor used to get the appropriate film thickness leading to erpendicular microdomain orientation.

4.4. Microdomain segregation and perpendicular orientation

In asymmetric diblock copolymers, microdomain segregation is controlled by four factors: the Flory-Huggins segment-segment interaction parameter (χ), degree of polymerization (N), the block volume fraction (f) and the molecular architecture. The product $\chi \cdot N$ controls the state of segregation in such a way that, for $\chi \cdot N$ <<10, the entropic energetic contribution of the system dictates the block copolymer molecules to remain a homogeneous mixture. For $\chi \cdot N$>>10, the enthalpic factors (immiscibility of polymer chains and chain stretching) leads the development of microdomain segregation. We have selected to study three diblock copolymers composed of PS and PMMA with different degrees of polymerization To obtain diblock copolymer thin films with microdomains oriented perpendicular to the substrate, the product $\chi \cdot N$ should exceeds the value of 10, meaning that microdomain segregation is energetically feasible.

The Flory-Huggins interaction parameter has been experimentally determined for PS and PMMA in the solid state as a function of the annealing temperature[135]:

$$\chi_{PS-PMMA} = (0.028 \pm 0.002) + \frac{(3.9 \pm 0.06)}{T} \qquad \textbf{Eq. 2}$$

where T is the absolute temperature.
Thin films were fabricated in all cases with an annealing step performed at 220°C, 493 K. Then, the Flory-Huggins interaction parameter can be determined:

$$\chi_{PS-PMMA} = 0.036 \pm 0.002$$

On the other hand, the degree of polymerization (N) for a given diblock copolymer can be calculated as a sum of the individual degrees of polymerization corresponding to the constituting polymers (N_A and N_B):

$$N = N_A + N_B \qquad \textbf{Eq. 3}$$

Considering the molecular weight of the styrene (MW_{PS}) and the methyl methacrylate monomers (MW_{PMMA}) as 104.1 g/mol and 100.1 g/mol, we can determine the degree of polymerization for a given PS-*b*-PMMA diblock copolymer ($N_{PS\text{-}PMMA}$) as follows:

$$N_{PS-PMMA} = N_{PS} + N_{PMMA}$$

$$N_{PS-PMMA} = \frac{(MW_{BCP} \cdot f_{PS})}{MW_{PS}} + \frac{(MW_{BCP} \cdot f_{PMMA})}{MW_{PMMA}}$$

According to these equations, the degree of polymerization of each PS-*b*-PMMA diblock copolymer employed can be calculated from the data exposed in Table 2.

The following degrees of polymerization were calculated:

$$N_{BCP\ large} = 3454$$

$$N_{BCP\ medium} = 1531$$

$$N_{BCP\ small} = 651$$

Then, the resulting product $\chi \cdot N$ varies depending on the polymerization degree as shown hereafter:

$$\chi_{PS-PMMA} \cdot N_{BCP\ large} = 0.036 \cdot 3454 = 124.3$$

$$\chi_{PS-PMMA} \cdot N_{BCP\ medium} = 0.036 \cdot 1531 = 55.1$$

$$\chi_{PS-PMMA} \cdot N_{BCP\ small} = 0.036 \cdot 651 = 23.4$$

For every PS-*b*-PMMA diblock copolymer selected, the product $\chi \cdot N$ is greater than 10 ($\chi \cdot N$ >>>10), ensuring the equilibrium state is governed by the enthalpy of the system.

In previous sections (Section 4.2 and section 4.3) the balance of the interfacial surface energies (substrate and free interface) have been addressed as well as the film thickness variation depending on the polymer concentration. It is well accepted that even on non-preferential (neutral) wetting surfaces, microdomain orientation perpendicular to the substrate is attained only under certain ranges of thicknesses, denoted perpendicular windows. These windows of thicknesses are unique for every system and strongly depends on characteristics of the selected random copolymer brushes used as neutral coatings.[103] This implies that the perpendicular window for each diblock copolymer thin film can be experimentally determined, which goes beyond the purpose of this work. We were focused on the generation of perpendicular microdomains at a certain thickness inside this perpendicular window, but we did not seek on determining the minimum or maximum thicknesses where the perpendicular orientation was achieved.

Two copolymer brush-modified surfaces were selected as neutral substrates and were combined with diblock copolymer molecules as detailed in Table 4 to create nanopatterned thin films. BCP medium and BCP small were spun coated at 7.5 mg/mL, 5 mg/mL respectively to obtain thin films of approximately 45 nm and 38 nm respectively. An annealing step at 220°C under vacuum was indispensable to get the equilibrium morphology. For this annealing process, a Spot Check® surface thermometer was required to record the effective temperature at the surface of the sample.

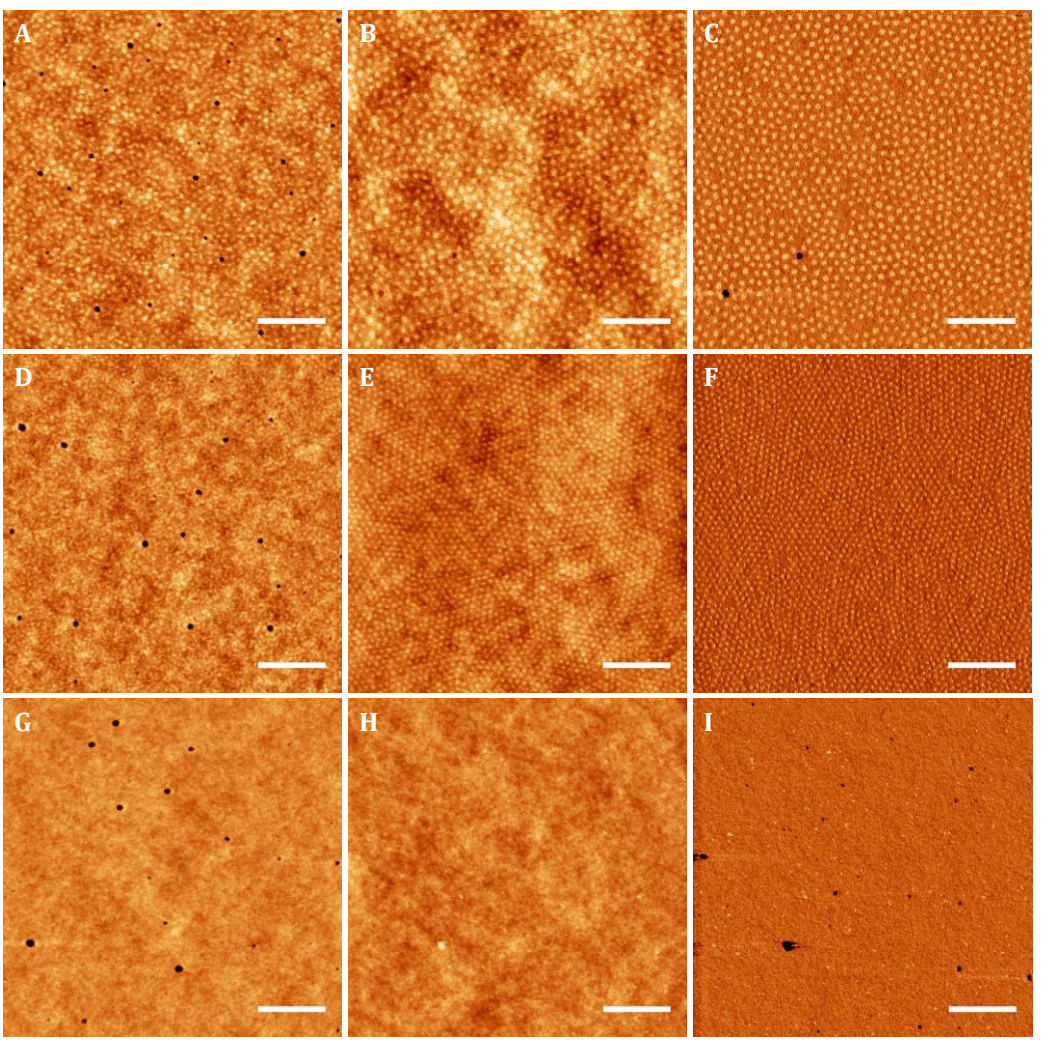

Figure 46. First column: topography of thin films after spin-coating; second column: topography after annealing at 220°C 3h; third column: phase after annealing at 220°C 3h. First row: BCP medium 7.5 mg/mL at 3000 rpm; second row: BCP small at 5 mg/mL at 3000 rpm; third row: RandomCP at 5 mg/mL at 3000 rpm

Differences up to 30°C were found between the Spot Check® surface thermometer and the temperature recorded by the oven thermometer, possibly due to deficient heat transfer triggered by the reduce pressure applied in the oven chamber. Thus, the interfacial energies of PS and PMMA were balanced with increasing annealing temperatures (170-220°C), which improves the pattern quality and can modify the perpendicular window range.[129]

In Figure 46, topographic and phase AFM images of BCP medium, BCP small and RandomCP of 45 nm, 38 nm and 39 nm in thickness before and after annealing are reported. Phase AFM images of the annealed diblock copolymer thin films (BCP medium and BCP small) showed different contrast between the brighter domains corresponding to perpendicular PMMA cylinders and the surrounding PS matrix due to the distinct viscoelastic properties of the segregated domains. These differences were not observable on the RandomCP thin film where the intrinsic random distribution of monomers over the polymeric chain impede the microdomain separation. Then, at the phase AFM image, a non-patterned and homogenous surface is evidenced. Topographic AFM images showed smooth surfaces where the PMMA domains appeared slightly higher (1-2 nm) than the PS matrix and become visible (Figure 46).

In previous studies[114] the perpendicular orientation of PMMA cylinder domains in diblock copolymers with a PS content of 0.71 was observed on surfaces neutralized with random copolymer brushes containing a maximum PS content of 0.72 reporting that higher PS proportion in the neutral coating resulted in structural defects of the thin films. In this work a brush layer containing 0.74 of PS was used as a non-preferential surface to promote the orientation of PMMA cylinders normal to the surface in BCP medium thin films with higher f_{PS} (f_{PS} 0.78). No parallel cylinders or bridging structures between cylinders were detected and hexagonally packed cylinders were successfully oriented perpendicular to the surface (Figure 46).

As mentioned before, the quality of the hexagonal lattice formed by the PMMA cylinders can be improved within the named perpendicular window. For instance, the PMMA domains of BCP medium thin films were perpendicularly oriented when spun-coated at a wide range of polymer concentrations (6-7.5 mg/mL) (Figure 47). However, the hexagonal arrangement of the self-assembled PMMA cylinders was improved at a polymer concentration of 7.5 mg/mL as

demonstrated by the closely-packed and highly ordered pattern generated (Figure 47).

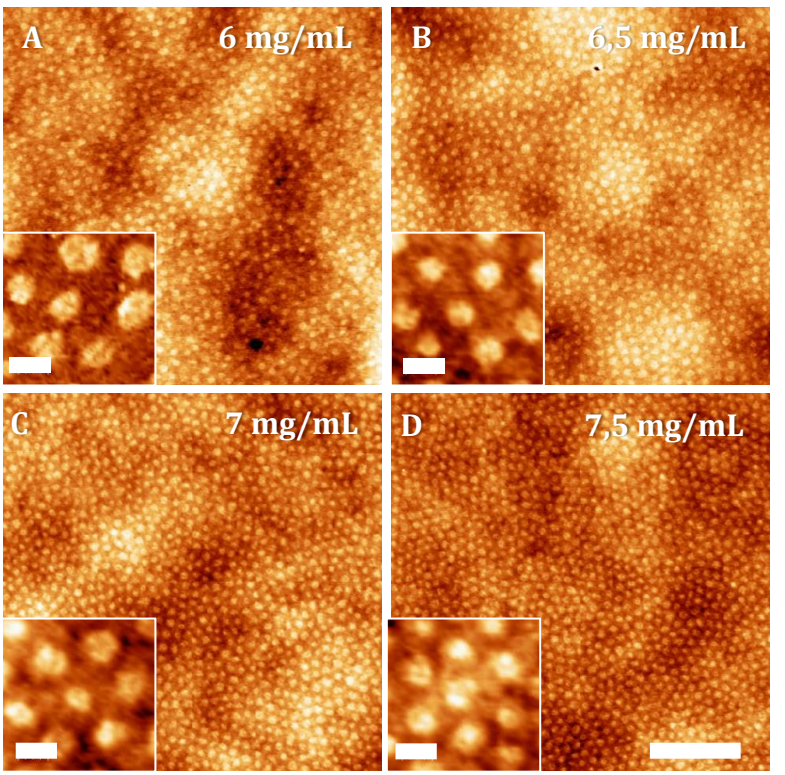

Figure 47. Topographic AFM images of BCP medium spun-coated at (A) 6 mg/mL, (B) 6.5 mg/mL, (C) 7 mg/m, and (D) 7.5 mg/mL (Scale bar: 400 nm; Z-scale: 5 nm) Insets show a representative zoom of the hexagonal arrangement for each polymer concentration (Scale bar: 38 nm).

Table 6. Characteristic parameters of copolymer thin films. BCP medium, BCP small and RancomCP spun coated at 7.5 mg/mL, 5 mg/mL and 5 mg/mL respectively were annealed at 220°C for 3h and film thickness, RMS roughness, diameter of PMMA cylinders, interdomain spacing and density of nanodomains were calculated from topographic and phase AFM images and SEM images.

	BCP medium	BCP small	RandomCP
t_0 (nm)	44,9 ± 0,7	38,5 ± 1,1	39,5 ± 0,9
RMS (nm)	0,8 ± 0,2	0,6 ± 0,1	0,38 ± 0,1
$Ø_{PMMA}$ (nm)	28,5 ± 1,8	21,4 ± 1,6	
L_0 (nm)	64,4 ± 4,7	36,9 ± 1,1	
nº dom/µm²	286,9 ± 11,6	525,5 ± 43,2	

The PMMA cylinder diameter ($Ø_{PMMA}$) and the interdomain spacing (L_0) were measured for both PMMA cylinder forming BCP medium and BCP small block copolymers (Table 6). BCP medium, with a higher degree of polymerization than BCP small, formed perpendicularly oriented PMMA cylinders of approximately 29 nm in diameter, 25% larger than the ones generated by the BCP small (21 nm in diameter), in agreement with reported sizes of similar systems and their L_0.[103,129,241] If the average areas of the PMMA cylinder are calculated, the differences between the BCP medium (638 nm^2/cylinder) and BCP small (360 nm^2/cylinder) are sensibly higher (up to 46%). On the other hand, the interdomain spacing of the hexagonally packed PMMA cylinders was approximately 64 nm and 37 nm for BCP medium and BCP small thin films, respectively. The number of domains per unit area was also characterized being the cylinder density ~ 45% larger for the BCP small compared with the BCP medium. In this sense, the larger area of PMMA cylinders of the BCP medium is compensated by the higher density of PMMA cylinders of the BCP small in such a way that both diblock copolymer thin films displayed the same percentage of PMMA area over the total surface area. This consideration is not trivial for the further use of these thin films as templates for protein nanopatterning where the PMMA areas will act as anchoring points for covalent binding. The generated BCP medium and BCP small thin films have the same global surface density of PMMA but different nanoscale distribution. In a third case, RandomCP thin films keep an equivalent proportion of PMMA (Table 2) without any structure at the nanoscale but a featureless mixture of PS and PMMA all over the surface and they will be treated as control surfaces for surface-bound protein patterning.

Surface roughness of BCP medium, BCP small and RandomCP thin films were characterized by AFM. In all cases, surface roughness (RMS roughness) was measured to be less than 1 nm (Table 6). Subtle differences in surface roughness between PS and PMMA domain are visible on the diblock copolymer surfaces, which can be derived from the tip-induced deformation of polymer chains caused by tapping-mode AFM imaging.[285] PMMA surfaces are resistant to AFM imaging, even in contact mode, showing no superficial modification. In contrast, upon AFM imaging, PS surfaces exhibited ripplelike structures at the surface. Since the deformation of laterally constrained polymers depends on several parameters such as the polymer chain mobility, molecular weight, temperature, number of scans or scan speed,[286] we held AFM imaging parameters and temperature constant to reduce possible variations. Independently, copolymer films with a

higher molecular weight are subjected in a greater proportion to deformation that might cause the depression of the centered PS regions, affecting the apparent surface roughness.

Surface roughness may be manipulated to alter cellular processes such as cell adhesion, proliferation or differentiation of various cell types.[287–289] However, to the best of our knowledge, cellular read out has proved to be affected by moderately rough surfaces, ranging from 5 to 15 nm, or higher roughness averages.[62,289–291] Therefore, BCP medium, BCP small and RandomCP thin films will be considered sufficiently smooth to prevent any possible effect on cell behavior derived from the surface roughness.

Substrates used for cell culture assays, are in permanent contact with protein, and its surface wettability might influence the protein-substrate interactions and therefore, promote unspecific protein adsorption.[250] The wettability of the nanostructured and non-structured thin films were analyzed by static water contact angle and compared with pristine PMMA and PS films. As shown in Table 7, pure PS and PMMA substrates are rather hydrophobic with relatively high water contact angles. For PS-*r*-PMMA random copolymer thin films it has been previously described that water contact angles increases with increasing PS fraction.[115] BCP medium and Random CP have a f_{PS} of 0.78 and 0.76 respectively, which dictates that their surface hydrophobicity shows no statistically significant differences with pristine PS. On the contrary, statistically significant differences were found between PS, RandomCP or BCP medium thin films water contact angles compared with PMMA surface, which is the minority component. From these results we can inferred that, in terms of surface wettability, the diblock copolymer substrates are comparable to PS, which is the standard polymeric material used as substrate for cell culture assays.

Table 7. Surface wettability for RandomCP and BCP medium thin films compared with bare PMMA and PS substrates (average values ± standard deviation from at least 5 independent measurements)

Surface composition	Water contact angle (°)
PMMA	83,2 ± 5,4
PS	96,6 ± 2,6
RandomCP	89,6 ± 2,0
BCP medium	96,8 ± 2,5

4.4.1. Perpendicular orientation of PMMA cylinders

The internal three-dimensional structure of PMMA cylinder forming diblock copolymers within the film thickness has been usually investigated by the selective removal of one of the blocks.[292] Upon exposure to ultraviolet light (UV), PS block crosslinks and becomes stiffer while PMMA monomers are degraded and become soluble in glacial acetic acid.[129,140] These differential photodegradable properties of PS and PMMA allow the fabrication of nanoporous thin films that are considered potential tools to booster a technological revolution in several fields such as microelectronics, photonics and material science.[101]

BCP small thin films were UV etched before annealing. Figure 48 (panel A and B) shows representative SEM and AFM images of these samples. The PMMA etched domains result in a domain morphology which is chaotic, presenting a broad range of pore sizes lacking any regularity over the surface. This structure is formed basically because the PMMA domains are not perpendicularly oriented.

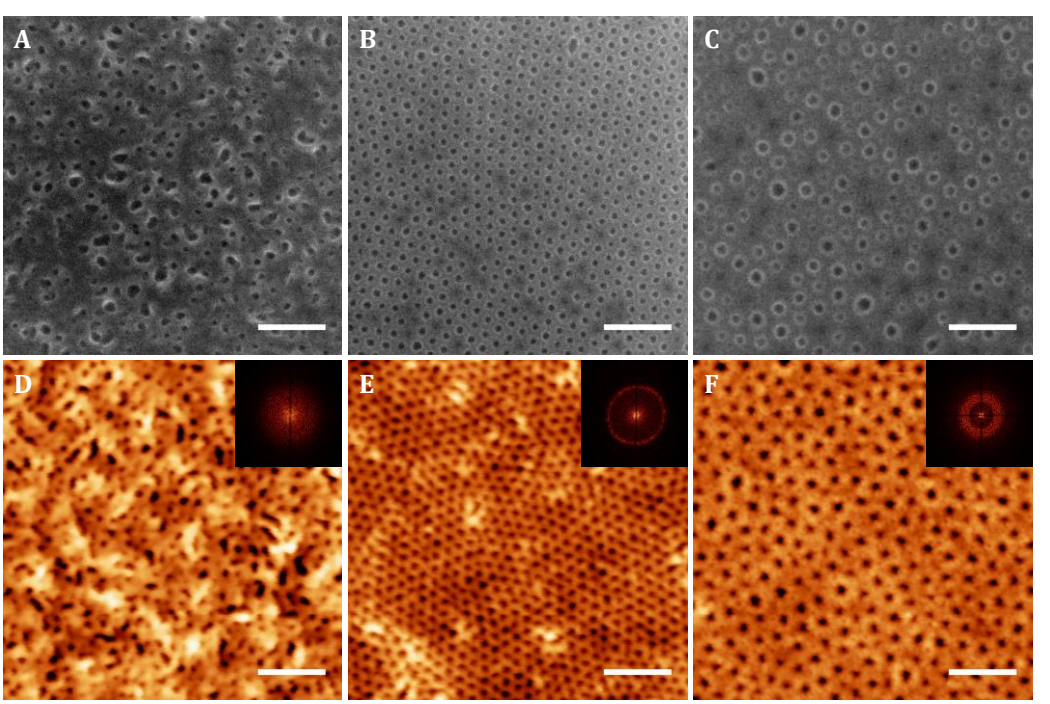

Figure 48 Block copolymer thin films after PMMA etching under UV light. SEM images at the upper part of the panel and AFM topography images at the bottom. (A and D) BCP small thin film

UV etched before and (B and E) after annealing; (C and F) BCP medium thin film UV etched after annealing

Both SEM and AFM images were consistent, showing a mixture of elongated and rounder pores with a poor degree of ordering. BCP small (Figure 48 B and E) and BCP medium (Figure 48 C and F) were also characterized after thermal annealing. Then, the topographic features showed spatial uniformity with a narrow distribution of pore sizes that were hexagonally packed. The pattern regularity depends, as evidenced before, on the degree of confinement, i.e, on the film thickness. In literature,[98] the optimum film thickness for the hexagonal arrangement of diblock copolymer molecules with a slightly smaller molecular weight than BCP small (PS-*b*-PMMA 46.8–18.0 kg/mol) was found to be between 28 and 36 nm. Concordantly, we found 38.5 nm as a proper thickness for BCP small to form perpendicular nanopatterns of PMMA domains surrounded by a PS matrix. As shown in this section, the control of film thickness as well as the annealing process are indispensable to obtain a perfectly perpendicular orientation of PMMA cylinders.

To confirm the degree of regularity of nanodomains, fast Fourier transformations (FFT) were performed from topographic AFM images. A ring-like pattern was recognised on both BCP small and BCP medium after thermal annealing, characteristic of a polycrystalline structure with randomly oriented grains.

For a better visualization of ambiguous defects in the crystal-like structure, either dislocations or disclintations, Voronoi diagrams can be obtained from the AFM images.[106] Voronoi diagrams are subdivisions of a given plane in polygons where the faces limit the area closest to a certain element. For our topographic AFM images, PMMA cylinders are considered the central elements and the number of sides of the polygons correspond to the number of neighboring cylinders. For asymmetric cylinder forming diblock copolymers, perfectly ordered structures will arrange following the bulk morphology in a hexagonal lattice, and the corresponding Voronoi diagram will display hexagons. Topographic AFM images and the corresponding Voronoi diagrams of BCP medium and BCP small thin films are illustrated in Figure 49. In the diagrams, 5-fold and 7-fold-coordinated cylinders associated to defective lattice sites in the grain boundaries are displayed in grey and black respectively. The relative number of defects known as the ratio between the number of defects out of the total number of cylinders, is 15.6% and

17.9% for BCP medium and BCP small respectively. Similar degrees of imperfection were experimentally found[106] and predicted by three-dimensional cell dynamics simulations[81]. These were reported for cylinder forming diblock copolymer thin films when laterally confined in large topographical patterns (side length ~25·L_0), where the walls influence in the lattice orientation is reduced.[282]

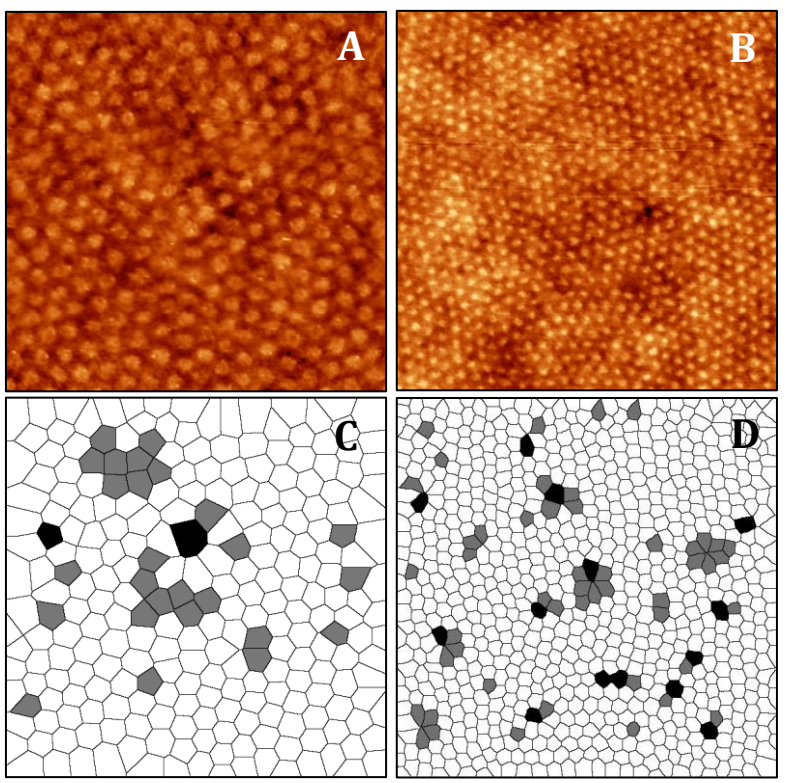

Figure 49. Topographic AFM images of BCP medium and BCP small and the corresponding Voronoi diagrams. The relative number of defects is indicated below the diagrams.

Long-range ordering with of diblock copolymers with non-defective hexagonal lattice has been demonstrated to be improved by a variety of techniques which include controlled solvent annealing,[112] solvent-assisted nanoimprint lithography,[293] application of electric field,[294] shear field,[281] chemical patterning[106] or topographical constrains.[105] A high degree of long-range order is rigorously required for certain nanotechnology applications such as the fabrication of photonic or plasmonic waveguides, while this relevance tends to be relegated to a second place for other biomedical applications such as generation of protein patterns. [295,296]

4.5. Generation of carboxylate groups by PMMA selective hydrolysis

Block copolymers have been explored as versatile tools for the generation of protein patterns either by acting as templates to be replicated by peptides or by the co-assembly of molecules as an integral part of the polymer chain.[297] The differential chemical properties of the forming blocks allow the directed modification of only one of the polymer fractions. PS-*b*-PMMA diblock copolymers have served as substrates for selective protein adsorption[147] but this process requires the profound control of non-equilibrium adsorption conditions. These circumstances might eventually reduce the pattern stability and fidelity for practical applications. These concerns were resolved by the incorporation of functional groups to the block copolymer structure. For example, iminodiacetic acid-functionalized PS homopolymer was blended with a PS-b-PHEMA diblock copolymer to immobilize histidine tagged recombinant proteins with a controlled orientation.[159] In another approach, by tailoring the PEO block with a maleimide group, the maleimide-functionalized polystyrene-block-poly(ethylene oxide) (PS-*b*-PEO) diblock copolymer was used to nanopattern small peptides through the maleimide-cystein linkage.[150]

For covalent binding of molecules, previous studies have reported that PMMA can be hydrolyzed under alkaline conditions, leading the formation of carboxylic acid moieties which can react with amine-containing molecules to form an amide bond.[149] The hydrolysis process can be performed in bulk or over the surface of a previously fabricated diblock copolymer thin film.

4.5.1. Hydrolysis in bulk

The PMMA block of BCP medium diblock copolymer was hydrolyzed in bulk to obtain methylacrylic acid groups along the polymer chain. To study the hydrolysis kinetics, the reaction was held during different periods of time, ranging from 1 h to 120 h. The resultant products were analyzed by Fourier Transform-Infrarred Spectroscopy (FT-IR) and ^{1}H Nuclear Magnetic Resonance (^{1}H NMR).

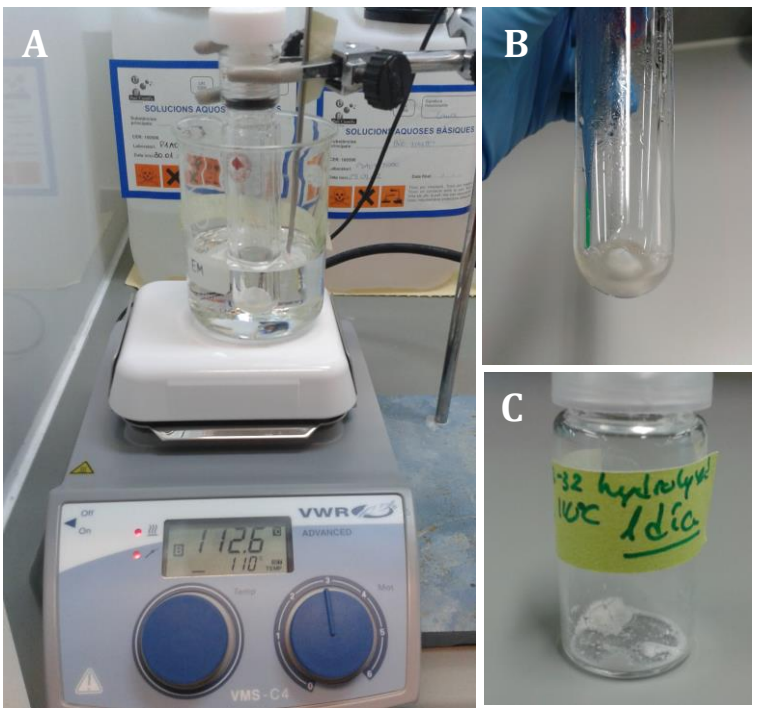

Figure 50. (A) Experimental set-up for the hydrolysis of BCP medium at 110°C; (B) zoom of the hydrolysis solution of BCP medium diblock copolymer after 24h at 110°C and (C) the hydrolyzed powder after neutralization, precipitation and drying.

The complete FT-IR spectrum for all the experimental conditions tested is shown in Figure 51. As the hydrolysis process progresses, a broader band of the O-H stretching vibration is expected to be found between 3700 cm^{-1} to 2400 cm^{-1}, wherein particularly, at 2600 cm^{-1} a vibration band has been reported,[298] corresponding to the O-H stretching related to carbonic acid dimers (Figure 52 A). The characteristic vibration band of the ester (C=O) of the native methyl methacrylate found at 1731 cm^{-1} is shifted after the hydrolysis to 1706 cm^{-1}, which corresponds to the generated carboxylic acid (C=O) (Figure 52B).[251,299] The absorption peak at 841 cm^{-1} comes from the symmetrical vibration of the methyl ester group (C=O=C) and it is perfectly visible in the non-hydrolyzed BCP medium sample. This peak fades with hydrolysis. On the other side, vibration bands at 1605 cm^{-1} and 1496 cm^{-1} assigned to the stretching vibrations of the benzene ring of the styrene monomers are permanently seen all over the hydrolysis process (Figure 52 D).[298]

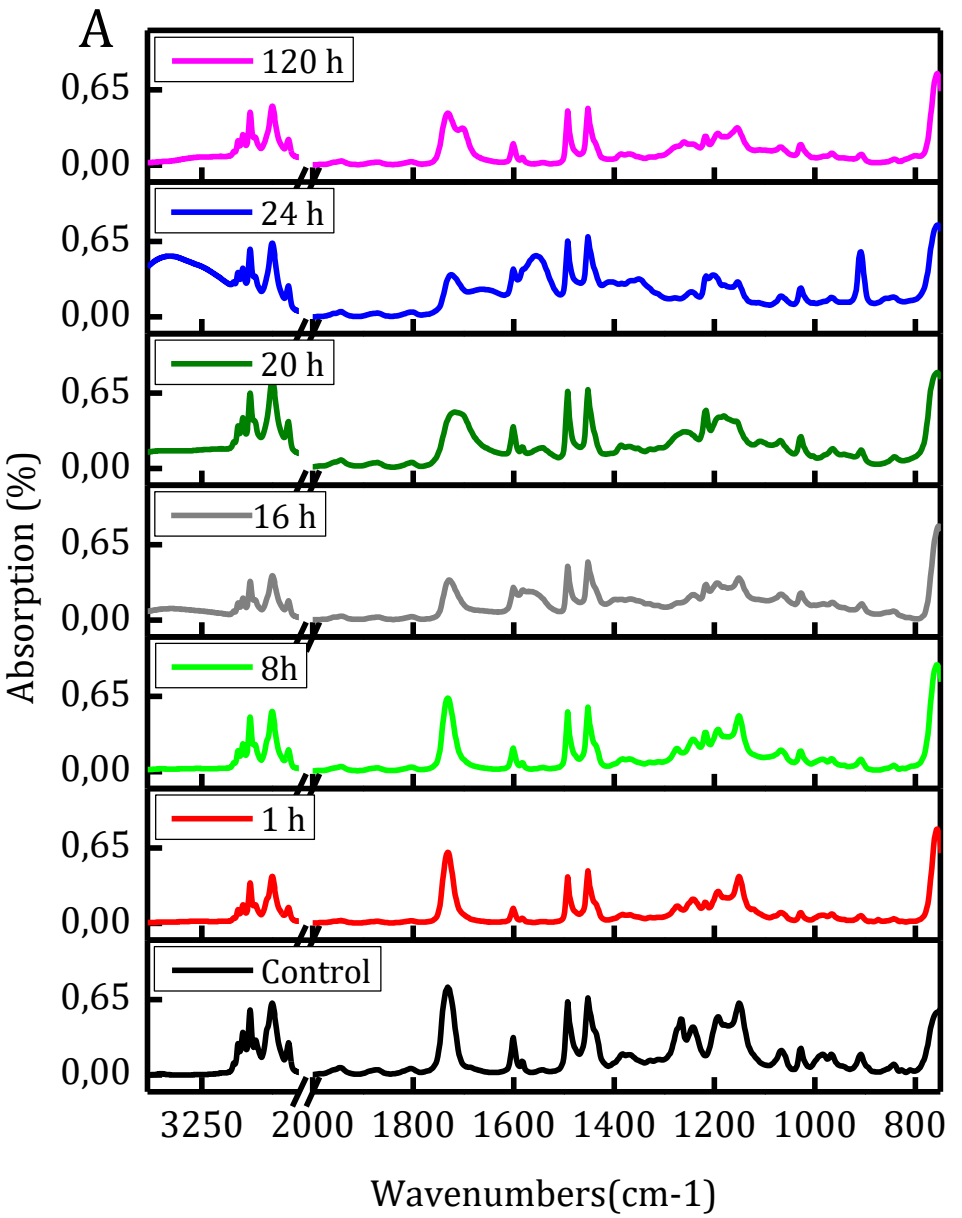

Figure 51. FT-IR spectra of BCP medium block copolymer hydrolyzed for different periods of time ranging from 1 h-120h. The characteristic vibration bands are found at: 3700 cm^{-1} to 2400 cm^{-1} for O-H; 1731 cm^{-1} for the ester (C=O); 1706 $cm^{-1}$for the carboxylic acid (C=O); 841 cm^{-1} for the methyl ester group (C=O=C) and at 1605 cm^{-1} and 1496 $cm^{-1}$for the benzene ring.

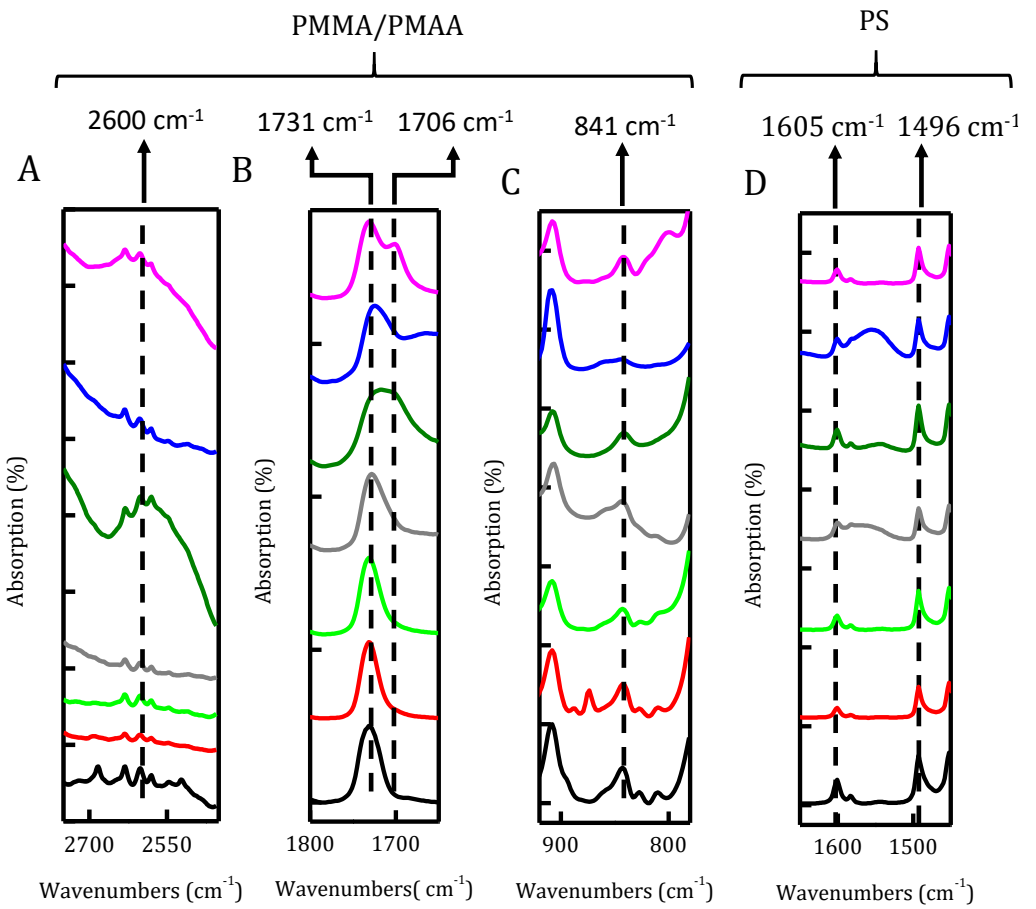

Figure 52. Enlargement of selected ranges in the FT-IR spectra form Figure 51. A) Vibrational band of O-H stretching vibration of carbonic acid dimers at 2600 cm-1, B) Vibrational shift of C=O stretching vibration of ester/acid carbonyl groups at 1731-1706 cm-1, C)symmetric vibration band of C=O-C of methyl methacrylate moieties; D) Absorption peaks of benzene ring of PS at 1605 cm-1 and 1496 cm-1. The color legend is correspond to the increasing hydrolysis times ranging from 1h to 120 h, as shown in the Figure 51.

As demonstrated here, experimental conditions selected were efficient for the hydrolysis in bulk. The FT-IR spectrum of the resultant product, PS-*b*-MMA/MAA after 20 h of hydrolysis showed clear evidences of the success of the process although, the quantitative estimation of the hydrolysis degree becomes very difficult to extract from these data.

To gain further insight, the hydrolysis of BCP medium diblock copolymer was evaluated by ^{1}H nuclear magnetic resonance (^{1}H NMR). ^{1}H NMR spectrum of BCP medium diblock copolymer was dissolved in deuterated chloroform, and analyzed as received without further purification. Analysis conditions were kept constant for the evaluation of the hydrolysis products obtained at different time

points. The degree of hydrolysis was calculated by comparison between the peak area of the protons of methyl methacrylate block (3.6 ppm) and the peak area of the phenyl protons of the polystyrene fraction (6.2-7.3 ppm)[300] as shown in Figure 53.

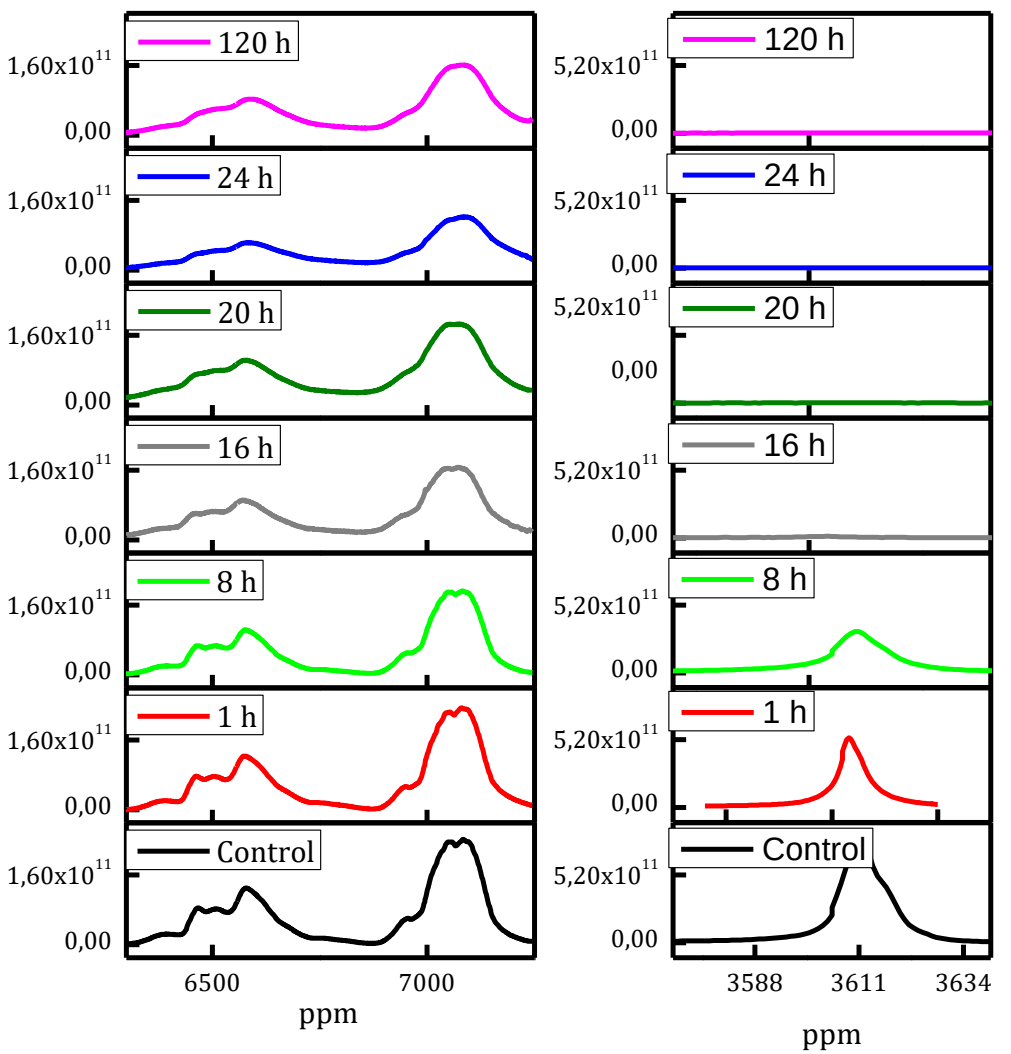

Figure 53. ^{1}H NMR spectra of BCP medium after different hydrolysis times. Spectral region corresponding to A) phenyl protons of the PS fraction and B) methyl protons of the PMMA block.

The determined ratio of the integrated areas increases with the hydrolysis progression. Proportionally, the degree of hydrolysis (%) can be computed probing the complete hydrolysis of the PMMA block after 120 h (Figure 54). If the ratio of hydrolysis is evaluated over time, the 42.59% of the methyl groups are hydrolyzed after 20 h and a complete hydrolysis is accomplished after 120 h (Figure 54).

A

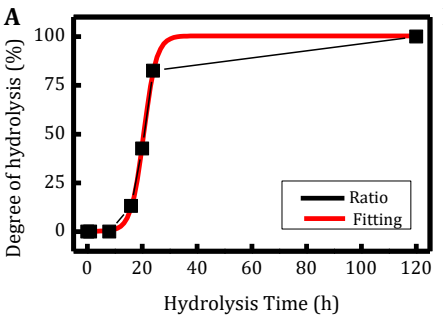

B

Hydrolysis Time (h)	Ratio Integrated Area	% Hydrolysis
0	5,6	0
1	5,9	0,01
8	9,0	0,02
16	261,4	13,1
20	835,2	42,6
24	1614,1	82,5
120	1953,2	100

Figure 54 Hydrolysis evolution. (A) Evolution of the alkaline hydrolysis over time. (C) Table: Hydrolysis time-periods tested; calculated ratio between the integrated peak areas of phenyl protons and the methyl protons; estimated hydrolysis degree (%).

Different solvents were tested for the dissolution of the hydrolyzed BCP medium at 5 mg/mL, including anhydrous toluene, dimethyl sulfoxide (DMSO) and chloroform. They were appropriate for the dissolution of the native BCP medium but failed in dissolving the hydrolyzed BCP medium polymer. Tetrahydrofuran (THF) was reported[301] as a solvent for triblock copolymer PS-b-PMMA-b-PMAA, and, as expected, using this polar solvent the hydrolyzed BCP medium was perfectly dissolved. However, when spin coating the solution on either native silicon oxide surfaces or brush-modified substrates, dewetting of the polymer solution was macroscopically observed. This dewetting behavior was detected when spin-coating any of the hydrolyzed BCP medium polymers with a degree of hydrolysis ranging from 13.13-100% (Figure 55).

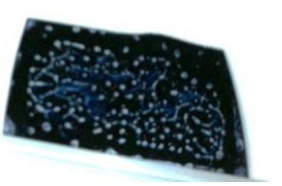

Figure 55. Hydrolyzed BCP medium (13.13% degree of hydrolysis) spin coated at 5 mg/mL concentration on a silicon substrate.

Film dewetting phenomenon has been extensively studied in literature under two scenarios: dewetting of the polymer from a surface due to unfavorable enthalpic interactions or dewetting of the polymer from a coated surface with the same composition due to entropic driving forces.[99,302,303] Although hydrolyzed BCP medium copolymer defers from a triblock copolymer in the block structure, the chemical composition is in fact a mixture of three components PS-b-PMMA/PMAA. Preventing dewetting of triblock copolymer thin films have required of highly complex gradient combinatorial approaches that allow the precise control of the

interfacial energy of the substrate.[132] The brush-modified surfaces previously developed in Section 4.2.2 are no longer neutral for the hydrolyzed BCP medium polymers and an extensive study would be necessary to design an appropriate neutral coating that mediates the perpendicular disposition of the PMMA/PMAA domains.

4.5.2. Hydrolysis on surface

Diblock copolymers can be tailored with chemical functionalities *via* two common methods: first, as described in the previous section, by synthetic routes to produce pre-functionalized diblock copolymers that are afterwards self-assembled in thin films and, second, by chemical surface reactions on self-assembled diblock copolymer thin films modifying the outer layer of the thin film. This second method offers the possibility to work on the surface of already perpendicularly self-assembled diblock copolymer thin films and circumvent any further adjustment of the wetting properties of interfaces.

BCP medium, BCP small and RandomCP thin films were hydrolyzed in alkaline conditions and samples were analyzed after 1 h and 5 h of hydrolysis by X-ray Photoelectron Spectroscopy (XPS) recording the C 1s and O 1s high-resolution peaks. For these polymer molecules, four different types of carbon atoms that contribute to the C 1s peak are found. They are listed in Table 8 based on their binding energy[149]: carbon bound to carbon or hydrogen (C–C and C–H, at 284.4 eV); carbon bound to another carbon which is linked to two oxygens (C–(COO), at 285.5 eV); carbon bound to an oxygen by a single bond (C–O, at 286.6 eV); and carbon bound to two oxygens in ester/acid moieties (O–C=0; at 288.8 eV). Moreover, from the aromatic ring of PS, π-π* transitions can be detected at 292 eV.

Table 8. Binding energies of the four components of the C 1s peak and the theoretical proportion of each one for BCP medium, BCP small and RandomCP considering the PS fraction for every diblock copolymer molecule.

Binding energy (eV)	Carbon	Proportion of carbon bonds (%)				
		PS	PMMA	BCP medium	BCP small	RandomCP
				F_{PS}=0.78	F_{PS}=0.68	F_{PS}=0.76
284.4	C–C & C–H	100	40	86.8	81.4	85.6
285.5	C–(COO)		20	4.4	6.2	4.8
286.6	C–O		20	4.4	6.2	4.8
288.8	O–C=0		20	4.4	6.2	4.8

To facilitate the identification of each carbon type in the chemical structure of PS-b-PMMA diblock copolymer before and after hydrolysis (Figure 56), carbon atoms have been encircled with the same color code depicted in Table 8.

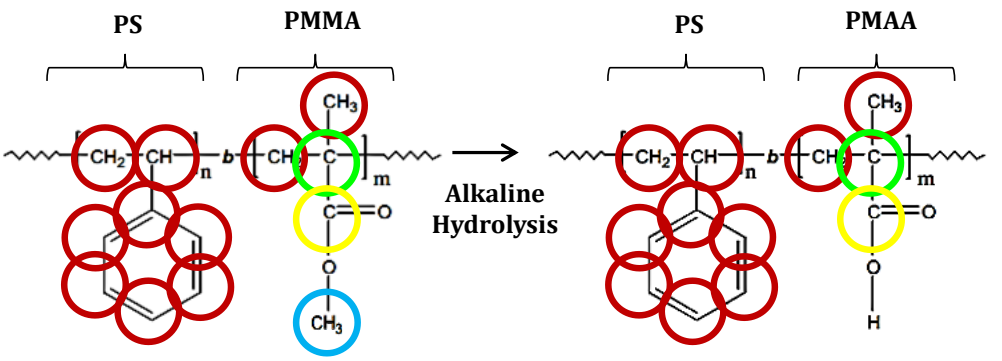

Figure 56. Schematics of the chemical structure of PS-b-PMMA diblock copolymers before and after alkaline hydrolysis. Carbon atoms are encircled according the color code used in Table 8.

During the hydrolysis process, the pending methyl group is removed from the methyl methacrylate monomer structure. The contribution of this carbon atom (C–O, at 286.6 eV) in the C 1s peak is then expected to be reduced concomitantly with the hydrolysis progression. Figure 57 presents the C 1s high-resolution peaks recorded on BCP medium, BCP small and RandomCP thin films at different hydrolysis times. The main contribution of the C 1s peak is shown at 284.4 eV, which comes from the carbon atoms bound to carbon or hydrogen but no significant differences appear in this spectral region after 1 h or 5 h of hydrolysis for any of the thin films analyzed.

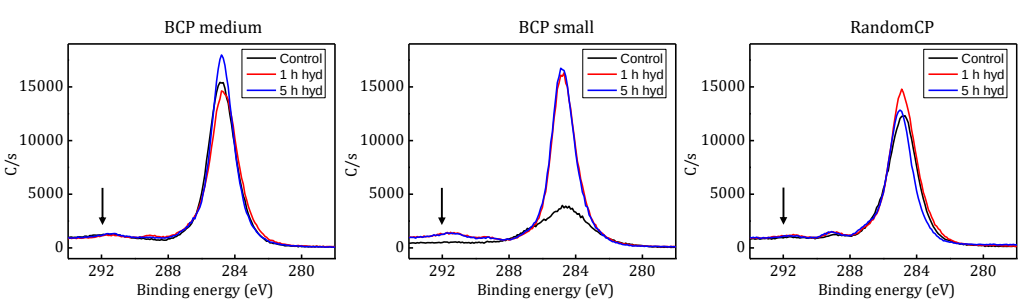

Figure 57. X-ray spectrometry measurements of BCP medium, BCP small and RandomCP thin films. C 1s high resolution XPS peaks obtained on non-hydrolyzed thin films (black line, "Control") and after 1-hour (red line, "1h hyd") and 5-hour of hydrolysis (blue line, "5 h hyd"). Black arrow indicates 292 eV peak for π-π* transitions of the aromatic ring.

The theoretical contributions of each atom of carbon to the C 1s peak have been calculated for PS block, PMMA block and for the BCP medium, BCP small and

RandomCP thin films according to their PS fraction (f_{PS}) (Table 8). In theory, the main peak at 284.4 eV accounts for the 86.8%, 81.4%, and 85.6% of the carbon signal for BCP medium, BCP small and RandomCP thin films respectively. The deconvolution of the signal to extract information about the additional carbon contributions becomes very imprecise, probably due to the relative low proportion of these carbon atoms in the chemical structure (4.4%, 6.2%, and 4.8% for BCP medium, BCP small and RandomCP thin films, respectively). Previously, Zuyderhoff *et al.* studied the chemical composition of different blends of PS/PMMA-*r*-PMAA by XPS and similar C 1s spectra were found when the proportion was 85/15 respectively.[304]

The O 1s high-resolution spectra of the PS-*b*-PMMA copolymers accounts for the contribution of two types of oxygen atoms present on the methyl methacrylate monomer: oxygen π-bonded to a carbon atom (O=C, at 532.2 eV) and oxygen bound to a carbon which is linked to another oxygen in ester functionalities (O–C=O, at 533.8 eV) (Table 9).

Table 9. Binding energies of the oxygen components of the O 1s peak and the theoretical proportion of each one for PMMA block and the hydrolyzed PMAA block.

Binding energy (eV)	Oxygen	Proportion of oxygen bonds (%)	
		PMMA	PMAA
532.2	**O=C**	**50**	**50**
532.6	**O–C**		**50**
533.8	**O–C=O**	**50**	

When hydrolyzed, PMMA is transformed in PMAA and the methyl ester moiety losses the methyl-terminal group and becomes a carboxylic group. As a result, the O–C=O oxygen is converted into another type of oxygen, O–C, which appears at 532.6 eV in the O 1s spectrum. In this way, following the increment of the 532.6 eV peak, the O 1s spectrum could shed light into the hydrolysis process. However, the resolution needed to discriminate between 532.2 eV and 532.6 eV peaks (Figure 58) exceeds the standard resolution of the technique (~0.76 eV)[305].

Due to the similarities of both the C 1s and the O 1s peaks of the native PS-*b*-PMMA and the resultant hydrolyzed PS-*b*-PMMA/PMAA no further information about the hydrolysis reaction can be extracted from the XPS analysis.

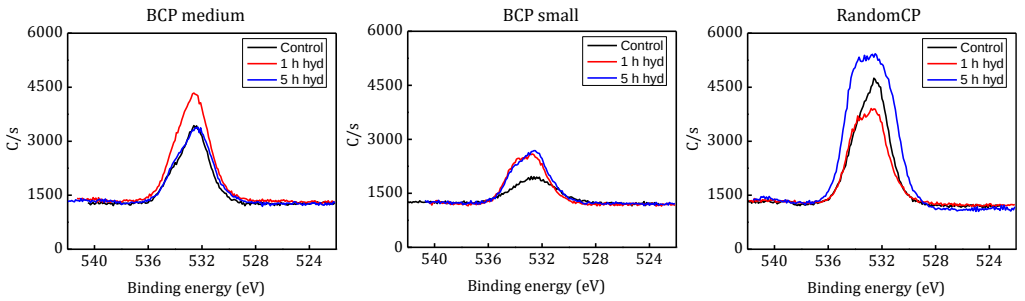

Figure 58. X-ray spectra of BCP medium, BCP small and RandomCP thin films. O 1s high resolution XPS peaks obtained by XPS on annealed thin films (black line, "Control") and after 1-hour (red line, "1h hyd") and 5-hour hydrolysis (blue line, "5 h hyd").

Additional attempts to characterize the degree of hydrolysis under alkaline conditions were inconsistent. Other spectroscopic techniques frequently used for surface chemical analysis, such us Attenuated Total Reflection-Fourier Transform Infrared Spectroscopy (ATR-FTIR) provide globally averaged data over micron length scales, but the described features to characterize in this work were on the order of 20-60 nm. These techniques are therefore of limited use when trying to determine chemical composition in two dimensions and at nanometer length scales. Other highly sophisticated techniques such as Nano-FTIR gave insights of a certain degree of hydrolysis but quantitative data was unreachable (Figure 59).

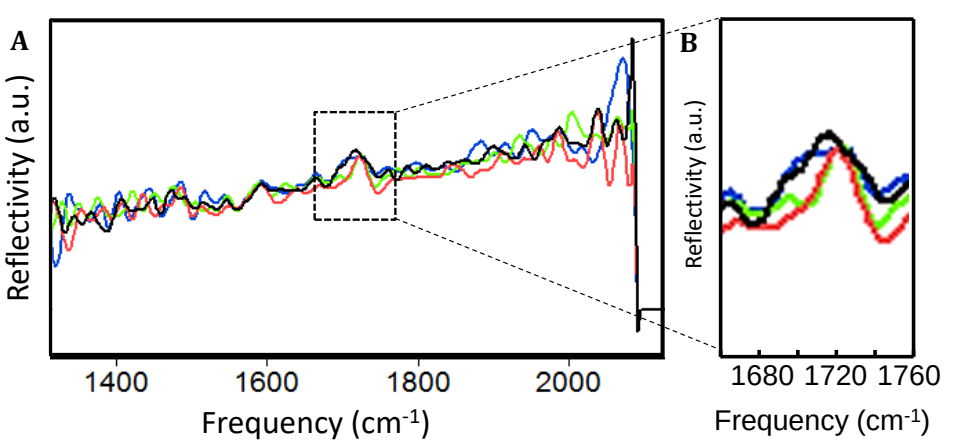

Figure 59. Reflectivity Nano-FTIR spectra. (A) Hydrolyzed (red and green lines) and non-hydrolyzed (blue and blacklines) BCP medium thin film samples were analyzed. The characteristic vibration bands are found at: 3700 cm^{-1} to 2400 cm^{-1} for O-H; 1731 cm^{-1} for the ester (C=O); 1706 cm^{-1} for the carboxylic acid (C=O); 841 cm^{-1} for the methyl ester group (C=O=C) and at 1605 cm^{-1} and 1496 cm^{-1} for the benzene ring. We measured a shift in the CO valence vibration from 1731 cm^{-1} (ester) to 1706 cm^{-1} (acid) in PS-PMMA hydrolyzed samples (in bulk, not on thin films).

Another critical aspect to take into account when processing a self-assembled diblock copolymer thin film of less than 50 nm in thickness is the necessary preservation of film integrity. This requirement should be strictly ensure all over the hydrolysis and functionalization processes to allow subsequent cellular studies. To address this question, BCP medium thin film was imaged after 0.5 h, 1 h and 5 h of hydrolysis by AFM (Figure 60). During the initial minutes, the alkaline solution erases the subtle differences in height between island and the PS matrix visible in the original sample (Figure 60A and B). As the hydrolysis progresses, the thin film roughness gradually increases from 0.5 nm at the starting time-point, up to 0.8 nm after 5 h of hydrolysis. Extended hydrolysis times over the BCP medium thin films (t>>5h) caused a noticeable erosion of the upper part of the PMMA cylinders. A holey-structure at the nanometer scale can be produced.

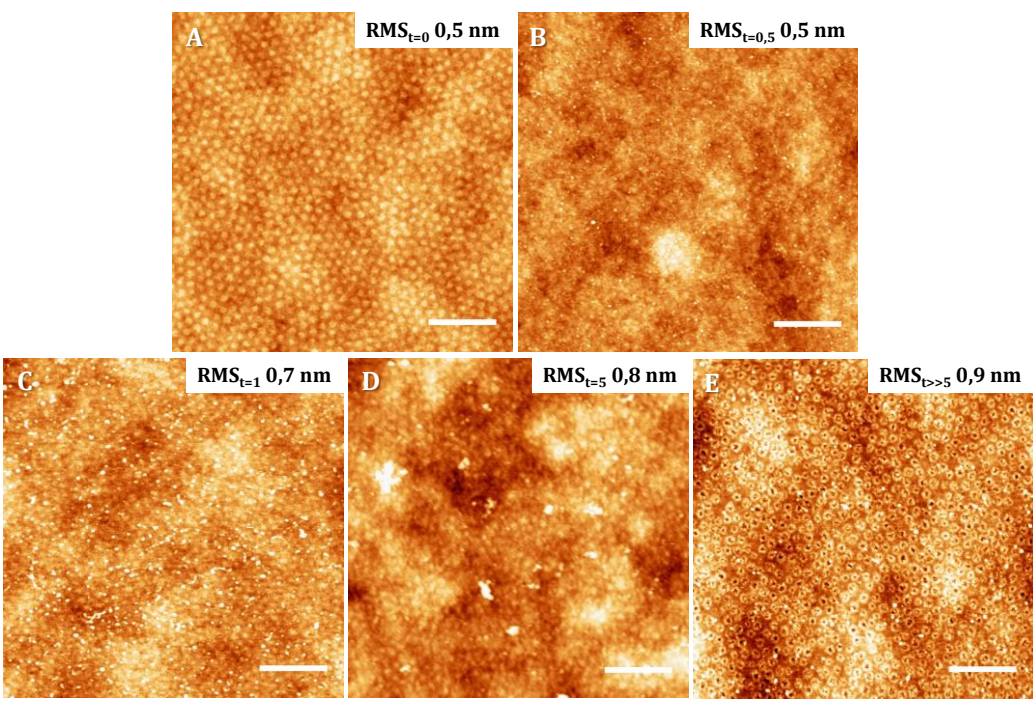

Figure 60. Evaluation of the hydrolysis effects on the thin film surface. Topography AFM images of BCP medium thin film at time A) 0 h, B) 0.5 h, C)1 h, D) 5 h and E) >>5 h of the hydrolysis reaction in sodium hydroxide 2M at 40°C (Inset: roughness of the surface (RMS); Scale bar 400 nm; Z-scale: 5 nm)

Alkaline hydrolysis has been safely applied to thick PMMA substrates for longer periods of time (16 h)[148]. However on thin films, this harsh process required a controlled exposure time (0.5 h to 5 h) to guarantee the conservation of the nanostructured thin film. Upon extended contact times, the alkaline solution can

be considered an alternative for PMMA selective degradation leading a nanoporous film, similarly to UV light irradiation[140].

The final objective of this section was the generation of carboxylic acid moieties on the surface that serve as anchoring points for ligand covalent -binding. Up to this point, the selected approaches for the determination of the carboxylic generation on the PMMA cylinder surfaces were unfruitful. It is important to remark that it does not mean that PMMA was not transformed into PMAA, but that we were unable to directly measure the degree of hydrolysis over the nanopatterned surface. However, indirect methods could help to determine the best hydrolysis conditions for protein binding. For this reason, we went a step beyond in the fabrication process, and studied a combination of hydrolysis, activation and incubation parameters to identify the optimum functionalization conditions for ligand nanopatterning on diblock copolymer surfaces.

4.6. Selective functionalization of diblock copolymer thin films

Protein patterning techniques have evolved within the past decades to enable the fabrication of micron- to nano-sized features.[91,306,307] Surface-bound biomolecule patterns have unveiled the role of the ligand spatial organization on cell behavior at the nanometer length scale.[308] In a seminal work, site-directed immobilization of thiol-containing peptides was performed on gold nanoparticle arrays fabricated by diblock copolymer micelle nanolithography. By click reaction, single molecules were covalently bound to nanostructured PS-b-PHEMA thin films and the hexagonal arrangement of the PS fraction was replicated[158]. Also, PS-b-PEO diblock copolymer was chemically modified with a maleimide group to link specifically to the cysteine amino-acid of certain proteins[150]. These reported strategies have the common purpose of patterning individual proteins that presumably can bind just one receptor. Conversely, the developed thin films in this work are ideal systems for multiple-ligand patterning in a clustered configuration.

Herein, covalent molecule nanopatterning was optimized by the systematic investigation of hydrolysis, activation and incubation parameters. Once the best conditions are defined, we aimed to reproduce the size and spacing of the self-assembled template underneath with the biologically relevant molecules such as cyclic(RGDfK)-PEG_3-NH_2 adhesive peptide or ephrinB1.

4.6.1. Functionalization optimization for covalent molecule-binding onto hydrolyzed polymeric thin films using Alexa Fluor® 647 hydrazide

BCP medium thin films were hydrolyzed with sodium hydroxide, activated by EDC/NHS chemistry and finally incubated with Alexa Fluor® 647 hydrazide (Table 3). Using a fluorescent molecule, the spatial distribution of the ligand can be evaluated by two complementary high-resolution techniques: AFM, analyzing the topographic features of the samples and STORM, recording the fluorescence signal location. Initially, functionalized BCP medium thin films were imaged by AFM and the ligand cluster size distribution was examined (Figure 61).

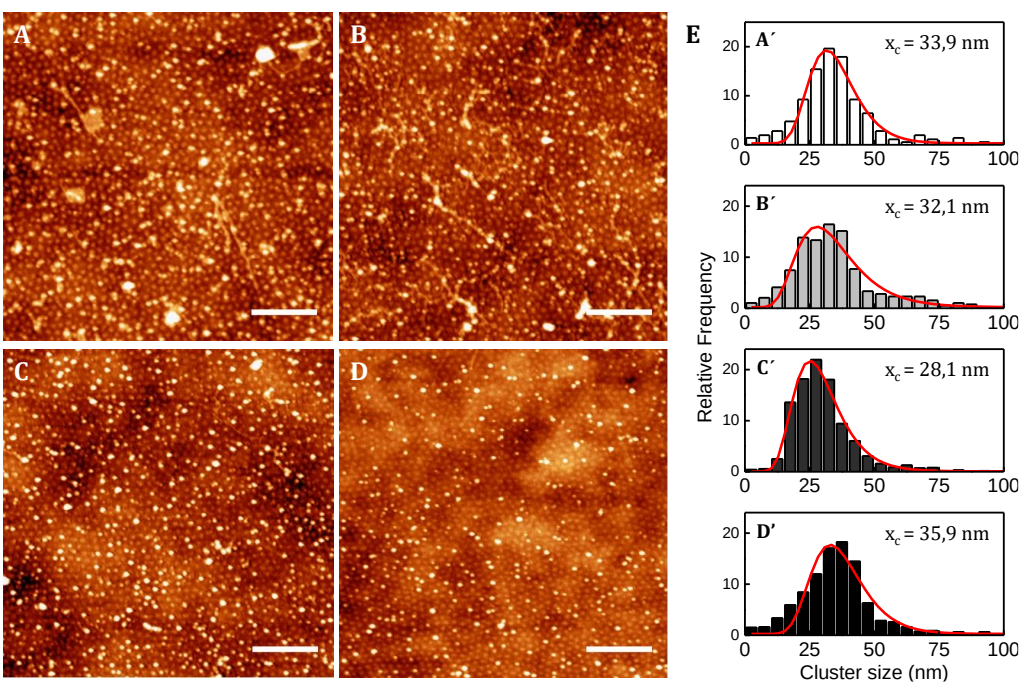

Figure 61. Optimization of the PMMA hydrolysis procedur on BCP medium thin filmse. AFM images of sample topography (in air) after sample hydrolysis and functionalization with Alexa Fluor 647 hydrazide fluorescent dye. (A) 30 min of hydrolysis time at 40ºC without agitation; (B) 30 min of hydrolysis time at 40ºC with agitation; (C) 1 h of hydrolysis at 40ºC with agitation and (D) 5 h of hydrolysis at 40ºC with agitation. A surfactant agent was added to the incubation solution in functionalization conditions C and D. (Scale bar: 500 nm). Images were processed and analyzed using WSxM software. First, images were flatten (simple flatten) and then the flooding algorithm was used to determine the size and distribution of the functionalized areas (attributed to regions with heights from 4 to 12 nm). (E) Histograms of fluorescence ligand cluster size for the evaluated functionalization conditions (A to D) and the most frequent diameter found on each surface. (Scale bar 400 nm; Z-scale: 10 nm).

The topographic images corresponding to "A" and "B" hydrolysis conditions (Figure 61 A and B) showed large ligand aggregates that bridged several PMMA/PMAA cylinders (ligand cluster diameter > 64 nm, which is the

interdomain spacing on BCP medium). Ligand clusters exhibited a broader range of sizes compared with the characteristic PMMA diameter (Figure 61 E, panel A' and panel B'). Although large ligand clusters accounts for less than the 10% of the total ligand aggregates generated by the "A" and "B" functionalization conditions, they represent more than the 25% of the total area covered by ligands (Figure 62).

The incorporation of 0.05% (v/v) of Tween 20 on a concentrated solution is reported to assist in preventing large molecule aggregates and reducing the non-specific binding on surfaces.[309] This surfactant was added to the incubation solution in functionalization conditions "C" and "D". Topographic imaging of the resultant ligand patterns (Figure 61 C and D) showed clusters with restricted dimensions, mostly confined to the PMMA/PMAA cylinder diameter. The "C" condition showed a narrow distribution of ligand cluster diameters centered at 28.1 nm. The abundance of large ligand species was significantly reduced by the surfactant addition to less than the 5% of the total number of ligand clusters for "C" and "D" conditions (Figure 62). Accordingly, a reduction of the ligand coverage attributed to large agglomerates was observed for both conditions. In particular, the functionalization parameters settled for "C" condition, achieved a 97% of small clusters (ligand cluster diameter < 64 nm) which accounted for the 90% of the total ligand coverage.

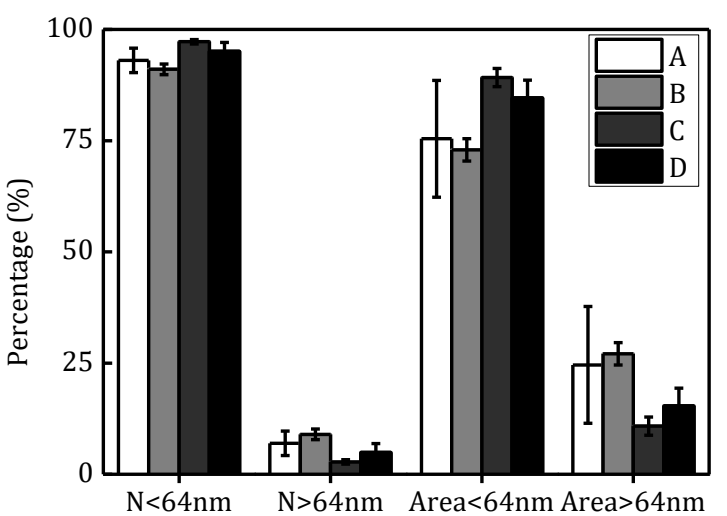

Figure 62. Percentage of ligand clusters with a diameter smaller (N<64 nm) and larger than 64 nm (N>64 nm) immobilized by A, B, C or D functionalization conditions on BCP medium thin films. Percentage of the total area covered by the ligands attributed to ligand clusters with diameters smaller (Area<64 nm) and larger than 64 nm (Area>64nm) immobilized by A, B, C or D functionalization conditions on BCP medium thin films.

Additionally, the ligand cluster density (functionalized domain/ μm^2) and the interparticle distance (distance between ligand clusters) obtained were analyzed (Table 10). "C" condition led to a clustered arrangement of ligands with the highest density of clusters per area and the smallest first neighboring distance. Applying "C" functionalization parameters, 105 ± 19 domains per square micron were covalently decorated with ligand clusters, which means a 37% of functionalization success ratio. Moreover, under these conditions, the interparticle distance was 58 nm, comparable to the interdomain spacing between PMMA/PMAA cylinders (~64 nm).

Table 10 Hydrolysis evaluation upon condition applied (specified on Figure 61). The optimum condition is highlighted in grey.

Hydrolysis condition	Functionalized domain/μm^2	Interparticle distance (nm)
A	**85 ± 21**	**72 ± 6**
B	**86 ± 17**	**65 ± 2**
C	**105 ± 19**	**58 ± 0**
D	**60 ± 16**	**72 ± 3**

Taken together, these results indicate that the best functionalization performance can be attributed to "C" condition. To further characterize the described ligand spatial distribution, STORM analysis was performed on Alexa Fluor® 647 hydrazide-functionalized BCP medium substrates, which provides information from larger and therefore, more representative areas of the sample. A relevant challenge to investigate biological system function is the attainment of protein nanopatterns over large surface areas and the proper characterization of those ones.[296] Figure 63 shows AFM and the reconstructed STORM images acquired from equivalent samples, although no direct correlation between the measurements is intended to be established.[183] Surface-bound patterns were homogeneously originated over large areas (Figure 63 A and D, imaged area ~ 300 μm^2) while still substantially preserving the restricted ligand cluster sizes.

Quantitatively, the domain size distribution extracted from STORM images was consistent to the distribution obtained by AFM (Figure 64). The trustworthy comparison between both techniques confirmed the vast majority of ligand clusters with a diameter ranging from 20-40 nm.

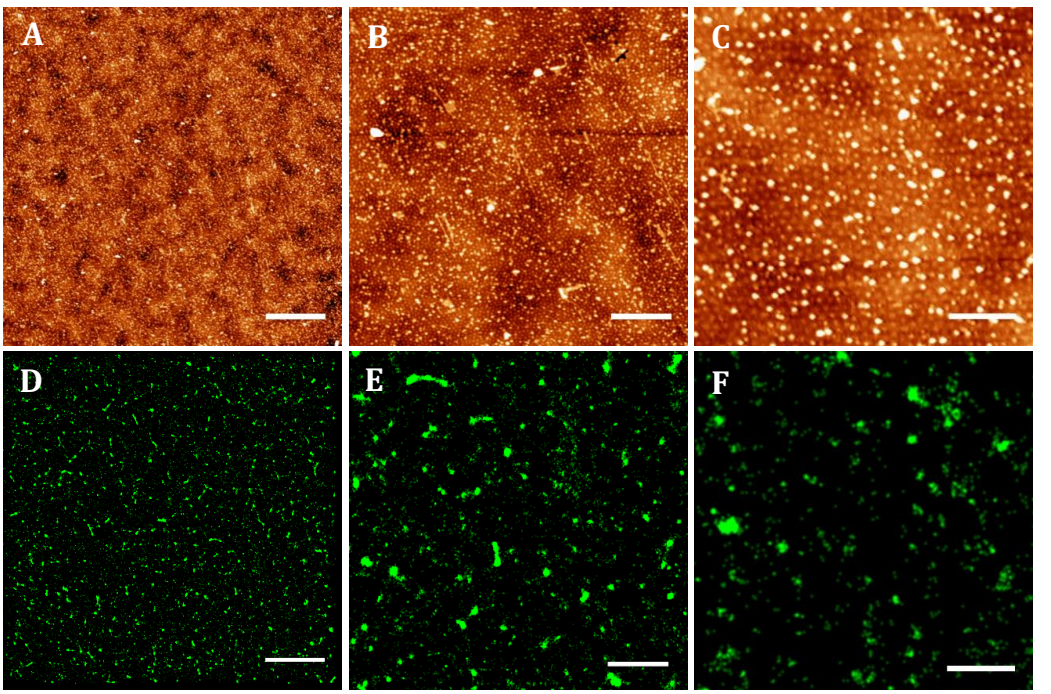

Figure 63. Alexa Fluor 647 hydrazide fluorescent dye nanopatterns are visible by AFM (A to C) and STORM measurements (D to F) at several magnifications. The average size of the clusters was determined as 27±15 nm from the AFM images and as 27±19 from the STORM pictures, in good agreement with the size of the PMMA domains on the block copolymer thin films (scale bar: 3 µm for A and D; 1 µm for B and E; 400 nm for C and F; Z-scale for AFM images: 10 nm)

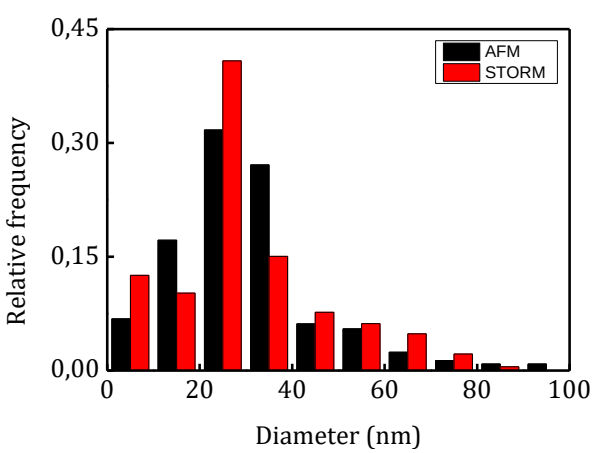

Figure 64. Quantitative analysis of the ligand cluster size distribution. Distribution of Alexa Fluor® 647 hydrazide cluster sizes immobilized on BCP medium thin films extracted from AFM or STORM images.

The robust approach selected for biomolecule immobilization was optimized to reliably replicate the nanometer dimensions of the underlying template. This nanopatterning approach showed a high potential for the

systematic study of cell responses under precisely defined surface cues. In particular, it covers the existing gap between single ligand patterning[70,71,150,158,255] and ligand patches larger than 100 nm[295,296] providing a ligand presenting platform in a controlled clustered distribution.

4.7. Cell adhesion on surfaces nanopatterned with adhesion peptides

4.7.1. Surface functionalization with cyclic(RGDfK)-PEG3-NH2 adhesive ligand

The cell-adhesive peptide arginine-glycine-aspartate (RGD), found in some extracellular matrix components, promotes integrin mediated-cell attachment.[196,310] RGD-decorated biomaterials have demonstrated the influence of micro and nanopatterns in regulating cell migration, growth, differentiation and apoptosis.[16,153,198,200,203,204,311] Of particular interest is the impact of spatially organized ligands in the formation of nascent adhesions. In a seminal work, Spatz *et al*. revealed that integrin clustering and focal adhesion formation is impaired when spacing between individual RGD peptides is larger than 67 nm.[71] To date, numerous patterning techniques have investigated the cell response to univalent ligands under different nanometric spatial configurations. However, the signal transduction often depends on multiple receptor-ligand recognition events that can be promoted by a multivalent ligand configuration. Some theoretical models have predicted the multivalent adhesive ligands distribution on the surface, but lack of a real characterization of the ligand presentation. [16,198,312,313] The platforms fabricated and characterized here on diblock copolymer surfaces could provide a platform to study the multivalent effects of nanopatterned ligands and their effects on cell-receptor signaling.

Cyclic(RGDfK)-PEG_3-NH_2 ligands were immobilized on BCP medium, BCP small and RandomCP thin films by the optimized functionalization procedure for covalent-binding previously described. Samples were imaged by AFM to unveil the ligand distribution over the three polymeric substrates. Figure 65 shows topographic AFM images performed in liquid of typical regions and a representative height profile for each one (denoted by a dashed black line in the image). RGD-ligands adopted a dot-like pattern on the PMMA circular areas surrounded by the PS matrix on BCP medium and BCP small thin films (Figure 65 D and E). The ligand cluster size is uniform and consistent with the dimensions of

the nanopatterned template beneath. In fact, BCP medium thin film, which provides a PMMA/PMAA cylinder diameter larger than BCP small thin film, presents a larger ligand cluster size than BCP small substrate as depicted in the height profiles. Moreover, the pitch of the height profile after RGD-covalent binding matches that of the original PS-*b*-PMMA patterns. Opposite to the nanostructured conformation of BCP medium and BCP small thin films, RandomCP thin films consist of a disordered mixture of styrene and methyl methacrylate monomers that generate a non-patterned template. (Figure 65 F)

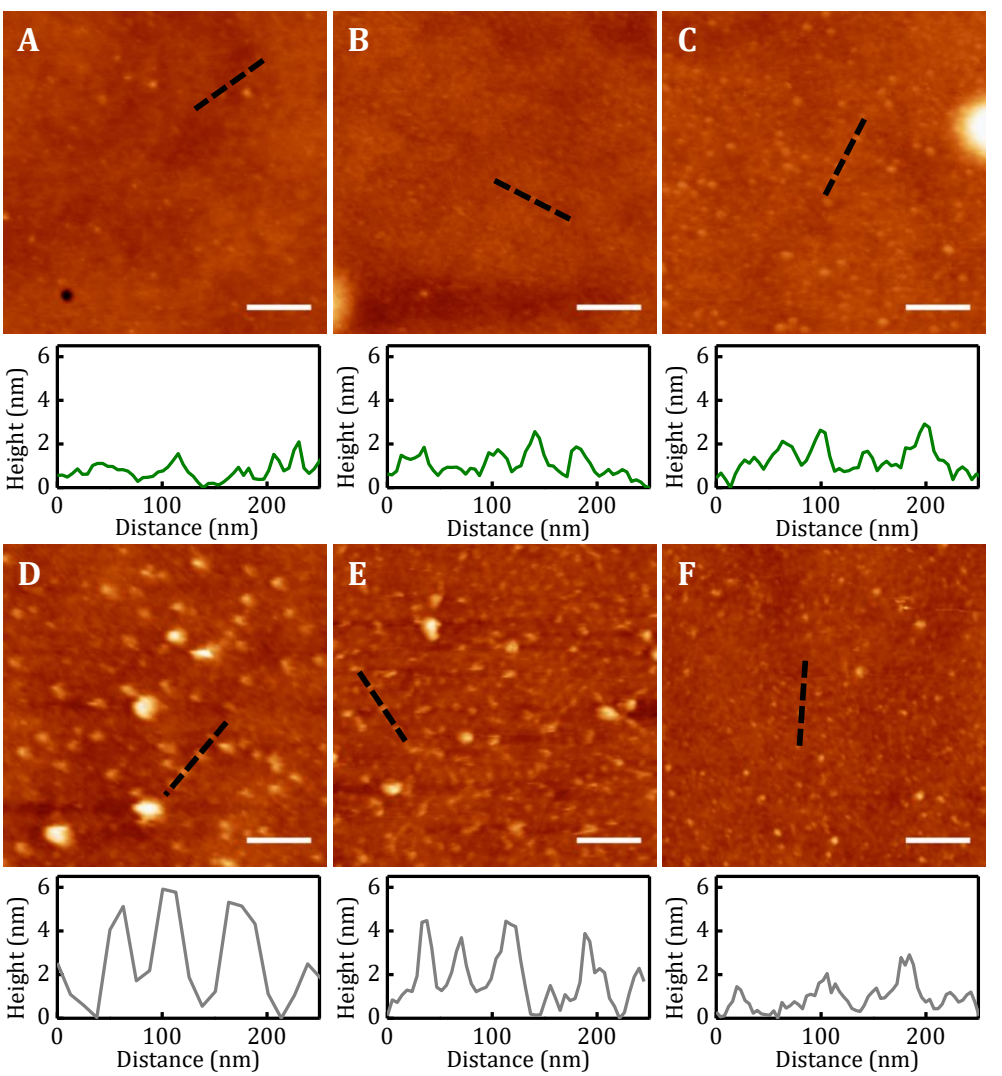

Figure 65. Topographic AFM images and height profiles of physically adsorbed (A to C) and covalently-bound (D to F) cyclic(RGDfK)-PEG$_3$-NH$_2$ on (A and D) BCP medium, (B and E) BCP small and (C and F) RandomCP thin films (scale bar 200 nm; Z-scale 20 nm). The height profile is denoted as a black dash line in the AFM images.

Consequently, PMMA/PMAA anchoring point are homogenously distributed over the surface and ligands are bound without a spatial restricted configuration.

In literature, similar PS-*b*-PMMA substrates were used to create protein arrays based on the preferential adsorption of certain proteins at the interface between PS regions and PMMA domains.[143,144] c(RGDfK)-PEG_3-NH_2 preferential absorption was also evaluated here on BCP medium, BCP small and RandomCP thin films skipping the hydrolysis step in the functionalization procedure. This was also a practical way to confirm that the binding of the RGD-ligand was occurring through the hydrolyzed methacrylic acid, *via* an amide bond. Physically adsorbed RGD-ligands barely remained attached to the BCP medium and BCP small thin films (Figure 65 A and B). Unlike covalently bound, physisorbed peptides shown no visible pattern. Ligand distribution on RandomCP was diffuse (Figure 65 C), which partially resembles the one obtained by the covalent immobilization. Since the spatial distribution of the adsorbed RGD ligands does not correlate with the nanopatterned substrates underneath, the AFM height profiles obtained from the three polymeric substrates were similar, without any regular feature.

4.7.2. Formation of focal adhesion contacts on cells cultured over surface-bound RGD peptides

The influence of the functionalization strategy (physical absorption or covalent bond) on cell adhesion was examined on the RGD-tailored substrates. Both functionalization strategies were applied to BCP medium, BCP small and RandomCP thin films and NIH/3T3 mouse embryonic fibroblasts were cultured on them for 4 h. Cell nuclei was stained with Hoechst (Figure 66, panel A to panel F) and the evaluation of cell adhesion after 4 h of incubation was performed. The mean percentages of adhered cells for every substrate and functionalization procedure are presented in Figure 66 G. The percentages of adhesion on the RGD-covalently bound surfaces are in the range between 70% and 78%. On the other hand, cell adhesion on BCP medium, BCP small and RandomCP surfaces with physically adsorbed RGD, is 25%, 36% and 56%, respectively. These values are significantly smaller than those obtained for the covalently-modify thin films. These results indicate that the covalent functionalization strategy applied to the three copolymer substrates promotes cell adhesion in the initial adhesion stages better than physically adsorbed ligands. Even in the Random CP surfaces where similar ligand distributions were created by adsorption and covalent binding

according to AFM measurements (Figure 65) cell adhesion was 15% higher when RGD ligands were anchored to the substrate through an amide bond than just physisorbed to the substrate.

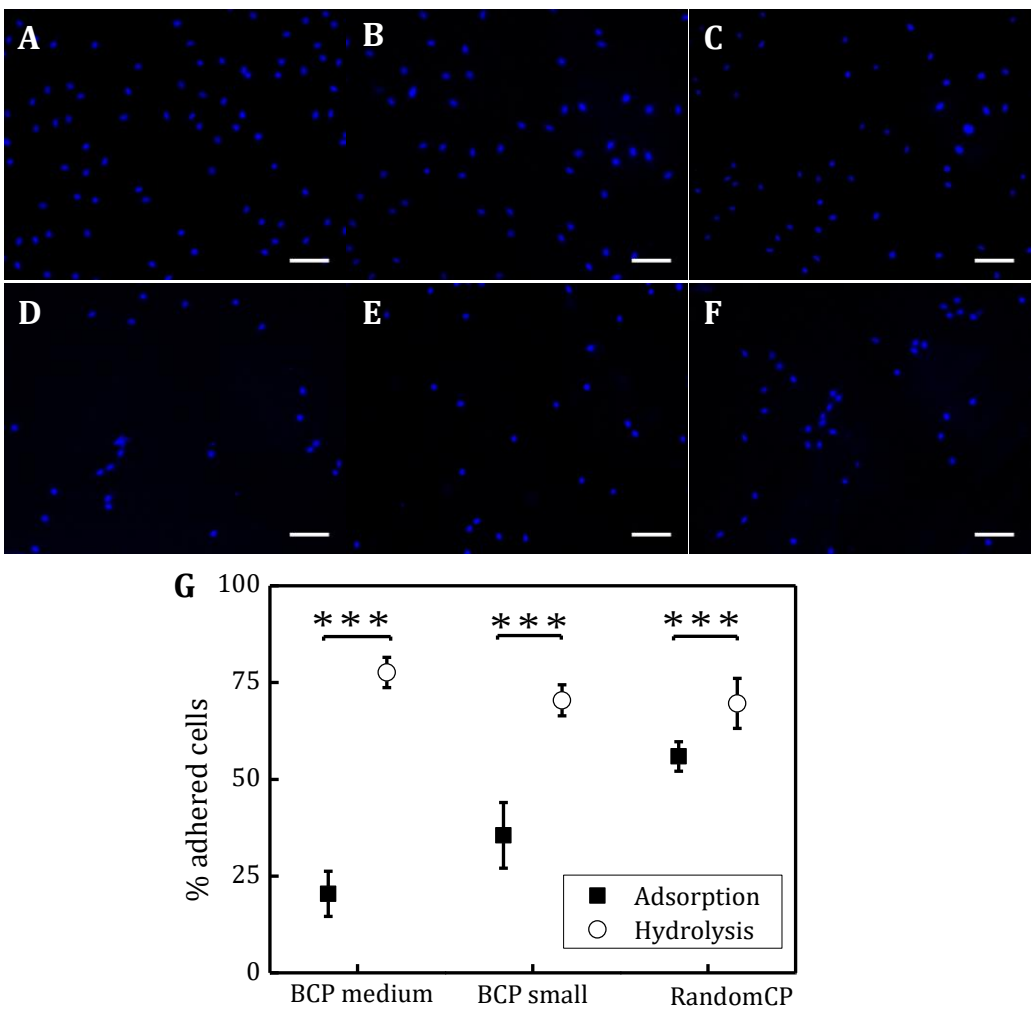

Figure 66. NIH/3T3 mouse embryonic fibroblast cell line cultured on cRGDfK-NH_2-PEG_3 modified surfaces for 4 h in starving medium. RGD peptide was physically adsorbed (A, B, C,) or covalently (D, E, F) bound to block copolymer surfaces: (A and D) BCP medium; (B and E) BCP small; (C and F) RandomCP. (Staining: Hoechst for nuclei (blue); Scale bar: 100 µm). (G) Percentage of cell adhered (with respect to the number of seeded cells) on adsorbed or covalently attached RGD-ligands on top of the three different substrates (p-value: significance level p<0.001; error bars represent the standard error of the mean).

The percentages of adhered fibroblasts showed no statistically significant differences when cultured on BCP medium, BCP small and RandomCP substrates covalently modified with RGD ligands. Previous reports described a decrease of cell density when single ligand interspacing was larger than 58 nm[69]. Our RGD-functionalized BCP medium substrates presented an interdomain spacing of 64

nm, however the negative correlation between ligand spacing and cell adhesion is not observed. The reason behind this reverted tendency may be the presentation of ligand in nanoclusters, which acted as multivalent entities enhancing integrin binding probability in comparison with single ligand arrays.

To gain more insight into cell adhesion and spreading processes over the surface presenting spatially-constrained ligands, NIH/3T3 fibroblasts were immunostained for the observation of nuclei (blue), actin fibers (red) and focal adhesion contacts (green) (Figure 67).

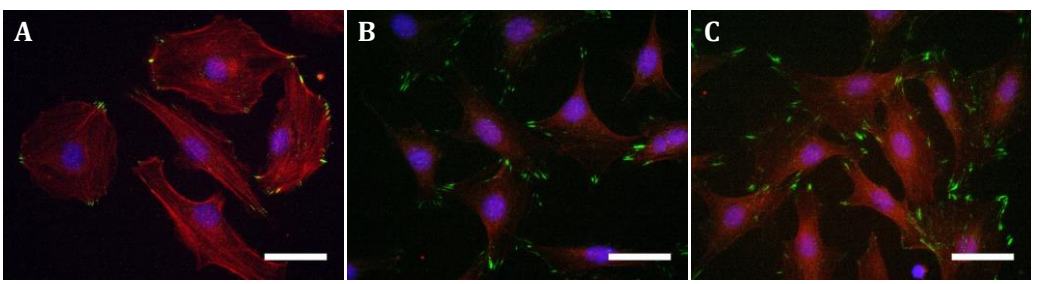

Figure 67. Representative fluorescence microscopy image of NIH/3T3 fibroblast cells plated on (A) BCP medium, (B) BCP small (C) RandomCP after c(RGDfK)-PEG$_3$-NH$_2$ ligand functionalization and BSA passivation under starving conditions (nuclei in blue, actin fibres in red and focal adhesion contacts in green) (scale bar, 25 μm).

Cell morphology descriptive parameters (spresding area, circularity, roundness and solidity) were evaluated and results are shown in Figure 68. The projected cell area was analyzed and no significant differences were noticeable after 4 h of cell culture. Noticeable, cell spreading was more homogeneous on BCP small surfaces, which showed a reduced variability in values of the projected cell areas. Solidity, circularity and roundness of adhered fibroblast shown no statistically significant differences among the ligand presenting surfaces. However, an increasing tendency in circularity was observed for the scattered

Unlike cell morphology parameters, focal adhesion formation exhibited clear differences depending on the spatial distribution of RGD ligands at the nanometer scale. The number of focal adhesion contacts per cell was almost doubled in BCP small and RandomCP when compared with BCP medium surfaces (Figure 69). Moreover, among BCP small and Random CP surfaces, focal adhesions were significantly more mature (focal adhesion area>1 μm^2) on the BCP small. Hence, in agreement with literature[263], focal adhesion formation and maturation is highly influenced by ligand spacing, and the closest ligand spacing presented by

BCP small surfaces promoted the formation of focal contacts and their maturation (Figure 69).

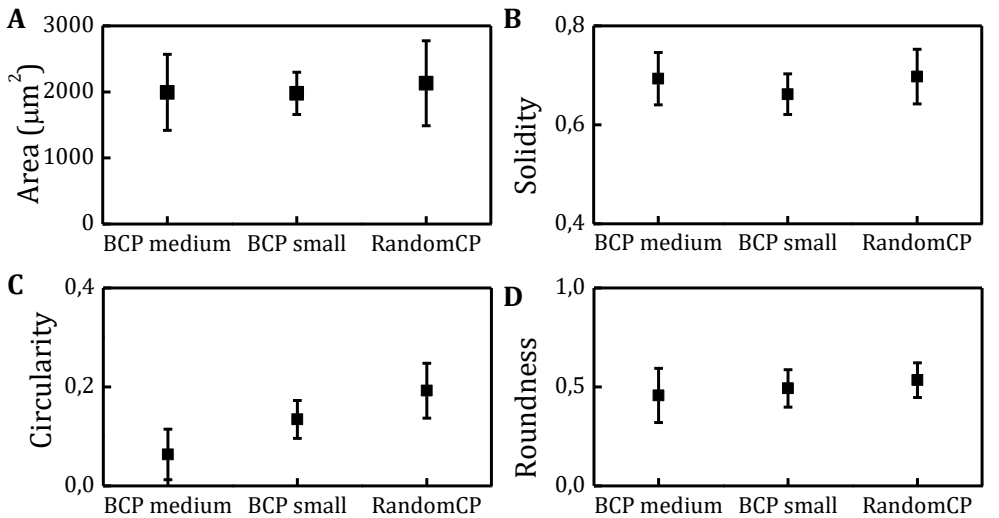

Figure 68. Morphological parameters of adhered cells on top of covalently bound c(RGDfK)-PEG₃-NH₂ peptide presented on BCP medium, BCP small and RandomCP. (A) Projected cell area, (B) solidity (C) circularity and (D) roundness of NIH/3T3 fibroblast after 4 h of cell culture (significance level tested p<0.05; error bars represent the standard deviations)

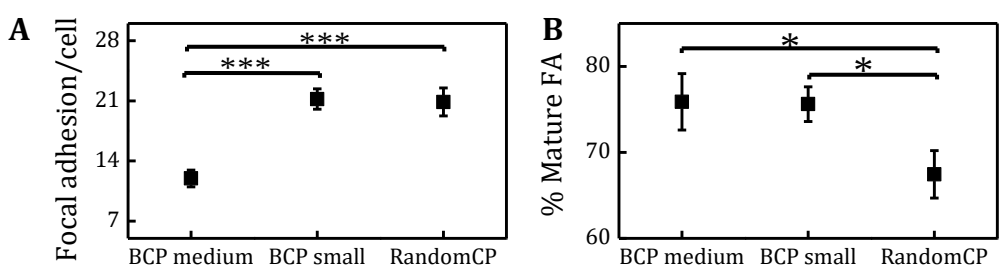

Figure 69. Focal adhesion analysis. (A) Number of focal adhesion per cell and (B) % of mature focal adhesions found after 4 h of cell culture in starving medium on c(RGDfK)-PEG₃-NH₂-functionalized BCP medium, BCP small and RandomCP thin films (: significance level p<0.001; error bars represent the standard error of the mean).***

Roca-Cusachs *et al*. discovered that integrin clustering caused a 7-fold increase in ligand adhesion strength through two mechanisms: the recruitment of cytoplasmic proteins that stabilized the focal adhesion complex and the increase in lateral integrin interactions. Our experiments show that focal adhesion maturation is favored by an aggregated ligand configuration as demonstrated by the 10% increase in mature focal adhesions found on BCP medium and BPC small surfaces compare with a random distribution (Figure 69 B). These results suggest that multivalent ligand presenting configurations could enhance integrin

reattachment, reduce their diffusion and thus, mediate stable integrin clustering at the cell membrane laying the foundation of the focal adhesion complex.

In this section, the nanopatterned platforms were validated by the study of focal adhesion formation. The results obtained were in excellent agreement with reported findings that indicate the primordial effect of interligand spacing in receptor signaling. .[69,71,150,200]

Notably, the developed ligand presenting surfaces provide a highly precise and well-characterized tool to study cell receptor processes. However, a countless relevant information about the cellular response is lost in every experiment due to a suboptimal evaluation of the cell behavior. Cell adhesion and spreading were analyzed by cell fixation and immunostaining at a single time point. The precious improvement in ligand presenting strategy should be complemented with a powerful technique that enable the quantitative evaluation of ligand-receptor interactions over time to get the most out about the study of cell response.

4.8. EphB2 receptor clustering dynamics

EphrinB1 ligand and EphB2 receptor are membrane-bound proteins involved in cell-cell interactions that, upon mutual recognition over neighboring cell membranes, form aggregates. These ligand-receptor clusters trigger the forward and reverse signaling responsible of cell attractive or repulsive interactions, cell proliferation, tissue boundary formation, cell migration or axon guidance (Figure 70).[9,213,233]

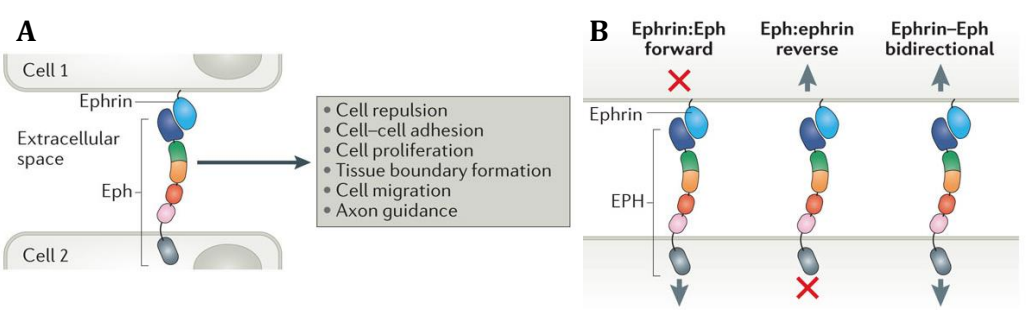

Figure 70. Eph receptors and ephrin ligands located at the cell of neighboring cells (A) direct several cellular processes through multidirectional signaling cascades including (B) forward signaling, reverse signaling or bidirectional signaling. Adapted with permission from [314] Copyright 2016. Nature Publishing Group.

In vitro experiments confirmed the capability of cells to respond variably to differentially oligomeric ephrinB1.[208] EphB2 receptor is only activated, if the

ephrinB1 ligand is presented in a membrane bound or oligomeric form.[315] A common strategy to get ligand-oligomers is through antibody-mediated clustering. For this purpose, it is widely used a disulphide-linked immunoglobulin Fc fusion form of ephrinB1 (ephrinB1/Fc), which forms dimers.[316] These dimers can form oligomers upon antibody-mediated clustering (anti-Fc antibody). It has been reported that EphB1 receptor phosphorylation was stimulated by the dimeric form of the ligands, ephrinB1/Fc, but cell attachment required multimeric clusters of ephrinB1, being tetramers enough to promote it.[208]

Eph-ephrin signaling microclusters (large-scale molecular assemblies) act as positional cues in tissue patterning during development by regulating cell adhesion and repulsion, depending on the degree of clustering (size and lifetime), activation and phosphorylation.[214,219] In recent years, the assembly, transport and internalization of such large-scale receptor molecular assemblies have been studied by the so-called spatial mutation technique, developed by the group of Prof. Groves.[10] The spatial mutation technique restricted the movement of the ligands to confined squared areas of 0.5 to 20 μm in lateral dimensions.[231,317] It has been reported that the physical manipulation of the organization of ephrinA1–EphA2 microclusters (high-order clusters) alters the cellular response to the ligand. In a more recent report, the same group has shown that arrays of gold nanodots presenting immobilized ligands also frustrate the transport of EphA2 microclusters.[234] However, despite it has been reported that receptor membrane domains with dimensions ranging from 10 to 200 nm, thus involving low order clusters or oligomers, mediate the spatial regulation of receptor signaling,[234,318] the dynamics of receptor clustering at this nanometer scale has barely been investigated.

Receptor clustering and signaling is highly modulated by ligand presentation, which can be tuned to foster cell response. As mentioned before, for decades soluble monomeric ephrin ligands have been regarded as ineffective for Eph receptor activation[315]. However, diffusive ligands in supported lipid bilayers as well as synthetically crosslinked ephrins have reported as capable of fully activate receptor oligomerization[216,231,232,319]. Herein we investigate receptor oligomerization dynamics of soluble and surface-bound ligand presentations. As ligand presenting surfaces, we tested: antibody-mediated clusters of ephrinB1 (in its dimerized form, ephrinB1/Fc) randomly attached to a PLL coated surface (AB-conjugated ephrinB1/Fc), ephrinB1/Fc randomly bound to a PLL-coated surface,

and surface-mediated nanoclusters of ephrinB1/Fc resembling the underlying block copolymer template. Thanks to surface bound ligand configuration, a stable input can be given to cell membrane receptors while a dynamic output, such as the receptor clustering and activation process, is thoroughly analyzed.

Our nanoscale patterned approach has the potential to provide insight into the roles of nanopattened-ephrinB1/Fc ligand presenting surfaces in EphB2 clustering and signaling. The nanopatterned ligand presenting platform that has been fabricated and characterized, will be employed in the following sections for this purpose. An important aspect to consider is the highly dynamic nature of the oligomerization and downstream signaling processes. Initially, receptors are aggregated into small oligomers that laterally diffuse in the cell membrane.[6] For the accurate tracking of these diffusive nanometric entities, an imaging technique with a high spatio-temporal resolution is mandatory. To account for these requirements, a novel and enhanced image analysis technique was applied. However, such an image technique had been never be applied to surface-bound nanopatterned ligands. Therefore we found primordial understanding the oligomerization and signal transduction dynamics of EphB2 receptors using the new imaging set up while stimulating the cells through the standard methodology in the field: AB-clustered EphrinB1/Fc aggregates administered as soluble ligands.

4.8.1. EphB2 receptor oligomerization analyzed by enhanced Number and Brightness techinque

The current model explaining Eph activation and clustering phenomena points out that the presentation of an ephrin dimer nucleates an Eph dimer in the adjacent cell membrane, activating the receptor by the resulting trans-phosphorylation.[208,320–322] Activated receptors then propagate the signal by recruiting neighboring monomers into oligomers and large-scale clusters (Figure 71).[213,214,319,322] The termination of the signal is produced by the endocytosis of the receptor clusters. This model presents a simple signaling scheme which barely explains some complex signal integration. It is unknown how such monotonic growth kinetics is able to sense and transduce different ligand concentrations or to identify the stoichiometry of the actively signaling Eph receptor complex[207,323]. For instance, during neuronal axon growth the initial miscellaneous location of Eph- and ephrin-expressing cell subpopulation is progressively altered by cell-cell contact and ends up in segregated populations.[324] This cell sorting is presumed to be caused by the cell reorganization to minimize Eph-ephrin repulsive

interactions.[325] Unfortunately, there are still unanswered questions regarding the onset and progression of signaling processes, such as, how the dynamic process of receptor clustering is able to orchestrate a modulated cell response that directs such large variety of downstream functions.[326]

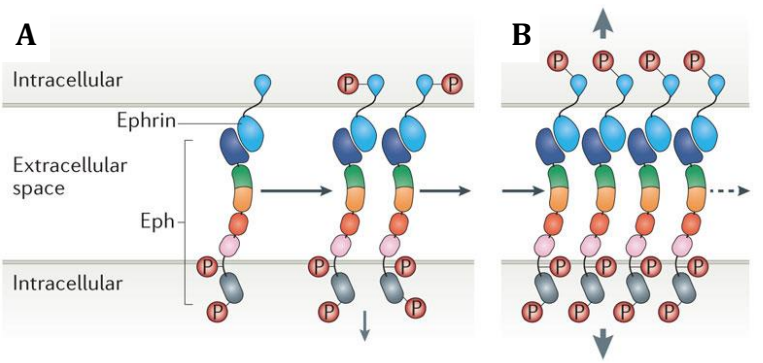

Figure 71. Oligomerization process. (A) The binding of an ephrin monomer to an Eph receptor nucleates the formation of an ephrin–Eph heterotetramer that initiates signaling. (B) This leads to the formation of higher-order clusters through the recruitment of freely diffusing receptors (not shown) or other ligand-bound Eph receptors (Tyr phosphorylation events are also illustrated). Adapted with permission from [314] Copyright 2016. Nature Publishing Group.

Conventional imaging tools are unable to answer these intricate questions, as they require not only molecular-level sensitivity over the area of an entire cell, but also temporal scales ranging from msec-sec times (over which receptor dynamics take place), to tens of minutes (over which cell responses are manifested). To unveil the oligomerization and signal transduction dynamics during Eph-ephrin signaling we integrated quantitative imaging and modeling.

Receptor aggregation was studied in transgenic human embryonic kidney 239T cells (HEK29T3) stably expressing the fusion protein EphB2 mRuby. The fluorescence signal was localized at the cell membrane, as shown in Figure 72.Figure 72 Only mRuby positive cells were selected by cell sorting to perform the cellular assays.

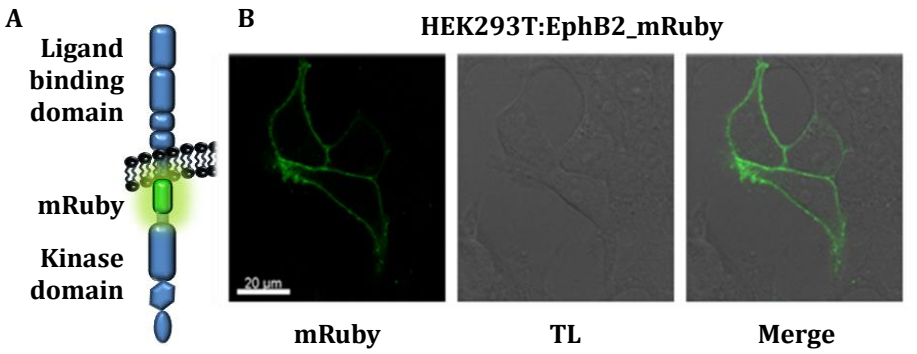

Figure 72. Transgenic cell line. (A) Domain structure of EphB2 where the ligand binding domain and the kinase domain are illustrated. (B) Fluorescent (mRuby) and transmitted light (TL) images of HEK293T cells transiently expressing EphB2_mRuby.

For quantitative imaging, an enhanced in-house developed version of Number and Brightness (N&B) analysis technique was implemented.[236] This method exploits the fluorescence fluctuations caused by short term variations in intensities of each pixel in an image. Conventional N&B analysis assumes that the fluorescence fluctuations are directly related to the molecular aggregation state, i.e. brightness, of the molecules. Therefore, it calculates the median oligomeric species of the protein out of the diverse species present in that pixel over a limited time window.[276,327] The enhanced Number and Brightness (eN&B) employs a statistical resampling method that provides the full histogram of receptor aggregation (i-mer distribution) within each pixel of an image (105 nm) over multiple time points instead of the single mean brightness value per pixel calculated by the conventional N&B (Figure 73). This version of the method broadens the temporal scale from seconds to tens of minutes. Cells were imaged using Total Internal Reflection Fluorescence (TIRF) microscopy, yielding high signal-to-noise images of cell membranes as they interacted with the ligand-functionalized surfaces. This approach offered the needed pixel size and temporal resolution required for eN&B analysis.

Figure 73 shows the fluorescence intensity fluctuations for two representative pixels, one from an AB-conjugated ephrinB1/Fc- stimulated cell (red line) and another from a control cell (black line). The collected data showed that fluctuations in fluorescence intensity increase their amplitud and decrease in their frequency when cells are stimulated with soluble ligands over the analyzed period of time (60 min).

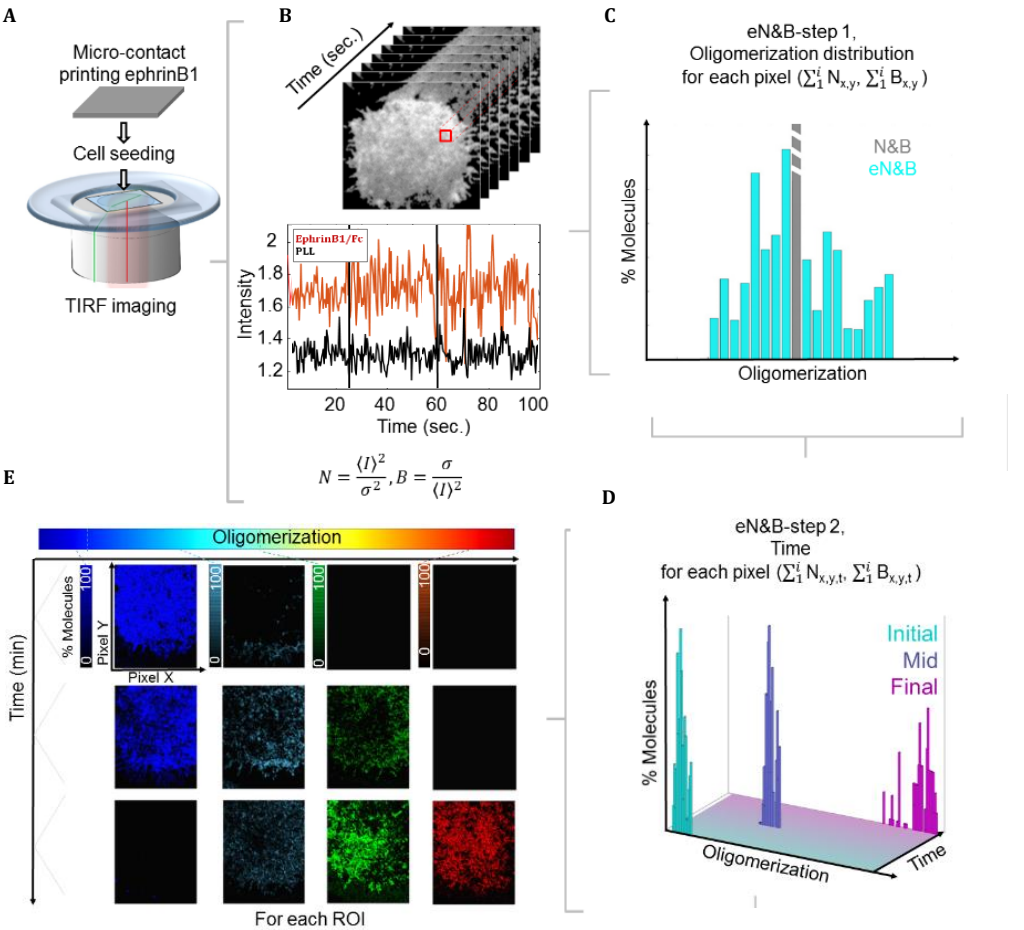

Figure 73. Enhanced Number and Brightness (eN&B). A) N&B protocol extended over n time points. For every time point a batch of 200 images was acquired at 2 Hz; subsequent time points were separated by approximately 5 min over a 60 min period. B) Fluorescence intensity fluctuations from single pixels at initial, mid and final experimental time points of cells cultured on AB-conjugated ephrinB1/Fc (red line) or poly-L-lysine (black line). C) Oligomeric distribution in each pixel achieved by statistically resampling 100 images out of the complete 200-image batch; the apparent number of molecules (N) and the brightness values (B) were calculated for each pixel in the image. D) Enhanced pixel brightness distributions englobed in a matrix containing the distribution of brightness species for every pixel in the image. The histogram ilustrate the brightness distributions of a single pixel at three different time points.

Those fluctuations yield the apparent Brightness (B) in the N&B analysis, which is calculated from the intensity signal of the TIRF image as:

$$B = \frac{\sigma^2}{\langle k \rangle} \qquad \textit{Eq. 4}$$

Where σ^2 is the intensity variance and $\langle k \rangle$ is the average intensity. Brightness values can be converted to mean oligomer sizes (i-mer number or number of monomers composing the oligomers) (Figure 73 C, grey central column) by by

linearly scaling the brightness value of the receptor in its monomeric form (Figure 74), which is experimentally obtained from the TIRF images of cells non-stimulated with ligands ($B_{monomer}$=1.17, relative to the background signal, this being $B_{background}$=1.00).

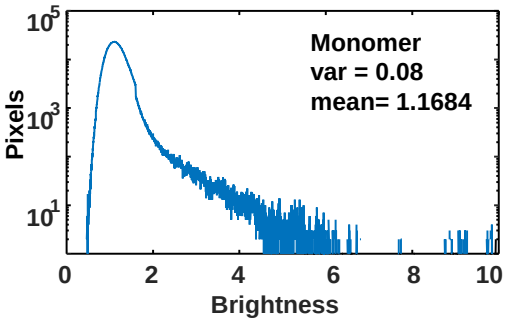

Figure 74. Monomer brightness used for calibration. Brightness distribution combined for N=4 cells plated on poly-L-lysine coated plates with no additional treatment (average brightness and variance are indicated).

By the enhanced mathematical algorithm (eN&B), the full histogram of receptor aggregation (oligomerization distribution) within each pixel of an image is obtained (Figure 73 C, blue histogram). Moreover, by performing the same operation over multiple time points, the oligomeric distribution of each pixel over time (oligomerization dynamics) can be determined (Figure 73 D). With this information, oligomerization maps that show in real time the aggregation state of the receptor can be obtained from time-lapse videos acquired in TIRF mode (Figure 75).

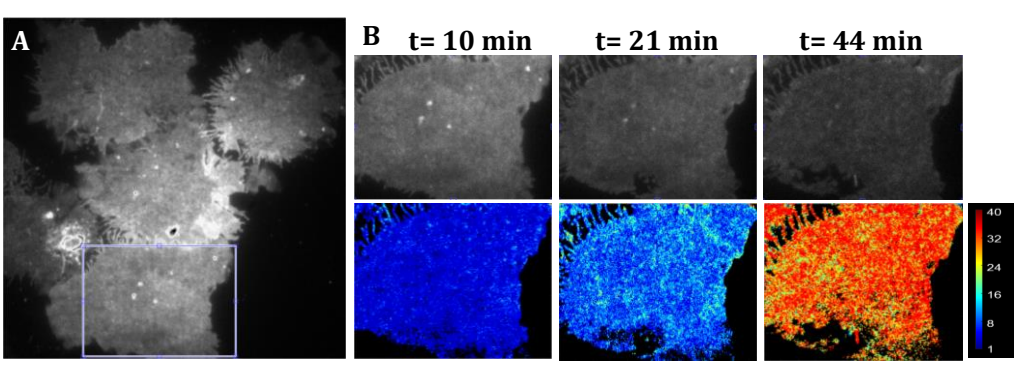

Figure 75. A representative TIRF image of (A) a group of five HEK293T cells expressing EphB2_mRuby cultured on an ephrinB1/Fc presenting surface coated with Poly-L-lysine. The purple square delimits the selected area to perform enhanced Number and Brightness analysis (eN&B). (B) Time-lapse images of the selected cell at 10, 21, and 44 min post-stimulation (first row) and the corresponding oligomerization maps provided by the eN&B technique (second row).

By this methodology, despite grey scale images of stimulated and unstimulated cells showed little variations over time (Figure 75), the corresponding brightness maps extracted by eN&B analysis reflected the efficient induction of EphB2 clustering on cells presented with ephrinB1. It can be see that upon stimulation with soluble AB-conjugated ephrinB1/Fc (Figure 76), receptor cluster distribution over the cell surface was heterogeneous and small number of large aggregates species were visualized on the oligomerization maps. In contrast, on unstimulated cells (anti-Fc antibody was used as control for these experiments) brightness state remains mainly uniform over time (Figure 76).

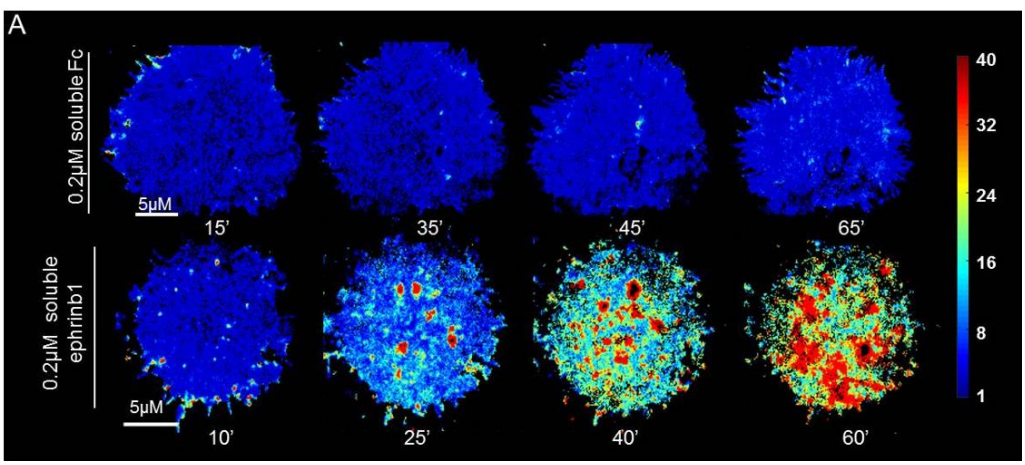

Figure 76. eN&B analysis of EphB2 clustering using soluble ligand stimulation. Time-lapse oligomerization maps of HEK293T:EphB2_mRuby cells were stimulated with 0.2μM Fc or 0.2μM ephrinB1 in solution. The weighted average i-mer species is color-coded according to the color bar.

The average oligomerization of EphB2 receptor at 60-min post-stimulation with soluble AB-conjugated ephrinB1/Fc (imer= 21.7±0.9) was significantly higher ($p<0.01$) than cells stimulated with AB-conjugated Fc (imer= 6.5±0.4) (Figure 77). Such averaged results indicate that receptor clustering was strong and specific to cells presented with ephrinB1. The eN&B analysis over time extracted a complete time-evolution plot of oligomers found in the illuminated cell membrane (i-mer plot). It revealed an orderly progression of Eph receptor aggregation after stimulation with AB-conjugated ephrinB1/Fc over the 60 minutes of observation (Figure 77). Oligomer curves are organized in an extraordinarily synchronized order over time according to their size.

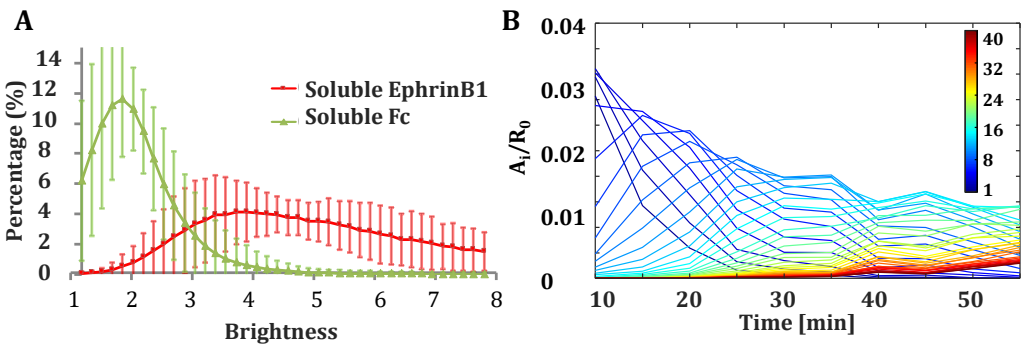

Figure 77. Oligomerization kinetics upon soluble AB-conjugated ephrinB1/Fc stimulation. (A) Relative distribution of average and standard deviation oligomerization values for multiple cells ($N_{ephrinB1}$= 40, N_{Fc}= 22) presented with the relevant ligand for 60 minutes. (B) i-mer evolution plot. Evolution of the concentration of each aggregate (Ai) over time from the cell in (Figure 76) stimulated with ephrinB1 in solution, normalized by the initial concentration of free receptor (R0). i-mer values are color-coded according to the color scale bar.

Initially low-ordered species dominate (monomer to pentamer) and within the first 30 min they promptly decreased leading to sequential appearance of intermediated-order species. A common profile is visible for each oligomeric state defined by an initial increase of relative abundance followed by a progressive decrease which drives the emergence of the immediately higher order i-mer curve (Figure 77 B). The eN&B analysis denotes that EphB2 clustering keeps increasing progressively over 60 min despite de fast depletion of the receptor monomer population. Therefore, higher order EphB2 oligomers cannot be assembled by the recruitment of EphB2 monomers, but, by the recruitment of small oligomers into larger complexes. [232]

To better understand the role of clustering dynamics and tyrosine kinase (TK) activation, we performed Western blot densitometry to measure the amount of phosphorylated EphB2 upon stimulation with several concentrations of ab-clustered ephrin/Fc ligands in solution. A dose-response curve showed an asymptotic profile of EphB2 activation kinetics (Figure 78). For all the concentrations within the broad range tested (two orders of magnitude) the receptor phosphorylation was quickly triggered during the initial 15 min after stimulation. Thereafter, the phosphorylation kinetics slows down and approaches saturation asymptotically at times around 30 to 45 min post-stimulation. EphB2 receptor phosphorylation shows a concentration-adapted response, with higher amount of phosphorylated receptors under the presence of higher concentrations of ephrinB1 ligands.

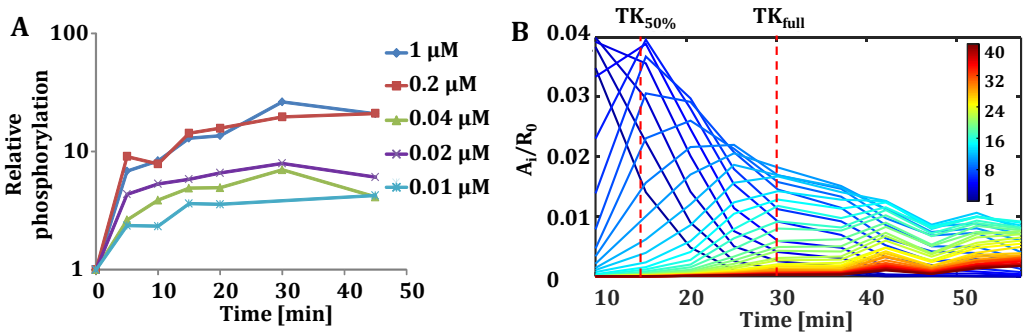

Figure 78. EphB2 activation kinetics. (A) EphB2 dose-response phosphorylation curve of cells stimulated with different soluble AB-conjugated ephrinB1/Fc concentrations measured by western blot densitometry. (B) i-mer evolution plot. Evolution of the concentration of each aggregate over time from the cell stimulated with ephrinB1 in solution. The i-mer value of every curve is color-coded according to the color scale bar. $TK_{50\%}$ and TK_{full} indicate the time point where 50% and the entire receptor population is phosphorylated, respectively.

Notably, these kinetics indicate that receptor activation and signaling primarily occur when low-order oligomers predominate (Figure 78 B). In fact, half-maximal or full (asymptotic) tyrosine kinase activation occur when hexamers ($TK_{50\%}$=6.6±3.6) or octamers (TK_{full}=8.5±4.6), respectively, are the mean oligomers in the population. This implies that all receptors are activated when intermediate-order or high-order oligomers are formed. Therefore, the later appearance of oligomers of 40-mers and beyond indicates that activation is decoupled from this high-order clustering. Receptor clustering did not show a saturation level probably thanks to continuous condensation of large aggregates.

4.8.2. Multivalent surface-bound nanopatterned ligands foster receptor oligomerization.

The oligomerization process has been studied by the use of AB-conjugated ephrinB1/Fc ligands in soluble configurations. Hexamers to octamers of EphB2 receptor have been identified as the actively signaling complexes triggering the half-maximal and full activation of the TK activity. However, and although ligand clustering is essential to trigger receptor signaling, it is still unclear if receptor oligomerization dynamics can be actually tuned by the ligand spatial distribution. Coherently, the interaction between multivalent ligands and receptor complexes has not been evaluated with molecular-level resolution.

A variety of tools have been designed to tailor ligand configuration at the nanometer scale and induce multivalent ligand-receptor interactions. The multivalent presentation of soluble ephrin ligands was investigated in conjugation

with DNA origami-based nanostructures called nanocalipers. Nanocalipers presenting ephrin dimers spaced 42.9 nm rapidly activated Eph receptor phosphorylation. In contrast, when ephrin ligands where spaced 100 nm, nanocaliper stimulation had no effect on receptor phosphorylation.[216] Another approach showed efficient stem cell differentiation into neurons when multivalent ephrin-hyaluronic acid conjugates were delivered in solution. Even more relevant, such multivalent conjugates promoted neurogenesis *in vivo*, in contrast with traditional antibody-mediated ligand clustering methodologies.[215]

However, the limited availability of methods providing single molecule sensitivity in the membrane of living cells hinders the quantification of the receptor complex stoichiometry upon multivalent stimulation. In this section, we take advantage of the advanced eN&B analysis to measure the EphB2 oligomerization process in live cells. In contrast with soluble configuration, we have developed a platform that produces ephrin-Eph receptor multivalent interactions through nanopatterns of surface-bound ephrin ligands.

EphrinB1/Fc ligands, either as dimers or as AB-conjugated ephrinB1/Fc aggregates were microcontact printed on poly-L-lysine (PLL) coated surfaces leading to random distribution of ligand molecules over the surfaces. In parallel, nanostructured diblock copolymer thin films were used as templates for nanopatterning of ephrinB1/Fc ligands in a surface-mediated clustered manner. EphrinB1/Fc presenting surfaces were characterized by AFM in liquid. Microcontact printed AB-conjugated ephrinB1/Fc appeared on the surface as extended conglomerates covering the majority of the surface area (~89%) (Figure 79 A). The corresponding height profiles show an uneven topography resulting from the successful conjugation of EphrinB1/Fc with the anti-Fc antibody to form aggregates. EphrinB1/Fc ligand displayed a random distribution with an intricate morphology over the surface (~67% functionalized area). The height profile exhibited topographic features of 6 nm in height, which correspond to the size reported for the ephrin protein.[208] This height value is smaller than the one found on the AB-conjugated ephrinB1/Fc which, due to the additional contribution in size of the AB, showed features between 10-20 nm in height.

A more sophisticated ligand distribution was achieved on self-assembled diblock copolymer thin films. BCP medium thin film was decorated with ephrinB1/Fc to induce multivalent ligand-receptor interactions. EphrinB1/Fc

were covalently bound to PMMA cylindrical domains following the functionalization procedure described in Section 4.6. AFM images showed ephrinB1/Fc clusters as discrete aggregates with a main diameter of 24±1 nm and a first neighboring distance between clusters of 58.3±0.7 nm (Figure 79 C). The mean functionalized area is a 9.3±0.5%, which implies that a 42.3% of the total PMMA available surface has been successfully functionalized.

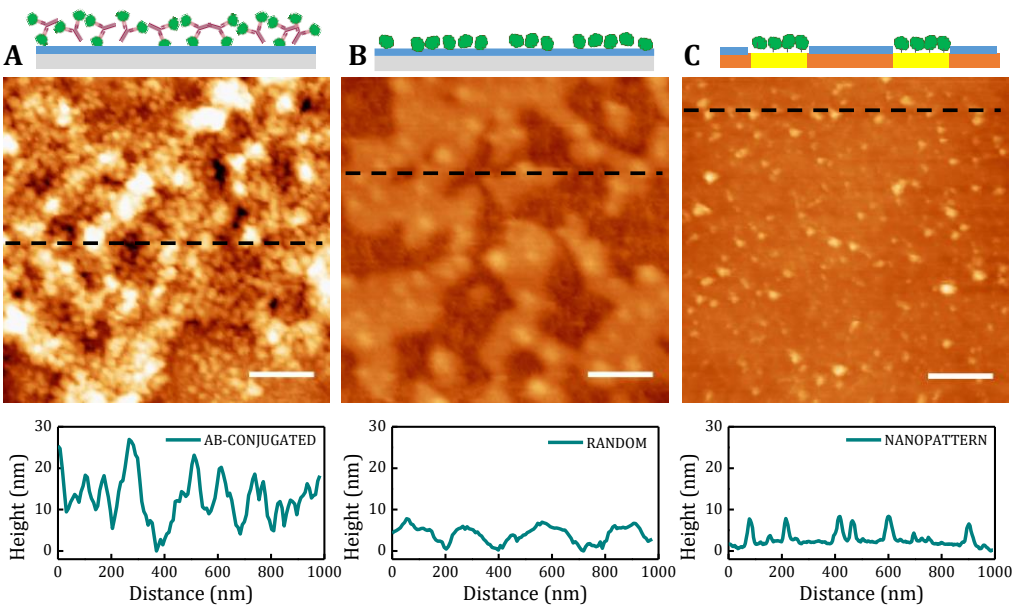

Figure 79. EphrinB1/Fc ligand presenting surfaces characterized by AFM. Schematic representation, topographic AFM image and height profile of A) Ab-conjugated ephrinB1/Fc microcontact printed on PLL coated coverslip. B) EphrinB1 ligand microcontact printed on PLL coated coverslip in a random fashion and C) covalently bound ephrinB1/Fc in a clustered configuration following nanopatterned BCP template. The dashed line indicates the location of the height cross section. (Scale bar: 200 nm, Z-scale: 25 nm).

We further explored surface-bound ephrinB1/Fc distribution by N-STORM (Figure 80). Immobilized ligands were properly recognized by the fluorescence antibodies in the three configurations: AB-conjugated ephrinB1/Fc randomly deposited on a PLL coated coverslip, ephrinB1/Fc randomly deposited on a PLL coated coverslip and ephrinB1/FC nanopatterned on BCP medium thin films. The fluorescence images acquired by conventional fluorescence microscopy showed a decreasing value of the average fluorescence intensity from AB-conjugated ephrinB1/Fc to random ephrinB1/Fc and ephrinB1/Fc nanopatterned surfaces (Figure 80, FLUORESCENCE ROW and Figure 81). These qualitative results suggested a higher surface density of immobilized ligands on the AB-conjugated ephrinB1/Fc functionalized substrate. However, this conventional technique

cannot spatially resolve the location of surface-bound ligands at the nanometer length scale.

For this purpose, samples were imaged using STORM microscopy. The information extracted from reconstructed super-resolution images was perfectly matching the AFM findings. Large ephrinB1/Fc ligand aggregates were observed on microcontact printed ephrinB1/Fc surfaces (AB-conjugated and random) (Figure 80). Moreover, STORM analysis consistently confirmed a nanoscale spatial organization of clusters restricted in size on BCP medium surfaces (Figure 80).

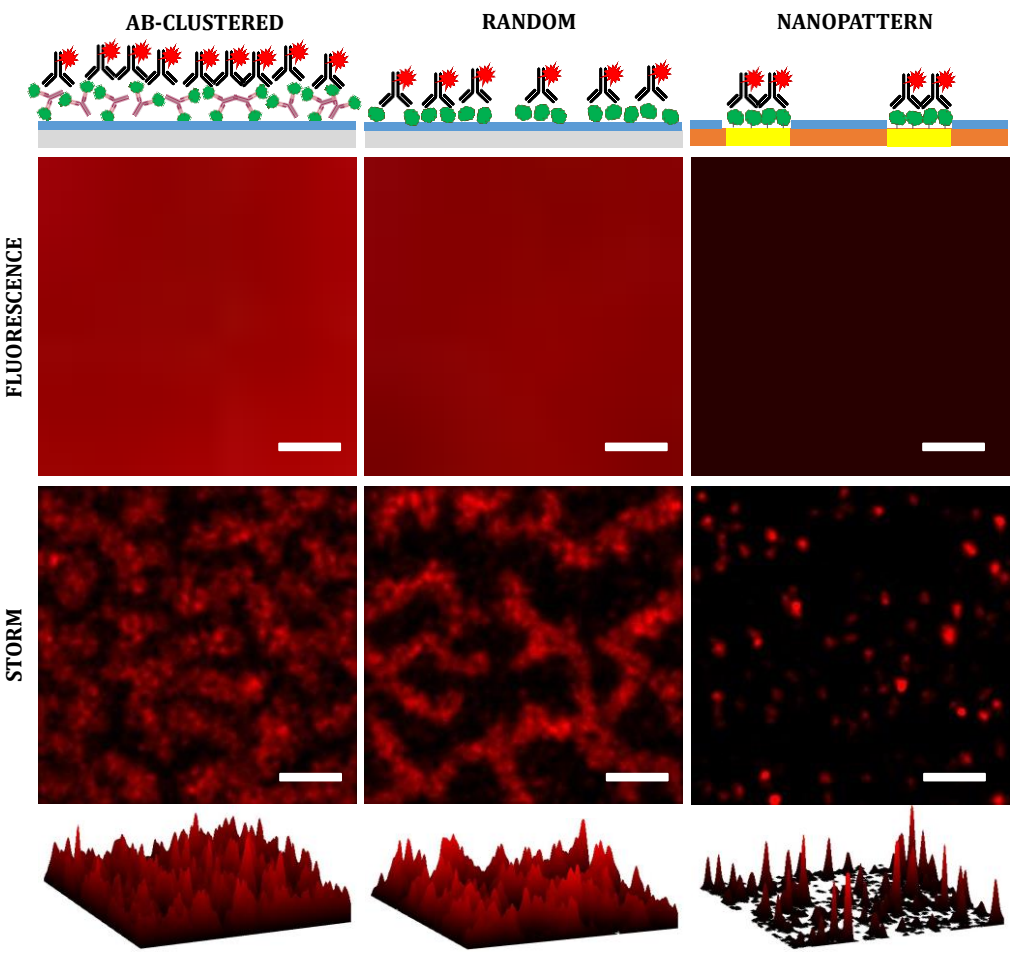

Figure 80. N-STORM analysis of surface–bound ephrinB1/Fc immunostained with goat anti-human IgG Alexa Fluor® 647 antibody. N-STORM images of A) Ab-conjugated ephrinB1/Fc microcontact printed on PLL coated coverslip. B) EphrinB1 ligand microcontact printed on PLL coated coverslip in a random fashion and C) covalently bound ephrinB1/Fc in a clustered configuration following nanopatterned BCP template (Scale bar, 400 nm).

The mean average diameter of the nanoclusters was measured as 27±19 nm, in agreement with the AFM measurements. Assuming that the size of the monomeric ephrinB1 proteins is 4.8x3x5.6 nm,[328] each nanocluster contains ~18 ephrinB1/Fc dimers, leading to a surface density of ~2500 ephrinB1/Fc ligands/μm^2. EphrinB1/Fc molecules were selectively located at the PMMA domains of the BCP medium thin films. The functionalized nanodomains restricted the global density whereas increases the local concentration of available ligands.

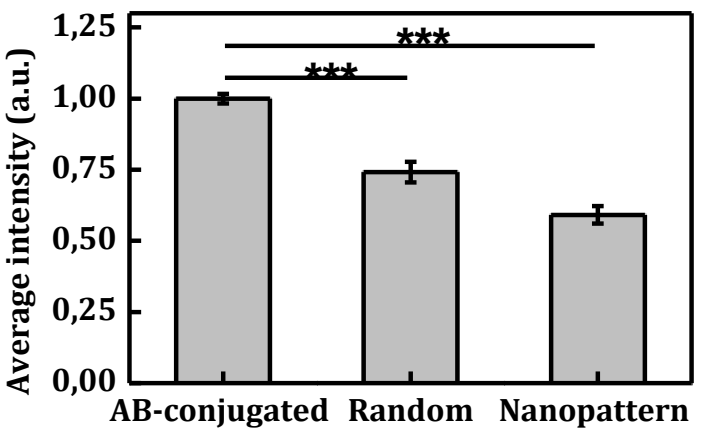

Figure 81. Average fluorescence intensity of immunostained Ab-conjugated ephrinB1/Fc microcontact printed on PLL coated coverslip, ephrinB1 ligand microcontact printed on PLL coated coverslip in a random fashion and covalently bound ephrinB1/Fc in a clustered configuration following nanopatterned BCP template. Statistically significant differences were found between the three functionalized surfaces.

Human embryonic kidney 293 (HEK293T) cells stably expressing EphB2 receptor labelled with mRuby were seeded on both ligand presenting surfaces. The fluorescence fluctuation of EphB2 receptors in live cell membranes upon interaction with the ligand-functionalized substrates was obtained using Total Internal Reflection Fluorescence (TIRF) time-lapse microscopy.

Figure 82 shows the TIRF images and corresponding oligomerization maps acquired from cells seeded on surface-mediated nanopatterns of ephrinB1/Fc dimeric ligands (panel A) and on surfaces with a random distribution of the same ligands (pamel Bl) at 10 min and 60 min post-ligand stimulation. For the time-lapse videos of the full oligomerization process on ligand stimulated cells, se Supplementary Information. At this point it is important to notice that ephrinB1/Fc dimers are not recognized to be effective in receptor clustering when administered in soluble form. The red color recorded on ligand nanopatterned substrates after 60 mins of substrate-cell contact denote a strong receptor

clustering into high-order oligomers. In contrast, at an equivalent time-point, low levels of stimulation were achieved by randomly-functionalized substrates. Both poly-L-lysine coated surfaces used as control substrates for the nanopattern (panel C) and the random (panel D) configurations showed blue color maps, corresponding to no relevant oligomerization at either 10 min or 60 min.

Complementarily to oligomerization maps, average brightness values and their correspondent equivalents to oligomerization state were calculated, thus leading to the values of mean oligomerization cluster size for each time point and ligand pattern presentation (Figure 82 E). After 60 min of stimulation with the ligand, the cells on the nanopatterned surfaces presented average oligomerization values (B_{NANO} = 26.3±0.4), significantly higher than cells stimulated without the nanopatterning (B_{RANDOM}= 11.4±0.1). The significantly lower average brightness values for both substrates in the absence of the ligand ($B_{NANO\text{-}PLL}$ =10.6±0.2 and $B_{RANDOM\text{-}PLL}$= 6.1±0.1) demonstrated the specificity of the EphB2 aggregation response to the presence of the ephrinB1/Fc ligand. When looking at the final distribution of oligomeric species at 60 min after stimulation, the nanopatterned surfaces showed a broad Gaussian distribution centered at 19-mers with negligible presence of low-order oligomers (< 5-mers) (Figure 82 F). On the contrary, the same ligand (ephrinB1/Fc dimers) presented randomly on the glass surfaces produced a distribution displaying a narrower peak centered at 9-mers, which includes a significant population of low-order oligomers (< 5-mers). Such low-order oligomers are dominant for both substrates not presenting the ephrinB1/Fc ligand.

Stein et al. suggested the possibility of producing ephrin ligand oligomers able to stimulate the oligomerization and signaling of Eph receptors through their immobilization on surfaces, as an alternative to antibody-crosslinking[207]. Our results reveal that surface-bound ephrinB1/Fc ligands immobilized on surfaces are not enough to produce an effective EphB2 receptor clustering. However, when the same ligands are presented in a nanopattern configuration created through the diblock-copolymer technology, they form areas with high local density of closely packed ligands. In this configuration, the ligands have the capability of inducing surface-bound receptor clustering.

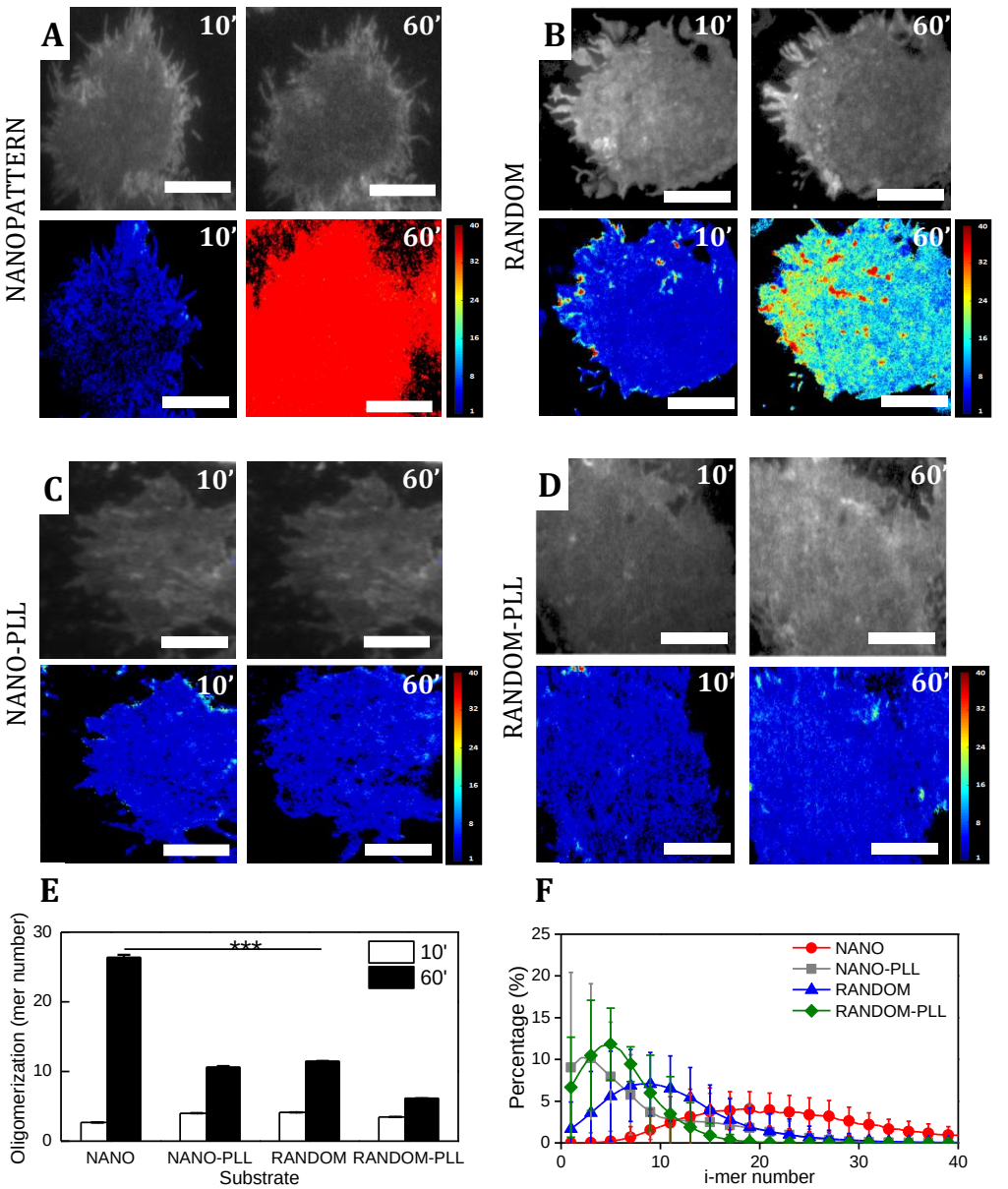

Figure 82. eN&B analysis of EphB2 clustering of HEK293T cells over ephrinB1/Fc dimer ligands in a nanopatterned (A)), random (Bl) fashion and their controls (C and D). TIRF images and corresponding oligomerization maps acquired at 10 min and 60 min of stimulation on: surface-mediated nanopatterned ephrinB1/Fc ligands on BCP medium thin films backfilled with poly-L-lysine (NANOPATTERN), poly-L-lysine coated BCP medium thin films (NANO-PLL), randomly distributed ephrinB1/Fc on poly-L-lysine coated glass coverslips (RANDOM) and poly-L-lysine coated glass coverslips (RANDOM-PLL). The colour code indicate the average i-mer species of EphB2 clusters. (E) Average oligomerization values (obtained from brightness values) at time 60 min for the four tested substrates. F) Distribution of average and standard deviation oligomerization values for multiple cells at time 60 min for the nanopatterned (red) and randomly distributed (blue) surface-bound ligands. ($N_{NANOPATTERN}$= 10, $N_{NANO-PLL}$= 15, N_{RANDOM}=19, $N_{RANDOM-PLL}$= 6). The pol-L-lysine substrate used as controls are the green and the grey line.

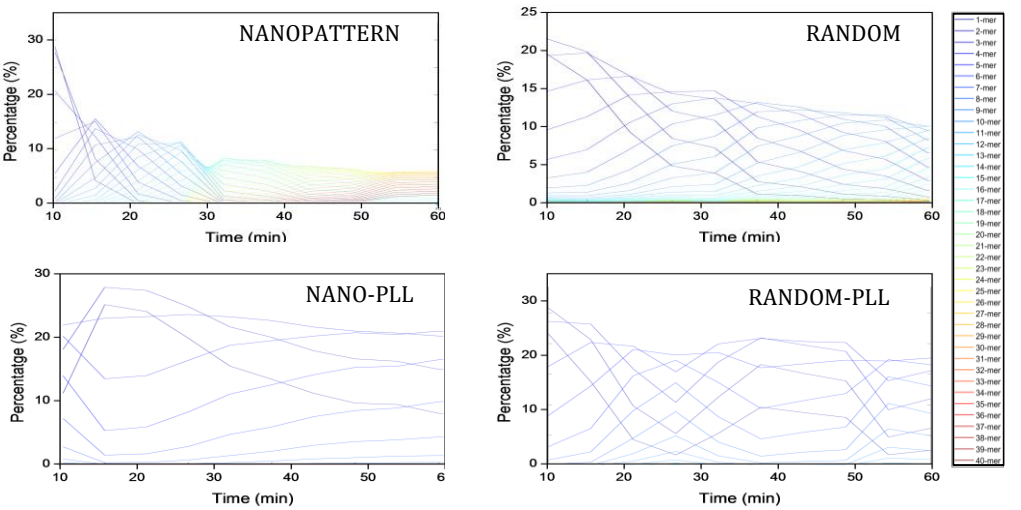

Figure 83. i-mer evolution plot of cells cultured on different ligand presenting surfaces. Percentages of each aggregates (i-mers) over time normalized by the initial concentration of free receptoror cells plated over ligand presenting surfaces: surface-mediated nanopatterned ephrinB1/Fc ligands on BCP medium thin films backfilled with poly-L-lysine (NANOPATTERN), poly-L-lysine coated BCP medium thin films (NANO-PLL), randomly distributed ephrinB1/Fc on poly-L-lysine coated glass coverslips (RANDOM) and poly-L-lysine coated glass coverslips (RANDOM-PLL). i-mer values are color-coded according to the color scale bar.

The evolution of the receptor oligomeric species over the 60 min of time frame considered is plotted in Figure 83. Each curve corresponds to the evolution of individual oligomeric species (i-mer plot), color-coded according to their increasing number of monomers. The nanopatterned surface shows the formation of low-order oligomers that disappear over the time giving rise to higher-order oligomeric species, which are the predominant species by the end of the experiment. This happens in an astonishing synchronized way. However, the i-mer plot corresponding to the random ligand disposition evidences the formation of low-order oligomer population that it is not depleted over the experimental time. A similar trend is found for the control samples, not presenting ephrin ligands.

Therefore, we compared the dynamics of the receptor clustering for the samples presenting the nanopatterned ephrinB1/Fc ligands (Figure 84, NANOPATTERN row) and AB-conjugated ephrinB1/Fc (Figure 84, AB-CLUSTERS row) format. Equivalent samples withot ligand served as controls (NANO-PLL and PLL) Snapshots of the oligomerization maps over the experimental timeframe (Figure 84) and their corresponding time-lapse movies (Supplementary Information) showed remarkable differences in the clustering dynamics. Upon stimulation with nanometric clusters of ephrinB1/Fc ligands, receptor aggregation

is accelerated, low order species are depleted at earlier time points (species containing between 1 and 4 receptors were depleted within the first 15 min) and the appearance of intermediate-order oligomer is prompted. Large receptor clusters are fully covering the cell membrane at min 35. On the contrary, large receptor oligomers appeared later on time at the surfaces presenting antibody-conjugated ligands.

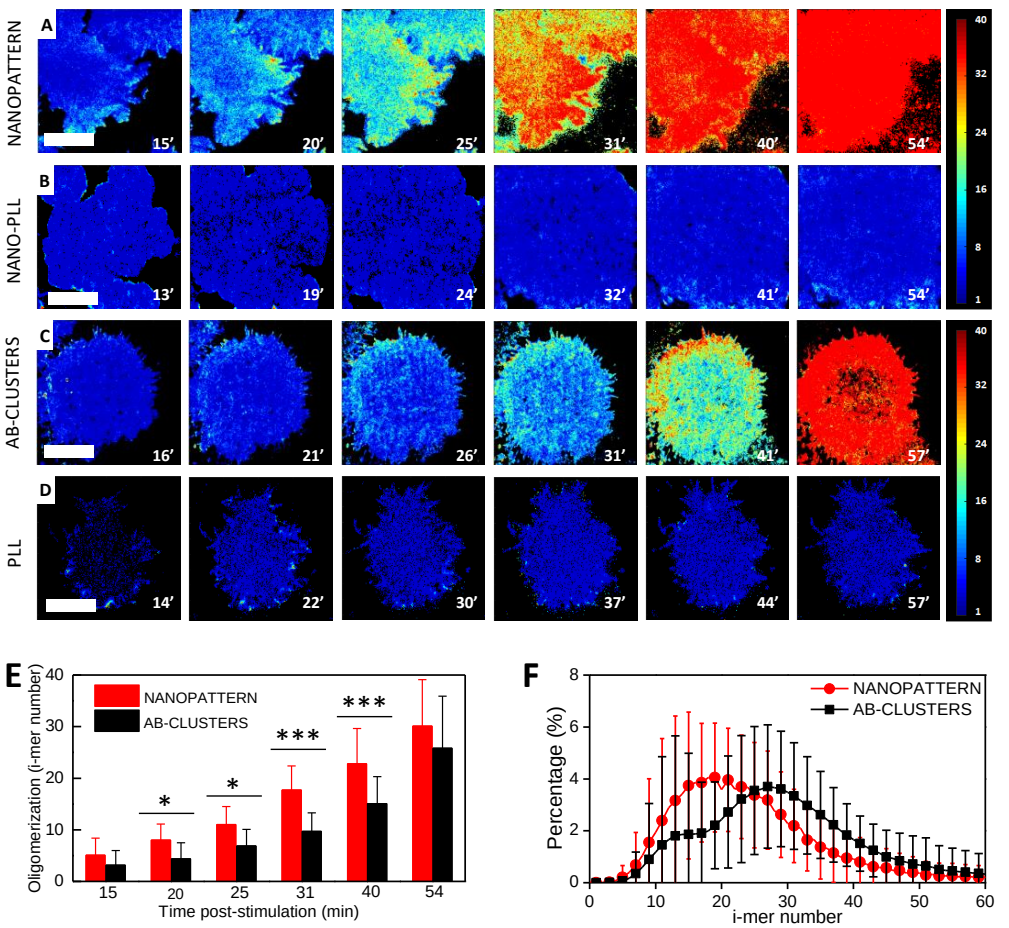

Figure 84. Clustered ephrinB1 presentation accelerates and potentiates EphB2 clustering. A) Time-lapse oligomerization maps from TIRF microscope images. HEK293T:EphB2_mRuby cells were seeded on poly-L-lysine coated surfaces (NANO-PLL and PLL, panels B and D) or surface-mediated ephrinB1/Fc presenting substrates with different ligand configurations: nanopatterned ephrinB1/Fc ligand on BCP medium thin films backfilled with poly-L-lysine (NANOPATTERN, panel A) or AB-conjugated ephrinB1/Fc randomly distributed on poly-L-lysine coated glass coverslips (AB-CLUSTERS, panel C) The color code indicate the average i-mer species of EphB2 clusters. E) Average oligomerization values (obtained from brightness values) at different time points for the two ligand presenting substrates. Statistical differences were denoted by * (p<0.5) and *** (p< 0.005) were computed by ANOVA. F) Distribution of average

and standard deviation oligomerization values for multiple cells at time 60 min for the nanopatterned (red) and AB-conjugated (black) ligands. $N_{NANOPATTERN}$= 10, $N_{AB\text{-}CLUSTERED}$=8.

Quantification of the mean oligomerization state for each time point showed significant differences for the nanopatterned ligand presenting surfaces already at 20 min after stimulation (Figure 84 E). However, it should be noticed that no statistically significant differences were found by the end of the experiment, at 54 min of time. The oligomer distribution at this final time point (Figure 84 F) shows Gaussian distributions centered at 19-mers for the nanopatterned sample and at 28 mers for the antibody clustered samples. It is worth noticing the shoulder of the peak corresponding to the antibody-conjugated presentation, which stands for a cell population that was not effectively stimulated by the ligand.

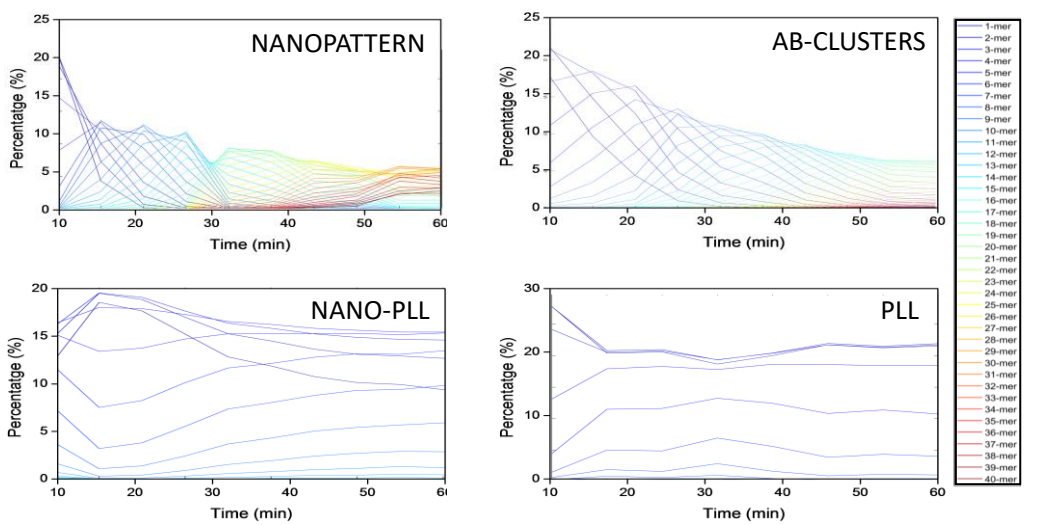

Figure 85. i-mer evolution plot off cells cultured on different ligand presenting surfaces. Percentages of each aggregates (i-mers) over time normalized by the initial concentration of free receptor cells plated over ligand presenting surfaces: surface-mediated nanopatterned ephrinB1/Fc ligands on BCP medium thin films backfilled with poly-L-lysine (NANOPATTERN), poly-L-lysine coated BCP medium thin films (NANO-PLL), randomly distributed antibody-conjugated ephrinB1/Fc on poly-L-lysine coated glass coverslips (AB-CLUSTERS) and poly-L-lysine coated glass coverslips (PLL). i-mer values are color-coded according to the color scale bar.

The time evolution plot of oligomeric species illustrates the accelerated receptor clustering dynamics when activation is triggered by the nanopatterned clusters of ephrinB1/Fc ligands (Figure 85, NANOPATTERN). A completely opposite oligomerization profile is obtained under induction with antibody-conjugated ligands where large receptor aggregates are displayed at longer time points (Figure 85, AB-CLUSTERS). Ordered and coordinated i-mer curves are

equally generated but appeared more compactly arranged for the nanopatterned ligands than on randomly distributed AB-conjugated ephrinB1/Fc. Indeed, under activation with nanopatterned clusters of ephrinB1/Fc ligands, receptor monomer polymerization is accelerated with shorter occurrence intervals (time of appearance of the 10% of the total population until the depletion of 90% of the total population) (Figure 86). Consequently, coalescence of intermediate-order species is also driven earlier than in previously tested conditions. The actively signaling oligomers (hexamers-octamers) are quickly formed after 15-20 min. Hence, the nanopatterned surface efficiently induced not only the formation and sustainability of receptor clusters but produced a 25-30% of acceleration in the oligomerization process (Figure 86). Of notice, surface ligand densities showed a 9-fold decrease for the nanopatterned substrates when compared to the antibody-conjugated ligand presenting surfaces, Therefore, we speculate that our nanopatterned platform was able to induce similar values of receptor clustering in a faster and more efficient way due to the presence of areas with highly packed ligands, able to elicit ligand-receptor multivalent interactions.

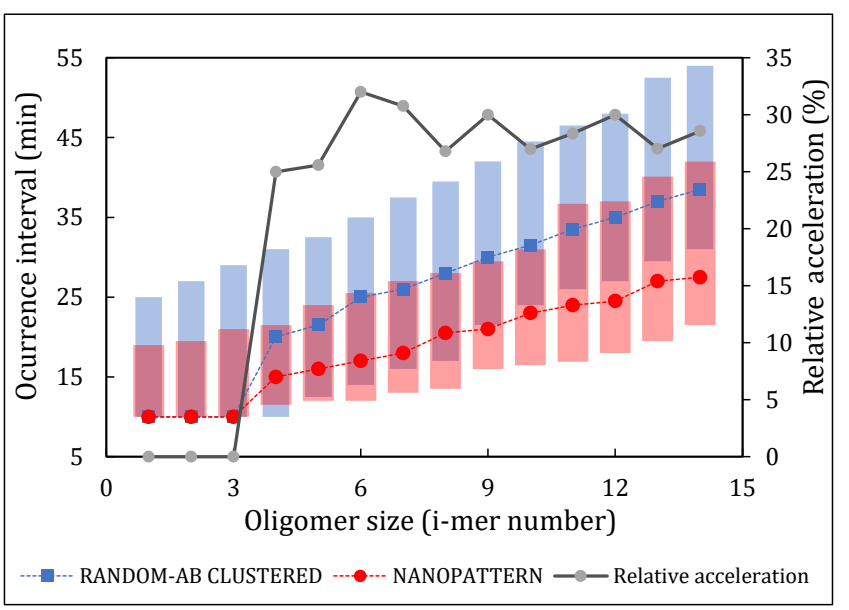

Figure 86. EphB2 receptor oligomerization acceleration on nanopatterned ephrinB1/Fc clusters.

By taking advantage of this platform, multivalent effects induced by surface-ligand presentation have been evidenced through the study of the Eph receptor aggregation dynamics in live cells. The nanopatterned surfaces have been proved as a powerful tool for the systematic study of receptor clustering

phenomena in combination with molecular-level sensitivity analysis techniques. In addition, the high efficiency in receptor cluster activation produced by our nanopatterned surfaces paves the way to the use of surface-induced multivalent interactions in improving the efficacy of bioactive materials or drug delivery systems.

5. Discussion

Nanostructured thin films were successfully produced using asymmetric PS-*b*-PMMA diblock copolymers under soft confinement on glass and silicon substrates. Film-substrate interfacial energy was neutralized for the non-preferential wetting of PS or PMMA blocks, leading to the perpendicular arrangement of highly ordered PMMA nanodomains. To tune substrate surface energy, two strategies were investigated, the first one based on silane self-assembled monolayers and the second one on random copolymer brushes.

The formation of silane self-assembled monolayers depends on multiple variables including the phase deposition, the deposition time, the temperature and the relative humidity. [329] All these factors should be controlled to ensure in one hand, the homogeneity of the self-assembled monolayers over large areas and, on the other hand, the reproducibility of the process. Unfortunately, the self-assembled monolayers fabricated herein with APTES and PF0S showed a defective structure which was inadequate for neutral coating purposes. Probably, an insufficient control of the water content during the coating process lead to variable grafting densities over the silicon substrates, since a strong dependence between those parameters have been previously reported.[117,127] Due to the experimental difficulties in controlling humidity in our laboratory environment, this strategy was discarded.

Alternatively, random copolymers were used to effectively tailor the surface energetics of the substrates, following a common strategy described in the field.[103,114,117,237] Hydroxyl-terminated random copolymer brushes were densely packed on the surfaces yielding a ~ 5 nm thick layer, in agreement with the minimum effective thickness preventing penetration of the diblock copolymer chains into the underlying surface.[121,122] The annealing step performed at 220°C which is a temperature that exceeds the glass transition temperature of the both polymer blocks, facilitates the diffusion of the brush polymer chains towards the interface to interact with the surface. The end-grafted brush layer resulted to be sensitive to sonication in toluene, so the removal of the ungrafted polymer chains was replaced by a rinsing step. These experimental conditions lead to uniform, defectless and technically flat random copolymer brushes over large areas, on both

silicon and glass coverslip substrates. Glass substrates are of special relevance for our final application, as transparent substrates are compatible with microscopy techniques commonly used for cellular studies.

For decades, self-assembled PS-*b*-PMMA diblock copolymers have been extensively exploited to fabricate defined structures such as lamellae[98,281] or cylinders[72,103,130] at the nanometer scale. Herein we selected two asymmetric PS-*b*-PMMA diblock copolymer molecules (BCP small and BCP medium) to form a dense array of perpendicularly oriented PMMA cylinders over the brush-modified substrates. Features with different dimensions in the nanometer scale were obtained, accordingly to their molecular weight. Under soft confinement, BCP small formed perpendicular PMMA cylinders featuring ~ 21 nm in diameter with a characteristic interdomain spacing of 37 nm, perfectly matching the lattice spacing reported for this polymer by Zucchi *et al*. (L_0=36 nm).[241] According to the larger molecular weight of BCP medium polymer, the PMMA cylinders generated showed a diameter of ~ 29 nm regularly separated by a distance of 64 nm. The final goal of most studies working with self-assembled diblock copolymers is miniaturizing feature sizes towards very small (< 10 nm) dimensions,[108,138,142] so diblock copolymers with high molar masses have attracted less attention. To the best of our knowledge, the lattice spacing of BCM medium (molecular weight: 158000 g/mol) was not previously described in literature. Nevertheless, our findings are in good agreement with the closest precedent, where a PS-*b*-PMMA with a molecular weight of 132000 g/mol formed cylindrical PMMA arrays over 30 nm in diameter and 62 nm in spacing.[129]

Under soft-confinement, an advantageous characteristic of diblock copolymer thin films composed of PS and PMMA is the facile equilibration of the interfacial interaction energies at the air-polymer interface by a thermal annealing process. Although the reported annealing temperatures equalizing the interfacial interaction energies of PS and PMMA ranged from 170-230°C,[72,137,139] the equilibrium morphology in our systems was only achieved when the temperature was *in-situ* controlled and exceeded 220°C. We found that these processing conditions had a great impact in the pattern quality and the reproducibility of the results.

Once surface wetting properties of both interfaces were successfully neutralized, BCP medium and BCP small film thicknesses were adjusted varying

the polymer solution concentrations used for spin coating. The equilibrium state in a diblock copolymer film strongly depends on its degree of confinement.[102] In fact, gradients of thicknesses have been screened to find the specific range of thicknesses prompting the perpendicular microdomain orientation.[330] This so-called perpendicular windows, which are commonly located in the vicinity of the lattice spacing (L_0) value,[130,140,331] can be broadened by choosing the optimal substrate-modifying random copolymer composition and annealing conditions.[100,131] We experimentally determined the specific film thickness providing the highest pattern regularity for BCP medium and BCP small. These thickness values were ~ 45 nm for BCP medium and ~ 38 nm for BCP small. We have to acknowledge that one of the limitations of our experiment approach is the commercial availability of block copolymer and, specifically, of hydroxyl-terminated random copolymer brushes, which might prevent the successful perpendicular arrangement of particular block copolymers by using this strategy.

Under such degree of confinement, the perpendicular orientation of PMMA cylinders was ensured, as demonstrated by the selective etching of PMMA domains. At the free interface, circular areas of PMMA domains were hexagonally arranged surrounded by a PS matrix. However, some ambiguous defects in the hexagonal lattice were exhibited, accounting for a relative number of defects of 15.6% for BCP medium and 17.9% for BCP small. There are several strategies that might improve the long range ordering,[279,293,332,333] being epitaxy[106,334,335] and graphoepitaxy[98,105] the ones preferred. They involve additional processing steps which increase the complexity of the fabrication procedures.[81] However, for some nanofabrication applications, such as for instance manufacturing of microelectronic devices,[86,98] the quality of the pattern is a vital issue and countless efforts are performed to get the smallest features perfectly arranged. Nevertheless, other biomedical applications including protein nanopatterning do not have such strict requirements and a low defect density in the hexagonal lattice is tolerated.[295,296]

Thus, we successfully fabricated and characterized two nanostructured diblock copolymer thin films presenting perpendicularly oriented PMMA cylinders with different feature sizes and interdomain distances, immersed in a chemically distinct matrix composed of PS. We also fabricated a featureless PS-r-PMMA thin film with a similar chemical composition to be used as a non-patterned control surface. Self-assembled diblock copolymer thin films offer exciting opportunities

to create surface-bound biomolecule patterns with nanometric resolution. A great variety of geometries[277,330] can be accessed acting as templates to be replicated by the bioactive molecules.[91] It is the precise spatial disposition of the patterned structures over large areas which gives the exceptional usefulness to this self-assembly approach. The functionalization process can be performed *via* two strategies both presenting advantages and challenges. The first one consists on the direct incorporation of a functional group into the block copolymer backbone which will be afterwards confined to a thin film. In a previous work performed by the group, poly(methyl methacrylate)-polystyrene-based diblock copolymers were modified by incorporating biotin in the PS block.[205] The biotin would be used to anchor streptavidin and further biotinylated biomolecules. Although the copolymer was successfully fabricated, the product stability was not optimized for long term applications. Following an analogous strategy, we performed a controlled alkaline hydrolysis[251] of the methyl pending groups present in the PMMA block ranging from a 13% to a 100% of hydrolysis. A very attractive property of this approach is that it is a batch production process, where large quantities of polymers are hydrolyzed at once, reducing the time-processing, and the costs. Numerous samples can be sequentially produced with the same chemical properties and if desired, the remaining product can be stored. Moreover, there are conventional analytical techniques such as FT-IR and 1H-NMR currently available which can provide a full-characterization of the resultant product. Despite all these advantages, there is a major drawback frustrating the success of this strategy. Once the polymer chains were hydrolyzed and spun coated, the films tended to dewet from the surface.[303] This dewetting behavior is thought to be a consequence of the polymer chain modification caused by the incorporation of a polar carboxylic group. Small variations in the polymer backbone are reported to condition the phase segregation of the modified diblock copolymer molecule.[128,336] Consequently, the previously defined neutral interfaces were inappropriate for the hydrolyzed diblock copolymer and they no longer acted as non-preferential surfaces. A thorough optimization of the surface wettability should be performed to find the equilibrium state of the hydrolyzed polymer preferentially using gradients of surface energy.[132]

The second strategy to generate protein nanopatterns is a post-functionalization approach in which diblock copolymer thin films are used as templates to be replicated by the biomolecules. The stability of the protein nanopatterning directly depends on the linking chemistry used to immobilize the

molecules on the surface.[167] In our case, the cylindrical PMMA domains generated at the surface of both BCP medium and BCP small thin films were hydrolyzed under alkaline conditions, yielding reactive carboxylic groups as molecular anchoring points at the surface. This superficial hydrolysis is extremely sensitive to the thin film defects produced by handling during the manufacturing process, so, if scratches were found, the thin films were eventually completely detached from the surface. Although great care had to be taken to preserve the film integrity during the fabrication, the self-assembled nanostructures were still perpendicularly oriented after hydrolysis as characterized by AFM and SEM. Nonetheless, the evaluation of the superficial degree of hydrolysis was nearly impossible to determine neither with conventional surface sensitive techniques nor even with highly sophisticated systems such as Nano-FTIR.[337] Probably, the low signal-to-noise ratio measured from such reduced amount of hydrolyzed material (the outmost surface layer of domains < 30 nm in diameter) and the nanometric resolution required to discriminate between adjacent domains were unbeatable limiting factors for these techniques.

We used an alternative shortcut to overcome this missing information, by directly analyzing the arrangement of surface-bound proteins under several functionalization conditions. Essentially, with a similar PMMA area susceptible to be hydrolyzed (~ 25%), the differences between the three surfaces (BCP medium, BCP small and RandomCP) arise fundamentally from the distinct spatial arrangement of the PMMA microdomains on the surface. This spatial distribution was replicated by the covalently attached molecules. An optimization of the functionalization parameters was necessary to get rid out of large ligand clusters and maximize the number of functionalized PMMA domains. In literature, several groups have developed diblock copolymer systems to create dense arrays of individual ligands [69,150,338,339] Other nanofabrication strategies have been described to produce ligand patterns featuring sizes that range from 120 nm to 1 μm.[14,15,29,174,206] However, the generation of nano-sized arrays where covalently immobilized ligands are pre-arranged in small clusters (< 50 nm) over large surface areas has not been reported. Moreover, this functionalization strategy is an immensely versatile method that enables the immobilization of any amine-terminated molecule[149] following the underlying diblock copolymer template.

The resulting spatial distribution of the nanopatterned ligands on the diblock copolymer surfaces was characterized not only by AFM but also by

STORM.[180,260] Traditionally, AFM imaging deciphers the position and the height of the immobilized molecules under physiological conditions, though it is a time-consuming technique which provides very local information.[168] Therefore, often, the overall density of fluorescent immobilized ligands is analyzed by conventional fluorescence microscopy, which allows the screening of more representative sizes of surface area. In several works, the success of the functionalization strategy was measured as a function of the global average fluorescence intensity.[150,158,167] However, if the global ligand density remains constant, the discrimination between different local densities is limited by the light diffraction.[180] Conversely, during the optimization of the functionalization process we found that STORM imaging provides quantitative information to determine the domain size of ligand clusters, which was in excellent agreement with the one provided by the AFM imaging.[168] Although no-direct correlation can be established between the AFM and the STORM images, the good agreement found between the measurements performed with both techniques suggest that the biomolecule pattern was uniform all over the sample and representative areas were imaged.

The results described above provide a versatile procedure to pattern biomolecules with nanometer-sized features, based on the selective post-functionalization of diblock copolymer templates. This approach circumvents the reported issues associated with polymer modifications prior thin film formation. Biomolecule nanopatterning has useful applications in different fields including for instance biosensors.[158,340] The miniaturization of protein nanoarrays can reduce the costs derived from the use of expensive reagents while simultaneously reducing the chip dimensions which can contribute towards the development of highly sensitive point-of-care testing devices.[341]

Protein nanopatterning is also biologically relevant, since cells recognize and differentially respond to spatially organized biomolecules. The latest advances in nanofabrication, and structural characterization techniques have drove the blooming of numerous nanopatterning techniques with sub-100 nm resolution.[50,128,200,202,205,342] Individual protein patterning techniques have been demanded to investigate the fundamental concepts of single-protein molecular recognition events in biological systems. In particular, the ligand-receptor interactions and downstream signaling was studied in detail thanks to the ability to produce site-specific patterns of relevant cellular ligands with single-molecule resolution.[68] In particular, nanoarrays of individual molecules, such as the well-

known adhesive oligopeptide RGD, have shed light into the complex signaling interactions between cells and their microenvironment. Relevant findings can be attributed to these spatially defined ligand presenting surfaces, including for instance the identification of a maximum integrin distance leading focal adhesion formation,[69,71] the influence of adhesion ligand density on cell migration,[200] the mechanosensing properties of integrins,[70] the relevance of the local ligand surface density versus the global ligand surface density[206] or the prolonged signaling triggered by surface-bound growth factors.[185]

However, numerous receptors including integrins,[189] T-cell receptors,[184] N-cadherins[48] or Eph receptors[214] require assembling into nanoclusters to be functional.[12] In fact, receptor density, distribution and clustering are spatial features that might have a dramatic influence on their downstream signaling.[343] Different strategies have been developed to artificially induce receptor clustering for example by synthetic dimerizers[323] or to disrupt receptor-enriched lipid-microdomains,[344] finally triggering an altered signaling response. As a simple alternative to present ligands in aggregates or clusters.[209,345] This strategy is found and evolutionarily preserved in nature. For instance, some adenovirus, gain access into cells by presenting clusters of cell-adhesive peptides on their surface that bind to multiple integrin receptors simultaneously, in what is called a multivalent ligand-receptor interaction.[209] Recently, soluble multivalent entities have been used to investigate the complex interactions of ligand-receptor binding events.[216,346] Theoretically, when ligands are clustered, the ligand-receptor encounter probability is lower than for homogenous ligands, while the opposite effect is shown for the rebinding probability, which increases in the aggregated configuration. We hypothesized that surface-mediated presentation of multivalent clusters of ligands can better mimic the extracellular environmental diversity helping to figure out the receptor clustering dynamics and afterwards, to finely tune the cellular response.

We initially validated our nanopatterned platforms studying focal adhesion formation, a process that has been usually investigated as a function of the density of adhesive ligands on a surface at the nanometer scale.[69,158,200,347] In 1991, Massia and Hubbell discovered that a minimum of six RGD ligands/μm^2, which corresponds to a theoretical interligand spacing of 440 nm was sufficient to promote cell spreading. The role of ligand clustering was evidenced by Maheshwari and co-workers, who demonstrated the relevance of the local ligand

density of adhesive peptides. Variations where originated by a clustered presentation of ligands *versus* a homogenous distribution, showing a great impact of ligand presentation on the cell behavior.[220,347] More recently, the formation of reliable cell-matrix interactions was investigated by force-dependent measurements and the adhesion strength was proven to be increased when multiple fibronectin domains where clustered within 40-60 nm beads.[348] Additional to cell adhesion strength, focal adhesion maturation was also favored by the clustered ligand presentation.[190]

BCP medium, BCP small thin films were functionalized with cRGDfK adhesive peptide, which clustered on the PMMA domains, while RandomCP thin films provided a non-patterned (homogeneous) ligand disposition. The cell adhesion assays showed that the percentage of adhered cells and the cell projected area was not significantly different between the three RGD-tethering surfaces. These results are in good agreement with the well-accepted idea that cell spreading efficiency is critically determined by the overall surface density of ligands,[198,206,349] which in our RGD-decorated substrates is expected to be comparable due to the similar percentage of area subjected to functionalization. In particular, cell density has reported to be reduced when interligand spacing is larger than 58 nm.[69,200] However, cells cultured on BCP medium thin films, where the pattern spacing is 64 nm, showed equivalent percentages of cell adhesion. This different behavior might be an indication of the presence of multivalent ligand-receptor interactions in our substrates, promoted by the clustered presentation of ligands according to the BCP medium nanostructured template.

On the other side, focal adhesion formation was stated to vary according to the local surface ligand density,[206,349] which implies two important parameters: ligand interspacing[69] and ligand cluster size.[350] We found that the number of focal adhesions per cell was almost doubled in BCP small and RandomCP substrates in comparison with BCP medium, where the ligand interspacing was larger (37 nm for BCP small *versus* 64 nm for BCP medium). Significant differences in focal adhesion maturation were also found between nanopatterned and non-patterned ligand presenting platforms. Focal adhesions were significantly more mature (FA>1 μm^2) on the nanopatterned ligands as demonstrated by paxillin staining. These results suggest that our developed strategy for multivalent presentation of ligands promoted the clustering of integrins in an effective way, and therefore the recruitment of protein adaptors required for the formation of mature focal

adhesions[351]. Hence, in agreement with literature, our results showed that focal adhesion formation and maturation processes were strongly influenced by the ligand spacing[71] as well as by the spatial arrangement of ligands in clusters.[263]

However, it remains unclear to what extent spatially defined ligand presentation modulates the receptor clustering dynamics and therefore the signal transduction. Studies focused in this direction can provide a better understanding of the underlying mechanisms that regulate cell behavior at the molecular level.[308] As mentioned before, many cellular receptors form clusters at the cell membrane. In particular, the ones involved in cell-cell communication form complex muti-component systems where a certain cell both responds and serves as a substrate for their neighbors. Therefore, clustering events occurring at a cell membrane have a straightforward impact on the signal received by neighboring cell. Engineered biomaterials could serve as useful tools to decipher spatially regulated ligand-receptor interactions. For this reason, we used BCP medium thin films as nanopatterned platforms to investigate ephrin-Eph receptor interactions.

Advances in nanofabrication techniques have renewed the field of spatially resolved cell signaling.[307] The ability to precisely control the ligand disposition at nanometer-length scales must evolve hand-in hand with advanced analysis techniques that allow to examine the receptor activation and clustering processes at the molecular level on the diffusive environment of living cell membranes.[352] Although optimum, to date, this has not been the case. Many cellular studies performed on nanopatterned substrates based their analysis in the indirect evaluation of cellular processes such as cell adhesion,[71,164] cytoskeleton remodeling,[174,226,317] cell migration[200,347] or cell differentiation.[153,313] Therefore, the impact of cell receptor clustering on its downstream signaling is investigated at long time points, usually when receptors form huge aggregates that are easy to follow with conventional microscopy techniques.[353] The initial ligand-mediated receptor activation and oligomerization processes are commonly overlooked. To assess those highly dynamic molecular interactions, imaging techniques needs to fulfill some essential requirements including high signal-to-noise ratio, molecular level sensitivity, high lateral and temporal resolution and compatibility with live cells. These conditions exclude many conventional microscopy techniques including phase contrast microscopy, fluorescence confocal microscopy, near-field scanning optical microscopy or scanning electron microscopy.[170,349] Advanced microscopy techniques such as single particle tracking, fluorescence correlation

spectroscopy, and high spatial and temporal-resolution fluorescence resonance energy transfer, have been recently used to study the spatial organization of transmembrane receptors.[354] However, the discrimination of different oligomer sizes with a spatio-temporal resolution is not straightforward.

Herein, we improved the intensity fluctuation-based analysis technique, termed Number and Brightness (N&B)[236] to reveal the oligomerization state of EphB2 receptors over time upon ephrinB1 stimulation. The in-house developed enhanced N&B technique (eN&B) was initially used to study the receptor oligomerization when ligands were delivered in a clustered soluble format, which is the conventional stimulation method performed in the field. Different oligomeric species were discriminated and evaluated during the initial 60 min post-stimulation with clustered soluble ligands. A perfectly orchestrated process was revealed where the population of low-order oligomers sequentially decreased leading the appearance of higher-order oligomers. This eN&B approach offers the unprecedented opportunity to investigate with molecular sensitivity the oligomeric forms of the EphB2 receptor during the early stages of the activation process, providing a much deeper understanding of the dynamic interactions governing this process. In fact, thanks to the results extracted from the eN&B analysis, a mathematical model was built where two phases were described: the polymerization phase, where monomers form oligomers and the condensation phase, where oligomers coalesce to form larger clusters.[275] The data predicted by this model was in excellent agreement with the experimental results provided by the eN&B analysis. Moreover, the maximum activation level (EphB2 phosphorylation) was measured to be reached within the first 15-30 min post-stimulation, corresponding with a predominant occurrence of pentamer-to octamers species.

Finally, EphB2 receptor oligomerization dynamics was studied in response to the precise presentation of surface-bound ligands. As a natural choice, receptor clustering phenomena was investigated over the previously described nanopatterned-ligand presenting platform and analyzed by eN&B technique. BCP medium thin film was functionalized with ephrinB1/Fc dimers leading to a spatial distribution in discrete clusters of ~18 ephrinB1 ligands, featuring sizes of 24-27 nm in diameter, spaced at least 58 nm, as confirmed by AFM and STORM analysis. The overall functionalized area was only a 9.3% of the surface. This surface-mediated ligand-nanopatterned substrate showed a completely different ligand

distribution when compared with the random immobilization strategy used for both ephrinB1/Fc dimers and antibody-conjugated ephrinB1/Fc, which were microcontact printed over the poly-L-lysine-coated surface. Their surface characterization unveiled that not only the overall functionalized area was significantly higher (7-fold and 9-fold higher for ephrinB1/Fc dimers and AB-conjugated ephrinB1/Fc respectively, as shown by AFM and demonstrated by the significant increase in fluorescence intensity), but also the distribution displayed was entangled with intricate regions of covered and non-covered areas. When immobilized on surface, the large and irregular aggregates formed by the antibody-conjugated ephrinB1/Fc aggregates were visible.

Receptor oligomerization was thoroughly analyzed upon stimulation with the ephrinB1/Fc presenting surfaces. The results showed that ephrinB1/Fc randomly immobilized on the surface was unable to trigger receptor oligomerization even if its surface coverage was 7-fold higher than on the nanopatterned surface. However, the ephrinB1/Fc ligand nanopatterns created through the diblock-copolymer technology have the capability of inducing surface-bound receptor clustering even at relatively low global ligand surface densities (9.3% surface coverage). Stein *et al*. reported that surface bound ephrinB1/Fc dimers stimulated receptor phosphorylation but did not promote cell attachment, which was promoted by ephrin/Fc oligomers formed through antibody crosslinking.[207] Although they suggested the possibility of producing such ligand oligomers through the densely-pack immobilization of ligands over surfaces, we did not observed such effect when the spatial distribution of ephrinB1/Fc was random. Actually, in our opinion, Stein was partially right assuming that surface-bound presentation could lead to an effective activation of receptor clustering, but failed when neglecting the remarkable effect of the spatial distribution. We hypothesize that the ligand presentation provided by the nanopatterned ligands increases the receptor-ligand rebinding probability, as previously reported for other soluble multivalent ligands,[216] thus, resulting in multivalent effects.

To elucidate the effects of surface-mediated ligand multivalent presentation in comparison with the standard antibody-mediated ligand clustering, EphB2 receptor oligomerization was analyzed by eN&B. These results showed that although the final average oligomerization state was not significantly different, the process driving towards that outcome differs. Upon stimulation with nanopatterned ephrinB1/Fc ligands on diblock copolymer surfaces, the EphB2

receptor clustering process was accelerated up to a 30% and consequently, the occurrence interval for each particular oligomer was reduced. Once more, this phenomenon might be explained by the ligand multivalency. Our regular-in-size nanopatterns are estimated to host ~ 18 ephrinB1 ligands while antibody-mediated clusters of ephrinB1/Fc are reported to form aggregates predominantly with 4-6 ephrin ligands.[207] Hence, our multivalent presenting platform is thought to provide a highly potent stimulation,[355] which might require lower ligand concentrations.

Defining a nanoscale organization of ligands can be a useful strategy to finely tune the receptor response to a pre-established level by setting the size and spacing of the nanopattern. The growing use of antibody-based drugs in the clinical setting underscores the need to better understand receptor clustering and its broader effects on signal transduction processes. Nanoscale multivalent conjugates could potentially activate receptor-ligand complexes more potently and thus less expensive. This new platform has biotechnological and biomedical applications including cell culture systems, bioactive materials and drug-delivery.

6. Conclusions

- A nanofabrication method was designed to produce nanostructured thin films using PS-*b*-PMMA diblock copolymers that self-assembled into cylindrical PMMA domains immersed in a PS matrix. Perpendicular arrays of PMMA cylinders were successfully obtained over large areas after the proper equilibration of the interfacial energies. Thin films were generated not only on silicon but also on glass substrates. The fabrication on glass substrates extended the potential applications of these nanopatterned structures as substrates for cellular assays.
- A simple functionalization strategy was optimized and implemented to create different biomolecule nanopatterns according to the underlying diblock copolymer template. Through the selective hydrolysis of PMMA domains, small peptides and proteins were covalently attached to the developed platforms leading to discrete clusters featuring 20-30 nm in size. Thanks to the functionalization process selected, any amine-bearing molecule can be immobilized, which demonstrates the versatility of the nanopatterning platform.
- The nanoclustered ligand-presenting platforms were used to investigate the role of the spatial distribution of adhesive peptides in cell adhesion and focal adhesion formation. It was observed that cell spreading was rather not affected by the local presentation of ligands when the global surface density was equivalent. Conversely, the spatial distribution of ligands showed a remarkable impact on focal adhesion formation, where the nanopatterned presentation of surface-bound ligands enhanced the maturation of focal adhesions. These findings suggest that ligand presentation in a clustered format might promote multivalent ligand-receptor interactions, therefore altering the cell response.
- EphB2 receptor oligomerization dynamics was explored upon stimulation with diverse ephrin-presenting surfaces. Surface-immobilization of ligands with random disposition was not sufficient to activate the receptor signaling. It was necessary a clustered presentation of ephrin ligands, where they form densely packed aggregates, to promote receptor oligomerization. When immobilized in clusters, the final receptor oligomerization response was equivalent to the one produced by antibody-mediated ligand clusters,

although the ephrin surface coverage was 9-fold lower in the first case. As evaluated by enhanced Number and Brightness analysis, receptor oligomerization, was spatially modulated and showed an accelerated profile upon stimulation with our nanopatterned platform. Together, these results validate our nanopatterned substrate as an effective platform for surface-based multi-ligand presentation.

7. References

1. Kramer, N. *et al.* In vitro cell migration and invasion assays. *Mutat. Res.* **752,** 10–24 (2013).
2. Cavey, M. & Lecuit, T. Molecular Bases of Cell – Cell Junctions Stability and Dynamics. *Cold Spring Harb. Perspect. Biol.* **1,** 1–19 (2009).
3. Bonnans, C., Chou, J. & Werb, Z. Remodelling the extracellular matrix in development and disease. *Nat. Rev. Mol. Cell Biol.* **15,** 786–801 (2014).
4. Kaminska, K. *et al.* The role of the cell-cell interactions in cancer progression. *J. Cell. Mol. Med.* **19,** 283–296 (2015).
5. Humphrey, J. D., Dufresne, E. R. & Schwartz, M. a. Mechanotransduction and extracellular matrix homeostasis. *Nat. Rev. Mol. Cell Biol.* **15,** 802–812 (2014).
6. Nussinov, R. The spatial structure of cell signaling systems. *Phys. Biol.* **10,** 45004 (2013).
7. Singhai, A. *et al.* Spatially defined EGF receptor activation reveals an F-actin-dependent phospho-erk signaling complex. *Biophys. J.* **107,** 2639–2651 (2014).
8. Lutolf, M. P. & Hubbell, J. a. Synthetic biomaterials as instructive extracellular microenvironments for morphogenesis in tissue engineering. *Nat. Biotechnol.* **23,** 47–55 (2005).
9. Egea, J. & Klein, R. Bidirectional Eph-ephrin signaling during axon guidance. *Trends Cell Biol.* **17,** 230–238 (2007).
10. Groves, J. T. Spatial mutation of the T cell immunological synapse. *Curr. Opin. Chem. Biol.* **10,** 544–550 (2006).
11. Martínez, E. *et al.* Stem cell differentiation by functionalized micro- and nanostructured surfaces. *Nanomedicine (Lond).* **4,** 65–82 (2009).
12. Ruprecht, V. *et al.* How cells respond to environmental cues – insights from bio-functionalized substrates. *J. Cell Sci.* **130,** 51–61 (2017).
13. Doh, J. & Irvine, D. J. Immunological synapse arrays : Patterned protein surfaces that modulate immunological synapse structure formation in T cells. *Proc. Natl. Acad. Sci.* **103,** 5700–5705 (2006).
14. Dillard, P., Pi, F., Lellouch, A. C., Limozin, L. & Sengupta, K. Nano-clustering of ligands on surrogate antigen presenting cells modulates T cell membrane adhesion and organization. *Integr. Biol. (Camb).* **8,** 287–301 (2016).
15. Massia, S. P. & Hubbell, J. a. An RGD spacing of 440 nm is sufficient for integrin alpha V beta 3-mediated fibroblast spreading and 140 nm for focal contact and stress fiber formation. *J. Cell Biol.* **114,** 1089–1100 (1991).
16. Irvine, D. J., Mayes, A. M. & Griffith, L. G. Nanoscale clustering of RGD peptides at surfaces using Comb polymers. 1. Synthesis and characterization of Comb thin films. *Biomacromolecules* **2,** 85–94 (2001).
17. Hynes, R. O. The extracellular matrix: not just pretty fibrils. *Science* **326,** 1216–9 (2009).
18. Wagner, D. O. *et al.* BMPs: from bone to body morphogenetic proteins. *Sci. Signal.* **3,** mr1 (2010).

19. Rashidi, H., Yang, J. & Shakesheff, K. M. Surface engineering of synthetic polymer materials for tissue engineering and regenerative medicine applications. *Biomater. Sci.* **2,** 1318 (2014).
20. Tawfick, S. *et al.* Engineering of micro- and nanostructured surfaces with anisotropic geometries and properties. *Adv. Mater.* **24,** 1628–74 (2012).
21. Wheeldon, I., Farhadi1, A., Bick, A. G., Jabbari, E. & Khademhosseini, A. Nanoscale tissue engineering: spatail control over cell-materials interactions. *Nanotechnology* **22,** 1–28 (2011).
22. Suresh, S. Semiconductor Nanomaterials, Methods and Applications: A Review. *Nanosci. Nanotechnol.* **3,** 62–74 (2013).
23. Yang, P., Yan, R. & Fardy, M. Semiconductor nanowire: Whats Next? *Nano Lett.* **10,** 1529–1536 (2010).
24. Goodnick, S. *et al.* Semiconductor nanotechnology: novel materials and devices for electronics, photonics and renewable energy applications. *Nanotechnology* **21,** 1–2 (2010).
25. Galvin, P. A nanobiotechnology roadmap for high-throughput single nucleotide polymorphism analysis. *Psychiatr. Genet.* **12,** 75–82 (2002).
26. Drmanac, R. *et al.* Human Genome Sequencing Using Unchained Base Reads on Self-Assembling DNA Nanoarrays. *Science* **327,** 78–81 (2010).
27. Lee, K.-B., Kim, E.-Y., Mirkin, C. a. & Wolinsky, S. M. The Use of Nanoarrays for Highly Sensitive and Selective Detection of Human Immunodeficiency Virus Type 1 in Plasma. *Nano Lett.* **4,** 1869–1872 (2004).
28. Biggs, M. J. P., Richards, R. G., Gadegaard, N., Wilkinson, C. D. W. & Dalby, M. J. The effects of nanoscale pits on primary human osteoblast adhesion formation and cellular spreading. *J. Mater. Sci. Mater. Med.* **18,** 399–404 (2007).
29. Dalby, M. J. *et al.* The control of human mesenchymal cell differentiation using nanoscale symmetry and disorder. *J. Dent. Res.* **84,** 407–413 (2005).
30. Gates, B. D. *et al.* New Approaches to Nanofabrication: Molding, Printing, and Other Techniques. *Chem. Rev.* **105,** 1171–1196 (2005).
31. Biswas, A. *et al.* Advances in top-down and bottom-up surface nanofabrication: Techniques, applications & future prospects. *Adv. Colloid Interface Sci.* **170,** 2–27 (2012).
32. Moreau, W. M. *Semiconductor lithography: principles and materials.* (1998).
33. Pfeiffer, H. C., Groves, T. R. & Newman, T. H. High-throughput, high-resolution electron-beam lithography. *IBM J. Res. Dev.* **32,** 494–501 (1988).
34. Denis, F. A., Pallandre, A., Nysten, B., Jonas, A. M. & Dupont-Gillain, C. C. Alignment and assembly of adsorbed collagen molecules induced by anisotropic chemical nanopatterns. *Small* **1,** 984–991 (2005).
35. Chen, W. & Ahmed, H. Fabrication of 5-7 nm wide etched lines in silicon using 100 keV electron-beam lithography and polymethylmethacrylate resist. *Appl. Phys. Lett.* **62,** 1499–1501 (1993).
36. Ricoult, S. G. *et al.* Large dynamic range digital nanodot gradients of biomolecules made by low-cost nanocontact printing for cell haptotaxis. *Small* **9,** 3308–3313 (2013).
37. Jiang, J., Li, X., Mak, W. C. & Trau, D. Integrated direct DNA/protein patterning and microfabrication by focused ion beam milling. *Adv. Mater.*

20, 1636–1643 (2008).
38. Mills, C. A. *et al.* Transparent micro- and nanopatterned poly(lactic acid) for biomedical applications. *J. Biomed. Mater. Res. - Part A* **76,** 781–787 (2006).
39. Karazisis, D. *et al.* The influence of controlled surface nanotopography on the early biological events of osseointegration. *Acta Biomater.* 1–13 (2017).
40. Hellriegel, C., Caiolfa, V. R., Corti, V., Sidenius, N. & Zamai, M. Number and brightness image analysis reveals ATF-induced dimerization kinetics of uPAR in the cell membrane. *FASEB J.* **25,** 2883–2897 (2016).
41. Qin, D., Xia, Y. & Whitesides, G. M. Soft lithography for micro- and nanoscale patterning. *Nat. Protoc.* **5,** 491–502 (2010).
42. Xia, Y. & Whitesides, G. M. Soft lithography. *Annu. Rev. Mater. Sci.* **28,** 153–184 (1998).
43. Kumar, A. & Whitesides, G. M. Features of gold having micrometer to centimeter dimensions can be formed through a combination of stamping with an elastomeric stamp and an alkanethiol 'ink' followed by chemical etching. *Appl. Phys. Lett.* **63,** 2000–2004 (1993).
44. Alom Ruiz, S. & Chen, C. S. Microcontact printing: A tool to pattern. *Soft Matter* **3,** 1–10 (2007).
45. Chen, C. S., Mrksich, M., Huang, S., Whitesides, G. M. & Ingber, D. E. Geometric Control of Cell Life and Death. *Science (80-.).* **276,** 1425–1428 (1997).
46. Csucs, G., Kunzler, T., Feldman, K., Robin, F. & Spencer, N. D. Microcontact Printing of Macromolecules with Submicrometer Resolution by Means of Polyolefin Stamps. *Langmuir* **19,** 6104–6109 (2003).
47. Shen, K., Thomas, V. K., Dustin, M. L. & Kam, L. C. Micropatterning of costimulatory ligands enhances CD4+ T cell function. *Proc. Natl. Acad. Sci. U. S. A.* **105,** 7791–7796 (2008).
48. Shi, P., Shen, K. & Kam, L. C. Local Presentation of L1 and N-Cadherin in Multicomponent, Microscale Patterns Differentially Direct Neuron Function In Vitro. *Dev. Neurobiol.* **67,** 1765–1776 (2007).
49. MacNearney, D., Mak, B., Ongo, G., Kennedy, T. E. & Juncker, D. Nanocontact Printing of Proteins on Physiologically Soft Substrates to Study Cell Haptotaxis. *Langmuir* **32,** 13525–13533 (2016).
50. Zhang, S. Fabrication of novel biomaterials through molecular self-assembly. *Nat. Biotechnol.* **21,** 1171–1178 (2003).
51. Bishop, K. J. M., Wilmer, C. E., Soh, S. & Grzybowski, B. A. Nanoscale forces and their uses in self-assembly. *Small* **5,** 1600–1630 (2009).
52. Gazit, E. Self-assembled peptide nanostructures: the design of molecular building blocks and their technological utilization. *Chem. Soc. Rev.* **36,** 1263 (2007).
53. Elemans, J. a. a. W., Rowan, A. E. & Nolte, R. J. M. Mastering molecular matter. Supramolecular architectures by hierarchical self-assemblyBasis of a presentation given at Materials Discussion No. 6, 12?14th September 2003, Durham, UK. *J. Mater. Chem.* **13,** 2661 (2003).
54. Zhang, S., Marini, D. M., Hwang, W. & Santoso, S. Design of nanostructured biological materials through self-assembly of peptides and proteins. *Curr. Opin. Chem. Biol.* **6,** 865–871 (2002).
55. Lohmüller, T. *et al.* Nanopatterning by block copolymer micelle

nanolithography and bioinspired applications. *Biointerphases* **6,** 1–12 (2011).
56. Rothemund, P. W. K. Folding DNA to create nanoscale shapes and patterns. *Nature* **440,** 297–302 (2006).
57. Zhang, B. J., Li, Y., Zhang, X. & Yang, B. Colloidal Self-Assembly Meets Nanofabrication : From Two- Dimensional Colloidal Crystals to Nanostructure Arrays. *Adv. Mater.* **22,** 4249–4269 (2010).
58. Oberhansl, S. *et al.* Facile modification of silica substrates provides a platform for direct-writing surface click chemistry. *Small* **8,** 541–545 (2012).
59. Oberhansl, S. *et al.* Mesopattern of immobilised bone morphogenetic protein-2 created by microcontact printing and dip-pen nanolithography influence C2C12 cell fate. *RSC Adv.* **4,** 56809–56815 (2014).
60. Hirtz, M., Oikonomou, A., Georgiou, T., Fuchs, H. & Vijayaraghavan, A. DPN116-Multiplexed biomimetic lipid membranes on graphene by dip-pen nanolithography. *Nat. Commun.* **4,** 1–8 (2013).
61. Sekula, S. *et al.* Multiplexed lipid dip-pen nanolithography on subcellular scales for the templating of functional proteins and cell culture. *Small* **4,** 1785–1793 (2008).
62. Dalby, M. J., Riehle, M. O., Sutherland, D. S., Agheli, H. & Curtis, A. S. G. Changes in fibroblast morphology in response to nano-columns produced by colloidal lithography. *Biomaterials* **25,** 5415–22 (2004).
63. Li, J. R., Lusker, K. L., Yu, J. J. & Garno, J. C. Engineering the spatial selectivity of surfaces at the nanoscale using particle lithography combined with vapor deposition of organosilanes. *ACS Nano* **3,** 2023–2035 (2009).
64. Tang, C., Lennon, E. M., Fredrickson, G. H., Kramer, E. J. & Hawker, C. J. Evolution of block copolymer lithography to highly ordered square arrays. *Science (80-.).* **322,** 429–432 (2008).
65. Park, C., Yoon, J. & Thomas, E. L. Enabling nanotechnology with self assembled block copolymer patterns. *Polymer (Guildf).* **44,** 6725–6760 (2003).
66. Cheng, J. Fabrication and Characterization of Nanostructures from Self-assembled Block Copolymers. 1–109 (2003).
67. Hu, H., Gopinadhan, M. & Osuji, C. O. Directed self-assembly of block copolymers : a tutorial review of strategies for enabling nanotechnology with soft matter. *Soft Matter* **10,** 3867–3889 (2014).
68. Spatz, J. P. *et al.* Ordered deposition of inorganic clusters from micellar block copolymer films. *Langmuir* **16,** 407–415 (2000).
69. Arnold, M. *et al.* Activation of integrin function by nanopatterned adhesive interfaces. *Chemphyschem* **5,** 383–388 (2004).
70. Cavalcanti-Adam, E. A. & Spatz, J. P. Receptor clustering control and associated force sensing by surface patterning : when force matters. *Nanomedici* **10,** 681–684 (2015).
71. Cavalcanti-Adam, E. a *et al.* Lateral spacing of integrin ligands influences cell spreading and focal adhesion assembly. *Eur. J. Cell Biol.* **85,** 219–224 (2006).
72. Ferrarese Lupi, F. *et al.* Rapid thermal processing of self-assembling block copolymer thin films. *Nanotechnology* **24,** 1–7 (2013).

73. Li, M. & Ober, C. K. Block copolymer patterns and templates. *Mater. Today* **9,** 30–39 (2006).
74. Anne-Valérie Ruzettle and Ludwik Leibler. Block copolymers in tomorrow ' s plastics. *Nat. Mater.* **4,** 19–31 (2005).
75. Knoll, A. *et al.* Phase Behavior in Thin Films of Cylinder-Forming Block Copolymers. *Phys. Rev. Lett.* **89,** 1–4 (2002).
76. Albert, J. N. L. & Epps III, T. H. Self-assembly of block copolymer thin films. *Mater. Today* **13,** 24–33 (2010).
77. Jung, Y. Templated self-assembly of siloxane block copolymers for nanofabrication. 1–171 (2009).
78. Matsen, M. W. & Schick, M. Stable and unstable phases of a diblock copolymer melt. *Phys. Rev. Lett.* **72,** 2660–2663 (1994).
79. Matsen, M. W. & Bates, F. S. Conformationally Asymmetric Block Copolymers. 945–952 (1996).
80. Matsen, M. W. & Bates, F. S. Unifying Weak- and Strong-Segregation Block Copolymer Theories. *Macromolecules* **29,** 1091–1098 (1996).
81. Darling, S. B. Directing the self-assembly of block copolymers. *Prog. Polym. Sci.* **32,** 1152–1204 (2007).
82. Khandpur, A. K. *et al.* Polyisoprene-Polystyrene Diblock Copolymer Phase Diagram near the Order-Disorder Transition. *Macromolecules* **28,** 8796–8806 (1995).
83. Bates, F. S. & Fredrickson, G. H. Block Copolymers—Designer Soft Materials. *Phys. Today* **52,** 32 (1999).
84. Bates, F. S. Polymer-Polymer Phase Behavior. *Science (80-.).* **251,** 898–905 (1991).
85. Gu, X., Gunkel, I., Russell, T. P. & Russell, T. P. Pattern transfer using block copolymers Subject Areas : Author for correspondence : *Philos. Trans. R. Soc. A.* 1–34 (2013).
86. Ruiz, R. *et al.* Density Multiplication and Improved Lithography by Directed Block Copolymer Assembly. *Science (80-.).* **321,** 936–939 (2008).
87. Park, S. *et al.* Macroscopic 10-terabit-per-square-inch arrays from block copolymers with lateral order. *Science* **323,** 1030–1033 (2009).
88. Niemz, A., Bandyopadhyay, K., Tan, E., Cha, K. & Baker, S. M. Fabrication of nanoporous templates from diblock copolymer thin films on alkylchlorosilane-neutralized surfaces. *Langmuir* **22,** 11092–11096 (2006).
89. Mugemana, C., Gohy, J.-F. & Fustin, C.-A. Functionalized nanoporous thin films from metallo-supramolecular diblock copolymers. *Langmuir* **28,** 3018–23 (2012).
90. Langer, R. & Tirrell, D. a. Designing materials for biology and medicine. *Nature* **428,** 487–492 (2004).
91. Mendes, P. M., Yeung, C. L. & Preece, J. a. Bio-nanopatterning of Surfaces. *Nanoscale Res. Lett.* **2,** 373–384 (2007).
92. IBM Brings Nature to Computer Chip Manufacturing. *IBM Press Release* 11 (2007).
93. Mai, Y. & Eisenberg, A. Self-assembly of block copolymers. *Chem. Soc. Rev.* **41,** 5969–5985 (2012).
94. Swann, J. M. G. & Topham, P. D. Design and application of nanoscale

actuators using block-copolymers. *Polymers (Basel).* **2,** 454–469 (2010).
95. Ryan, a J. *et al.* Responsive brushes and gels as components of soft nanotechnology. *Faraday Discuss.* **128,** 55–74 (2005).
96. Mezzenga, R. & Ruokolainen, J. Nanocomposites: Nanoparticles in the right place. *Nat. Mater.* **8,** 926–928 (2009).
97. Zhao, Y. *et al.* Small-molecule-directed nanoparticle assembly towards stimuli-responsive nanocomposites. *Nat. Mater.* **8,** 979–985 (2009).
98. Park, D.-H. The fabrication of thin films with nanopores and nanogrooves from block copolymer thin films on the neutral surface of self-assembled monolayers. *Nanotechnology* **18,** 1–7 (2007).
99. Geoghegan, M. & Krausch, G. Wetting at polymer surfaces and interfaces. *Prog. Polym. Sci.* **28,** 261–302 (2003).
100. Suh, H. S., Kang, H., Nealey, P. F. & Char, K. Thickness dependence of neutral parameter windows for perpendicularly oriented block copolymer thin films. *Macromolecules* **43,** 4744–4751 (2010).
101. Fasolka, M. J. & Mayes, A. M. BLOCK COPOLYMER THIN FILMS : Physics and Applications. *Annu. Rev. Mater. Res.* **31,** 323–355 (2001).
102. Segalman, R. a. Patterning with block copolymer thin films. *Mater. Sci. Eng. R Reports* **48,** 191–226 (2005).
103. Andreozzi, A., Poliani, E., Seguini, G. & Perego, M. The effect of random copolymer on the characteristic dimensions of cylinder-forming PS-b-PMMA thin films. *Nanotechnology* **22,** 1–8 (2011).
104. Kim, M., Han, E., Sweat, D. P. & Gopalan, P. Interplay of surface chemical composition and film thickness on graphoepitaxial assembly of asymmetric block copolymers. *Soft Matter* **9,** 6135–6141 (2013).
105. Cheng, J. Y., Mayes, A. M. & Ross, C. A. Nanostructure engineering by templated self-assembly of block copolymers. *Nat. Mater.* **3,** 823–828 (2004).
106. Xu, J., Russell, T. P., Ocko, B. M. & Checco, A. Block copolymer self-assembly in chemically patterned squares. *Soft Matter* **7,** 3915–3919 (2011).
107. Han, E., Kim, M. & Gopalan, P. Chemical Patterns from Surface Grafted Resists for Direct Assembly of Block Copolymers. *ACS Nano* (2012).
108. Park, S. M. *et al.* Sub-10 nm nanofabrication via nanoimprint directed self-assembly of block copolymers. *ACS Nano* **5,** 8523–8531 (2011).
109. Thurn-Albrecht, T. *et al.* Ultrahigh-density nanowire arrays grown in self-assembled diblock copolymer templates. *Science* **290,** 2126–2129 (2000).
110. Thurn-Albrecht, T., DeRouchey, J., Russell, T. P. & Kolb, R. Pathways toward electric field induced alignment of block copolymers. *Macromolecules* **35,** 8106–8110 (2002).
111. Shen, L., Zhu, J. & Liang, H. Heterogeneous patterns on block copolymer thin film via solvent annealing : Effect on protein adsorption. *J. Chem. Phys.* **142,** 1–7 (2015).
112. Vayer, M. *et al.* Perpendicular orientation of cylindrical domains upon solvent annealing thin films of polystyrene-b-polylactide. *Thin Solid Films* **518,** 3710–3715 (2010).
113. Albert, J. N. L., Baney, M. J. & Epps, T. H. Generation of Monolayer Gradients in Surface Energy and Surface Chemistry for Block Copolymer Thin Film

Studies. *ACS Nano* **3,** 3977–3986 (2009).
114. Han, E., Stuen, K. O., La, Y.-H., Nealey, P. F. & Gopalan, P. Effect of Composition of Substrate-Modifying Random Copolymers on the Orientation of Symmetric and Asymmetric Diblock Copolymer Domains. *Macromolecules* **41,** 9090–9097 (2008).
115. Ham, S. *et al.* Microdomain orientation of PS-b-PMMA by controlled interfacial interactions. *Macromolecules* **41,** 6431–6437 (2008).
116. Ji, S. *et al.* Preparation of neutral wetting brushes for block copolymer films from homopolymer blends. *Adv. Mater.* **20,** 3054–3060 (2008).
117. In, I., La, Y. H., Park, S. M., Nealey, P. F. & Gopalan, P. Side-chain-grafted random copolymer brushes as neutral surfaces for controlling the orientation of block copolymer microdomains in thin films. *Langmuir* **22,** 7855–7860 (2006).
118. Kellogg, G. J. *et al.* Observed Surface Energy Effects in Confined Diblock Copolymers. *Phys. Rev. Lett.* **76,** 2503–2506 (1996).
119. Mansky, P., Russell, T. P., Hawker, C. J., Pitsikalis, M. & Mays, J. Ordered diblock copolymer films on random copolymer brushes. *Macromolecules* **30,** 6810–6813 (1997).
120. Huang, E., Rockford, L., Russell, T. P. & Hawker, C. J. Nanodomain control in copolymer thin films. *Nature* **395,** 757–758 (1998).
121. Ryu, D. Y., Shin, K., Drockenmuller, E., Hawker, C. J. & Russel, T. P. A Generalized Approach to the Modifiction of Solid Surfaces. *Science (80-.).* **308,** 236–238 (2005).
122. Ryu, D. Y. *et al.* Surface modification with cross-linked random copolymers: Minimum effective thickness. *Macromolecules* **40,** 4296–4300 (2007).
123. Peters, R. D., Yang, X. M., Kim, T. K. & Nealey, P. F. Wetting behavior of block copolymers on self-assembled films of alkylchlorosiloxanes: Effect of grafting density. *Langmuir* **16,** 9620–9626 (2000).
124. Sohn, B. H. & Yun, S. H. Perpendicular lamellae induced at the interface of neutral self-assembled monolayers in thin diblock copolymer ® lms. *Polymer (Guildf).* **43,** 2507–2512 (2002).
125. Peters, R. D., Yang, X. M., Kim, T. K., Sohn, B. H. & Nealey, P. F. Using Self-Assembled Monolayers Exposed to X-rays To Control the Wetting Behavior of Thin Films of Diblock Copolymers. *Langmuir* **16,** 4625–4631 (2000).
126. Delorme, N., Bardeau, J.-F., Bulou, A. & Poncin-Epaillard, F. Controlled modification of octadecyltrichlorosilane self-assembled monolayer by CO2 plasma. *Thin Solid Films* **496,** 612–618 (2006).
127. Liu, P. H., Thébault, P., Guenoun, P. & Daillant, J. Easy orientation of diblock copolymers on self-assembled monolayers using UV irradiation. *Macromolecules* **42,** 9609–9612 (2009).
128. Reynhout, I. C., Delaittre, G., Kim, H.-C., Nolte, R. J. M. & Cornelissen, J. J. L. M. Nanoscale organization of proteins via block copolymer lithography and non-covalent bioconjugation. *J. Mater. Chem. B* **1,** 3026–3030 (2013).
129. Guarini, K. W., Black, C. T. & Yeung, S. H. I. Optimization of diblock copolymer thin film self assembly. *Adv. Mater.* **14,** 1290–1294 (2002).
130. Jeong, U. *et al.* Enhancement in the Orientation of the Microdomain in Block Copolymer Thin Films upon the Addition of Homopolymer. *Adv. Mater.* **16,**

533–536 (2004).
131. Han, E. *et al.* Perpendicular Orientation of Domains in Cylinder-Forming Block Copolymer Thick Films by Controlled Interfacial Interactions. *Macromolecules* **42,** 4896–4901 (2009).
132. Epps, T. H., DeLongchamp, D. M., Fasolka, M. J., Fischer, D. A. & Jablonski, E. L. Substrate surface energy dependent morphology and dewetting in an ABC triblock copolymer film. *Langmuir* **23,** 3355–3362 (2007).
133. Estévez, M., Fernández-Ulibarri, I., Martínez, E., Egea, G. & Samitier, J. Changes in the internal organization of the cell by microstructured substrates. *Soft Matter* **6,** 582 (2010).
134. Comelles, J., Hortigüela, V., Samitier, J. & Martínez, E. Versatile gradients of covalently bound proteins on microstructured substrates. *Langmuir* **28,** 13688–97 (2012).
135. Russell, T., Jr, R. H. & Seeger, P. Temperature dependence of the interaction parameter of polystyrene and poly (methyl methacrylate). *Macromolecules* **23,** 890–893 (1990).
136. Yue, Z., Sivaniah, E. & Hashimoto, T. SAXS analysis of the Order-disorder transition and the interaction parameter of Polystyrene-block-poIy(methyl methacrylate). *Macromolecules* **41,** 9948–9951 (2008).
137. Seguini, G. *et al.* Thermally induced self-assembly of cylindrical nanodomains in low molecular weight PS-b-PMMA thin films. *Nanotechnology* **25,** 1–6 (2014).
138. Sinturel, C., Bates, F. S. & Hillmyer, M. A. High X-Low N Block Polymers: How Far Can We Go? *ACS Macro Lett.* **4,** 1044–1050 (2015).
139. Albert, J. N. L. & Epps, T. H. Self-assembly of block copolymer thin films. *Mater. Today* **13,** 24–33 (2010).
140. Thurn-Albrecht, T. *et al.* Nanoscopic templates from oriented block copolymer films. *Adv. Mater.* **12,** 787–791 (2000).
141. Peng, B. Q., Tseng, Y., Darling, S. B. & Elam, J. W. Nanoscopic Patterned Materials with Tunable Dimensions via Atomic Layer Deposition on Block Copolymers. *Adv. Mater.* **22,** 5129–5133 (2010).
142. Rahman, A. *et al.* Sub-50-nm self-assembled nanotextures for enhanced broadband antireflection in silicon solar cells. *Nat. Commun.* **6,** 1–6 (2015).
143. Kumar, N. & Hahm, J. I. Nanoscale protein patterning using self-assembled diblock copolymers. *Langmuir* **21,** 6652–6655 (2005).
144. Lau, K. H. A., Bang, J., Kim, D. H. & Knoll, W. Self-assembly of Protein Nanoarrays on Block Copolymer Templates. *Adv. Funct. Mater.* **18,** 3148–3157 (2008).
145. Liu, D., Che Abdullah, C. A., Sear, R. P. & Keddie, J. L. Cell adhesion on nanopatterned fibronectin substrates. *Soft Matter* **6,** 5408–5416 (2010).
146. Liu, D., Wang, T. & Keddie, J. L. Protein Nanopatterning on Self-Organized Poly (styrene-b-isoprene) Thin Film Templates. *Langmuir* **25,** 4526–4534 (2009).
147. Kumar, N., Parajuli, O., Gupta, A. & Hahm, J. I. Elucidation of protein adsorption behavior on polymeric surfaces: Toward high-density, high-payload protein templates. *Langmuir* **24,** 2688–2694 (2008).
148. Lagunas, A. *et al.* Cell adhesion and focal contact formation on linear RGD

molecular gradients: study of non-linear concentration dependence effects. *Nanomedicine Nanotechnology, Biol. Med.* **8,** 432–439 (2017).
149. Lagunas, A., Comelles, J., Martínez, E. & Samitier, J. Universal chemical gradient platforms using poly(methyl methacrylate) based on the biotin-streptavidin interaction for biological applications. *Langmuir* **26,** 14154–14161 (2010).
150. George, P. A., Doran, M. R., Croll, T. I., Munro, T. P. & Cooper-White, J. J. Nanoscale presentation of cell adhesive molecules via block copolymer self-assembly. *Biomaterials* **30,** 4732–4737 (2009).
151. George, P. a, Donose, B. C. & Cooper-White, J. J. Self-assembling polystyrene-block-poly(ethylene oxide) copolymer surface coatings: resistance to protein and cell adhesion. *Biomaterials* **30,** 2449–2456 (2009).
152. Kim, Y. *et al.* Efficient Site-Specific Labeling of Proteins via Cysteines. *Bioconjug. Chem.* **19,** 786–791 (2008).
153. Frith, J. E., Mills, R. J., Hudson, J. E. & Cooper-White, J. J. Tailored integrin-extracellular matrix interactions to direct human mesenchymal stem cell differentiation. *Stem Cells Dev.* **21,** 2442–2456 (2012).
154. Lummerstorfer, T. & Hoffmann, H. Click Chemistry on Surfaces: 1,3-Dipolar Cycloaddition Reactions of Azide-Terminated Monolayers on Silica. *J. Phys. Chem. B* **108,** 3963–3966 (2004).
155. Rozkiewicz, D. I., Jańczewski, D., Verboom, W., Ravoo, B. J. & Reinhoudt, D. N. 'Click' chemistry by microcontact printing. *Angew. Chemie - Int. Ed.* **45,** 5292–5296 (2006).
156. Liu, X., Zheng, H. N., Ma, Y. Z., Yan, Q. & Xiao, S. J. Microwave irradiated click reactions on silicon surfaces via derivertization of covalently grafted poly(PEGMA) brushes. *J. Colloid Interface Sci.* **358,** 116–122 (2011).
157. Bertoldo, M., Zampano, G., Terra, F. La, Villari, V. & Castelvetro, V. Amphiphilic amylose-g-poly(meth)acrylate copolymers through 'click' onto grafting method. *Biomacromolecules* **12,** 388–398 (2011).
158. Shen, L. *et al.* Two dimensional nanoarrays of individual protein molecules. *Small* **8,** 3169–3174 (2012).
159. Shen, L. & Zhu, J. Oriented Protein Nanoarrays on Block Copolymer Template. *Macromol. Rapid Commun.* **37,** 494–499 (2016).
160. Jeong, U. *et al.* Phase behavior of mixtures of block copolymer and homopolymers in thin films and bulk. *Macromolecules* **36,** 3626–3634 (2003).
161. Dimitriou, M. D. *et al.* A General Approach to Controlling the Surface Composition of Poly (ethylene oxide) -Based Block Copolymers for Antifouling Coatings. *Langmuir* **27,** 13762–13772 (2011).
162. Campos, L. M. *et al.* Development of Thermal and Photochemical Strategies for Thiol - Ene Click Polymer Functionalization. *Macromolecules* **47,** 7063–7070 (2008).
163. Lagunas, A. *et al.* Synthesis of a polymethyl(methacrylate)- polystyrene-based diblock copolymer containing biotin for selective protein nanopatterning. *Polym. Chem.* **7,** 212–218 (2016).
164. Killops, K. L. *et al.* Nanopatterning Biomolecules by Block Copolymer Self-Assembly. *ACS Macro Lett.* **1,** 758–763 (2012).

165. Dalby, M. J., Riehle, M. O., Johnstone, H. J. H., Affrossman, S. & Curtis, A. S. G. Polymer-demixed nanotopography: control of fibroblast spreading and proliferation. *Tissue Eng.* **8,** 1099–1108 (2002).
166. Dalby, M. J. Topographically induced direct cell mechanotransduction. *Med. Eng. Phys.* **27,** 730–742 (2005).
167. Speetjens, F. W. *et al.* Post-Fabrication Placement of Arbitrary Chemical Functionality on Microphase-Separated Thin Films of Amine-Reactive Block Copolymers. *ACS Macro Lett.* **3,** 1178–1182 (2014).
168. Ebensteina, Y., Natalie Gassmana, Kima, S. & Weiss, S. Combining atomic force and fluorescence microscopy for analysis of quantum-dot labeled protein–DNA complexes Yuval. *J. Mol. Recognit.* **22,** 397–402 (2009).
169. PETERS, K.-R. Collection Deficiencies of Scanning Electron Microscopy Signal Contrasts Measured and Corrected by Differential Hysteresis Image Processing. *Scanning* **18,** 539–555 (1996).
170. Lin, P., Lin, S., Wang, P. C. & Sridhar, R. Techniques for physicochemical characterization of nanomaterials. *Biotechnol. Adv.* **32,** 711–726 (2014).
171. Lehnert, D. *et al.* Cell behaviour on micropatterned substrata: limits of extracellular matrix geometry for spreading and adhesion. *J. Cell Sci.* **117,** 41–52 (2004).
172. Hyun, J., Zhu, Y., Liebmann-Vinson, A., Beebe, T. P. & Chilkoti, A. Microstamping on an activated polymer surface: Patterning biotin and streptavidin onto common polymeric biomaterials. *Langmuir* **17,** 6358–6367 (2001).
173. Ogaki, R., Lyckegaard, F. & Kingshott, P. High-Resolution Surface Chemical Analysis of a Trifunctional Pattern Made by Sequential Colloidal Shadowing. *ChemPhysChem* **11,** 3609–3616 (2010).
174. Coyer, S. R. *et al.* Nanopatterning reveals an ECM area threshold for focal adhesion assembly and force transmission that is regulated by integrin activation and cytoskeleton tension. *J. Cell Sci.* **125,** 5110–5123 (2012).
175. Born, M. A. X. & Wolf, E. *Principles of optics*. (Cambridge University Press, 1999).
176. Hell, S. W. & Wichmann, J. Breaking the diffraction resolution limit by stimulated emission : stimulated-emission-depletion fluorescence microscopy. *Opt. Lett.* **19,** 780–782 (1994).
177. Hell, S. W. Far-Field Optical Nanoscopy. *Science (80-.).* **316,** 1153–1158 (2007).
178. Gustafsson, M. G. L. Nonlinear structured-illumination microscopy : Wide-field fluorescence imaging with theoretically unlimited resolution. *Proc. Natl. Acad. Sci.* **102,** 13081–13086 (2005).
179. Betzig, E., Lewis, A., Harootunian, A., Isaacson, M. & Kratschmer, E. Near Field Scanning Optical Microscopy (NSOM). *Biophys. J.* **49,** 269–279 (1986).
180. Rust, M. J., Bates, M. & Zhuang, X. Sub-diffraction limit imaging by stochastic optical reconstruction microscopy (STORM). *Nat. Methods* **3,** 793–795 (2006).
181. Betzig, E. *et al.* Imaging Intracellular Fluorescent Proteins at Nanometer Resolution. *Science (80-.).* **313,** 1642–1646 (2006).
182. Hess, S. T., Girirajan, T. P. K. & Mason, M. D. Ultra-High Resolution Imaging

by Fluorescence Photoactivation Localization Microscopy. *Biophys. J.* **91,** 4258–4272 (2006).
183. Gramlich, M. W., Bae, J., Hayward, R. C. & Ross, J. L. Fluorescence imaging of nanoscale domains in polymer blends using stochastic optical reconstruction microscopy (STORM). *Opt. Express* **22,** 8438–8450 (2014).
184. Sherman, E., Barr, V. & Samelson, L. E. Super-resolution characterization of TCR-dependent signaling clusters. *Immunol. Rev.* **251,** 21–35 (2013).
185. Schwab, E. H. *et al.* Nanoscale Control of Surface Immobilized BMP-2: Toward a Quantitative Assessment of BMP-Mediated Signaling Events. *Nano Lett.* **15,** 1526–1534 (2015).
186. Kleinman, H. K., Philp, D. & Hoffman, M. P. Role of the extracellular matrix in morphogenesis. *Curr. Opin. Biotechnol.* **14,** 526–532 (2003).
187. Giancotti, F. G. Integrin Signaling. *Science (80-.).* **285,** 1028–1033 (1999).
188. ffrench-Constant, C. & Colognato, H. Integrins: versatile integrators of extracellular signals. *Trends Cell Biol.* **14,** 678–686 (2004).
189. Kanchanawong, P. *et al.* Nanoscale architecture of integrin-based cell adhesions. *Nature* **468,** 580–584 (2010).
190. Roca-Cusachs, P. *et al.* Integrin-dependent force transmission to the extracellular matrix by α-actinin triggers adhesion maturation. *Proc. Natl. Acad. Sci. U. S. A.* **110,** 1–10 (2013).
191. Roca-Cusachs, P., Iskratsch, T. & Sheetz, M. P. Finding the weakest link: exploring integrin-mediated mechanical molecular pathways. *J. Cell Sci.* **125,** 3025–3038 (2012).
192. Gallant, N. D., Michael, K. E. & Garcı, J. Cell Adhesion Strengthening : Contributions of Adhesive Area , Integrin Binding , and Focal Adhesion Assembly. *Mol. Biol. Cell* **16,** 4329–4340 (2005).
193. Hu, Y. *et al.* FAK and paxillin dynamics at focal adhesions in the protrusions of migrating cells. *Sci. Rep.* **4,** 1–7 (2014).
194. Wehrle-haller, B. Assembly and disassembly of cell matrix adhesions. *Curr. Opin. Cell Biol.* **24,** 569–581 (2012).
195. Kuo, J., Han, X., Hsiao, C., Iii, J. R. Y. & Waterman, C. M. Analysis of the myosin-II-responsive focal adhesion proteome reveals a role for β - Pix in negative regulation of focal adhesion maturation. *Nat. Publ. Gr.* **13,** 383–393 (2011).
196. Ruoslahti, E. RGD and other recognition sequences for integrins. *Annu. Rev. Cell Dev. Biol.* **12,** 697–715 (1996).
197. Comisar, W. a, Kazmers, N. H., Mooney, D. J. & Linderman, J. J. Engineering RGD nanopatterned hydrogels to control preosteoblast behavior: a combined computational and experimental approach. *Biomaterials* **28,** 4409–4417 (2007).
198. Maheshwari, G., Brown, G., Lauffenburger, D. A., wells, A. & Griffith, L. G. Cell adhesion and motility depend on nanoscale RGD clustering. *J. Cell Sci.* **113,** 1677–1686 (2000).
199. Geiger, B., Spatz, J. P. & Bershadsky, A. D. Environmental sensing through focal adhesions. *Nat. Rev. Mol. Cell Biol.* **10,** 21–33 (2009).
200. Arnold, M. *et al.* Induction of cell polarization and migration by a gradient of nanoscale variations in adhesive ligand spacing. *Nano Lett.* **8,** 2063–2069 (2008).

201. Hirschfeld-warneken, V. C. *et al.* Cell adhesion and polarisation on molecularly defined spacing gradient surfaces of cyclic RGDfK peptide patches. *Eur. J. Cell Biol.* **87,** 743–750 (2008).
202. Jiang, F., Ho, H., Howard, J. & Mu, D. J. Assembly of collagen into microribbons : effects of pH and electrolytes. *J. Struct. Biol.* **148,** 268–278 (2004).
203. Huang, J. & Ding, J. Nanostructured interfaces with RGD arrays to control cell–matrix interaction. *Soft Matter* **6,** 3395–3401 (2010).
204. Wang, X. *et al.* Effect of RGD nanospacing on differentiation of stem cells. *Biomaterials* **34,** 2865–2874 (2013).
205. Lagunas, A. *et al.* Tailoring RGD local surface density at the nanoscale toward adult stem cell chondrogenic commitment. *Nano Res.* **2,** 1–13 (2016).
206. Deeg, J. a *et al.* Impact of local versus global ligand density on cellular adhesion. *Nano Lett.* **11,** 1469–1476 (2011).
207. Stein, E. *et al.* Eph receptors discriminate specific ligand oligomers to determine alternative signaling complexes, attachment, and assembly responses. *Genes Dev.* **12,** 667–678 (1998).
208. Stein, E. *et al.* Eph receptors discriminate specific ligand oligomers to determine alternative signaling complexes , attachment , and assembly responses. *Genes Dev.* **12,** 667–678 (1998).
209. Ng, Q. K. *et al.* Engineering Clustered Ligand Binding Into Nonviral Vectors: αvβ3 Targeting as an Example. *Mol. Ther.* **17,** 828–836 (2009).
210. Kim, Y. E., Kim, Y.-N., Kim, J. a, Kim, H. M. & Jung, Y. Green fluorescent protein nanopolygons as monodisperse supramolecular assemblies of functional proteins with defined valency. *Nat. Commun.* **6,** 7134 (2015).
211. Pasquale, E. B. Eph receptor signalling casts a wide net on cell behaviour. *Nat. Rev. Mol. Cell Biol.* **6,** 462–475 (2005).
212. Macrae, M. *et al.* A conditional feedback loop regulates Ras activity through EphA2. *Cancer Cell* **8,** 111–118 (2005).
213. Himanen, J. P. *et al.* Architecture of Eph receptor clusters. *Proc. Natl. Acad. Sci.* **107,** 10860–1865 (2010).
214. Janes, P. W., Nievergall, E. & Lackmann, M. Concepts and consequences of Eph receptor clustering. *Semin. Cell Dev. Biol.* **23,** 43–50 (2012).
215. Conway, A. *et al.* Multivalent ligands control stem cell behaviour in vitro and in vivo. *Nat. Nanotechnol.* **8,** 831–8 (2013).
216. Shaw, A. *et al.* Spatial control of membrane receptor function using ligand nanocalipers. *Nat. Methods* **11,** 841–846 (2014).
217. Dunn, K. E. *et al.* Guiding the folding pathway of DNA origami. *Nature* **525,** 82–86 (2015).
218. Paviolo, C., Chon, J. W. M. & Clayton, A. H. A. Inhibiting EGFR clustering and cell proliferation with gold nanoparticles. *Small* **11,** 1638–1643 (2015).
219. Hartman, N. C. & Groves, J. T. Signaling clusters in the cell membrane. *Curr. Opin. Cell Biol.* **23,** 370–376 (2011).
220. Koo, L. Y., Irvine, D. J., Mayes, A. M., Lauffenburger, D. a & Griffith, L. G. Co-regulation of cell adhesion by nanoscale RGD organization and mechanical stimulus. *J. Cell Sci.* **115,** 1423–1433 (2002).

221. Comisar, W. a, Hsiong, S. X., Kong, H.-J., Mooney, D. J. & Linderman, J. J. Multi-scale modeling to predict ligand presentation within RGD nanopatterned hydrogels. *Biomaterials* **27,** 2322–2329 (2006).
222. Mossman, K. D., Campi, G., Groves, J. T. & Dustin, M. L. Altered TCR signaling from geometrically repatterned immunological synapses. *Science* **310,** 1191–1193 (2005).
223. Bosch, B., Heipertz, E. L., Drake, J. R. & Roche, P. A. Major histocompatibility complex (MHC) class II-peptide complexes arrive at the plasma membrane in cholesterol-rich microclusters. *J. Biol. Chem.* **288,** 13236–13242 (2013).
224. Ferez, M., Castro, M., Alarcon, B. & van Santen, H. M. Cognate peptide-MHC complexes are expressed as tightly apposed nanoclusters in virus-infected cells to allow TCR crosslinking. *J Immunol* **192,** 52–58 (2014).
225. Castro, M. *et al.* Receptor pre-clustering and T cell responses: Insights into molecular mechanisms. *Front. Immunol.* **5,** 1–11 (2014).
226. Yu, C. han, Wu, H. J., Kaizuka, Y., Vale, R. D. & Groves, J. T. Altered actin centripetal retrograde flow in physically restricted immunological synapses. *PLoS One* **5,** 1–9 (2010).
227. Dillard, P., Varma, R., Sengupta, K. & Limozin, L. Ligand-mediated friction determines morphodynamics of spreading T cells. *Biophys. J.* **107,** 2629–2638 (2015).
228. Hartman, N. C., Nye, J. a & Groves, J. T. Cluster size regulates protein sorting in the immunological synapse. *Proc. Natl. Acad. Sci. U. S. A.* **106,** 12729–12734 (2009).
229. Caculitan, N. G. *et al.* Size-based chromatography of signaling clusters in a living cell membrane. *Nano Lett.* **14,** 2293–2298 (2014).
230. Ketchum, C., Miller, H., Song, W. & Upadhyaya, A. Ligand mobility regulates B cell receptor clustering and signaling activation. *Biophys. J.* **106,** 26–36 (2014).
231. Xu, Q., Lin, W. C., Petit, R. S. & Groves, J. T. EphA2 receptor activation by monomeric ephrin-A1 on supported membranes. *Biophys. J.* **101,** 2731–2739 (2011).
232. Salaita, K. *et al.* Restriction of receptor movement alters cellular response: physical force sensing by EphA2. *Science* **327,** 1380–1385 (2010).
233. Nievergall, E., Lackmann, M. & Janes, P. W. Eph-dependent cell-cell adhesion and segregation in development and cancer. *Cell. Mol. Life Sci.* **69,** 1813–1842 (2012).
234. Lohmüller, T., Xu, Q. & Groves, J. T. Nanoscale obstacle arrays frustrate transport of EphA2-ephrin-A1 clusters in cancer cell lines. *Nano Lett.* **13,** 3059–3064 (2013).
235. Abulrob, A. *et al.* Nanoscale imaging of epidermal growth factor receptor clustering: Effects of inhibitors. *J. Biol. Chem.* **285,** 3145–3156 (2010).
236. Digman, M. A., Dalal, R., Horwitz, A. F. & Gratton, E. Mapping the Number of Molecules and Brightness in the Laser Scanning Microscope. *Biophys. J.* **94,** 2320–2332 (2008).
237. Mansky, P. Controlling Polymer-Surface Interactions with Random Copolymer Brushes. *Science (80-.).* **275,** 1458–1460 (1997).
238. Yadav, A. R., Sriram, R., Carter, J. A. & Miller, B. L. Comparative study of

solution-phase and vapor-phase deposition of aminosilanes on silicon dioxide surfaces. *Mater. Sci. Eng. C* **35,** 283–290 (2014).
239. Kurth, D. G. & Bein, T. Thin-Films of (3-Aminopropyl)Triethoxysilane on Aluminum-Oxide and Gold Substrates. *Langmuir* **11,** 3061–3067 (1995).
240. Horcas, I. *et al.* WSXM: a software for scanning probe microscopy and a tool for nanotechnology. *Rev. Sci. Instrum.* **78,** 1–8 (2007).
241. Zucchi, I. a, Poliani, E. & Perego, M. Microdomain orientation dependence on thickness in thin films of cylinder-forming PS-b-PMMA. *Nanotechnology* **21,** 1–5 (2010).
242. Borah, D. *et al.* Molecularly functionalized silicon substrates for orientation control of the microphase separation of PS-b-PMMA and PS-b-PDMS block copolymer systems. *Langmuir* **29,** 2809–2820 (2013).
243. Ton-That, C., Shard, A. G. & Bradley, R. H. Thickness of spin-cast polymer thin films determined by angle-resolved XPS and AFM tip-scratch methods. *Langmuir* **16,** 2281–2284 (2000).
244. Çaykara, T. & Güven, O. UV degradation of poly(methyl methacrylate) and its vinyltriethoxysilane containing copolymers. *Polym. Degrad. Stab.* **65,** 225–229 (1999).
245. Li, L. *et al.* Thermally stable and solvent resistant honeycomb structured polystyrene films via photochemical cross-linking. *J. Mater. Chem.* **19,** 7222–7227 (2009).
246. Cooley, J. W. & Turkey, J. W. An algorithm for the machine calculation of complex Fourier series. *Math. Comput.* **19,** 297–301 (1965).
247. Glynn, E. F. Fourier Analysis and Image Processing Fourier Analysis and Image Processing • History • Periodic Signals • Fourier Analysis • 2D FFT and Image Processing. *Signals* (2007).
248. Lee, K. L. & Chen, L. H. A New Method for Coarse Classification of Textures and Class Weight Estimation for Texture Retrieval. *Pattern Recognit. image Anal.* **12,** 400–410 (2002).
249. La, Y. H., Edwards, E. W., Park, S. M. & Nealey, P. F. Directed assembly of cylinder-forming block copolymer films and thermochemically induced cylinder to sphere transition: A hierarchical route to linear arrays of nanodots. *Nano Lett.* **5,** 1379–1384 (2005).
250. Zuyderhoff, E. M. & Dupont-Gillain, C. C. Nano-organized collagen layers obtained by adsorption on phase-separated polymer thin films. *Langmuir* **28,** 2007–2014 (2012).
251. Erhardt, R. *et al.* Amphiphilic Janus micelles with polystyrene and poly(methacrylic acid) hemispheres. *J. Am. Chem. Soc.* **125,** 3260–3267 (2003).
252. Royal, C. M. Properties of Poly (methyl Methacrylate-co-methacry LC Acid) Copolymers Obtained by Partial Hydrolysis of PMMA. 327–338
253. Amenabar, I. *et al.* Hyperspectral infrared nanoimaging of organic samples based on Fourier transform infrared nanospectroscopy. *Nat. Commun.* **8,** 14402 (2017).
254. Chalovich, J. M. & Eisenberg, E. Super-resolution Microscopy of Lipid Bilayer Phases. *J Am Chem Soc.* **133,** 4664–4667 (2011).
255. Huang, J. *et al.* Impact of Order and Disorder in RGD Nanopatterns on Cell

Adhesion 2009. *Nano Lett.* **9,** 1111–1116 (2009).
256. Stamm, M. *Polymer Surfaces and Interfaces: Characterization, Modification and Applications*. (Springer Berlin Heidelberg, 2008).
257. Hersel, U., Dahmen, C. & Kessler, H. RGD modified polymers: biomaterials for stimulated cell adhesion and beyond. *Biomaterials* **24,** 4385–4415 (2003).
258. Juerg H. Beer, K. T. S. & Coller, B. S. Immobilized Arg-Gly-Asp (RGD) Peptides of Varying Lengths as Structural Probes of the Platelet Glycoprotein IIb/IIIa Receptor. *Blood* **79,** 117–129 (1992).
259. Fischer, M. J. E. in *Surface Plasmon Resonance: Methods and Protocols* (eds. Mol, N. J. & Fischer, M. J. E.) 55–73 (Humana Press, 2010). doi:10.1007/978-1-60761-670-2_3
260. Zhuang, X. Nano-imaging with STORM. *Nat. Photonics* **3,** 365–367 (2009).
261. Dempsey, G. T., Vaughan, J. C., Chen, K. H., Bates, M. & Zhuang, X. Evaluation of fluorophores for optimal performance in localization-based super-resolution imaging. *Nat. Methods* **8,** 1027–1036 (2011).
262. Marchand, É., Spindler, F. & Chaumette, F. ViSP: A generic software platform for visual servoing. *IEEE Robot. Autom. Mag.* **12,** 40–52 (2005).
263. Selhuber-Unkel, C., López-García, M., Kessler, H. & Spatz, J. P. Cooperativity in adhesion cluster formation during initial cell adhesion. *Biophys. J.* **95,** 5424–5431 (2008).
264. Paul, J. H. Use of Hoechst dyes 33258 and 33342 for enumeration of attached and planktonic bacteria. *Appl. Environ. Microbiol.* **43,** 939–944 (1982).
265. Chazotte, B. Labeling cytoskeletal F-Actin with rhodamine phalloidin or fluorescein phalloidin for imaging. *Cold Spring Harb. Protoc.* **5,** 2006–2009 (2010).
266. Turner, C. E. Paxillin and focal adhesion signalling. *Nat. Cell Biol.* **2,** E231–E236 (2000).
267. Schaller, M. D. Paxillin: a focal adhesion-associated adaptor protein. *Oncogene* **20,** 6459–6472 (2001).
268. Rohani, N., Parmeggiani, A., Winklbauer, R. & Fagotto, F. Variable Combinations of Specific Ephrin Ligand/Eph Receptor Pairs Control Embryonic Tissue Separation. *PLoS Biol.* **12,** 1–20 (2014).
269. Sheffler-Collins, S. I. & Dalva, M. B. EphBs: An integral link between synaptic function and synaptopathies. *Trends Neurosci.* **35,** 293–304 (2012).
270. Lohmüller, T. *et al.* Supported Membranes Embedded with Fixed Arrays of Gold Nanoparticles. *Nano Lett.* **11,** 4912–4918 (2011).
271. Rudolph, J. *et al.* A dual role of EphB1/ephrin-B3 reverse signaling on migrating striatal and cortical neurons originating in the preoptic area: should I stay or go away? *Front. Cell. Neurosci.* **8,** 1–20 (2014).
272. Watts, K. C. & Husain, O. A. N. Optimal use of the cationic the preparation of cell monolayers for diagnostic cytopathology. *J. Clin. Pathol.* **37,** 829–831 (1984).
273. Wilbur, J. L., Kumar, A., Kim, E. & Whitesides, G. M. Microfabrication by microcontact printing of self-assembled monolayers. *Adv. Mater.* **6,** 600–604 (1994).

274. Shen, K., Qi, J. & Kam, L. C. Microcontact printing of proteins for cell biology. *J. Vis. Exp.* 8–10 (2008).
275. Ojosnegros, S. *et al.* Cell-cell communication signaling modulated by polymerization-condensation of receptors. *Under Rev.*
276. Trullo, A., Corti, V., Arza, E., Caiolfa, V. R. & Zamai, M. Application limits and data correction in number of molecules and brightness analysis. *Microsc. Res. Tech.* **76,** 1135–1146 (2013).
277. She, M.-S., Lo, T.-Y. & Ho, R.-M. Controlled Ordering of Block Copolymer Gyroid Thin Films by Solvent Annealing. *Macromolecules* **47,** 175–182 (2014).
278. Mansky, P. *et al.* Interfacial Segregation in Disordered Block Copolymers: Effect of Tunable Surface Potentials. *Phys. Rev. Lett.* **79,** 237–240 (1997).
279. Chang, T.-H. *et al.* Directed self-assembly of block copolymer films on atomically-thin graphene chemical patterns. *Sci. Rep.* **6,** 1–9 (2016).
280. Han, E. *et al.* Photopatternable imaging layers for controlling block copolymer microdomain orientation. *Adv. Mater.* **19,** 4448–4452 (2007).
281. Pujari, S., Keaton, M. a., Chaikin, P. M. & Register, R. a. Alignment of perpendicular lamellae in block copolymer thin films by shearing. *Soft Matter* **8,** 5358–5363 (2012).
282. Dess, R., Pinna, M. & Zvelindovsky, A. V. Cell Dynamics Simulations of Cylinder-Forming Diblock Copolymers in Thin Films on Topographical and Chemically Patterned Substrates. *Macromolecules* **46,** 1923–1931 (2013).
283. Wang, Q., Yan, Q., Nealey, P. F. & de Pablo, J. J. Monte Carlo simulations of diblock copolymer thin films confined between two homogeneous surfaces. *J. Chem. Phys.* **112,** 450–464 (2000).
284. Sunday, D. F. *et al.* Template – Polymer Commensurability and Directed Self-Assembly Block Copolymer Lithography. 595–603 (2015). doi:10.1002/polb.23675
285. Leung, O. M. & Goh, M. C. Orientational Ordering of Polymers by Atomic Force Microscope Tip-Surface Interaction. *Science (80-.).* **255,** 64–66 (1992).
286. Zhang, H., Honda, Y. & Takeoka, S. Tapping-mode AFM study of tip-induced polymer deformation under geometrical confinement. *Langmuir* **29,** 1333–1339 (2013).
287. Kaur, G. *et al.* Regulation of osteogenic differentiation of rat bone marrow stromal cells on 2D nanorod substrates. *Biomaterials* **31,** 1732–1741 (2010).
288. Jin, C. Y. *et al.* Nanoscale surface topography enhances cell adhesion and gene expression of madine darby canine kidney cells. *J. Mater. Sci. Mater. Med.* **19,** 2215–2222 (2008).
289. Gentile, F. *et al.* Cells preferentially grow on rough substrates. *Biomaterials* **31,** 7205–7212 (2010).
290. Dalby, M. J. *et al.* Fibroblast reaction to island topography: changes in cytoskeleton and morphology with time. *Biomaterials* **24,** 927–935 (2003).
291. Allbritton, H. S. and N. L. In-Situ Roughening of Polymeric Microstructures. *ACS Appl Mater Interfaces.* **2,** 1086–1093 (2010).
292. Kim, D. H., Lin, Z., Kim, H. C., Jeong, U. & Russell, T. P. On the replication of

block copolymer templates by poly(dimethylsiloxane) elastomers. *Adv. Mater.* **15,** 811–814 (2003).
293. Simão, C. *et al.* Order quantification of hexagonal periodic arrays fabricated by in situ solvent-assisted nanoimprint lithography of block copolymers. *Nanotechnology* **25,** 1–8 (2014).
294. Xu, T., Zhu, Y., Gido, S. P. & Russell, T. P. Electric Field Alignment of Symmetric Diblock Copolymer Thin Films. *Macromolecules* **37,** 2625–2629 (2004).
295. Malmström, J. *et al.* Large area protein patterning reveals nanoscale control of focal adhesion development. *Nano Lett.* **10,** 686–694 (2010).
296. Agheli, H., Malmström, J., Larsson, E. M., Textor, M. & Sutherland, D. S. Large area protein nanopatterning for biological applications. *Nano Lett.* **6,** 1165–1171 (2006).
297. Malmström, J. & Travas-Sejdic, J. Block Copolymers for Protein Ordering. *J. Appl. Polym. Sci.* **131,** 40360–40372 (2014).
298. Ogura, K. & Sobue, H. Infrared spectroscopic approaches to polymer transitions. II. The transition of hydrogen bonding in styrene-methacrylic acid (St-MAA) copolymers. *Polym. J.* **3,** 153–158 (1972).
299. Rufino, E. S. & Monteiro, E. E. C. Infrared study on methyl methacrylate – methacrylic acid copolymers and their sodium salts. *Polymer (Guildf).* **44,** 7189–7198 (2003).
300. Hiller, W., Sinha, P. & Pasch, H. Online HPLC-NMR of PS -b- PMMA and Blends of PS and PMMA , 2 - LCCC-NMR at Critical Conditions of PMMA a. *Macromol. Chem. Phys.* **210,** 605–613 (2009).
301. Mori, H. & Müller, A. H. E. New polymeric architectures with (meth) acrylic acid segments. *Prog. Polym. Sci.* **28,** 1403–1439 (2003).
302. Xie, R., Karim, A., Douglas, J. F., Han, C. C. & Weiss, R. A. Spinodal Dewetting of Thin Polymer Films. *Phys. re* **81,** 1251–1254 (1998).
303. Becker, J. *et al.* Complex dewetting scenarios captured by thin-film models. *Nat. Mater.* **2,** 59–63 (2003).
304. Zuyderhoff, E. M., Dekeyser, C. M., Rouxhet, P. G. & Dupont-Gillain, C. C. An AFM, XPS and wettability study of the surface heterogeneity of PS/PMMA-r-PMAA demixed thin films. *J. Colloid Interface Sci.* **319,** 63–71 (2008).
305. Louette, P., Bodino, F. & Pireaux, J.-J. Poly(methyl methacrylate) (PMMA) XPS Reference Core Level and Energy Loss Spectra. *Surf. Sci. Spectra* **12,** 69–73 (2005).
306. Chung, K., DeQUACH, J. a. & Christman, K. L. Nanopatterned Interfaces for Controlling Cell Behavior. *Nano Life* **1,** 63–77 (2010).
307. Tran, H., Killops, K. L. & Campos, L. M. Advancements and challenges of patterning biomolecules with sub-50 nm features. *Soft Matter* **9,** 6578–6586 (2013).
308. Ekerdt, B. L., Segalman, R. A. & Schaffer, D. V. Spatial organization of cell-adhesive ligands for advanced cell culture. *Biotechnol. J.* **8,** 1411–1423 (2013).
309. Fischer, M. J. E. in *Methods in Molecular Biology* **627,** 147–155 (2010).
310. von der Mark, K., Park, J., Bauer, S. & Schmuki, P. Nanoscale engineering of biomimetic surfaces: cues from the extracellular matrix. *Cell Tissue Res.* **339,**

131–153 (2010).
311. Lim, J. Y. & Donahue, H. J. Cell sensing and response to micro- and nanostructured surfaces produced by chemical and topographic patterning. *Tissue Eng.* **13,** 1879–1891 (2007).
312. Petrie, T. A. *et al.* Multivalent Integrin-Specific Ligands Enhance Tissue Healing and Biomaterial Integration. *Sci. Transl. Med.* **2,** 1–13 (2010).
313. Lee, K. Y. *et al.* Nanoscale Adhesion Ligand Organization Regulates Osteoblast Proliferation and Differentiation. *Nano Lett.* **4,** 1501–1503 (2004).
314. Kania, A. & Klein, R. Mechanisms of ephrin-Eph signalling in development, physiology and disease. *Nat. Rev. Mol. Cell Biol.* **17,** 240–56 (2016).
315. Davis, S. *et al.* Ligands for EPH-related receptor tyrosine kinases that require membrane attachment or clustering for activity. *Science* **266,** 816–819 (1994).
316. Beckmann, M. P. *et al.* Molecular characterization of a family of ligands for eph-related tyrosine kinase receptors. *EMBO J.* **13,** 3757–3762 (1994).
317. Salaita, K. *et al.* Restriction of receptor movement alters cellular response: physical force sensing by EphA2. *Science* **327,** 1380–1385 (2010).
318. Abulrob, A. *et al.* Nanoscale imaging of epidermal growth factor receptor clustering: Effects of inhibitors. *J. Biol. Chem.* **285,** 3145–3156 (2010).
319. Seiradake, E., Harlos, K., Sutton, G., Aricescu, A. R. & Jones, E. Y. An extracellular steric seeding mechanism for Eph-ephrin signaling platform assembly. *Nat Struct Mol Biol* **17,** 398–402 (2010).
320. Himanen, J. P. *et al.* Crystal structure of an Eph receptor-ephrin complex. *Nature* **414,** 933–938 (2001).
321. Day, B. *et al.* Three distinct molecular surfaces in Ephrin-A5 are essential for a functional interaction with EphA3. *J. Biol. Chem.* **280,** 26526–26532 (2005).
322. Nikolov, D. B., Xu, K. & Himanen, J. P. Eph/ephrin recognition and the role of Eph/ephrin clusters in signaling initiation. *Biochim. Biophys. Acta - Proteins Proteomics* **1834,** 2160–2165 (2013).
323. Schaupp, A. *et al.* The composition of EphB2 clusters determines the strength in the cellular repulsion response. *J. Cell Biol.* **204,** 409–422 (2014).
324. Passante, L. *et al.* Temporal regulation of ephrin/Eph signalling is required for the spatial patterning of the mammalian striatum. *Development* **135,** 3281–3290 (2008).
325. Jørgensen, C. *et al.* Cell-specific information processing in segregating populations of Eph receptor ephrin-expressing cells. *Science (80-.).* **326,** 1502–9 (2009).
326. Pitulescu, M. E. & Adams, R. H. Eph / ephrin molecules –– a hub for signaling and endocytosis Eph / ephrin molecules — a hub for signaling and endocytosis. *Genes Dev.* **24,** 2480–2492 (2010).
327. Unruh, J. R. & Gratton, E. Analysis of Molecular Concentration and Brightness from Fluorescence Fluctuation Data with an Electron Multiplied CCD Camera. *Biophys. J.* **95,** 5385–5398 (2008).
328. Nikolov, D. B., Li, C., Barton, W. A. & Himanen, J. P. Crystal structure of the ephrin-B1 ectodomain: Implications for receptor recognition and signaling.

Biochemistry **44,** 10947–10953 (2005).
329. Onclin, S., Ravoo, B. J. & Reinhoudt, D. N. Engineering silicon oxide surfaces using self-assembled monolayers. *Angew. Chemie - Int. Ed.* **44,** 6282–6304 (2005).
330. Smith, A., Douglas, J., Meredith, J., Amis, E. & Karim, A. Combinatorial Study of Surface Pattern Formation in Thin Block Copolymer Films. *Phys. Rev. Lett.* **87,** 15503 (2001).
331. Black, C. T. & Bezencenet, O. Nanometer-Scale Pattern Registration and Alignment by Directed Diblock Copolymer Self-Assembly. *IEEE Trans. Nanotechnol.* **3,** 412–415 (2004).
332. Luo, M. & Epps, T. H. Directed block copolymer thin film self-assembly: Emerging trends in nanopattern fabrication. *Macromolecules* **46,** 7567–7579 (2013).
333. Jeong, S. J., Kim, J. Y., Kim, B. H., Moon, H. S. & Kim, S. O. Directed self-assembly of block copolymers for next generation nanolithography. *Mater. Today* **16,** 468–476 (2013).
334. Yang, J. K. W. *et al.* Complex self-assembled patterns using sparse commensurate templates with locally varying motifs. *Nat. Nanotechnol.* **5,** 256–260 (2010).
335. Stoykovich, M. P. & Nealey, P. F. Block copolymers and conventional lithography. *Mater. Today* **9,** 20–29 (2006).
336. Kennemur, J. G., Hillmyer, M. A. & Bates, F. S. Synthesis, Thermodynamics, and Dynamics of Poly(4- tert - butylstyrene - b - methyl methacrylate). *Macromolecules* **45,** 7228–7236 (2012).
337. Amenabar, I. *et al.* Structural analysis and mapping of individual protein complexes by infrared nanospectroscopy. *Nat. Commun.* **4,** 2890 (2013).
338. Tran, H. *et al.* Hierarchically ordered nanopatterns for spatial control of biomolecules. *ACS Nano* **8,** 11846–11853 (2014).
339. Wiesbauer, M. *et al.* Nano-anchors with single protein capacity produced with STED lithography. *Nano Lett.* **13,** 5672–5678 (2013).
340. Li, X. *et al.* Block Copolymer Modified Surfaces for Conjugation of Biomacromolecules with Control of Quantity and Activity. (2013).
341. Betancourt, T. & Brannon-Peppas, L. Micro-and nanofabrication methods in nanotechnological medical and pharmaceutical devices. *Int. J. Nanomedicine* **1,** 483–495 (2006).
342. Cresce, A. V., Silverstein, J. S., Bentley, W. E. & Kofinas, P. Nanopatterning of recombinant proteins using block copolymer templates. *Macromolecules* **39,** 5826–5829 (2006).
343. Caré, B. R. & Soula, H. a. Impact of receptor clustering on ligand binding. *BMC Syst. Biol.* **5,** 48 (2011).
344. Parpal, S., Karlsson, M., Thorn, H. & Strålfors, P. Cholesterol Depletion Disrupts Caveolae and Insulin Receptor Signaling for Metabolic Control via Insulin Receptor Substrate-1, but Not for Mitogen-activated Protein Kinase Control. *J. Biol. Chem.* **276,** 9670–9678 (2001).
345. Montet, X., Funovics, M., Montet-Abou, K., Weissleder, R. & Josephson, L. Multivalent effects of RGD peptides obtained by nanoparticle display. *J. Med. Chem.* **49,** 6087–6093 (2006).

346. Kong, H. J., Hsiong, S. & Mooney, D. J. Nanoscale cell adhesion ligand presentation regulates nonviral gene delivery and expression. *Nano Lett.* **7,** 161–166 (2007).
347. Maheshwari, G., Brown, G., Lauffenburger, D. a, Wells, a & Griffith, L. G. Cell adhesion and motility depend on nanoscale RGD clustering. *J. Cell Sci.* **113 (Pt 1,** 1677–86 (2000).
348. Roca-cusachs, P., Gauthier, N. C. & Sheetz, M. P. Clustering of alphfa-5-beta-1 integrins determines adhesion strength whereas alpha-5-beta3 and talin enable mechanotransduction. *Proc. Natl. Acad. Sci.* **106,** (2009).
349. Schvartzman, M. *et al.* Nanolithographic control of the spatial organization of cellular adhesion receptors at the single-molecule level. *Nano Lett.* **11,** 1306–12 (2011).
350. Cavalcanti-adam, E. A., Arnold, M., Schwieder, M. & Blu, J. Cell interactions with hierarchically structured nano-patterned adhesive surfaces †. 72–77 (2009). doi:10.1039/b815634d
351. Slater, J. H. & Frey, W. Nanopatterning of fibronectin and the influence of integrin clustering on endothelial cell spreading and proliferation. *J. Biomed. Mater. Res. A* **87,** 176–95 (2008).
352. Kam, L. C., Shen, K. & Dustin, M. L. Micro- and nanoscale engineering of cell signaling. *Annu. Rev. Biomed. Eng.* **15,** 305–26 (2013).
353. Cebecauer, M., Spitaler, M., Sergé, A. & Magee, A. I. Signalling complexes and clusters: functional advantages and methodological hurdles. *J. Cell Sci.* **123,** 309–20 (2010).
354. Bethani, I., Skånland, S. S., Dikic, I. & Acker-Palmer, A. Spatial organization of transmembrane receptor signalling. *EMBO J.* **29,** 2677–88 (2010).
355. Conway, A. *et al.* Multivalent ligands control stem cell behaviour in vitro and in vivo. *Nat. Nanotechnol.* **8,** 831–838 (2013).

8. Resumen en castellano

Estudio de la respuesta celular inducida por la presentación de ligandos nano-agrupados sobre superficies compuestas por copolímeros en bloque

En los tejidos, las células reciben múltiples señales tanto de naturaleza física como química del entorno que las rodea. Inmersas en un entorno tridimensional, las células interactúan entre sí y con la matriz proteica que las envuelve. Además, hasta ellas difunden diversos factores solubles que transmiten señales químicas revelantes implicadas en el correcto funcionamiento celular. Ante tan complejo entorno, las células son capaces de reconocer de manera diferencial los estímulos que reciben y responder a todos ellos a través de complejos mecanismos intracelulares de señalización.

Recientemente, se han desarrollado herramientas altamente sofisticadas que permiten estudiar el comportamiento celular ante una presentación definida de ligandos. Se ha demostrado que fenómenos tan relevantes como la adhesión, la proliferación o la diferenciación celular son sensibles a la distribución espacial nanométrica de ligandos en superficie. Múltiples receptores celulares, cuando son estimulados por sus correspondientes ligandos, necesitan agruparse y formar clústers que modulan la transmisión de la señal. Desafortunadamente, todavía se desconocen los pormenores de la activación y la dinámica de agregación de los mismos ante las múltiples combinaciones espaciales de ligandos.

Por este motivo, este trabajo tiene como objetivo el desarrollo de superficies que permitan la presentación controlada de ligandos en grupos nanométricos para analizar el efecto de los mismos en los procesos de señalización intracelular. Para abordar este ambicioso objetivo, se desarrolló una plataforma a partir de copolímeros en bloque cuya principal particularidad es que se autoensamblan, generando estructuras nanométricas. El copolímero en bloque más utilizado en este ámbito es el compuesto por poliestireno y poli(metil metacrilato) (PS-b-PMMA). En este estudio se utilizaron dos copolímeros en bloque con distinta fracción volumétrica de cada uno de los componentes, de

manera que se autoensamblan generando cilindros nanométricos de PMMA inmersos en una matriz de PS. Cuando se depositan en una capa fina sobre un sustrato de silicio o de vidrio, y se controla tanto el grosor de la capa como la energía superficial del sustrato, se puede conseguir que los cilindros se posicionen de forma perpendicular y ordenada sobre la superficie.

Para ello, en primer lugar se modificó la energía superficial del sustrato mediante el anclaje de polímeros con una disposición de monómeros aleatoria. Por otro lado, el grosor de la capa fina se controló mediante la concentración de la solución empleada y esta capa fina se sometió a un tratamiento térmico a 220°C en vacío que permite equilibrar las tensiones superficiales del PS y del PMMA. De este modo, se fabricaron dos plataformas nanoestructuradas con patrones circulares compuestos de cilindros de PMMA (21 y 28 nm de diámetro) separados por una matriz de PS.

Una vez obtenidas las plataformas nanostructuradas, se diseñó un proceso de funcionalización que permitiera la localización de pequeños grupos de ligandos sobre los dominios nanométricos de PMMA. Para ello, se realizó una hidrólisis superficial de los grupos metilos del PMMA, generando así grupos ácidos más reactivos que posibilitan la unión covalente de cualquier molécula con un grupo amino terminal. En este tipo de moléculas se incluyen todas las proteínas y pequeños péptidos, lo cual pone de manifiesto la gran versatilidad de la estrategia de funcionalización.

La caracterización de la disposición espacial de los ligandos se realizó mediante microscopía de fuerzas atómicas, y se corroboró utilizando una novedosa técnica de alta resolución denominada microscopía de reconstrucción óptica estocástica, que permite confirmar el estado de agregación de los ligandos biológicamente activos.

Para validar la utilidad de estas superficies nanoestructuradas, primeramente se inmovilizó un conocido ligando de adhesión celular y se monitorizó la respuesta celular, en concreto evaluando la formación de contactos focales. Los resultados demostraron que sobre estas superficies, los fibroblastos se expandían de tal manera que el área ocupada por las células era equivalente en todos los sustratos. En cambio, cuando se analizó en detalle las estructuras macromoleculares que forman los receptores en la membrana celular tras la activación por parte del ligando, se observaron diferencias significativas. El

número de contactos focales formados en la superficie donde los grupos de ligandos estaban más separados, era menor que en aquellos cuya distancia entre ligandos era menor. Por otro lado, aquellas superficies donde los ligandos se presentaban en grupos fomentaban la maduración de los contactos focales, revelando de este modo que este proceso puede manipularse utilizando estrategias de presentación de ligandos como la desarrollada en esta tesis.

Tras verificar el potencial de nuestras plataformas, se indagó en el proceso de agregación del receptor EphB2 ante ligandos (efrinas) con una distribución nanométrica variada. Para alcanzar la resolución espacio-temporal necesaria y ser capaces de distinguir entre los diferentes oligómeros formados por el receptor, se empleó una innovadora técnica que analiza las fluctuaciones en intensidad de cada uno de los pixeles de imágenes de fluorescencia. En combinación con un modelo matemático, se demostró que la agregación de receptores para formar hexámeros y octámeros impulsa la activación máxima del receptor EphB2.

Anteriormente, se había descrito que los ligandos solubles individuales eran incapaces de activar el receptor y de promover su oligomerización. En cambio, la presentación controlada de ligandos en grupos nanométricos, no sólo fomenta la activación del receptor, sino que además acelera la formación de clústers, demostrando nuevamente la efectividad de los ligandos nanoagrupados como moduladores y potenciadores del dinámico proceso de oligomerización.

A la vista de los resultados obtenidos, se puede concluir que hemos sido capaces de desarrollar una plataforma nanoestrucuturada mediante copolímeros en bloque para su posterior modificación covalente con ligandos celulares cuya distribución en nanoagregados favorece las interacciones multivalentes con los receptores.

De este modo, estas plataformas tienen potenciales aplicaciones a la hora de promover una respuesta concreta de los receptores, en función del tamaño del grupo de ligandos y del espaciado entre ellos. Este tipo de ligandos multivalentes se presentan como una atractiva estrategia para activar los complejos receptor-ligando de manera más potente, y por lo tanto, menos costosa. Por lo tanto, las posibles aplicaciones de estos sistemas de presentación de ligandos comprenden desde aplicaciones biotecnológicas a aplicaciones biomédicas, incluyendo sistemas de cultivo celular, materiales bioactivos y administración de fármacos.

9. Appendices

In this section, techniques for fabrication or characterization are presented in detail, which were used for the thesis work but were only shorly mentioned in the experimental section

9.1. Stochastic optical reconstruction microscopy

STORM is one of the so-called super-resolution fluorescence microscopy techniques and it is based on the localization photoswitchable with high-precision. With this imaging technique, lateral resolutions of 20 nm can be achieved, thus largely beating the resolution of by conventional fluorescence microscopy, which is limited by the diffraction of light.

To achieve super-resolution, in each imaging cycle, only a fraction of the fluorophores are turned on by exciting them using different wavelengths. By this, signal overlapping is avoided and their positions can be determined with nanometric resolution. This process es repeated for a multiple number of cycles, each of them producing a stochastically different subset of fluorophores to be switched on. The positions of the excited fluorophores can be then combined to reconstruct an overall image (Figure A. 1).

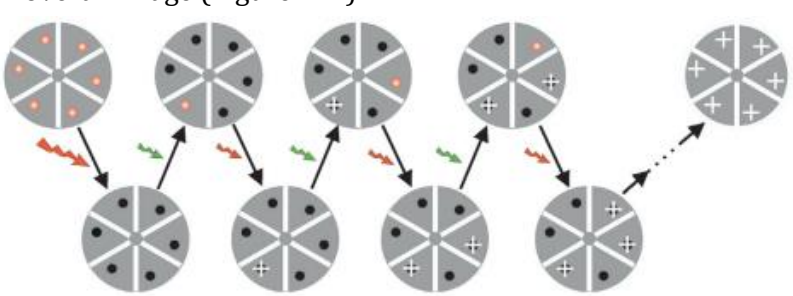

Figure A. 1 Schematics of a STORM imaging sequence using a hypothetical hexameric object labeled with red fluorophores that can be switched between a fluorescent and a dark state by a red and green laser, respectively. All fluorophores are first switched to the dark state by a strong red laser pulse. In each imaging cycle, a green laser pulse is used to switch on only a fraction of the fluorophores to give an optically resolvable set of active fluorophores. Next, under red illumination, these molecules emit fluorescence until they are switched off, allowing their positions (white crosses) to be determined with high accuracy. The overall image is then reconstructed from the fluorophore positions obtained from multiple imaging cycles. (Adapted from Rust et al., Nature Publishing Group))

STORM can be used with total-internal-reflection fluorescence microscope, low-power continuous-wave lasers and employing photoswitchable dyes. The resolution of STORM is limited by the accuracy with which individual switches can be localized during a switching cycle. The fluorescence image from a single switch gives the point-spread function and a Gaussian fit to this image is then used to localize the position of the fluorophore (centroid). Centroid positons will be then added for the image reconstruction.

The instrument used in this thesis is a Nikon instrument (N-STORM) that combines "STochastic Optical Reconstruction Microscopy" technology (licensed from Harvard University) and Nikon's Eclipse Ti research inverted microscope. A schematics of the instrument is depicted in Figure A. 2.

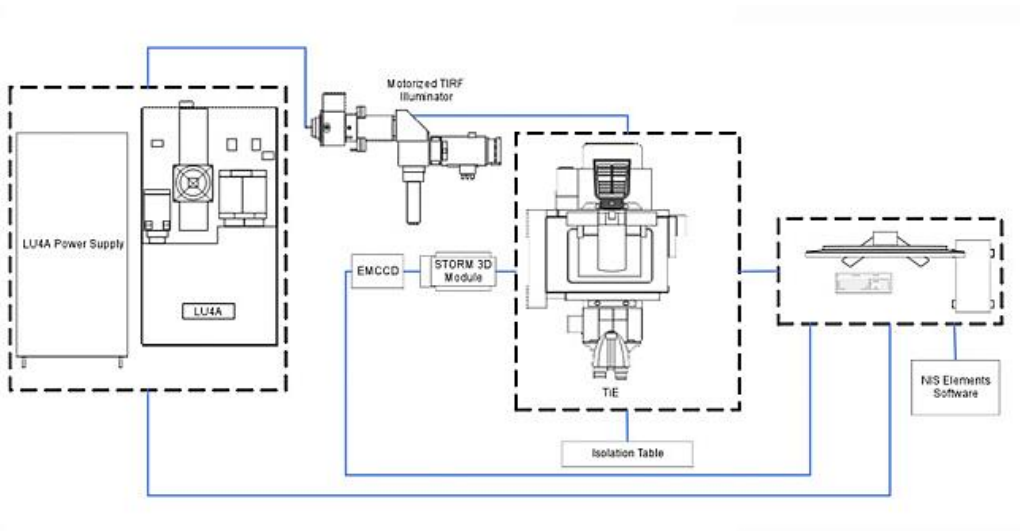

Figure A. 2 Schematics of the N-STROM set-up used in for the measurements presented in this thesis (www.nikoninstruments.com

)

9.2. Nanoscale Fourier transform infrared (nano-FTIR) spectroscopy

Infrared spectroscopy is a highly employed methodology for the chemical and structural characterization of materials. Its spatial resolution and sensitivity however, are limited by the diffraction of light, thus preventing its application to the study of nanomaterials. Nanoscale Fourier transform infrared (nano-FTIR) spectroscopy makes possible enable infrared imaging and spectroscopy with nanoscale spatial resolution. nano-FTIR spectroscopy is based on atomic force microscopy (AFM). It uses a monochromatic or broadband infrared radiation that it is scattered by a metal-coated AFM tip. The tip acts as an antenna and concentrates the incident infrared field at the very tip apex to a nanoscale spot size, locally exciting infrared-vibrational resonances in the sample that modify the tips scattered field. The AFM tip can illuminated with radiation coming from a thermal source, an infrared laser continuum or a synchrotron. Fourier transform spectroscopy of the scattered light yields a local infrared vibrational spectrum (point spectrum) of the sample surface with a spatial resolution similar of about 30 nm. (Figure A.3) [1] Spectroscopic infrared nanoimaging can then be obtained by recording a nano-FTIR spectrum at each pixel of a 2D image.

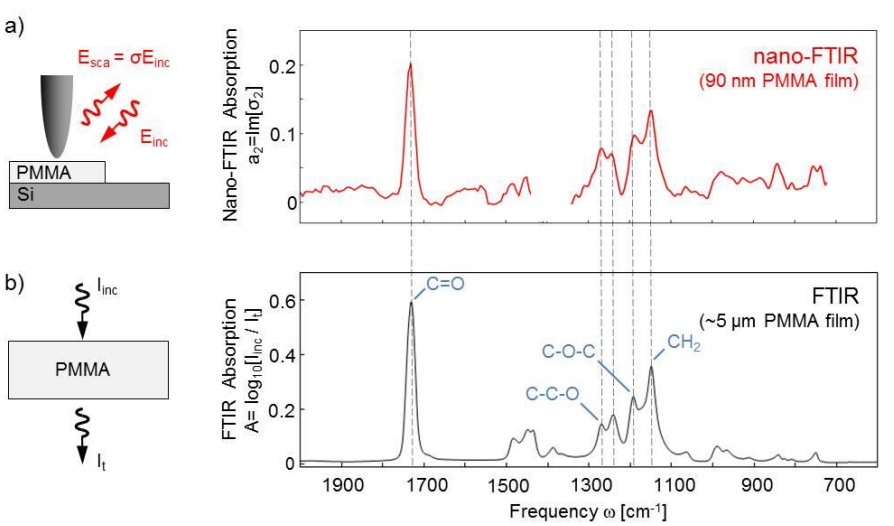

Figure A. 3 Schematic differences between the IR spectra obtained by nano-FTIR and FTIR (www.neaspec.com)

In this thesis, nano-FTIR spectroscopy has been performed by using a tunable laser continuum. To produce nanoimaging, multiple bandwidth-limited nano-FTIR spectra at each pixel of a 2D sample area recorded and stitched together. The tunable laser has a 350 cm^{-1} effective bandwidth and covers the spectral range from 1,000 to 1,900 cm^{-1}. An scheme of the set-up of the instrument is depicted in Figure A.4.

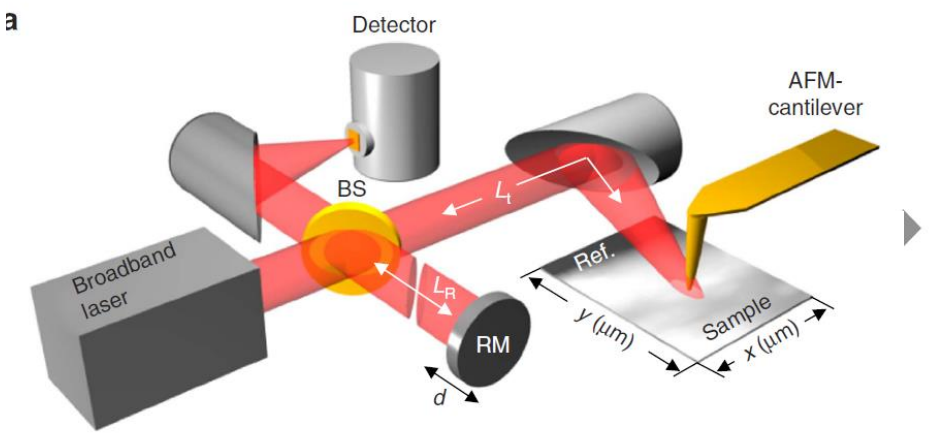

Figure A.4. Schematics of the experimental set-up of nano-FTIR from Neaspec GmbH. (www.neaspec.com)

[1] Amenabar, I. *et al.* Hyperspectral infrared nanoimaging of organic samples based on Fourier transform infrared nanospectroscopy. *Nat. Commun.* **8,** 14402 (2017)

9.3. Number and Brightness (N&B) analysis technique

Number and brightness (N&B) is an analysis method capable of measuring the average number of molecules and aggregation (brightness) in each pixel in a series of fluorescence microscopy images. It was originally developed by Qian and Elson (1990) for measurements of molecules in solution, and then it was adapted by Enrico Gratton's lab for live-cell studies[1-2]. The N&B theory exploits the variance in the fluorescence intensity fluctuations of the serial images to extract oligomerization values, representative of the molecular diversity in a single pixel. Given two series of equal average intensities, the larger is the variance, the less molecules contribute to this average. The ratio of the square of the average (first moment) intensity ($\langle k \rangle^2$) to the variance (second moment, σ^2) is proportional to the average number of particles (N). The apparent Brightness, which represents the molecular aggregation level, is calculated as the ratio of variance (σ^2) to average intensity ($\langle k \rangle$).

$$N = \frac{\langle k \rangle^2}{\sigma^2}$$

$$B = \frac{\sigma^2}{\langle k \rangle}$$

N&B works optimally in the msec to sec range, which is ideal to perform single measurements of fast interacting proteins, but the formation of larger aggregates require longer exposition.

We in here have used an in-house developed version of this analytical technique that enhances the statistical resolution of the method and at the same time expanded the time window of analysis covering the gap between sec to tens of minutes. This method, now called enhanced Number and Brightness (eN&B), can now provide the distribution of oligomeric species contained inside single pixels during long periods of times through a custom-built algorithm,[3] which makes an ideal tool for the study of molecular dynamics in living cells.

In the work presented in this thesis this method was applied to analyze time-lapse images obtained by total internal reflex ion microscopy (TIRF). TIRF is

a type of microscopy in which a very thin region of a specimen, usually less than 200 nanometers can be observed. When applied to cells, usually this means that we are observing only events taking place at their basal membrane, which is in contact with the surface. TIRF uses an evanescent wave to selectively illuminate and excite fluorophores in a restricted region close to the glass-water interface (Figure A.5). The evanescent wave is generated only when the incident light is totally internally reflected at this glass-water interface. The evanescent electromagnetic field decays exponentially from the interface, and thus penetrates to a depth of only approximately 200 nm into the sample medium. The selective visualization of the plasma membrane renders the features and events on the plasma membrane in living cells with high axial resolution.

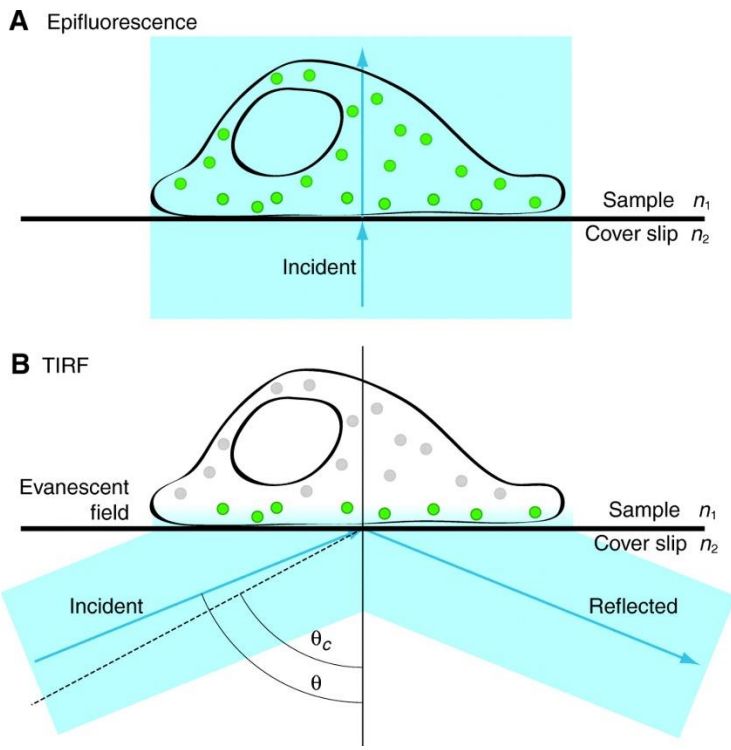

Figure A.5. Schematics of (A) epifluorescence microscopy and (B) TIRF microscopy. https://cam.facilities.northwestern.edu/588-2/tirf-microscopy/

[1] Digman, M.A., Dalal, R., Horwitz, A.F. & Gratton, E. Mapping the number of molecules and brightness in the laser scanning microscope. Biophysical journal 94, 2320-2332 (2008).

[2] Digman, M.A., Stakic, M. & Gratton, E. Raster image correlation spectroscopy and number and brightness analysis. Methods in enzymology 518, 121-144 (2013).

[3] Ojosnegros S., Cutrale F., Rodriguez D., Otterstrom J.J., Chiu C., Hortigüela V., Tarantino C., Seriola A., Mieruszynski S., Martinez E., Lakadamyali M., Raya A., & Fraser S.E. Cell-cell communication signalling modulated by polymerization-condensation of receptors. *Under review*

10. Publications

Author's journal articles:

Nanopatterns of surface-bound ephrinB1 ligands produce multivalent effects on EphB2 receptor clustering.
Hortigüela V., Larrañaga E., Ojosnegros S., Cutrale F., Seriola A., Lagunas A., Andilla J., Loza-Alvarez P., Samitier J. & Martínez E.
In preparation

Cell-cell communication signalling modulated by polymerization-condensation of receptors.
Ojosnegros S., Cutrale F., Rodriguez D., Otterstrom J.J., Chiu C., **Hortigüela V.**, Tarantino C., Seriola A., Mieruszynski S., Martinez E., Lakadamyali M., Raya A., & Fraser S.E.
Under review

Methods for rectifying cell motions in vitro: Breaking symmetry using microfabrication and microfluidics.
Comelles J., **Hortigüela V.**, Martínez E., & Riveline D.
In E. K. Paluch (Ed.), Biophysical methods in cell biology, (2015) Volume 125 (pp. 437-452) Academic Press.

Cells as Active Particles in Asymmetric Potentials: Motility under External Gradients.
Comelles, J., Caballero, D., Voituriez, R., **Hortigüela, V.**, Wollrab, V., Godeau, A., Samitier, J., Martínez, E. & Riveline, D.
Biophysical Journal, (2014) 107(7), 1513 – 1522.

Protein patterning on hydrogels by direct microcontact printing: application to cardiac differentiation.
G. Castaño, A., **Hortigüela, V.**, Lagunas, A., Cortina, C., Montserrat, N., Samitier, J. & Martínez, E.
RSC Advances, (2014) 4(55), 29120-29123.

Continuous bone morphogenetic protein-2 gradients for concentration effect studies on C2C12 osteogenic fate.

Lagunas, A., Comelles, J., Oberhansl, S., **Hortigüela, V.**, Martínez, E. & Samitier, J. Nanomedicine: NBM, (2013) 9(5), 694-701.

Versatile gradients of covalently bound proteins on microstructured substrates. Comelles, J., **Hortigüela, V.**, Samitier, J. & Martínez, E.
Langmuir, (2012) 28(38), 13688-13697.